Photoelectron Spectroscopy of Reactive Intermediates with Synchrotron Radiation

A THESIS SUBMITTED TO THE UNIVERSITY OF SOUTHAMPTON

FOR THE DEGREE OF

DOCTOR OF PHILOSOPHY

FABRIZIO INNOCENTI

SCHOOL OF CHEMISTRY

UNIVERSITY OF SOUTHAMPTON

OCTOBER 2004

UNIVERSITY OF SOUTHAMPTON

ABSTRACT

FACULTY OF SCIENCE
SCHOOL OF CHEMISTRY

Doctor of Philosophy

PHOTOELECTRON SPECTROSCOPY OF REACTIVE INTERMEDIATES WITH SYNCHROTRON RADIATION

by Fabrizio Innocenti

The work described in this thesis is a study of unstable species in the gas phase using photoelectron spectroscopy. The overall aim of this work was to study the photoionization behaviour of reactive species using photoelectron spectroscopy with Synchrotron Radiation. UV photoelectron spectroscopy studies of the N and S atoms and the OH, OD, SH, NO and CF radicals have been performed using Synchrotron Radiation. Constant ionic state (CIS) angular resolved experiments have been made. In these experiments, autoionizing resonances have been observed and assigned to members of series of Rydberg states converging towards higher ionic limits.

For the first time Rydberg series converging to the fourth ionization limit of S atoms have been observed and assignments have been proposed.

The relative photoionization cross section of the first PE band of CF radicals has been measured as a function of photon energy and Rydberg series converging to the second PE band of CF have been observed for the first time.

Vibrational and rotational resolution has been obtained in OH and OD CIS spectra. For each reactive atom and molecule studied, measurement of angular distributions of photoelectrons allowed insight into the photoionization dynamics to be obtained.

MEMORANDUM

This thesis is an account of original research performed by the author in the School of Chemistry of the University of Southampton, between October 2001 and October 2004. Where findings of other work have been used, due reference has been given.

Acknowledgments

First of all I would like to tank my supervisor, Professor John M. Dyke, for his help, invaluable support and encouragement during these three years. Thanks also to Dr. Alan Morris for having provided important experimental and technical help especially during his stay in Trieste in the "grappa" field.

I am also grateful to the rest of the research group, particularly Lucia, Ed, Giacomino, Manuel, Inma and Santy. Thanks for the wonderful company!

Many thanks to all the people I worked with in Trieste, especially Lucia who did all the night shifts, Manuel and Romeo for their tireless effort, Professor John B. West and Dr. Stefano Stranges for their helpful advices.

I am very grateful to Professor Dolores Gauyacq and her group in France, especially Séverine, Stephane and Niloufar, for the lovely time I spent in Orsay.

Finally I thank Loredana and Fabrice, without you the time here would not have been the same!

Fabrizio

Table of Contents

List of Figures

List of Tables

Chapter 1

1 INTRODUCTION

The work described in this thesis is a study of unstable species in the gas phase using spectroscopic techniques. Unstable species, including complexes and radicals, are currently receiving a great deal of attention from the chemistry community as a result of recent developments in experimental and theoretical methods. All of the chemical properties of molecules are a consequence of their electronic structure, in particular the nature of their valence electrons. Chemical reactions proceed by movement of electrons, hence to understand the properties of molecules knowledge of their electronic structure is important. Such knowledge has been gained through a variety of spectroscopic methods.

The techniques for performing vacuum ultraviolet studies of photoionization in the gas phase were introduced about four decades ago[1]. Two general methods have been employed:

- analysing the kinetic energy spectrum of photoelectrons (Photoelectron Spectroscopy, PES), and
- measuring the intensities of mass-selected ions as functions of incident photon energy (Photoionization Mass Spectroscopy, PIMS).

The results included in this thesis have been obtained by the use of the PES technique.

1.1 Photoelectron Spectroscopy (PES)

Photoionization is the term used to describe the process whereby radiation ejects one or more electrons from an atom or molecule. The origin of the subject may be traced back to the end of the last century when Hertz[2], in 1887, made the first observation of ionization of matter through the interaction of ultraviolet radiation with a solid. This discovery led Einstein[3] to describe, in 1905, the photoelectric effect from a theoretical point of view.

1.1.1 Basic principles

Photoelectron spectroscopy (PES) is a technique for investigating the electronic structure of atoms and molecules[4]. This involves photoionization of the atom or molecule of interest and subsequent measurement of the kinetic energy of the ejected electron. If a sufficiently energetic photon interacts with an atom to produce a photoelectron and a corresponding photoion, the basic process can be written as:

$$A + h\nu \rightarrow A^{+} + e^{-} \qquad \text{Eq. 1.1}$$

From the laws of energy and momentum conservation, it is easily seen that the kinetic energy of the photoelectron ejected from level i, $E_{e,kin,i}$, is given by the difference between the photon energy $h\nu$ and the binding energy of level i, $E_{bind,i}$:

$$E_{e,kin,i} = h\nu - E_{bind,i} \qquad \text{Eq. 1.2}$$

In principle this is a simple technique, it requires a source of monochromatic and sufficiently energetic radiation, a sample, an electron kinetic energy analyser and an electron detector. Hence, in a photoelectron spectroscopy experiment a target is irradiated by a monochromatic photon beam and the released photoelectrons are analysed according to their kinetic energies. Obviously, this technique is capable of providing information about the electron binding energies for all levels i that can be ionized.

Radiation of tens of eV of energy, in the region called the vacuum ultraviolet (VUV), is sufficiently energetic to ionize electrons from valence orbitals. With

radiation in the region called the extreme ultraviolet (XUV), whose energy is between tens and hundreds of eV, electrons from more tightly bound orbitals can also be ionized.

Photoelectron spectroscopy has been evolving during the last thirty years, when Synchrotron Radiation has been used as the photon source[5]. Synchrotron Radiation is emitted by electrons moving at relativistic velocities, tangentially to the electron flight path. Synchrotron Radiation can be monochromatized and tuned continuously in the range of energy from the far-infrared to the hard X-ray region, in contrast to radiation at fixed wavelength in the VUV region which is emitted by most rare-gas discharge lamps.

Synchrotron Radiation is also naturally polarized and angle resolved experiments can be carried out with greater sensitivity than with an unpolarized source.

The study of a reactive intermediate with photoelectron spectroscopy using monochromatized Synchrotron Radiation[6,7] should allow more information to be obtained on the molecular ionic states produced and the associated photoionization processes than a PES study with a low pressure discharge of an inert gas as the photon source[8-10], in particular:

- a study of the relative band intensities in the valence photoelectron spectrum of a small molecule as a function of the ionizing photon energy can provide valuable information to assist band assignment
- measurement of photoelectron angular distributions at fixed photon energy allows information on photoionization dynamics to be obtained
- an autoionization resonance, once identified, can give rise to extra structure over that observed in a photoelectron spectrum recorded off resonance[11-14]. This effect was first observed by Price[15] for the oxygen molecule where one of the neon discharge resonance lines coincided with a resonance in O_2; the resulting photoelectron spectrum showed considerably more vibrational structure than one taken using the helium discharge line.

It was this last point which initially attracted the Southampton PES group to use Synchrotron Radiation because in a number of previous investigations some of the valence photoelectron bands of the reactive species studied, when recorded with a

HeI (21.22 eV) photon source, showed an intense adiabatic component with very little intensity in other vibrational components. Such an observation for the first photoelectron band of a short-lived molecule is particularly disappointing, since measurement of the vibrational level separations in the ground ionic state is usually one of the main objectives of the experiment[16,17].

For the second point, the polarization properties of the Synchrotron Radiation Source can be utilized to measure angular distribution parameters[18]. This facility can be important in identifying the ionic symmetries associated with new structure observed in the photoelectron spectrum, as well as being a powerful method of showing the presence of weak underlying structure in the photoionization continuum.

In order to achieve the aim of the first point, the constant ionic state (CIS) technique is used, in which the photoelectron spectrometer is set on a particular ionic vibrational level known to belong to the species of interest, and the exciting wavelength is then scanned in synchronism with the kinetic energy of the electrons that are detected. In this way a relative partial ionization cross section of the molecule is obtained, and new structure in the continuum is observed. In fact, very little is known about the ionization continua of short-lived molecules and this method is an ideal way of obtaining such information.

1.1.2 Angle resolved experiments

In angle resolved experiments photoelectrons are selected according to their kinetic energy and the angle θ with respect to the polarization vector of the ionizing radiation at which they are emitted. The relative photoionization cross section σ_i and the asymmetry parameter β_i may be calculated as well. These parameters are related to the experimentally observed intensity of level $I_i(\theta)$ by[6]:

$$I_i(\theta) \propto \frac{d\sigma_i}{d\Omega} = \frac{\sigma_i}{4\pi}\left[1 + \frac{\beta_i}{4}(1 + 3P\cos 2\theta)\right] \qquad \text{Eq. 1.3}$$

where $d\sigma_i/d\Omega$ is the differential cross section and P is the degree of linear polarization of the incoming radiation.

The photoelectrons are not emitted isotropically; their angular distribution is determined by β_i. By measuring the intensity $I_i(\theta)$ at two different angles, θ, the relative cross section and the asymmetry parameter can be easily calculated.

1.1.3 Constant Ionic State spectra

In addition to photoelectron spectra, constant ionic state (CIS) spectra can also be recorded with a Synchrotron Radiation Source[19]. A CIS spectrum is the measurement of the cross section for photoionization to a specific ionic state as a function of the photon energy. A resonance in a CIS spectrum can occur when the energy of the incident radiation is equal to an excitation energy to a neutral state above the ionization limit to produce an excited state that autoionizes and modifies the process in Eq. 1.1 to the following:

$$A + h\nu \rightarrow A^* \qquad \text{Eq. 1.4}$$

$$A^* \rightarrow A^+ + e^- \qquad \text{Eq. 1.5}$$

For this kind of spectrum the evaluation of the photoionization parameters σ_i and β_i as a function of the photon energy can reveal information on the excited state and free electron wavefunctions and can lead to a better understanding of the dynamics of the photoionization process.

1.2 Molecular photoelectron spectroscopy

The chemical properties of a molecule are determined by its electronic structure, in particular by the character of its valence electrons.

When the species investigated is a molecule, there are additional possibilities of vibrational and rotational excitation on ionization; Eq. 1.2 then became:

$$E_{e,kin,i} = h\nu - E_{bind,i} - \Delta E_{vib} - \Delta E_{rot} \qquad \text{Eq. 1.6}$$

where ΔE_{vib} is the change in vibrational energy and ΔE_{rot} is the change in rotational energy on ionization.

The resolution normally achievable in VUV photoelectron spectroscopy allows vibrational structure to be resolved in most light molecules. In contrast resolution of rotational structure is beyond the capabilities of conventional PES, with some small exceptions[20,21].

In the case of fixed photon energy, the direct photoionization of molecules can be written schematically as:

$$M(v'') + h\nu \rightarrow M^+(v^+) + e^- \qquad \text{Eq. 1.7}$$

and the distribution of intensity of the v^+ vibrational components of a photoelectron band can be approximated by the *Franck-Condon Factors* (FCFs), as described in the later theoretical section (Chapter 2.3), the square of the overlap integral between the vibrational wavefunctions of the initial ($\Psi_{M,v''}$) and ionic (Ψ_{M^+,v^+}) states:

$$I_{v^+ \leftarrow v''} \propto \left| \int_0^{+\infty} \Psi_{M^+,v^+}(R) \Psi_{M,v''}(R) dR \right|^2 \qquad \text{Eq. 1.8}$$

In the case of resonant photoionization, when the cross section for photoionization to a specific ionic state is measured as function of the photon energy:

$$M(v'') + h\nu \rightarrow M^*(v') \qquad \text{Eq. 1.9}$$

$$M^*(v') \rightarrow M^+(v^+) + e^- \qquad \text{Eq. 1.10}$$

the distribution of intensity of the v^+ vibrational components of a photoelectron band can be expressed by the following expression:

$$I_{v^+ \leftarrow v' \leftarrow v''} \propto \left| \int_0^{+\infty} \Psi_{M^+,v^+}(R) \Psi_{M^*,v'}(R) dR \right|^2 \times \left| \int_0^{+\infty} \Psi_{M^*,v'}(R) \Psi_{M,v''}(R) dR \right|^2 \qquad \text{Eq. 1.11}$$

which is a product of the FCFs for the two steps involved.

Any molecular system possesses a wealth of highly excited neutral states that may be accessed by resonant absorption of radiation. In particular there exist Rydberg states[22] that are grouped into series converging to ionic limits.

1.2.1 Resonant effect and Rydberg states

Rydberg electronic states are hydrogen-like states resulting from promotion of an electron to an orbital in which its average distance from the centre of the molecule is much larger than that of the other lower-energy electrons. This state can be described by electronic configurations where one orbital has a principal quantum number greater than those of the other occupied orbitals. From the point of view of the distant electron, the molecule is little different from an ion with a +1 charge, since the nuclei, total charge +N, are screened by (N-1) electrons. The electronic configuration of the unexcited electrons corresponds to a state of the positively charged ion, and for this reason it is conventionally called the ionic core.

The energies of Rydberg states follow the formula[22]:

$$E_n = I - \frac{R}{(n-\delta)^2} \qquad \text{Eq. 1.12}$$

where I is the ionization energy for complete removal of the excited electron, R is the Rydberg constant, δ is the quantum defect and n is the principal quantum number.

The quantum defect, δ, allows for the deviation of the Rydberg energy levels from that expected for a 1-electron system. Its magnitude reflects the penetration of the Rydberg orbital into the ionic core and it is related to the radial distribution of the excited orbital.

Many of these discrete states are situated above the first ionization limit, and thus lie within an ionization continuum. When the energy of an incident photon matches that of a transition to one of these Rydberg states, two processes become viable: direct photoionization and resonant photoabsorption to the neutral state M^*.

At these resonant wavelengths there is a significant probability of an excited neutral state M^* being generated as an alternative to direct ionization to M^+. The production of the excited state can be quite large, as cross sections for resonant one-photon absorption are larger than those for photoionization at a given wavelength.

The excited neutral state can then decay by autoionization. This is a common decay route for Rydberg states although fluorescence and non-radiative processes are also possible.

1.3 Reactive Intermediates

The exact nature of short-lived reactive species in the gas-phase is very varied. One class of species which are commonly short-lived in the gas-phase are radicals. Radicals are usually defined as neutral molecules with one or more unpaired electrons. They are frequently found to play important roles in areas such as combustion, atmospheric chemistry and energy transfer in chemical laser systems. The method of study of short-lived molecules depends upon the molecule, and the system in which it is to be studied. For *in situ* study of molecules prepared by a rapid gas phase reaction, it is necessary to study the molecules immediately after production otherwise their partial pressure will be reduced by reaction. Short-lived species, both neutral and ionized, are of great importance in atmospheric and astrophysical chemistry. Reaction intermediates, despite being present in low partial pressure, can have a major influence on the gas phase chemistry. Due to experimental difficulties, short-lived molecules of fundamental importance in these areas have not been thoroughly studied, and their electronic structure, which may be complex, not fully investigated.

The Southampton PES group has concentrated on the study of reactive intermediates as its main research topic. Initial work was performed on short-lived molecules, formed in the gas phase in discharges[23-25] or by chemical reaction[26]. A review of PES investigations performed in Southampton using HeI (21.22 eV) and HeII (40.81 eV) radiation from discharge lamps can be found in reference (17) and a review of the work performed to date with Synchrotron Radiation is contained in reference ([27]).

The study of the electronic structure of short-lived radical species in the gas-phase forms the major part of this work.

1.4 Aims of the Project and Structure of the Thesis

The overall aim of this thesis was to study the photoionization behaviour of reactive species using photoelectron spectroscopy with Synchrotron Radiation with particular focus on the electronic structures of species that play key roles in the chemistry of

the Earth's atmosphere. This should allow information to be obtained on neutral as well as ionic states of the reactive species investigated. All the measurements have been made at the ELETTRA third generation Synchrotron Radiation Source (BL 4.2R) in Trieste[28], Italy. In this thesis the theory and the fundamental principles behind photoionization and resonant states is presented in Chapter 2, while Chapter 3 outlines a brief introduction of the characteristics of Synchrotron Radiation. Chapter 4 describes the experimental apparatus used for the study of PES of reactive intermediates. The results of angular distribution studies on OH and OD radicals, nitrogen atoms, S atoms and SH radicals, NO and CF radicals are presented in Chapters 5 to 10 respectively. Finally, Chapter 11 concludes the thesis with a summary of the project, and outlines some possibilities for further work.

An Appendix lists the papers which have been published so far during this Ph.D studentship. It includes a joint project performed with the Orsay group, part of the EC *"Reactive Intermediates"* Network, using Synchrotron Radiation, a joint project with the ETH Zurich photoelectron group on a study of ozone with ZEKE-PFI photoelectron spectroscopy and a joint project with the Aarhus group using Synchrotron Radiation on a study of absolute photoionization cross-section of Ca^+ ions.

References

[1] J. Berkowitz and B. Ruscic *Vacuum Ultraviolet Photoionization and Photodissociation of Molecules and Clusters*, edited by C.Y. Ng, World Scientific ed.London, 1991.

[2] H. Hertz
Annalen der Physik **31**, 983 (1887).

[3] A. Einstein
Annalen der Physik **17**, 132 (1905).

[4] J. H. D. Eland *Photoelectron Spectroscopy*, Butterworths & Co ed.Oxford, 1984.

[5] V. Schmidt *Electron Spectrometry of Atoms using Synchrotron Radiation*, Cambridge University Press ed.New York, 1997.

[6] J. B. West *Vacuum Ultraviolet Photoionization and Photodissociation of Molecules and Clusters*, edited by C.Y. Ng, World Scientific ed.London, 1991.

[7] I. Nenner and J. A. Beswick *Handbook on Synchrotron Radiation*, edited by G.V. Marr, Elsevier ed.Amsterdam, 1987; Vol. II.

[8] J. M. Dyke, L. Golob, N. Jonathan, A. Morris and M. Okuda
Journal of The Chemical Society Faraday Transactions 2 **70**, 1828 (1974).

[9] J. M. Dyke, N. Jonathan and A. Morris
Internal Review of Physical Chemistry **2**, 3 (1982).

[10] J. Baker, M. Barnes, M. C. R. Cockett, J. M. Dyke, A. M. Ellis, M. Feher, E. P. F. Lee, A. Morris and H. Zamanpour
Journal of Electron Spectroscopy and Related Phenomena **51**, 487 (1990).

[11] D. M. P. Holland, J. B. West and M. A. Hayes
Journal of Chemical Physics **148**, 241 (1990).

[12] K. Codling, A. C. Parr, D. L. Ederer, R. Stockbauer, J. B. West, B. E. Cole and J. L. Dehmer
Journal of Physic B - Atomic and Molecular Physics **14**, 657 (1981).

[13] P. Natalis, J. E. Collin, J. Delwiche, G. Caprace and M. J. Hubin
Journal of Electron Spectroscopy and Related Phenomena **17**, 205 (1979).

[14] J. A. R. Samson
Physical Review **28 c**, 303 (1976).

[15] W. C. Price *Molecular Spectroscopy*, edited by P. Hepple, Institute of Petroleum ed.London, 1968.

[16] J. M. Dyke
Journal of The Chemical Society Faraday Transactions 2 **83**, 67 (1987).

[17] M. C. R. Cockett, J. M. Dyke and H. Zamanpour *Vacuum Ultraviolet Photoionization and Photodissociation of Molecules and Clusters*, edited by C.Y. Ng, World Scientific ed.London, 1991.

[18] J. B. West, J. M. Dyke, A. Morris, T. G. Wright and S. D. Gamblin
Journal of Physic B - Atomic and Molecular Physics **32**, 2763 (1999).

[19] A. Haworth, D. G. Wilden and J. Comer
Journal of Electron Spectroscopy and Related Phenomena **37**, 291 (1985).

[20] L. Asbrink and J. W. Rabalais
Chemical Physics **12**, 1821 (1971).

[21] J. W. Rabalais, T. Bergmark, L. O. Werme, L. Karlsson and K. Siegbahn
Physica Scripta **3**, 13 (1971).

[22] A. B. F. Duncan *Rydberg series in atoms and molecules*, Academic Press ed.New York, 1971.

[23] N. Jonathan, D. J. Smith and K. J. Ross
Chemical Physics Letters **9**, 217 (1971).

[24] N. Jonathan, A. Morris, K. J. Ross and D. J. Smith
Journal of Chemical Physics **54**, 4954 (1971).

[25] N. Jonathan, A. Morris, M. Okuda, K. J. Ross and D. J. Smith
Faraday Discussion Chemical Society **54**, 1 (1972).

[26] L. Andrews, J. M. Dyke, N. Keddar, N. Jonathan and A. Morris
Journal of American Chemistry Society **106**, 229 (1984).

[27] J. D. Barr, L. J. Beeching, A. DeFanis, J. M. Dyke, S. D. Gamblin, N. Hooper, A. Morris, S. Stranges, J. B. West, A. E. Wright and T. G. Wright
Journal of Electron Spectroscopy and Related Phenomena **108**, 47 (2000).

[28] http://www.elettra.trieste.it

Chapter 2

2 FUNDAMENTAL PRINCIPLES

Experimental investigations of the photoionization process began in 1887 when Hertz discovered the photoelectric effect[1]. However the understanding of the process had to wait until the crucial theory proposed by Einstein[2] in 1905, that electromagnetic radiation could be considered to be quantized in the form of photons, each with energy $h\nu$. In this Chapter the basic relations governing the photoionization process will be presented. Photoelectron spectroscopy with a fixed wavelength radiation source and photoelectron spectroscopy with a tuneable wavelength radiation source are considered from a fundamental point of view.

2.1 Photoelectron spectroscopy with a fixed wavelength radiation source

The aim of photoelectron spectroscopy (PES) is to provide information on the ionic states of atoms and molecules. Irradiation of a sample with sufficiently energetic photons causes direct ionization of that sample. Typically, photons of several tens of eV in energy are required, and suitable photon sources are those emitting vacuum ultraviolet radiation. A particular ionic state M_i^+ may be formed in this manner provided that the energy of ionization to that state, IE_i is less than the photon energy $h\nu$. The kinetic energy of the photoelectron, E_{kin}, is given by:

$$E_{kin} = h\nu - IE_i - \Delta E_{vib} - \Delta E_{rot} \qquad \text{Eq. 2-1}$$

where ΔE_{vib} and ΔE_{rot} are the differences in vibrational and rotational energy on ionisation. Typically rotational resolution is not achieved in a conventional PE spectrum because the spectral resolution is too low, so the ΔE_{rot} term is averaged into IE_i to give IE_i'.

The resolution for this kind of experiment is typically in the region of 200 cm^{-1} (0.025 eV), hence vibrational structure can usually be resolved. This allows an estimation of the vibrational constant ω_e^+ in an ionic state from analysis of a vibrationally resolved photoelectron band. It is assumed, to a first approximation, that all excess energy over ($IE_i' + \Delta E_{vib}$) is released as electron kinetic energy, since the electron is much lighter than any molecular or atomic ion, and the law of conservation of momentum ensures that the change in kinetic energy of the ion is negligible.

A photoelectron spectrum is recorded by counting photoelectrons produced per unit time over a range of kinetic energies, with the photon energy fixed, and it thus provides a map of cationic states of a molecule. In a photoelectron spectrum, one band will be observed for ionization to each ionic state accessed.

The direct ionization processes that are allowed in photoelectron spectroscopy are governed by selection rules for the electronic and vibrational changes that may occur

on ionization. In general the probability that a direct transition between the molecule ground state characterized by the eigenfunction Ψ'' and the final (ion plus free electron) state characterized by Ψ' is determined by the square of the transition moment integral[3,4]:

$$\overline{M} = \langle \Psi'' | \Sigma \overline{p} | \Psi' \rangle \qquad \text{Eq. 2-2}$$

where $\overline{p}$ is the electric dipole moment operator and the sum extends over all electrons i and nuclei j; Ψ'' and Ψ' are functions of the electron, r, and nuclear, R, coordinates.

Using the Born-Oppenheimer approximation, the initial and final eigenfunctions can be separated into the product of electronic and nuclear wavefunctions:

$$\Psi(r;R) = \Psi_{es}(r;R)\Psi_n(R) \qquad \text{Eq. 2-3}$$

The nuclear wavefunction, $\Psi_n(R)$, is treated simply as a vibrational function, $\Psi_n \equiv \Psi_v$, as by reference to a rotating molecule coordinate system the rotation may be neglected here.

The dipole operator can also be separated into an electronic and a nuclear dependent part $\Sigma_{i,j}\overline{p} = \Sigma_i \overline{p}_e + \Sigma_j \overline{p}_n$. Substituting these results into Eq. 2-2 the transition moment integral becomes:

$$\overline{M} = \iint \Psi_{es}^{*}''(r;R)\Psi_v^{*}''(R) \left| \Sigma_i \overline{p}_e + \Sigma_j \overline{p}_n \right| \Psi_{es}'(r;R)\Psi_v'(R) d\tau_e d\tau_n \qquad \text{Eq. 2-4}$$

This integral can be separated according to the electronic and nuclear dipole operators:

$$\overline{M} = \int \Psi_v^{*}''(R)\Psi_v'(R) d\tau_n \int \Psi_{es}^{*}''(r;R) \left| \Sigma_i \overline{p}_e \right| \Psi_{es}'(r;R) d\tau_e$$

$$+ \int \Psi_v^{*}''(R) \left| \Sigma_j \overline{p}_n \right| \Psi_v'(R) d\tau_n \int \Psi_{es}^{*}''(r;R)\Psi_{es}'(r;R) d\tau_e \qquad \text{Eq. 2-5}$$

Since electronic eigenfunctions belonging to different states are orthogonal to one another, the second term in Eq. 2-5 vanishes for electronic transitions. If then the dependence of Ψ_{es} on the nuclear coordinates is neglected, assuming that the variation of $\overline{p}_e$ with R is negligible, Eq. 2-5 becomes:

$$\overline{M} = \int \Psi_v^{*}"(R)\Psi_v{}'(R)d\tau_n \int \Psi_{es}^{*}"(r;R_0)|\Sigma_i \overline{p}_e|\Psi_{es}{}'(r;R_0)d\tau_e \qquad \text{Eq. 2-6}$$

This equation consists of a factor which depends on the nuclear motion alone and a factor depending on the electronic motion alone.

From the above considerations, the photoionization transition probability may be written as:

$$P \propto \left| \int \Psi_v^{*}"(R)\Psi_v{}'(R)d\tau_n \right|^2 \left| \int \Psi_{es}^{*}"(r;R_0)|\Sigma_i \overline{p}_e|\Psi_{es}{}'(r;R_0)d\tau_e \right|^2$$

$$\propto \left|\overline{M}_v\right|^2 \left|\overline{M}_{es}\right|^2 \qquad \text{Eq. 2-7}$$

The first term is called the *Franck-Condon Factor* and the second term is the electronic transition moment squared.

2.1.1 Electronic selection rules

Photoelectron transitions are allowed whenever the integral, $\overline{M}_{es}$, of Eq. 2-7 is different from zero. Only single-electron transitions are permitted in photoionization because the operator in $\overline{M}_{es}$ is a one-electron operator. If the wavefunctions for the neutral and ionized states are constructed from the same set of molecular orbitals and a one-electron operator is used, only states characterized by an electronic configuration differing from that of the neutral molecule by one molecular orbital will be allowed in PES.

For systems in which spin-orbit interaction is small, the electronic eigenfunctions including spin Ψ_{es} can be treated as a product of an orbital and a spin function:

$$\Psi_{es} = \Psi_e \times \Psi_s \qquad \text{Eq. 2-8}$$

Since the dipole operator does not operate on spin coordinates, the transition moment may be factorized as:

$$\left\langle \Psi_e^{*}" \middle| \overline{p}_e \middle| \Psi_e{}' \right\rangle \left\langle \Psi_s" \middle| \Psi_s{}' \right\rangle \qquad \text{Eq. 2-9}$$

The spin wavefunctions corresponding to different spin values are orthogonal to another; therefore the second integral in Eq. 2-9 vanishes for states of different spin. Photoelectron transitions are thus allowed only between initial and final states of the same total spin, that is, $\Delta S = 0$. In determining the spin of the final state, it is necessary to consider the spin of the positive ion and the photoelectron. This combined spin must be equal to that of the initial molecular state if the transition is to be allowed. Since the photoelectron has half-integral spin, the spins of the molecule and ion must differ after ionization by $\pm 1/2$. Hence, for closed-shell molecules with singlet neutral ground states, only doublet ionic states may be accessed, one for each orbital ionized. Many short-lived molecules have only partially filled outer shells, so that ionization from each orbital may yield more than one cationic state. Hence, the correspondence between the number of doubly filled levels and number of bands in a PE spectrum, observed in a closed-shell molecule, is lost.

2.1.2 Vibrational selection rules

The probability of a vibrational transition during the ionization process is proportional to[3]:

$$\left|\overline{M}_v\right|^2 = \left|\left\langle \Psi_v^{*}{}'' \middle| \Psi_v{}' \right\rangle\right|^2 \equiv \left|\left\langle \Psi_v^{*}{}'' \middle| \Psi_v^{+} \right\rangle\right|^2 \qquad \text{Eq. 2-10}$$

where, for the ionization process, $\Psi_v{}' \equiv \Psi_v^{+}$.

This quantity corresponds to the square of the vibrational overlap integral; as mentioned before (Section 2.1.1) it is called the *Franck-Condon Factor* and is largely responsible for the relative intensities of the vibrational components in a photoelectron band. This overlap integral does not vanish by orthogonality because Ψ_v^{+} and Ψ_v'' are vibrational functions belonging to different electronic states. Moreover the intensity of a vibrational component in an electronically allowed transition is proportional to the absolute square of the overlap integral of the vibrational wavefunctions of the initial and final states; hence the transitions are favoured when there is a large overlap between the vibrational wavefunctions.

Potential energy curves are shown in Figure 2.1 for a hypothetical molecule *AB* in its ground state and the corresponding molecular ion AB^+ in two possible ionic states, and the corresponding photoelectron band envelops.

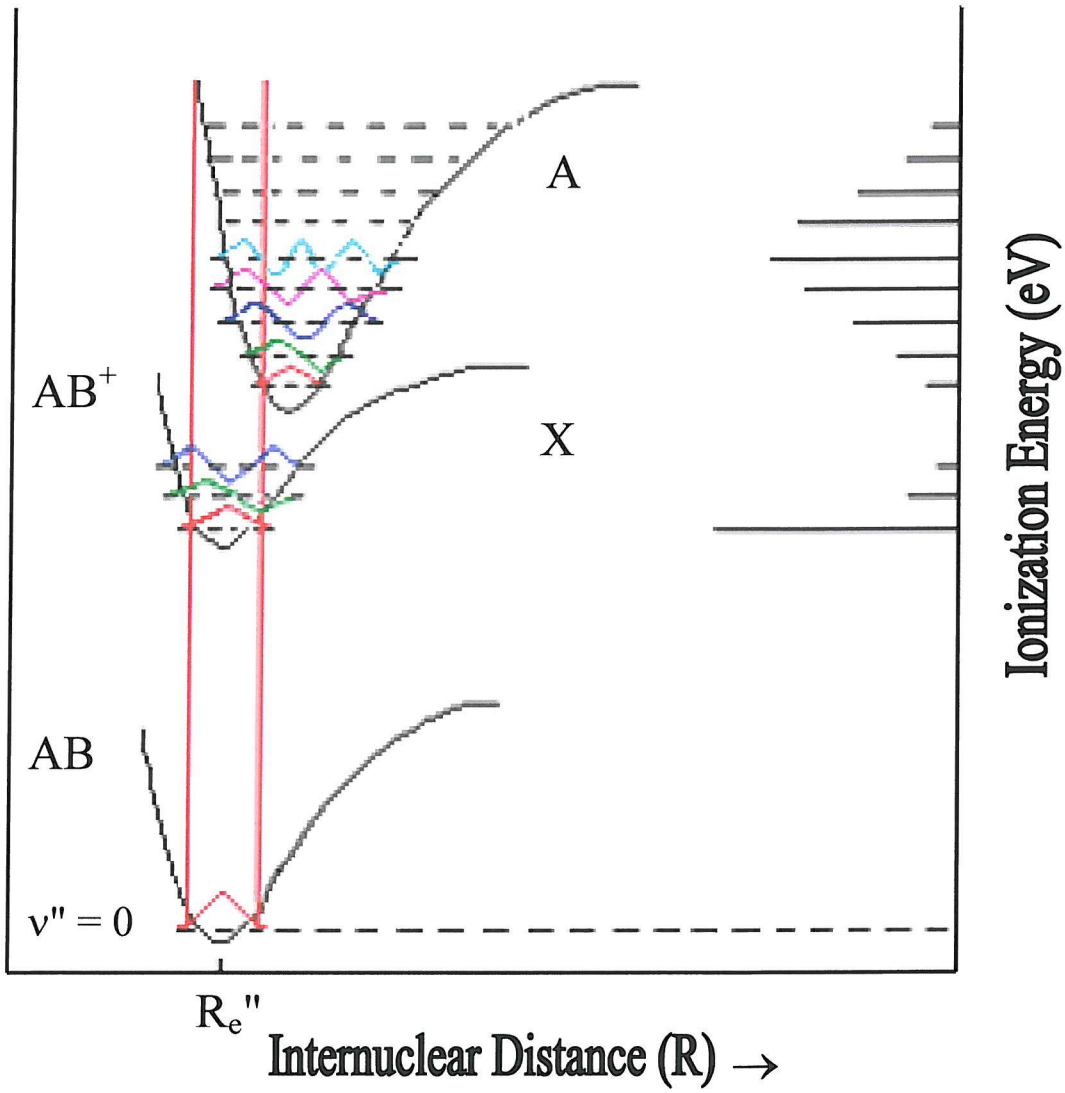

Figure 2.1 *Potential energy curves for a molecule AB in its ground state and the corresponding molecular ion AB^+ state in two different ionic states.*

Both narrow and broad bands are frequently observed in photoelectron spectra, which have led to the definition of two different ionization energies (adiabatic and vertical ionization energies).

The Adiabatic Ionization Energy (AIE)[5] is the energy required to ionize from the lowest vibrational level of a molecule to the lowest vibrational level of an ionic state, as in the process AB^+, $v^+=0 \leftarrow AB$, $v"=0$.

The Vertical Ionization Energy (VIE)[5] is the energy required to ionize from the lowest vibrational level of a molecule to an ionic state vibrational level that gives a maximum value for the overlap integral in Eq. 2-10. In practice, the VIE is measured as the most intense component of a photoelectron band.

The vibrational eigenfunctions drawn in Figure 2.1 are intended to approximate those of an anharmonic oscillator.

The wavefunctions for the $v = 0$ levels are bell-shaped curves whose maxima lie between the classical turning points of the vibrational level. The eigenfunctions of the higher vibrational levels have broad maxima or minima near the classical turning points of the motion and several maxima and minima between the turning points. The contributions to the overlap integral from these intermediate maxima and minima will roughly cancel one another.

Considering the $v^+ = 0 \leftarrow v" = 0$ band, the product of the two eigenfunctions for $v" = 0$ and $v^+ = 0$ at each R value, and, therefore, the integral of this product over all R values, is greatest when the minima of the two potential curves lie exactly one above the other. As the potential minima become separated, the overlap between the $v" = 0$ and $v^+ = 0$ eigenfunctions decreases and the intensity of the $v^+ = 0 \leftarrow v" = 0$ band is reduced. When the minima of the two potential curves lie at equal internuclear distances, the overlap integral for the $v^+ = 0 \leftarrow v" = 0$ band is large, but it is obviously small for the $v^+ = 1 \leftarrow v" = 0$ or higher levels since the positive and negative contributions to the integral effectively cancel each other.

The shapes of photoelectron bands can provide useful information concerning the type of electron ejected. Referring to Figure 2.1, the ion has the same nuclear configuration in the ground ionic state, X, as in the molecular ground state. Such a configuration is produced by ejection of a nonbonding electron. The resulting spectrum exhibits a very intense $v^+ = 0 \leftarrow v" = 0$ band followed by a relatively short progression. In this case, the AIE and VIE will coincide. When the ionization involves an orbital which has strong bonding (or antibonding) characteristics, the

maximum value for the overlap integral will occur for some level $v^+ > 0$ and the AIE and VIE will be different. As example, curve A in Figure 2.1 represents a potential surface in which the internuclear distance R_e is increased from its ground state value, i.e. a bonding electron has been removed from the neutral molecule. In the corresponding photoelectron band, the *Franck-Condon* maximum appears near the middle of a long vibrational progression.

The energies of vibrational levels in a diatomic molecule may be represented by the anharmonic oscillator expression[5]:

$$\varepsilon_{v^+} = \frac{E}{hc} = \left(v^+ + \frac{1}{2}\right)\omega_e - \left(v^+ + \frac{1}{2}\right)^2 \omega_e x_e \qquad \text{Eq. 2-11}$$

where v^+ is the vibrational quantum number of the vibrational levels in the ionic state, ω_e is a vibrational constant (normally it has units of cm^{-1}) and $\omega_e x_e$ is an anharmonicity constant.

If the vibrational structure in a PE band is resolved, this can yield further information on the associated ionic state. The spacing, ΔG, between successive vibrational components can be expressed as[5]:

$$\Delta G = \omega_e - 2\omega_e x_e\left(v^+ + 1\right) \qquad \text{Eq. 2-12}$$

If an electron is ejected from a nonbonding orbital, the bond strengths of the molecule and ion will be altered very little. Hence, ionization from a nonbonding molecular orbital tends to leave the internuclear separation in the ion, R_e^+, essentially the same as that in the initial neutral state; similarly ω_e^+ should be similar to ω_e". For such a case a narrow PE band would be expected with the $v^+ = 0 \leftarrow v" = 0$ band as the most intense transition, as shown in Figure 2.1, case X.

When an electron is ejected from a bonding orbital, the bond strength is weakened and the internuclear separation in the corresponding ion is larger than in the neutral parent. Since $R_e^+ > R_e$" a broad vibrational progression should be observed in the photoelectron band, as shown in Figure 2.1, case A with $\omega_e^+ < \omega_e$".

The contrary if the electron ejected is antibonding, the bond in the ion will be stronger i.e. $\omega_e^+ > \omega_e$" and $R_e^+ < R_e$".

Thus, for a diatomic molecule, comparison of measured values of ω_e^+ with the, usually well known, ω_e" of the ground state, along with a consideration of the shape of the photoelectron band, may allow the bonding nature of the orbital from which ionization occurred to be determined.

2.2 Photoelectron Spectroscopy with a tuneable wavelength radiation source

Above the first ionization threshold there exists a profusion of neutral states, to which photoabsorption may occur when the photon energy coincides with the transition energy from the ground state. Such resonant absorption processes may compete with direct photoionization, and the decay mechanisms of these super-excited states can have a strong effect on the photoionization cross section at resonant photon energies.

Excited neutral states may be classified into two categories, valence and Rydberg state, although the distinctions between the two are often difficult to make (and states of each type may mix with each other).

2.2.1 Valence and Rydberg states

In atomic systems, the valence shell consists of the set of atomic orbitals with the same principal quantum number as that of the highest occupied orbital in the ground state[6]. Therefore in atoms a valence state is one which has an electronic configuration in which no electron is excited to an orbital outside the valence shell. An atomic Rydberg state is obtained when an electron is promoted outside the valence shell. In molecules composed of elements of the same period, such as CO, a molecular valence shell may be defined in the same way, as having an electronic configuration made up of molecular orbitals which are expressed as linear combination of atomic orbitals with principal quantum numbers, corresponding to the valence shell of the atoms.

Rydberg states are highly excited states in which an electron moves in an orbital with a large spatial distribution and a large principal quantum number. The electronic configuration of the passive electrons corresponds to a state of the positively charged ion and is called the ionic core. Rydberg states are atomic-like in character and the transition energies E_n to these states can be fitted to an expression of the form[6]:

$$E_n = I - \frac{R}{(n-\delta)^2} \qquad \text{Eq. 2-13}$$

where I is the ionization energy of the orbital from which the Rydberg electron was promoted, R is the Rydberg constant (13.61 eV), δ is the quantum defect and n is the principal quantum number. Each Rydberg state is a member of a series converging to a particular ionization limit of energy I. This definition is suitable for both atomic and molecular systems. In a molecule, a Rydberg state is considered to be pseudo-atomic, since to an electron in a spatially extensive Rydberg orbital, the molecular core will appear as a point charge, leading to near hydrogenic behaviour. The extent of the departure from hydrogenic (one-electron) behaviour is described by the effective quantum number, $n - \delta$; for $\delta = 0$ the Rydberg orbital is exactly described by a hydrogenic atomic orbital, whereas a non-zero value of δ is used to fit the energy levels of a system with more than one electron. The magnitude of the quantum defect reflects the degree of penetration of the Rydberg orbital into the molecular ionic core, which is strongly dependent on the radial distribution function of that orbital, and on the nuclear charges of the atoms from which the molecule is constructed. Qualitatively, the greater the penetration of the wavefunction into the core, the larger is the effective nuclear charge seen and the larger the value of δ. The radial probability distribution functions of atomic *s* orbitals tend to have fairly large amplitudes close to the nucleus, while those of *p* orbitals have less amplitude at short radius, and *d* orbitals even less[7]. Thus the *s* orbitals experience the highest effective nuclear charge, so the quantum defect for an *ns* Rydberg orbital is high. Quantum defects for *np* and *nd* orbitals are progressively lower as the degree of penetration of those orbitals into the core decreases. In a heavy atom or molecule, the greater

nuclear charge tends to make quantum defects larger than in a light system, where the electron-core interactions are weaker.

Typical values of δ for first row atoms (e.g. C, N, O) and second row atoms (e.g. Si, P, S) are reported in Table 2-1[8].

Table 2-1: *Typical values of quantum defect δ for first row and second row atoms*

	$\delta(ns)$	$\delta(np)$	$\delta(nd)$
1st Row	1.0	0.5	0.1
2nd Row	2.0	1.5	0.3

Molecular Rydberg orbitals will normally be characteristic of a particular atom in the molecule, so in a diatomic molecule *AB*, where *A* and *B* are from rows 1 and 2 respectively, some Rydberg states may exhibit quantum defects typical of *A*, and others may have δ values closer to those expected for *B*.

Every ionic state in an atom or molecule will have Rydberg series converging to it. Since the ionic core interacts only weakly with the Rydberg electron, the core will closely resemble the ionic state that lies at the series limit, and so the spectroscopic constants for a member of the Rydberg series will be similar to those of the ion. The similarity of the Rydberg state core to the ion at the series limit grows as the principal quantum number of the Rydberg orbital increases, so that as the ionization limit is reached there is a seamless transition into the continuum[9]. The quantum defect, δ, in a series also tends towards an asymptotic limit with increasing *n*. This convergence is a consequence of the nature of high *n* Rydberg orbitals: as *n* increases, the average radius of the Rydberg orbital grows rapidly. An electron in a spatially extensive orbital spends much more time at a distance from the core than close to it, and so it interacts less strongly with the core, and the Rydberg state resembles more closely the ion. The average radius of a Rydberg orbital is proportional to $(n - \delta)^2$ [10]: for high values of *n* the Rydberg molecule can extend over more than 100 Å. Such

large molecules have high collisional cross sections and the reactions (mainly charge-transfer) of highly excited Rydberg states have generated considerable interest[11]. Rydberg series are regularly observed in absorption and ionization spectra, and the extrapolation of series limits is an effective way of determining accurate ionization energies.

Transitions to Rydberg states are subject to the electric dipole selection rules for optical absorption. Many of these rules depend upon the particular coupling cases that apply to the states in question; for example most commonly for diatomic molecules the states may be considered under *Hund's case a* or *Hund's case b*, for which the following selection rules are relevant[4]:

I. $\Delta\Lambda=0, \pm1$

II. $\Delta S=0$

III. $\Sigma^+ \leftrightarrow \Sigma^+ \quad \Sigma^- \leftrightarrow \Sigma^- \quad \Sigma^+ \not\leftrightarrow \Sigma^-$

IV. $g \leftrightarrow u \quad g \not\leftrightarrow g \quad u \not\leftrightarrow u$

It should, however, be noted that Rydberg states are more appropriately described by *Hund's case d* since the shape of the molecule is not transmitted to the excited electron and its rotation is barely noticed.

The overall symmetry of a Rydberg state is determined by the coupling of the angular momenta of the excited electron and the ionic core. In a diatomic molecule the Rydberg orbital may be assigned a principal quantum number n and an azimuthal quantum number l, so that as in an atomic system there are *ns*, *np*, *nd* ... series. The cylindrical form of a diatomic molecule requires that another label, λ, be attached to each orbital, depending on the projection of the orbital angular momentum along the internuclear axis, and this is denoted as σ, π, δ ... symmetry[6] for $\lambda = 0, 1, 2$ .... Thus examples of Rydberg orbitals are $3s\sigma$, $5p\sigma$, $5p\pi$, $4d\sigma$, $4d\pi$, $4d\delta$ ..., or $nl\lambda$ in general. These subdivisions of the p and d (and higher) orbitals each have a slightly different quantum defect as they do not interact with the cylindrical core in exactly the same manner.

A Rydberg state may thus be described by the ionic core around which it is built, that is the limiting state to which it converges, and the symmetry of the Rydberg orbital. The orbital angular momentum of the Rydberg electron may be determined experimentally, by determination of the quantum defect for a state. This may be used in conjunction with the symmetry of the ionic core to determine the symmetry of the Rydberg state.

In cases where an absorption band is sufficiently well resolved to obtain rotational structure in the upper state, and thus derive the symmetry of that state, it is possible to determine the symmetry of the ion at the series limit, which may also be unknown.

In the present study such a potential case was found for the OH and OD work (see Chapter 5).

2.2.2 Decay mechanisms

The interaction of a vacuum ultraviolet photon with a molecule may lead to the direct production of continuum states (dissociation or ionization), or absorption to a discrete state, often a Rydberg state. Once an electron has been promoted to a Rydberg orbital, the excited neutral state will decay by one of several mechanisms[12].

For a diatomic molecule *AB*, in the absence of any collisions, these mechanisms are:

I. Re-radiation: $AB+h\nu \rightarrow AB^* \rightarrow AB+h\nu$

II. Predissociation $AB+h\nu \rightarrow AB^* \rightarrow A+B$

III. Ion pair formation $AB+h\nu \rightarrow AB^* \rightarrow A^+ + B^-$

IV. Autoionization $AB+h\nu \rightarrow AB^* \rightarrow AB^+ + e^-$

Fluorescent re-radiation is known to occur from Rydberg states, but will normally only take place if the other decay channels are unavailable. The radiative lifetime of an excited state of a diatomic molecule is typically of the order of 10^{-8} sec [13], while autoionization and predissociation are frequently observed to be more rapid than one vibrational period, which is of the order of 10^{-13} sec. Hence, fluorescent decay is not usually competitive with the other decay processes.

Mechanisms II., III. and IV. are only viable if the excited state lies above the threshold for formation of their respective products.

Predissociation arises from the interaction of the bound state AB^* with an unbound one, resulting in a radiationless transition to the repulsive state and fragmentation of the molecule. This tends to take place over a fairly narrow energy range, in the region where the two potential curves intersect[13], and need not affect all levels of AB^*. Ion pair formation is a special case of predissociation, in which two ionic products are formed[14]. No photoelectron is emitted in this mechanism, so that PE spectra should be unaffected by ion pair formation.

Autoionization is another radiationless transition, one that occurs when the excited neutral state interacts with an ionization continuum that exists at the same energy. The transition occurs by the loss of an electron, and this can have a profound effect on the overall ionization process. There are four possible types of autoionization mechanism: rotational, vibrational, spin-orbit and electronic[15]. When a Rydberg state lies above the threshold for ionization to the particular ionic state due to rotational or vibrational excitation in the core, rotational and vibrational autoionization may occur. The Rydberg state may autoionize by transfer of energy from the core to the excited electron, which then leaves. Vibrational autoionization requires a strong interaction between the core and the Rydberg electron, and also involves a breakdown of the Born-Oppenheimer approximation, since nuclear and electronic motions are correlated in this mechanism. Studies of vibrational autoionization have revealed that the process favours the minimum possible change in vibrational quantum number, usually $\Delta v = -1$ [15,16]. Since the separation between consecutive vibrational levels in the ion is relatively small, only Rydberg states of high n that converge to an upper v^+ level will lie above a lower v^+ level. Since the probability of absorption to Rydberg states is approximately a function of $(n - \delta)^{-3}$, excitation to, and thus autoionization from these states is weak; hence vibrational autoionization is not considered to be an important process in most molecules. The same applies to rotational autoionization. Spin-orbit autoionization is only observable where the spin orbit coupling constant in the limiting ionic core is large. Electronic autoionization involves a transition from a Rydberg state built upon one (excited) ionic state interacting with a continuum

corresponding to a lower one[17]. Rydberg states based upon the ground ionic state cannot autoionize electronically. Electronic autoionization is a result of interactions between the Rydberg state and the continuum, and may be visualised in one of two ways. Either the excited core relaxes to a lower energy configuration, and the energy so released is transferred to the Rydberg electron, or the Rydberg electron returns to its original orbital and the excess energy is used to eject another electron, again leaving the ion in the less excited state. Either way, it is a two electron process, requiring the close approach of the Rydberg electron to the core; only electronic motions are involved, so the Born-Oppenheimer approximation still holds. Electronic autoionization is found to be the dominant autoionization process in most diatomic molecules, where there are sufficient excited ionic states to yield fairly high densities of Rydberg states for several eV above the first ionization threshold.

A photoionization efficiency spectrum, recorded by measuring the total ion yield as a function of the photon energy, will show structure arising from the two competing processes: direct and resonant ionization. The background level in such a spectrum depends mainly on the cross section for direct photoionization, which normally varies slowly and smoothly with photon energy. Superimposed upon this continuous background are discrete structures that correspond to resonant absorption to electronically autoionizing Rydberg states, where the total ionization yield is usually enhanced by decay from these super excited neutral states.

2.2.3 Autoionization resonances

The mixing between discrete states above the first ionization energy and continuum states gives rise to autoionization phenomena. In the photoelectron spectrum they manifest themselves as excursions in the partial and total cross section as well as in the asymmetry parameter. The shape of the line of an autoionizing resonance can be a sharp feature and it can be observed as a decrease, an increase or an asymmetric profile in the cross section. The reason for this is the interference between the amplitudes of the direct and indirect processes resulting in a characteristic Fano profile[9,18] where the cross section can be expressed as:

$$\sigma(E) = \sigma_a \frac{(q+\varepsilon)^2}{1+\varepsilon^2} + \sigma_b \qquad \text{Eq. 2-14}$$

In this equation σ_a and σ_b represent two portions of the cross section which correspond respectively to transitions to states of the continuum that do and do not interact with the discrete autoionizing state. In Eq. 2-14, the reduced energy ε is defined as:

$$\varepsilon = \frac{E - E_r}{\Gamma/2} \qquad \text{Eq. 2-15}$$

where E_r is the resonance energy and Γ is the natural width of the autoionizing state which represents the interaction between the discrete state and the continuum.
The Fano line profile parameter q may be defined as:

$$q = \sqrt{\frac{2}{\pi \cdot \Gamma}} \frac{\langle \gamma_i | D | \Phi \rangle}{\langle \gamma_d | D | \Phi \rangle} \qquad \text{Eq. 2-16}$$

where γ_d and γ_i are respectively the final state wavefunctions for the direct and indirect ionization process, D is the electric dipole moment operator and Φ is the wavefunction of the initial state. The q parameter characterizes the line profile: neglecting the background cross section, the resonance has a maximum at $\varepsilon_{max} = 1/q$ and is zero at $\varepsilon_0 = -q$. The sign of q thus determines whether the maximum occurs before or after the minimum. In Figure 2.2 typical Fano profiles are shown as a function of ε for five different values of q. The magnitude of q indicates the relative probabilities of the transition to the Rydberg state and direct ionization.
Another parameterization of Eq. 2-14 is frequently used by defining a correlation index ρ^2 and a cross section for photon energies outside of the resonance region $\sigma_c = \sigma_a + \sigma_b$ as:

$$\rho^2 = \frac{\sigma_a}{\sigma_a + \sigma_b} \qquad \text{Eq. 2-17}$$

Eq. 2-14 can then be rewritten as:

$$\sigma(E)=\sigma_c\left[\frac{(q+\varepsilon)^2}{1+\varepsilon^2}\rho^2+(1-\rho^2)\right] \qquad \text{Eq. 2-18}$$

A direct numerical fit of the observed spectrum to the Fano formula of Eq. 2-18 may become unreliable for an atomic transition involving a narrow resonance[19]. The fitting function is the convolution of the Fano profile in Eq. 2-18 and the instrumental function F(E,Ω) where Ω is the energy resolution measured by the full width at half maximum (FWHM):

$$\sigma(\mathrm{E},\Omega)=\int_{-\infty}^{\infty}\sigma(\mathrm{E}-\mathrm{E}')\cdot \mathrm{F}(\mathrm{E}',\Omega)\mathrm{dE}' \qquad \text{Eq. 2-19}$$

It is often a good approximation to assume a Gaussian distribution as the instrumental function; alternatively a weighted combination of Gaussian and Lorentzian distributions can be used[19]. An analytical expression for Eq. 2-19 does not exist so it has to be solved numerically.

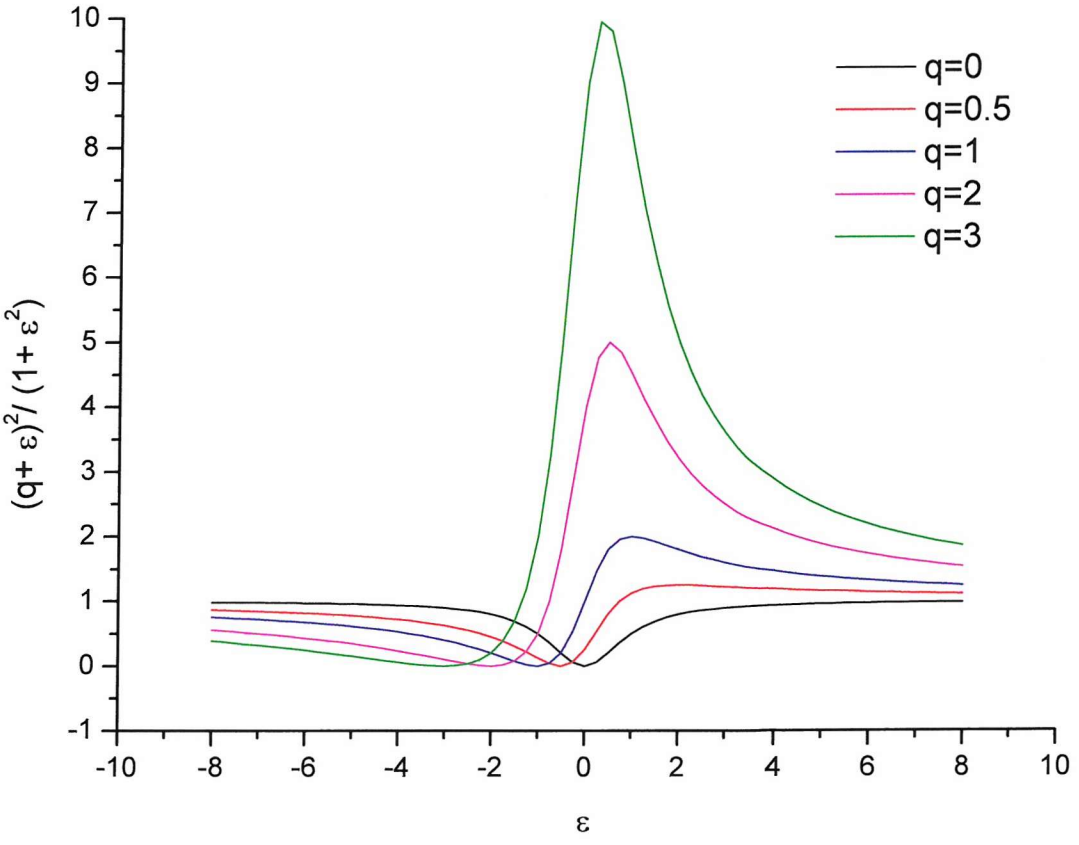

Figure 2.2 *Typical Fano profiles as function of ε for five different values of q.*

An autoionizing resonant state may have a strong effect on a spectrum, with positive or negative features being observed. These features may be observed in photoionization, photoabsorption or photodissociation spectra, and in measurements of the angular distribution parameter. It has been shown that it is possible to use Fano's theory to fit experimental line shapes and determine values of q, ρ^2 and Γ for single resonant states[18] and entire Rydberg series[9]. In the present thesis such a study was performed for the N atom work (see Chapter 6) and codes for fitting the experimental data to the Eq. 2-19 have been written in this work using the program Mathematica.

2.2.4 Multichannel quantum-defect parameterization

Photoabsorption cross sections in regions of autoionization can be parameterized with a lineshape formula based on multichannel quantum defect theory (MQDT) analogous to the Fano's resonance formula[9,18].

Fano's parametrization considers isolated autoionizing states coupled to degenerate continua. It is valid for the case in which the widths of the resonances are comparable with the separation of the resonances in a Rydberg series.

A way of describing an entire series of interacting autoionizing series is to use an MQDT approach first developed by Seaton[20]. Variants of MQDT have been developed by Seaton[20,21], Giusti-Suzor *et al.*[22] and other workers[23,24].

A simple special case involves one series of Rydberg states autoionizing in one continuum. Dubau *et al.*[25] derived a parameterization for this case of two interacting channels, one open and one closed. Connerade[23] has given a detailed discussion of this parameterization while Giusti-Suzor *et al.*[22] derived the same formula using an alternative set of MQDT parameters.

The compact expression of the cross section is:

$$\sigma(E) = \sigma_a \frac{(\varepsilon + q)^2}{\varepsilon^2 + 1} \qquad \text{Eq. 2-20}$$

where σ_a is the cross section averaged over resonances, q is a profile index and the periodic energy scale ε is defined as:

$$\varepsilon = \frac{\tan[\pi(\upsilon + \delta)]}{W} \qquad \text{Eq. 2-21}$$

where δ is the quantum defect. The quantity W is related to the resonance width Γ_n via:

$$\Gamma_n = \frac{2W\,R}{\pi(n-\delta)^3} \qquad \text{Eq. 2-22}$$

while the effective principal quantum number $\upsilon = (n - \delta)$ is related to the photon energy E_n and the series limit I via:

$$\upsilon = n - \delta = \sqrt{\frac{R}{I - E_n}} \qquad \text{Eq. 2-23}$$

Eq. 2-21 gives $\varepsilon = 0$ for $\upsilon_n = (n - \delta)$ and this corresponds to the centre of a resonance[21] for each n. From Eq. 2-23, the values of these resonance energies E_n are:

$$E_n = I - \frac{R}{(n-\delta)^2} \qquad \text{Eq. 2-24}$$

An extension of Eq. 2-20 to include many channel cases using procedures outlined by Seaton[21], Giusti-Suzor *et al.*[22] and Cooke[24] has been presented by Ueda[26].
In the case of one closed channel and many open channels, a term σ_b is added to Eq. 2-20 which expresses the non resonant contribution of the open channels[26].

$$\sigma(E) = \sigma_a \frac{(q+\varepsilon)^2}{1+\varepsilon^2} + \sigma_b \qquad \text{Eq. 2-25}$$

If more than one closed channel exists in the region of interest and, if these channels do not interact either directly or through open channels, the photoionization cross section can be given by a superimposition of Eq. 2-25 over the k closed channels i.e.:

$$\sigma(E) = \sum_k \sigma_{ak} \frac{(q_k + \varepsilon_k)^2}{1+\varepsilon_k^2} + \sigma_b \qquad \text{Eq. 2-26}$$

If an energy region contains one open channel and many degenerate closed channels, the photoionization cross section can be written:

$$\sigma(E) = \sigma_a \frac{\left(1+\sum_k q_k/\varepsilon_k\right)^2}{\left(1+\left(\sum_k q_k/\varepsilon_k\right)^2\right)} \qquad \text{Eq. 2-27}$$

In this work, codes for fitting the experimental data to Eq. 2-25, 26 and 27 have been written using the program Mathematica to be used in the analysis of the S atom data (see Chapter 8).

The parameters σ_a, σ_b, δ, q and W in equations Eq. 2-25, 26 and 27 are energy independent. However, a slow variation with the energy has to be introduced to obtain a better fit of the experimental data[25]. This is achieved using a set of parameters linear in the reduced energy $X = (I - E)/R$. The parameters (generically named p) are then written as $p = p_a + p_b X$.

2.2.5 The Franck-Condon Factor in autoionization

The radiation used in PES is of sufficiently high energy to excite electrons to discrete neutral states which are above the ionization threshold. If an atom or molecule is excited to such a state, autoionizing transitions can take place from the discrete state to the ionization continuum. This process is observed in PES as irregularities in the intensities of members of a vibrational progression and broadening of vibrational bands due to the relatively short lifetimes of the autoionizing states (~10^{-14} sec)[13].

Autoionization accompanying photoexcitation can be represented by:

$$AB + h\nu \rightarrow AB^* \rightarrow AB^+ + e^- \qquad \text{Eq. 2-28}$$

where AB^* is the molecule, or atom, in a highly excited state. Highly excited states (Rydberg states) converge to second, third or higher ionization energies. When a molecule is excited by photons whose energy coincides with that of an autoionizing resonance, there is a high probability of exciting the molecule to this autoionizing state with a well defined vibrational quantum number. If the lifetime of this autoionizing state is greater than one vibrational period, then the photoelectron

spectrum can be expected to be dependent on the *Franck-Condon Factor* for transitions from the autoionizing state of the neutral molecule to the final state of the ion. In Figure 2.3 the *Franck-Condon Factors* in autoionization are illustrated.

In the example in Figure 2.3, direct ionization to AB^+ from AB leads to a narrow photoelectron band since the equilibrium geometries of the initial and final states are similar. The autoionizing state AB^* lies at longer equilibrium bond length than that of AB^+ resulting in a broad contribution to the overall photoelectron spectrum. The selection rules for autoionization[3] are derived from the expression for the radiationless transition probability γ from the autoionizing level Ψ_a to the final state Ψ_f:

$$\gamma = \frac{4\pi^2}{h}\left|\left\langle \Psi_f \middle| \overline{W} \middle| \Psi_a \right\rangle\right|^2 \qquad \text{Eq. 2-29}$$

where $\overline{W}$ is a perturbation function representing certain terms in the Hamiltonian. Since $\overline{W}$ is totally symmetric, it follows that the states Ψ_f and Ψ_a must have common symmetry species in order for the radiationless transition probability to be non zero, that is:

$$\Gamma(\Psi_f) = \Gamma(\Psi_a) \qquad \text{Eq. 2-30}$$

or if the overall wavefunction is separated in the electronic, vibrational and rotational motion the selection rule in Eq. 2.30 becomes:

$$\Gamma(\Psi_e\Psi_v\Psi_\tau)_f = \Gamma(\Psi_e\Psi_v\Psi_\tau)_a \qquad \text{Eq. 2-31}$$

Information about the electronic states responsible for autoionizing resonances can be obtained from a study of photoelectron spectra. The calculation of vibrational intensities in photoelectron spectra perturbed by autoionization has received considerable attention[9,17,18,27]. When the source line-width $\delta(h\nu)$ is larger than the width of the autoionization line Γ_n, the relative intensities of the vibrational levels in a PE spectrum, recorded at a photon energy corresponding to the maximum intensity of the autoionizing states, is given by[28]:

$$I \propto F_{if} + F_{ia} \cdot F_{af} \cdot \frac{\pi \cdot q^2 \Gamma_n}{2 \cdot \delta(h\nu)} \qquad \text{Eq. 2-32}$$

where F_{if} is the *Franck-Condon Factor* for direct ionization from the initial ground molecular state *i* to the final ionic state *f*, F_{ia} is the *Franck-Condon Factor* for the transition to the autoionizing level *a*, F_{af} is the *Franck-Condon Factor* for the transition from the autoionizing level to the final ionic state and *q* is the Fano line profile index. The assumptions are made that the excited states have the same vibrational constant as the ionic state on which it is built, only one electronic state is populated by the decay of the autoionizing level and only one autoionizing state is involved in the ionizing process[3].

In the work presented in this thesis, excited states are probed by recording constant ionic state (CIS) spectra using Synchrotron Radiation. A CIS spectrum monitors the intensity of a single photoelectron feature as the photon energy is scanned. When the photon energy is coincident with a transition to an autoionizing state, discrete structure can be observed in the CIS spectrum.

2.2.6 Selection rules for autoionization of atoms

For Russell-Saunders coupling[29,30] the selection rules allow only the following transitions:

$\Delta L = 0, \pm 1$ ($L = 0 \leftarrow/\rightarrow L = 0$), $\Delta S = 0$, $\Delta J = 0, \pm 1$ ($J = 0 \leftarrow/\rightarrow J = 0$),

$\Delta l = \pm 1$ for the electron moved

In addition to the above selection rules, in the case of an atomic autoionizing state the following rule has to be considered[31]:

no change of parity (Laporte rule)

where *parity* is determined for an atom by summing the *l* value for all electrons ($\Sigma_i l_i$) and determining whether the value (*parity*) is even or odd.

The complete lack of restriction on the value of *l* of the free electron often allows finding a continuum state for which the selection rules for L, for S and for J are fulfilled, but the rule for parity cannot always be fulfilled simultaneously. These points are considered in more details in Chapter 6 and 7 on N and S atoms.

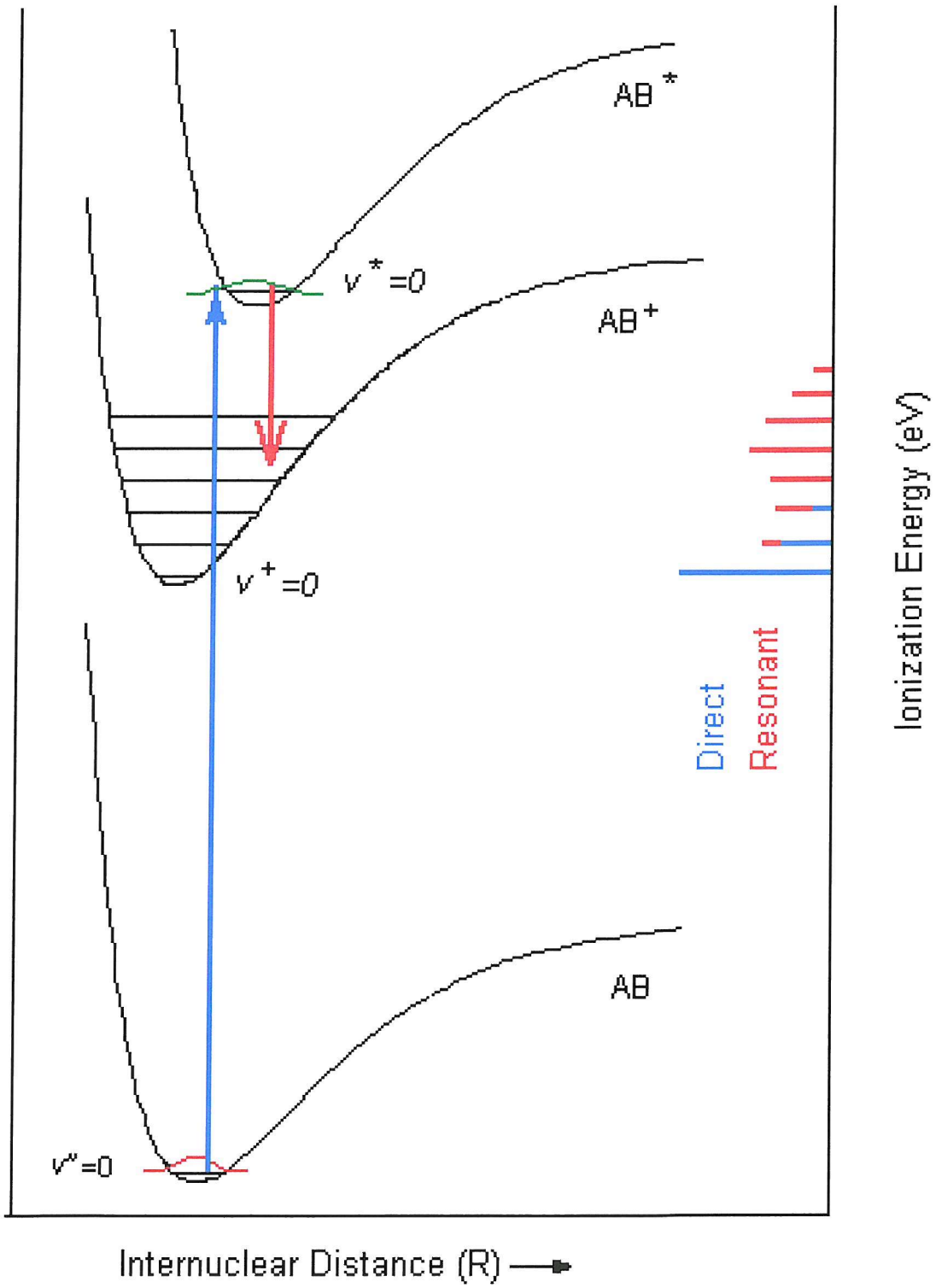

Figure 2.3 *A schematic diagram which illustrates the Franck-Condon Factors in autoionization.*

2.2.7 *Photoelectron angular distribution*

Yang[32] has shown that when a photon interacts with an unpolarized atomic or molecular target, in the electric dipole approximation then the angular correlation between the incident photon and any ejected particle is proportional to a linear combination of *1* and $cos^2\theta$, where θ measures the ejection angle of the outgoing particle, typically an electron, with respect to the polarization vector of the incident photon. The upper limit of two on the powers of $cos\theta$ that determine the angular distribution is fixed by the orbital angular momentum of unity imparted to the target by the absorbed photon in the electric dipole approximation. The angular distribution has no term linear in $cos\theta$ since parity is conserved in a photoabsorption process.

In general the differential cross section for photoionization of an unpolarized target by incident linearly polarized radiation in the electric dipole approximation may be written as[33]:

$$\left[\frac{d\sigma}{d\Omega}\right]_{lin.pol.} = \frac{\sigma}{4\pi}\left[1+\beta P_2(\cos\theta)\right] \qquad \text{Eq. 2-33}$$

where σ is the total photoionization cross section, β is the asymmetry parameter,

$$P_2(\cos\theta) \equiv \frac{1}{2}\left(3\cos^2\theta - 1\right) \qquad \text{Eq. 2-34}$$

and θ is measured with respect to the polarization vector of the incident radiation. It is possible to see from Eq. 2-33 that the angular distribution is determined completely by the asymmetry parameter β, which comprises all of the dynamical information relevant to the angular distribution. The total cross section σ determines the overall intensity of the process; the requirement that $d\sigma/d\Omega$ be positive for all values of θ limits the magnitude of β to the range $-1 \le \beta \le 2$.

Angular momentum and parity conservation laws are then used to deduce those cases in which the β parameter assumes an analytically known constant value in the electric dipole, Russell-Saunders coupling approximation[29].

If an atom A is considered initially in a state defined in the Russell-Saunders coupling approximation, the orbital angular momentum, spin angular momentum,

total angular momentum, and parity quantum numbers will be $\bar{L}_0$, $\bar{S}_0$, $\bar{J}_0$ and π_0 respectively. Consider a low-energy photoionization process ($h\nu$ < 100 eV) for which the electric dipole approximation is good and the incident photon, $h\nu$, can be considered to impart an angular momentum $j_{h\nu} = 1$ and parity $\pi_{h\nu}$ = -1 to the atom. The final state of the ion A^+ is specified by $\bar{L}_c$, $\bar{S}_c$, $\bar{J}_c$ and π_c and the photoelectron is specified by $\bar{l}$, $\bar{s}$, $\bar{j}$, π_e=$(-1)^l$. This general process can be written schematically as[34]:

$$A(\bar{L}_0, \bar{S}_0, \bar{J}_0, \pi_0) + h\nu(j_{h\nu} = 1, \pi_{h\nu} = -1) \rightarrow A^+(\bar{L}_c, \bar{S}_c, \bar{J}_c, \pi_c) + e^-(\bar{l}, \bar{s}, \bar{j}, \pi_e = (-1)^l)$$

Eq. 2-35

The differential cross section for this photoionization process can be separated into contributions characterized by alternative magnitudes of the angular momentum transfer, defined by[34]:

$$\bar{j}_t \equiv \bar{j}_{h\nu} - \bar{l} = \bar{J}_c + \bar{s} - \bar{J}_0 \qquad \text{Eq. 2-36}$$

provided no measurement is made of either the photoelectron spin or the orientation of the residual ion. In Russell-Saunders coupling, spin angular momentum and orbital angular momentum are separately conserved. The angular momentum imparted by the photon affects only the orbital angular momentum of the system, thus: $\bar{S}_0 = \bar{S}_c + \bar{s}$ and $\bar{L}_0 + \bar{j}_{h\nu} = \bar{L}_c + \bar{l}$

These equations restrict the general Eq. 2-36 to the following Russell-Saunders coupling expression:

$$\bar{j}_t \equiv \bar{j}_{h\nu} - \bar{l} = \bar{L}_c - \bar{L}_0 \qquad \text{Eq. 2-37}$$

The constraints of parity conservation must also be considered:

$$\pi_0 \times \pi_{h\nu} = \pi_c \times \pi_e \qquad \text{Eq. 2-38}$$

which in the electric dipole approximation reduces to:

$$\pi_0 \pi_c = (-1)^{l+1} \qquad \text{Eq. 2-39}$$

In the electric dipole approximation, then, the allowed values of the angular momentum transfer $\bar{j}_t$ are determined in general by Eq. 2-36 and Eq. 2-39 and are determined in the Russell-Saunders coupling approximation by Eq. 2-37 and Eq. 2-39. In either case, once the allowed values of $\bar{j}_t$ have been determined, the asymmetry parameter β may be represented as the following weighted average[35-37]:

$$\beta = \frac{\Sigma_{j_t} \sigma(j_t)\beta(j_t)}{\Sigma_{j_t} \sigma(j_t)} \qquad \text{Eq. 2-40}$$

where the sum extends over all allowed values of j_t, and $\beta(j_t)$ and $\sigma(j_t)$ are the asymmetry parameter and the partial photoionization cross section characteristic of a given value of $\bar{j}_t$. When $\bar{j}_t$ is "parity favoured", $\pi_0\pi_c = (-1)^{j_t}$ and $\beta(j_t)$ and $\sigma(j_t)$ may be written in terms of certain scattering amplitudes $S_l(j_t)$ as follows[35-37]:

$$\beta_{fav}(j_t) = \frac{(j_t+2)|S_+(j_t)|^2 + (j_t-1)|S_-(j_t)|^2 - 3\sqrt{j_t(j_t+1)}[S_+(j_t)S_-^+(j_t)]}{(2j_t+1)(\ |S_+(j_t)|^2 + |S_-(j_t)|^2\ )} \qquad \text{Eq. 2-41}$$

$$\sigma_{fav}(j_t) = \frac{2j_t+1}{2L_0+1}[\ |S_+(j_t)|^2 + |S_-(j_t)|^2\ ] \qquad \text{Eq. 2-42}$$

where the subscripts ± or 0 on the amplitudes $S_l(j_t)$ indicate that the photoelectron orbital angular momentum $\bar{l}$ has the value $j_t \pm 1$ or j_t respectively[34].

When $\bar{j}_t$ is "parity unfavoured", $\pi_0\pi_c = (-1)^{j_t+1}$ and $\beta(j_t)$ and $\sigma(j_t)$ assume a particularly simple form[36]:

$$\beta_{unfav}(j_t) = -1 \qquad \text{Eq. 2-43}$$

$$\sigma_{unfav}(j_t) = \frac{2j_t+1}{2L_0+1}|S_0(j_t)|^2 \qquad \text{Eq. 2-44}$$

The angular momentum transfer theory expression for the asymmetry parameter β given in Eq. 2-40 is, in general, energy dependent due to the energy dependence of the scattering amplitudes $S_l(j_t)$[34], in terms of which both the cross sections $\sigma(j_t)$ and asymmetry parameters $\beta(j_t)$ are defined. Since β is defined in terms of a ratio of

energy-dependent factors, the possibility exists that the energy dependence may cancel, leaving an analytically determined constant value for β. A necessary condition for this to occur is that only a single value of $\bar{j}_t$ contributes to the process under study. In general there are always at least two values of $\bar{j}_t$. In Russell-Saunders coupling, however, Eq. 2-37 implies that $\bar{j}_t$ will be *restricted to a single value* when either $\bar{L}_c$ or $\bar{L}_0$ is zero, in which case $\bar{j}_t$ will have the value of the other one of this pair. When only a single value of $\bar{j}_t$ is permitted, then the cross sections in Eq. 2-40 cancel, giving for the asymmetry parameter the expression:

$$\beta = \beta(j_t) \qquad \text{Eq. 2-45}$$

For an unfavoured value of $\bar{j}_t$, β= -1 and hence the angular distribution is energy independent. For a favoured value of $\bar{j}_t$ in general β is energy dependent. This energy dependence arises since the photoelectron orbital angular momentum can usually have two allowed values, $l = j_t \pm 1$, in favoured photoionization processes. The interference between the scattering amplitudes $S_l(j_t)$ for these two values of $\bar{l}$ causes $\beta(j_t)$ to vary with energy. In the special case of $j_t = 0$, however, $\bar{l}$ has only the single value +1, due to angular momentum conservation, in which case Eq. 2-41 shows that $\beta(j_t = 0) = +2$. In all other cases in which only a single value of $\bar{j}_t$ contributes to a particular photoionization process, $\beta(j_t)$ is energy dependent.

When the photoelectron angular distribution is predicted to be energy dependent in Russell-Saunders coupling, then the evaluations of $\beta(j_t)$ and $\sigma(j_t)$ may be carried out in terms of the scattering amplitudes $S_l(j_t)$ for the photoionization process in Eq. 2-35. The scattering amplitudes $S_l(j_t)$ may be expressed in the Russell-Saunders coupling approximation in terms of reduced dipole matrix elements as follows[38]:

$$S_l(j_t) = \sqrt{\frac{4\pi}{3.}\frac{}{c}h\nu}\cdot i^l e^{-i\sigma_l}\Sigma_L\sqrt{2L+1}\begin{Bmatrix} L_c & l & L \\ 1 & L_0 & j_t \end{Bmatrix}\left\langle L_0 S_0 E_0 \left\| \Sigma_{j=1}^{N} r_j \right\| \Psi^{-}_{L_c S_c l L E} \right\rangle \qquad \text{Eq. 2-46}$$

where the initial state is indicated by its energy E_0 and term level L_0S_0, and the energy normalized channel function $\Psi^{-}_{L_c S_c l L E}$ describes the N-particle final state of

energy $E = E_0 + h\nu$. The phase factors $i^l e^{-i\sigma_l}$, where σ_l is the Coulomb phase shift, and the minus sign on the final state wavefunction, indicate that incoming wave boundary conditions have been imposed on the final state: namely at large separation, $r \to \infty$, where r is the photoelectron radial coordinate, the photoelectron has angular momentum $\bar{l}$, the core has $\bar{L}_c$, and the two are coupled to form the total angular momentum $\bar{L}$. For smaller separations r between the photoelectron and the ionic core, $\Psi^-_{L_c S_c l L E}$ represents a multichannel wavefunction, having non-zero components in all allowed final state channels having the same total orbital and spin angular momentum $\bar{L}$ and $\bar{S}_0$. The initial state correspondingly is described by a multiconfiguration wavefunction, all of whose components have the same total orbital and spin angular momentum $\bar{L}_0$ and $\bar{S}_0$. In general, the reduced dipole amplitude in Eq. 2-46 contains contributions from all open and closed channels which may be populated from the ground state and which are then scattered by electron-electron interactions into the final state. When such interchannel scattering is not treated, when the initial state is represented by a single configuration rather than by a multiconfiguration wavefunction, and when the multiple structure of the photoionization transition is ignored, as is done in the central-potential model approximation[39,40], Eq. 2-46 reduces to the central-potential model in the limit of isotropic electron-ion interactions:

$$S_l(j_t) \propto \delta(j_t, l_0) \cdot i^l e^{-i\sigma_l} (-1)^{l_0 - l_{\max}} \sqrt{l_{\max}} (2l_0 + 1)^{-1} e^{-i\delta_{\varepsilon l}} R_{\varepsilon l} \qquad \text{Eq. 2-47}$$

where $\delta_{\varepsilon l}$ is the photoelectron's phase shift and $R_{\varepsilon l}$ is the radial dipole integral. Substituting Eq. 2-47 in Eq. 2-41 gives the Cooper-Zare result[33]:

$$\beta = \frac{l_0(l_0-1)R^2_{l_0-1} + (l_0+1)(l_0+2)R^2_{l_0+1} - 6l_0(l_0+1)R_{l_0-1}R_{l_0+1}\cos(\sigma_{l_0+1} + \delta_{l_0+1} - \sigma_{l_0-1} - \delta_{l_0-1})}{(2l_0+1)\cdot(\, l_0 R^2_{l_0-1} + (l_0+1)R^2_{l_0+1}\,)} \qquad \text{Eq. 2-48}$$

where the explicit dependence of the phase shift and radial dipole matrix elements on energy ε has been omitted for simplicity.

Using Eq. 2-48 it is possible calculate the β values for some atomic ionizations, summarized in Table 2-2.

Table 2-2: *Calculated β values for the some atomic ionizations.*

Transition	β value
$s \rightarrow p$	$\beta = 2$
$p \rightarrow s$	$\beta = 0$
$p \rightarrow d$	$\beta = 1$
$d \rightarrow p$	$\beta = 0.2$
$d \rightarrow f$	$\beta = 0.8$

Analogous behaviour is observed in molecules: if a molecular orbital is composed primarily of atomic s orbitals, β will be large and the outgoing electron wave will have predominately p character[5].

From an experimental point of view the β parameter can be evaluated applying Eq. 2-33 expressed as:

$$\frac{d\sigma}{d\theta} = \frac{\sigma}{4\pi}\left[1 + \frac{\beta}{4}(3P\cos 2\theta + 1)\right] \qquad \text{Eq. 2-49}$$

to the intensities measured at $\theta = 0°$

$$I_0 = \frac{\sigma}{4\pi}(1+\beta) \qquad \text{Eq. 2-50}$$

and $\theta = 60°$

$$I_{60} = \frac{\sigma}{4\pi}\left(\frac{8-\beta}{8}\right) \qquad \text{Eq. 2-51}$$

with linearly polarized radiation ($P = 1$) and calculating the ratio R:

$$R = \frac{I_0}{I_{60}} = \frac{(1+\beta)}{\left(\frac{8-\beta}{8}\right)} \Rightarrow \beta = \frac{8(R-1)}{R+8} \qquad \text{Eq. 2-52}$$

or instead of recording spectra at $\theta = 60°$, measuring the intensity at $\theta = 54° 44'$ (in this case the measured intensity is proportional to the total photoionization cross section and independent by β)

$$I_{54°44'} = \frac{\sigma}{4\pi} \qquad \text{Eq. 2-53}$$

with linearly polarized radiation ($P = 1$) and calculating the ratio R:

$$R = \frac{I_0}{I_{54°44'}} = (1+\beta) \Rightarrow \beta = R - 1 \qquad \text{Eq. 2-54}$$

By recording spectra at two or more angles, θ, it is possible to measure the β values, obtaining further information about the photoionization process, mainly concerning the character of the initial orbital and the nature of the free electron wavefunction.

2.3 Conclusions

In this Chapter a review of the fundamental principles related to photoelectron spectroscopy has been presented. PES with a fixed wavelength radiation source and PES with a tuneable wavelength radiation source have been considered from a fundamental point of view.

The basic relations governing the photoionization process have been outlined and have been applied to the analysis of the results obtained in this thesis in Chapters 5 to 10.

References

[1] H. Hertz
Annalen der Physik **31**, 983 (1887).

[2] A. Einstein
Annalen der Physik **17**, 132 (1905).

[3] J. W. Rabalais *Principles of Ultraviolet Photoelectron Spectroscopy*, Wiley & Sons ed.New York, 1977.

[4] H. Herzberg *Molecular Spectra and Molecular Structure*, D. van Nostrand Company Inc. ed.New York, 1966; Vol. III.

[5] J. H. D. Eland *Photoelectron Spectroscopy*, Butterworths ed.Oxford, 1984.

[6] A. B. F. Duncan *Rydberg series in atoms and molecules*, Academic Press ed.New York, 1971.

[7] M. B. Robin *Higher Excited State of Polyatomic Molecules*, Academic Press ed.New York, 1974.

[8] C. E. Moore *Atomic Energy Levels*, National Bureau of Standards ed.Washington, 1949.

[9] U. Fano and J. W. Cooper
Physics Review **137**, 1364 (1965).

[10] J. Berkowitz *Photoabsorption, Photoionization and Photoelectron Spectroscopy*, Academic Press ed.New York, 1979.

[11] F. B. Dunning and R. F. Stebbings *Rydberg States of Atoms and Molecules*, Cambridge University Press ed.Cambridge, 1983.

[12] P. M. Guyon and I. Nenner
Applied Optics **19**, 4068 (1980).

[13] H. Herzberg *Molecular Spectra and Molecular Structure*, D. van Nostrand Company Inc. ed.New York, 1966; Vol. I.

[14] K. P. Lawley and R. J. Donovan
Journal of The Chemical Society Faraday Transactions 2 **89**, 1885 (1993).

[15] R. S. Berry
Journal of Chemical Physics **45**, 1228 (1966).

[16] J. Berkowitz and W. A. Chupka
Journal of Chemical Physics **51**, 2341 (1969).

[17] A. L. Smith
Journal of Quantitative Spectroscopy and Radiative Transfer **10**, 1129 (1970).

[18] U. Fano
Physics Review **124**, 1866 (1961).

[19] T. K. Fang and T. N. Chang
Physical Review A: Atomic, Molecular, and Optical Physics, 1998, Vol. 57, pp 4407.

[20] M. J. Seaton
Proceedings of the Physical Society **88**, 801 (1966).

[21] M. J. Seaton
Reports on Progress in Physics **46**, 167 (1983).

[22] A. Giusti-Suzor and U. Fano
Journal of Physics B **17**, 215 (1984).

[23] J. P. Connerade
Journal of Physics B **16**, 329 (1983).

[24] W. E. Cooke and C. L. Cromer
Physical Review A **32**, 2725 (1985).

[25] J. Dubau and M. J. Seaton
Journal of Physics B **17**, 381 (1984).

[26] K. Ueda
Physical Review A **35**, 2484 (1987).

[27] F. H. Mies
Physics Review **175**, 164 (1968).

[28] D. Cubric, A. A. Willis, J. Comer and P. Hammond
Journal of Physics B-Atomic Molecular and Optical Physics **29**, 4151 (1996).

[29] H. N. Russell and F. A. Saunders
Astrophysic Journal **61**, 38 (1925).

[30] J. M. Hollas *Modern Spectroscopy*, Wiley & Sons ed.Chichester, 1996.

[31] H. G. Kuhn *Atomic Spectra*, Longmans ed.London, 1964.

[32] C. N. Yang
Physics Review **74**, 764 (1948).

[33] J. Cooper and R. N. Zare *Lectures in Theoretical Physics*, edited by S. Geltman, K.T. Mahanthappa and W.E. Brittin ed.New York, 1967; Vol. XI-C.

[34] V. Schmidt *Electron Spectrometry of Atoms using Synchrotron Radiation*, Cambridge University Press ed.New York, 1997.

[35] U. Fano and D. Dill
Physics Review A **6**, 185 (1972).

[36] D. Dill and U. Fano
Physics Review Letters **29**, 1203 (1972).

[37] D. Dill
Physics Review A **7**, 1976 (1973).

[38] A. F. Starace *Handbook der Physik*, edited by W. Melhorn ed.Berlin, 1982; Vol. 31.

[39] D. Dill, S. T. Manson and A. F. Starace
Physics Review Letters **32**, 971 (1974).

[40] D. Dill, A. F. Starace and S. T. Manson
Physics Review A **11**, 1596 (1975).

Chapter 3

3 SYNCHROTRON RADIATION

Synchrotron Radiation has a number of special characteristics which make electron synchrotron and storage ring sources powerful as research instruments and as facilities for technological applications. Synchrotron Radiation has a continuous spectrum ranging from infrared to X-ray wavelengths, it is highly intense and it is strongly polarized. A single storage ring can provide a considerable number of ports at which equipment for utilizing photon beams may be installed. The properties of a Synchrotron Radiation beam depend both on the emission process itself and on the electron optics of the storage ring or accelerator from which the radiation is obtained.

3.1 The Synchrotron Radiation

Natural Synchrotron Radiation from charged particles spiralling around magnetic field lines in space is as old as the stars, for example the light that is seen from the Crab Nebula[1] arises from this source.

Synchrotron Radiation and its use as a scientific tool have an interesting history. The prediction of the phenomenon, the search for this new kind of radiation, its discovery and ideas for its potential usefulness are indeed an interesting case history. The phenomenon that an electron in a circular trajectory would radiate was predicted in a pre-quantum and a pre-relativistic language almost 100 years ago. At that time, it was well known from classical electrodynamics that accelerated charged particles radiate. In 1897 Larmor[2] gave an expression for the instantaneous total power radiated by a single, nonrelativistic electron as:

$$P = \frac{2}{3}\frac{e^2}{c^2}\frac{dv^2}{dt} = \frac{2}{3}\frac{e^2}{m^2c^3}\frac{dp^2}{dt} \qquad \text{Eq. 3.1}$$

where e is the charge on the electron, c is the velocity of light, v and p are the velocity and momentum of the charged particle, respectively, and m is its rest mass. In 1898, Lienard[3] published an extension of Larmor's formula for the rate of radiation from the centripetal acceleration of an electron in a circular trajectory. Schott[4] further developed the classical theory in connection with early models of the atom and in an attempt to describe the discrete nature of atomic spectra. As is well known, the Bohr model of the atom described the regularities in atomic spectra elegantly and the results of Schott's work were forgotten for a long time. No attempts were made to verify experimentally the conclusions of the classical theory and for more than 30 years radiation from an accelerated charge was mentioned only in textbooks.

After this early work, quite some time elapsed without noticeable progress until, in the 1940's, the subject of radiation from relativistic electrons received new attention in university and industrial laboratories, when the building of multimillion volt accelerators began and the classical radiation loss of accelerated electrons was again investigated.

Short-wavelength Synchrotron Radiation generated by relativistic electrons in circular accelerators is only a half-century old. The first observation[5], since it was visible radiation that was seen, came at the General Electric Research Laboratory in Schenectady, New York, on April 24, 1947.

3.2 Discovery and Development of Synchrotron Radiation

In 1945, the *synchrotron* was proposed as the new accelerator for high-energy physics, designed to push particles, in this case electrons, to higher energies than a *cyclotron*, the particle accelerator used at the time.

An accelerator takes stationary charged particles, such as electrons, protons and positrons, and drives them to velocities near the speed of light.

The General Electric (GE) Laboratory in Schenectady built the world's second synchrotron, and it was with this machine in 1947 that Synchrotron Radiation was first observed. The optical radiation from the electron beam was first seen on April the 24th 1947[5]. On that April day Robert Langmuir and Herbert Pollock were running the machine and were trying to push the electron gun and its associated pulse transformer to the limit. Some intermittent sparking had occurred, and the technician Floyd Haber was asked to observe this effect with a mirror around the protective wall which separated the machine from the control room. He signalled to turn off the synchrotron as "he saw an arc in the tube". Pollock recorded these observations in his laboratory notebook[5], noting that the beam was stable and of small cross section (approximately 1 mm square).

In May 1947, Elder, Gurewitsch, Langmuir and Pollok published a letter[6,7] in which they reported their visual observation of Synchrotron Radiation. In this letter the polarization properties were also noted.

For high-energy physicists performing experiments at an electron accelerator, Synchrotron Radiation is a nuisance which causes a loss of particle energy. However, condensed-matter physicists realized that this was exactly what was needed to investigate electrons surrounding the atomic nucleus and the position of atoms in molecules.

In the 55 years since, Synchrotron Radiation has become a premier research tool for the study of matter in all its forms, as facilities around the world constantly evolved to provide this radiation in ever more useful forms.

3.2.1 The first generation: parasitic operation

With the work of Codling and Madden[8], measurements began in the early 1960s at the new NBS facility in Washington (Synchrotron Ultraviolet Radiation Facility or SURF) to determine the potential of Synchrotron Radiation as a source for spectroscopy in the ultraviolet (the wavelength for peak radiated power per unit wavelength was 335 Å with this synchrotron). Absorption spectra of noble gases revealed a large number of previously unobserved resonances due to inner-shell and two-electron excitations, including doubly excited helium, which remains today a prime test bed for studying electron-electron correlation. These findings further stimulated the growing interest in Synchrotron Radiation. Establishment of SURF began the first generation of Synchrotron Radiation facilities, sometimes also called parasitic facilities because the accelerators were built and usually operated primarily for high-energy or nuclear physics. However, the NBS synchrotron had outlived its usefulness for nuclear physics and was no longer used for this purpose.

If SURF headed the first generation, it was not by much, as activity was also blossoming in both Europe and Asia. At the Frascati laboratory (Rome) in 1962, researchers began measuring absorption in thin metal films using a 1.15 GeV synchrotron[9]. In the same period scientists in Tokyo formed the INS-SOR (Institute for Nuclear Studies-Synchrotron Orbital Radiation) group and by 1965 were making measurements of soft X-ray absorption spectra of solids using radiation from a 750 MeV synchrotron[10,11]. The trend toward higher energy and shorter wavelengths took a big leap with the use of the 6 GeV Deutsches Elektronen-Synchrotron (DESY) in Hamburg, which began operating for both high-energy physics and Synchrotron Radiation in 1964. With Synchrotron Radiation available at wavelengths in the X-ray region down to 0.1 Å, experimenters at DESY were able to begin absorption measurements of solids, notably metals and alkali halides, and of photoemission in aluminium[12].

3.2.2 The storage rings

While the number of synchrotrons was growing, the next major advance was the development of electron storage rings, the basis for all of today's synchrotron sources. Around 1970, Tantalus in Stoughton, Wisconsin, a 240 MeV storage ring, originally planned and operated in the 1960s as a test facility for the advanced accelerators concept, but later operated exclusively for Synchrotron Radiation work, came into full operation[13-15]. The first spectrum was measured in 1968. In subsequent years, improvements enabled Tantalus to reach its peak performance, add a full complement of ten beamlines with monochromators, and become in many respects a model for today's multi-user Synchrotron Radiation Facilities.

These first generation storage rings were electron-positron colliding-beam machines that were operated to provide the highest possible collision rates without blowing up the beams, a condition that generally meant low beam currents. Under these conditions, parasitic operation meant a severely limited output of synchrotron radiation, thereby motivating a clamour for second generation storage rings designed for and dedicated to the production of Synchrotron Radiation.

Even before the second generation facilities were in full use, synchrotron users recognized that a new generation of storage rings with a still lower emittance and long straight sections for undulators would permit achieving even higher brightness and with it, a considerable degree of spatial coherence.

Third generation synchrotron radiation facilities represent the current state-of-the-art in synchrotron sources. The race to develop a new generation of Synchrotron Radiation Sources with vastly enhanced performance has already begun, namely to design and build fourth generation synchrotrons.

The candidate with the best scientific case for a fourth generation source is the hard X-ray (wavelength less than 1 Å) free-electron laser (FEL) based on a very long undulator in a high-energy electron linear accelerator. Such a device would have a peak brightness many orders of magnitude beyond that of the third generation sources, as well as pulse lengths of 100 fs or shorter, and would be fully coherent.

3.3 Theory of Synchrotron Radiation

An accelerating charged particle, such as one travelling on a curved trajectory, emits radiation. For a slowly moving electron ($v << c$, where v is the velocity of the electron and c is the velocity of light) the expected radiation is emitted with a more or less doughnut shaped angular distribution with a single wavelength equal to the circumference of the orbit[16]. However, when moving at relativistic speeds ($v \approx c$), this radiation is emitted in a very narrow cone tangential to the path of the particle[17] as pictured in Figure 3.1.

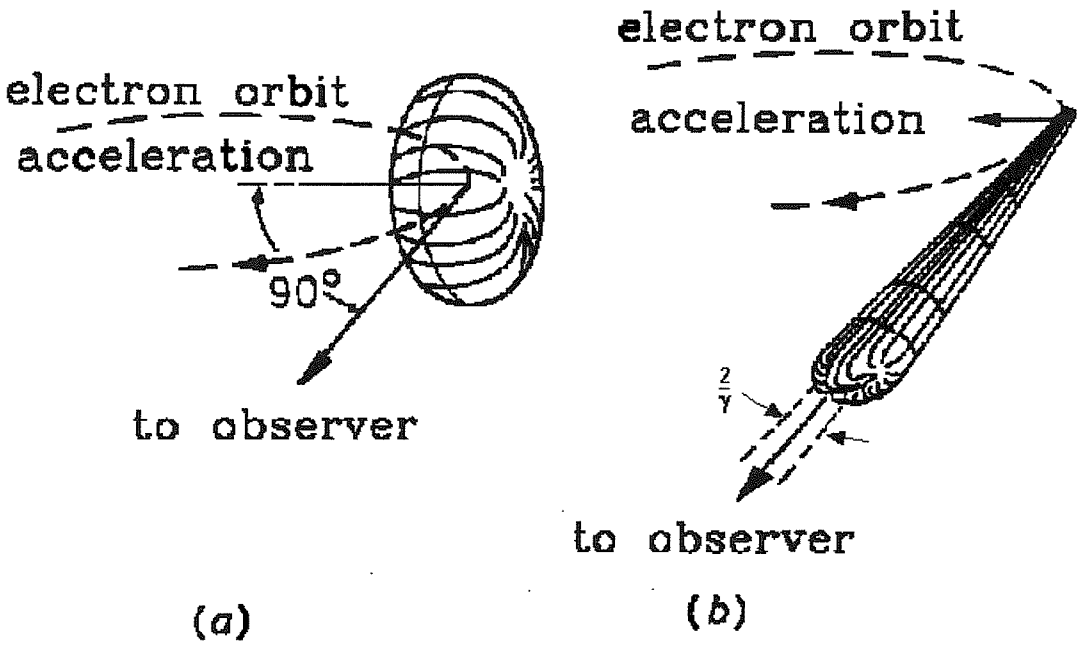

Figure 3.1 *Emission pattern of an electron circulating with velocity v:*
(a) $v<<c$
(b) $v \approx c$

The properties of Synchrotron Radiation produced from an electron (or positron) beam traversing a magnetic field are determined essentially by the behaviour of a single electron moving along a macroscopic circle. However due to the relativistic velocity of the circulating electron, the radiation emission pattern is pushed into the

forward direction. Because of this effect an observer fixed in space can see the Synchrotron Radiation only for a short time interval. According to Fourier analysis such a short pulse contains frequencies up to a critical value:

$$\omega_c = \frac{2\gamma^3 c}{R} \qquad \text{Eq. 3.2}$$

where γ is the Lorentz contraction factor[17] and R is the radius of the orbit. Thus the energy spectrum of Synchrotron Radiation extends up to very high harmonics, or equivalently to very high energies. Due to the longitudinal and transverse oscillations of the circulating electrons, the energy spectrum of Synchrotron Radiation is a continuous distribution.

There are three types of magnetic structures commonly used to produce Synchrotron Radiation: bending magnets, undulators and wigglers.

3.3.1 Bending magnet

A bending magnet causes a single curved trajectory as pictured in Figure 3.2. The result is a fan of radiation around a bend. The instantaneous power radiated[18] by a single electron around the whole orbit is:

$$P = \frac{2}{3}\frac{e^2 c\gamma^4}{R^2} \qquad \text{Eq. 3.3}$$

where e is the charge of an electron, c is the velocity of light, γ is the Lorentz contraction factor[17] and R is the radius of the orbit. From Eq. 3.3 the radiated power increases with the fourth power of the particle energy, as γ is proportional to the kinetic energy of the electron, and decreases with the square of the orbital radius. Most radiation is emitted for high-energy electrons in a circular motion with a small radius. Since the radiation from different electrons is emitted incoherently, the total intensity is obtained by simply summing the contributions from all electrons[18].

Some useful equations are the energy radiated[18]:

$$\delta E(keV) = \frac{88.5E^4(GeV)}{R(m)} \qquad \text{Eq. 3.4}$$

where E is the electron energy and δE is the energy radiated by a single electron per revolution, and the critical photon energy[19]:

$$\varepsilon_c(eV) = \frac{3e\hbar B\gamma^2}{2m} = \frac{2218E^3(GeV)}{R(m)} \qquad \text{Eq. 3.5}$$

where ε_c is the critical photon energy, B is the magnetic field and m is the electron rest mass.

The critical photon energy is that for which half the radiated power is in higher energy photons and half is in lower energy photons. As such it provides a primary parameter for characterizing bending magnet radiation and it is a measure of how far the spectrum extends into the X-ray region[19].

The radiation spectrum from a bending magnet is very broad, analogous to white radiation from an X-ray light bulb and the emission angle is typically $1/\gamma$.

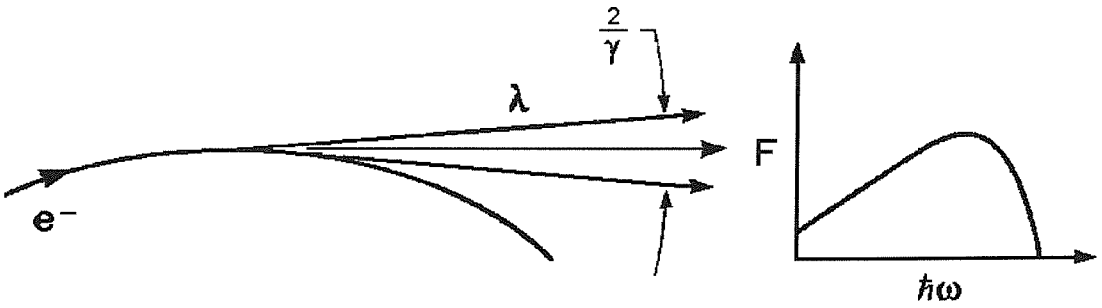

Figure 3.2 *Bending magnet radiation and the related radiation spectrum.*

3.3.2 Undulators

Undulators are periodic magnetic structures with relatively weak magnetic fields. The periodicity and the weak magnetic field cause an electron to move in a harmonic oscillation when it moves in the axial direction, resulting in a motion characterized by small angular excursions as shown in Figure 3.3, smaller than the angular width of the natural radiation cone, $1/\gamma$, normally associated with Synchrotron Radiation.

The characteristic emission angle is narrowed by a factor of $\sqrt{N}$, where N is the number of magnetic periods (typically of order 100)[19].

In contrast to the smooth spectral distribution of radiation from a bending magnet, radiation from an undulator shows characteristic maxima due to the periodic magnetic structure of the undulator: the magnetic field with N periods of length λ_u produces an oscillatory path for the electrons which is similar to the response generated by $2N$ bending magnets.

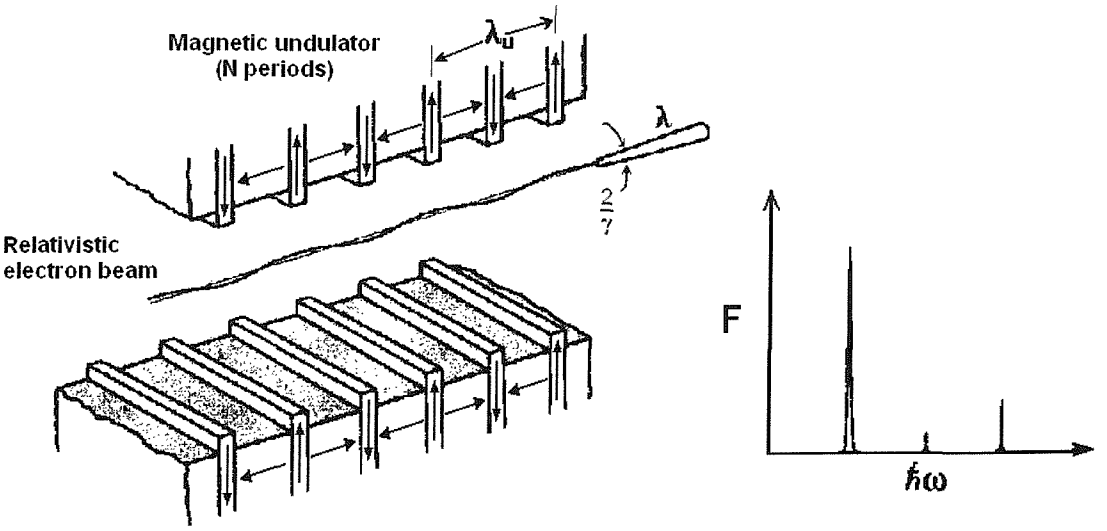

Figure 3.3 *Undulator radiation and the related radiation spectrum.*

A characteristic parameter for a periodic magnet is the non-dimensional magnetic strength K[19] that relates the maximum deflection angle α of the electron path to the natural opening angle $1/\gamma$ of the natural radiation cone. It is given by:

$$K = \frac{\alpha}{1/\gamma} = \frac{1}{2\pi}\frac{eB_0\lambda_u}{mc} \qquad \text{Eq. 3.6}$$

where B_o is the magnet field strength.

For an undulator $K \leq 1$, hence the interference between electromagnetic waves emitted by the same electron at different undulators yields a redistribution of the spatial and spectral intensity. The condition for constructive interference follows from the proper timing for the movement of the electron and its emission of radiation with wavelength λ: the time taken by the electron to travel through one undulator period λ_u minus the time taken by radiation to travel this distance must equal to $n\lambda/c$, where n is an integer.

For radiation emitted at angles θ (in the plane of the undulator) and ψ (in the plane perpendicular of the undulator) with respect to the undulator axis, the wavelength of the nth harmonic radiation λ_n is[20]:

$$\lambda_n = \frac{1}{n}\frac{\lambda_u}{2\gamma^2}\left[1+\frac{K^2}{2}+\gamma^2\theta^2+\gamma^2\psi^2\right] \qquad \text{Eq. 3.7}$$

The harmonics are characteristic of the spectrum of the observed undulator radiation. Hence, it is advantageous to work at the energy of such harmonics and to adapt the value of λ_n for a given undulator to the experimental needs. This is done usually by changing the gap between the permanent magnets of the undulator, which, in turn, changes the parameter K, and thus λ_n .

Another important measure of the radiation emitted by electrons traversing a periodic magnet undulator is the brightness (the power ΔP radiated from an area ΔA into a solid angle $\Delta\Omega$), and in particular the spectral brightness in terms of photon flux within the central cone F_{cen}. This is defined as[19]:

$$B = \frac{F_{cen}\cdot(N/1000)}{\Delta A\cdot\Delta\Omega\cdot(0.1\%bandwidth)} \qquad \text{Eq. 3.8}$$

Synchrotron Radiation from undulators can have brightness three orders of magnitude higher than that from bending magnets. The narrowed resultant radiation cone in combination with a tightly confined electron beam leads to radiation with small angular divergence and relatively narrow spectral width, properties generally associated with coherence properties of lasers.

A further important property of undulator radiation concerns its polarization characteristics. The degree of linear polarization $P_L(\theta, \omega)$ is easily obtained from the

power $P(\lambda, \psi)$ radiated around the whole orbit into a wavelength interval $d\lambda$ and an interval $d\psi$ of the angle ψ by a single ultra relativistic ($\gamma >> 1$) monoenergetic electron[18]:

$$P(\lambda,\psi) = \frac{27}{32\pi^3}\frac{e^2 c}{R^2}\left(\frac{\lambda_c}{\lambda}\right)^4 \gamma^8 [1+(\gamma\psi)^2]^2 \{K_{2/3}^2(\xi) + \frac{(\gamma\psi)^2}{1+(\gamma\psi)^2} K_{1/3}^2(\xi)\} \qquad \text{Eq. 3.9}$$

$$\text{with} \quad \xi = \frac{\lambda_c}{2\lambda}[1+(\gamma\psi)^2]^{3/2} \qquad \text{Eq. 3.10}$$

where λ_c is the "characteristic wavelength", R denotes the radius of curvature and $K_{1/3}$ and $K_{2/3}$ are modified Bessel functions of the second kind.

The two terms in the curly brackets of Eq. 3.9 are associated with the intensities in the two directions of polarization, $I_{//}$ and $I_{\perp}$, having the electric vector parallel and perpendicular to the plane of the orbit. It can be seen that:

$$P_L = \frac{I_{//} - I_{\perp}}{I_{//} + I_{\perp}} = \frac{K_{2/3}^2(\xi) - \frac{(\gamma\psi)^2}{1+(\gamma\psi)^2} K_{1/3}^2(\xi)}{K_{2/3}^2(\xi) + \frac{(\gamma\psi)^2}{1+(\gamma\psi)^2} K_{1/3}^2(\xi)} \qquad \text{Eq. 3.11}$$

Since the two components of the electric vector have a well defined phase relation with respect to each other, namely + π/2 or - π/2 above or below the plane of the orbit, respectively, the degree of circular polarization P_c can also be calculated with decomposition of the elliptically polarized wave into right-hand or left-hand waves with intensity I_R and I_L:

$$P_c = \frac{I_R - I_L}{I_R + I_L} = \pm\frac{2\sqrt{I_{//} I_{\perp}}}{I_{//} + I_{\perp}} = \pm\frac{2K_{1/3}(\xi)K_{2/3}(\xi)\left[\frac{(\gamma\theta)^2}{1+(\gamma\theta)^2}\right]^{1/2}}{K_{2/3}^2(\xi) + \frac{(\gamma\theta)^2}{1+(\gamma\theta)^2} K_{1/3}^2(\xi)} \qquad \text{Eq. 3.12}$$

where the positive and negative signs correspond to $\psi > 0$ or $\psi < 0$ respectively. The circular polarization is zero for $\theta = 0$ and approaches one for $|\theta| \to \infty$. Above and below the plane the right-handed and left-handed components dominate respectively.

In practice circularly polarized radiation can be obtained by masking part of the beam.

3.3.3 Wigglers

Wigglers are a strong magnetic field version of undulators. Due to strong fields, $K >> 1$, and the oscillation amplitude and concomitant radiated power is larger. The radiation cone is broader in both space and angle. The radiation spectrum is similar to that of bending magnets, as pictured in Figure 3.4, but characterized by a much larger photon flux and a shift to harder X-rays (shorter wavelengths). Although more power is radiated, wiggler radiation is less bright because of the substantially increased radiation cone.

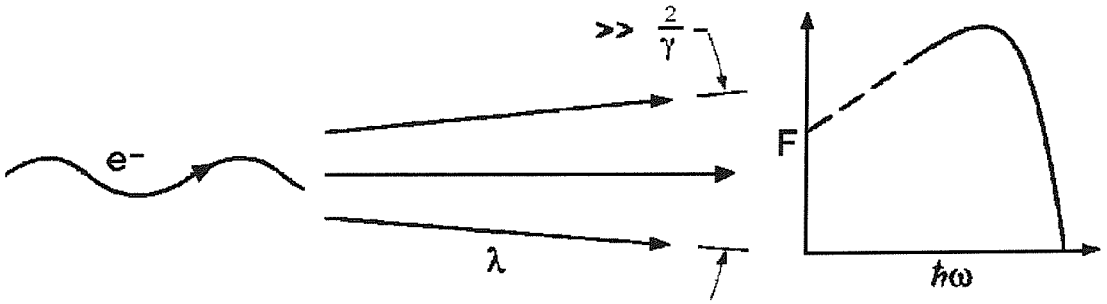

Figure 3.4 *Wiggler radiation and the related radiation spectrum.*

The energy radiated in a single turn forms only a small fraction of the energy of the electron itself (< 0.01%). This is why the effects of the emission of radiation on the motion of one electron can, to a first approximation, be neglected. However, this lost energy needs to be restored and this is achieved by incorporating radio frequency (RF) cavities around the orbit. For this reason the electron beam in a storage ring is not a continuous stream, but rather a highly modulated density function consisting of axial bunches. The spacing of these bunches is set by the RF used to restore power to

the electrons to compensate for power lost to Synchrotron Radiation. The RF is fed to a microwave cavity operating in a mode with an axial electric field, synchronised to the orbit frequency so that slower electrons receive a small acceleration, while faster electrons receive a small deceleration. In this way, in a particular RF cavity, a potential well is set up that tends to trap available electrons into a series of bunches that travel around the ring at the speed of light with a separation equal to the RF wavelength[21].

3.4 The ELETTRA Synchrotron Radiation

ELETTRA[22] is a large multidisciplinary Synchrotron Radiation Laboratory, open for use by researchers in basic and applied fields such as materials and life sciences, physics, chemistry and geology. ELETTRA is an ultra-bright radiation source in the spectral range from UV to X-rays. It offers an international and competitive environment to researchers from Universities, national Laboratories and enterprises from all over the world.

ELETTRA, a third generation electron storage ring, has been in operation since October 1993. It has been optimised in the VUV and soft X-ray range, with an electron energy between 2.0 and 2.4 GeV. It has a spectral brightness of up to 10^{19} photons/s/mm^2/mrad^2/0.1%bw and feeds over 20 beam lines in the range from a few eV to tens of keV (wavelengths from infrared to X-rays).

The storage ring is made up of four types of magnets: bending magnets that deflect the circulating electron beam into a closed circular path, quadrupoles that focus the beam, sextupoles that compensate chromatic and non-linear effects, and steering magnets that perform small adjustments to the circular trajectory. The ring is made up of twelve identical groups of magnets forming a ring roughly 260 m in circumference. The electrons are accelerated in a LINAC (LINear ACcelerator) and then injected into the ring. Electrons start off from a ceramic disc that is heated to very high temperature. An electric field of up to 100 kV draws out the electrons that are then accelerated through various RF structures that make up the LINAC. The LINAC is composed of the Gun (that houses the ceramic disc), a low energy

bunching section and several high-energy sections. The overall length of the LINAC is 66 m and it contains seven high-energy sections each 6 m long. Between accelerating sections quadrupole magnets keep the beam focused. The LINAC operates at 3 GHz and generates a pulse of electron bunches that are accelerated to a final energy which can be as high as 1.2 GeV. In order not to lose electrons as they are accelerated, the entire LINAC is under vacuum, as is the transfer line and the storage ring. In this way collisions with gas molecules, that would otherwise cause the loss of electrons, are avoided. The electrons exiting the LINAC are then transported to the inner part of the storage ring by a transfer line (a series of deflection and focussing magnets). Both the LINAC and transfer line are below ground in order not to interfere with beamlines in the experimental hall and also for reasons of radiation safety. The storage ring is filled by a multi-turn injection process whereby pulses of electrons are gradually fed into the ring ten times a second until the desired current is achieved. Filling the ring to high currents takes usually several minutes. The electrons circulating in the ring do so in a metal vacuum chamber. The vacuum that is maintained in the ring must be of very high quality, since unlike the LINAC and transfer line where an electron passes through once, in the ring the electrons travelling close to the speed of light traverse a given point more than a million times in one second. To maintain a long beam lifetime the chance of electrons colliding with gas molecules has to be reduced. The situation is further complicated by the copious emission of Synchrotron Radiation, around 90 kW of power just from the bending magnets. The unused radiation must be absorbed in special places otherwise chamber deformation and photoelectron release of surface gases will occur. The energy lost by the electrons when emitting Synchrotron Radiation is compensated by RF cavities. Four single cell cavities are used and they are positioned between dipole magnets in the dispersion region thereby allowing maximum use of the long straight sections for insertion devices (wigglers and undulators). The cavities, operating at 500 MHz, produce a longitudinally bunched beam, in synchronization with the RF field. The maximum number of electron bunches, separated by 2 ns, that can fit in the ring circumference is 432.

The results presented in this Thesis have been obtained at BL 4.2, the Circular Polarized Beamline at ELETTRA.

3.4.1 The BL 4.2 Circular Polarized Beamline

The BL 4.2 Circular Polarized Beamline at ELETTRA provides radiation in the photon energy range 5 - 1000 eV (12 - 2500 Å)[23]. The photon source is an electromagnetic elliptical wiggler (EEW). In this EEW the vertical magnetic field due to the permanent magnet poles is combined with a horizontal field generated by a horizontal array of electromagnets. By moving the permanent magnets it is possible to modify the intensity of the vertical magnetic field and hence the horizontal displacement of the electrons, while the vertical displacement is slightly changed by changing the current intensity passing through the coils of the electromagnets. In this way there is the possibility of changing the mode of operation of the insertion device from elliptical wiggler to elliptical undulator mode, whilst maintaining optimum characteristics of polarization and photon flux over a wide spectral range. The polarization of the associated emitted radiation can be changed from left-handed to right-handed by reversing the horizontal field. Two independent monochromators, one working at normal incidence, from 5 to 35 eV, and the other working at grazing incidence, from 30 to 1200 eV, have been designed to cover the entire spectral range efficiently. In practice, during this project only the monochromator working at normal incidence was used with the gold coating.

A schematic layout of the beamline in the normal incidence configuration (NIM) is shown in Figure 3.5.

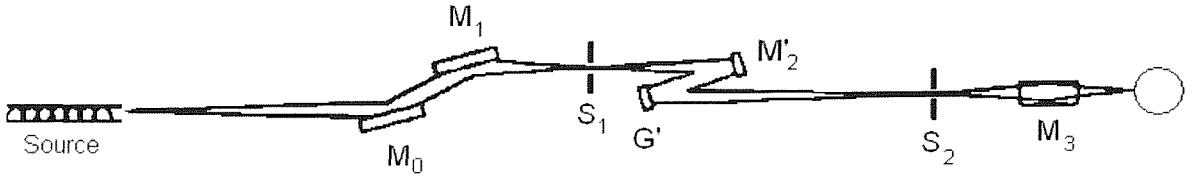

Figure 3.5 *Layout of the beamline in Normal Incidence Configuration.*

The first mirror, M_0, of the beamline is a flat mirror used at 2.5° grazing incidence, which diverts the radiation vertically. This mirror protects the following optical elements from the hard portion of the radiation spectrum. The second mirror, M_1, has a toroidal shape and returns the radiation parallel to the orbit plane with 2.5° grazing incidence. It has been designed to focus the radiation into the entrance slit, S_1, of the monochromator along the tangential direction (magnification 1/3) and into the exit slit, S_2, of the monochromator along the radial direction (magnification 2/3). The monochromator consists of a cylindrical mirror, M'_2, and a set of two interchangeable spherical gratings, G'. After the entrance slit the radiation is deflected vertically by means of a normal incidence convex cylindrical mirror, M'_2, whose coating could be either gold or aluminium. The radiation is then diffracted and focused onto the exit slit by a spherical grating, G', illuminated at normal incidence with a constant 2° included angle. The combination of M'_2 and G' provides a focus at the exit slit S_2 with a degree of astigmatism correction. Only the first outside order of the diffracted beam is focused onto the exit slit. The radiation is then refocused onto the sample by the toroidal mirror, M_3, with a magnification equal to one. The mirror M_3 diverts the radiation by 5° in the horizontal plane. The positions of these mirrors can be manually adjusted to maximise the photon flux, measured by a photodiode at the end of the spectrometer. In order to protect the vacuum in the beamline and in the storage ring, a series of valves are present along the beamline, which automatically shut when the pressure rises higher than preset limits. The last valve is a window valve transparent to visible light. This permits alignment of the spectrometer with the beamline, using the visible components of the zero order from the monochromator passing through the window valve.

The energy resolution at 20 eV with $S_1 = S_2 = 50$ μm is ≈ 3 meV. This value has been determined experimentally with the measurements on N atom (see Chapter 6).

3.5 Conclusions

In this Chapter a review of the properties of Synchrotron Radiation are presented. A brief history of Synchrotron Radiation from the first discovery of Synchrotron Radiation to the following developments until the present days has been outlined. In this thesis, Synchrotron Radiation was used as a tuneable wavelength radiation source and the results presented have been obtained at the BL 4.2 Circular Polarized Beamline at ELETTRA. A detailed description of this beamline has been presented.

References

[1] http://hyperphysics.phy-astr.gsu.edu/hbase/astro/crab.html

[2] J. Larmor
Phil. Magazine **44**, 503 (1897).

[3] A. Lienard
L'Eclairage Elec. **16**, (1898).

[4] G. A. Schott *Electromagnetic Radiation*, Cambridge University Press ed.Cambridge, 1912.

[5] H. C. Pollock
American Journal of Physics **51**, 278 (1983).

[6] F. R. Elder, A. M. Gurewitsch, R. V. Langmuir and H. C. Pollock
Physical Review **71**, 829 (1947).

[7] F. R. Elder, R. V. Langmuir and H. C. Pollock
Physical Review **74**, 52 (1948).

[8] K. Codling and R. P. Madden
Journal of Applied Physics **36**, 380 (1965).

[9] A. Balzarotti, M. Grandolfo and M. Piacentini
Lettere al Nuovo Cimento **3**, 15 (1970).

[10] T. Sagawa, Y. M. Iguchi, M. Sasanuma, T. Wasu, S. Yamaguchi, A. Ejiri, S. Fujiwara, M. Nakamura, T. Masuoka, T. Sasaki and T. Oshio
Japanese Journal of Physical Society **21**, 2587 (1966).

[11] T. Sagawa, Y. M. Iguchi, M. Sasanuma, M. Yokota, S. Yamaguchi, A. Ejiri, S. Fujiwara, M. Nakamura, T. Masuoka, T. Sasaki and T. Oshio
Japanese Journal of Physical Society **21**, 2602 (1966).

[12] R. Haensel and C. Kunz
Zeitschrift fur Angewandte Physik **23**, 276 (1967).

[13] K. J. Button, H. A. Gebbie and B. Lax
Indian Economic Journal **2**, 202 (1966).

[14] E. M. Rowe and F. E. Mills
Particle Accelerator **4**, 221 (1973).

[15] C. Gahwiller, F. C. Brown and H. Fujita
Review of Scientific Instrumentation **41**, 1275 (1970).

[16] R. P. Feynman *The Feynman lectures of physics*, Addison-Wesley ed.Reading, 1963.

[17] J. D. Jackson *Classical Electrodynamics*, Wiley ed.New York, 1962.

[18] C. Kunz *Synchrotron Radiation*, Kunz C. ed.New York, 1979.

[19] D. Attwood *Soft X-rays and extreme ultraviolet radiation*, Cambridge University Press ed.New York, 2000.

[20] V. Schmidt *Electron Spectrometry of Atoms using Synchrotron Radiation*, Cambridge University Press ed.New York, 1997.

[21] S. Krinsky, M. L. Perlman and R. E. Watson *Handbook on Synchrotron Radiation*, edited by E.E. Koch ed.Amsterdam, 1983; Vol. 1A, Chapter 2.

[22] http://www.elettra.trieste.it

[23] A. Derossi, F. Lama, M. Piacentini, T. Prosperi and N. Zema
Review of Scientific Instrumentation **66**, 1718 (1995).

Chapter 4

4 EXPERIMENTAL DETAILS

In this Chapter, sections 4.1 and 4.2, the synchrotron photoelectron spectrometer used to obtain the results presented in this thesis is described. This was designed specifically for the study of reactive intermediates using synchrotron radiation. Section 4.3 describes how the reactive molecules studied in this work have been prepared.

4.1 The photoelectron spectrometer

A number of ultraviolet photoelectron spectrometers have been built at Southampton and elsewhere[1-6] to study short-lived molecules. The spectrometer used in this work was specially designed by Dr. Alan Morris to be utilised initially at the Daresbury Laboratory Synchrotron Radiation Source[7], and later at ELETTRA[8]. Angle resolved studies can be performed with this instrument[9].

The essential components of a photoelectron spectrometer are a source of suitable radiation, an ionization chamber in which molecules or atoms can be ionized, an electron energy analyser, an electron detector and a recorder. Additionally, the spectrometer must be evacuated to suitably low pressure, otherwise the VUV radiation will be absorbed, photoelectrons will be scattered and the detector will not operate.

This spectrometer was designed and constructed in Southampton, mainly of aluminium alloy and other non-magnetic materials. It is modular, with separate chambers for the ionization region and the electron analyser, separated by narrow entrance slits. Each chamber is evacuated by a turbomolecular pump; this differential pump system prevents contamination of the Synchrotron Radiation beamline optics. Moreover an electrostatic lens system was introduced between the ionization chamber and the analyser to allow the operation of the analyser at constant pass energy, and to further reduce contamination of the analyser.

The supporting frame incorporates several features to facilitate alignment of the spectrometer with the (non-moveable) photon beam; this is depicted schematically in Figure 4.1. The base of the frame, labelled A in Figure 4.1, has wheels for mobility and has adjustable legs that allow the spectrometer to be raised for alignment purposes. Plate B is pivoted at a point directly under the photon beam axis, again to assist with alignment. Plate C slides in and out of the horizontal plane in Figure 4.1, so that the spectrometer may be moved into position before connection to the beamline system. The upper supporting section, labelled D, may be used to translate the spectrometer in the other horizontal direction.

Further schematic diagrams of the spectrometer are presented in Figures 4.2 and 4.3, which show the principal features of the design.

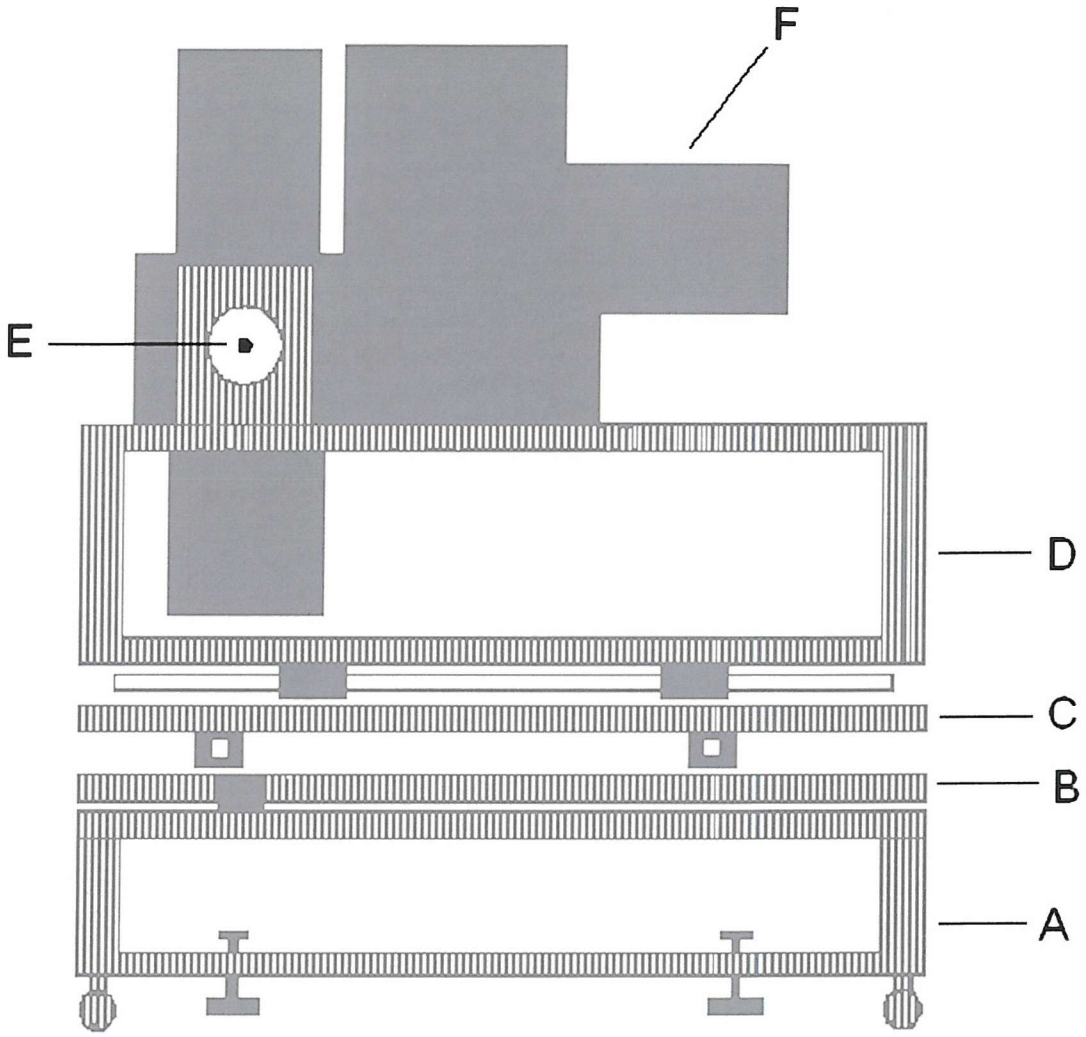

Figure 4.1 *Schematic picture of the spectrometer and supporting frame*

A: Wheeled Base Frame	*D: Translation Plate 2*
B: Pivoted Plate	*E: Photon Beam axis*
C: Translation Plate 1	*F: Spectrometer*

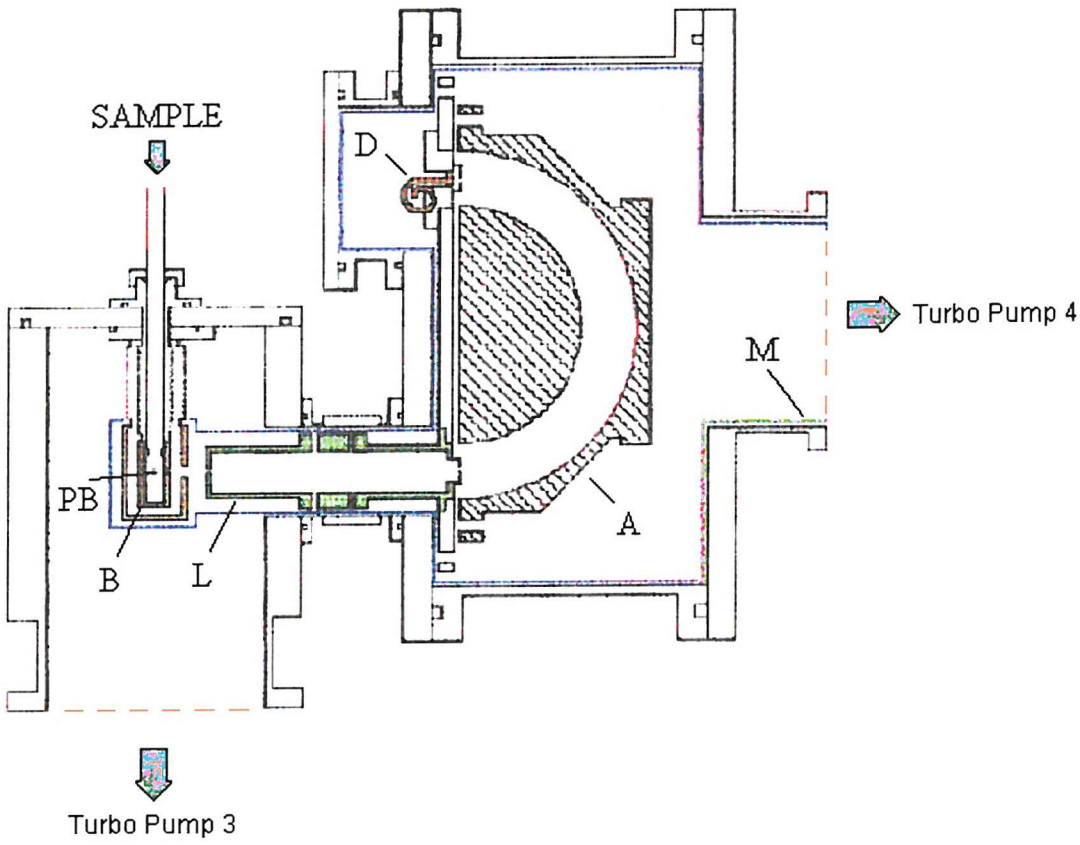

Figure 4.2 *Cross section of the Analyser system and Ionization Chamber*

A: Hemispherical analyser
B: Boxes for differential Pumping
D: Electron Detector
L: Electron Lens
M: μ-metal Shield
PB: Photon Beam

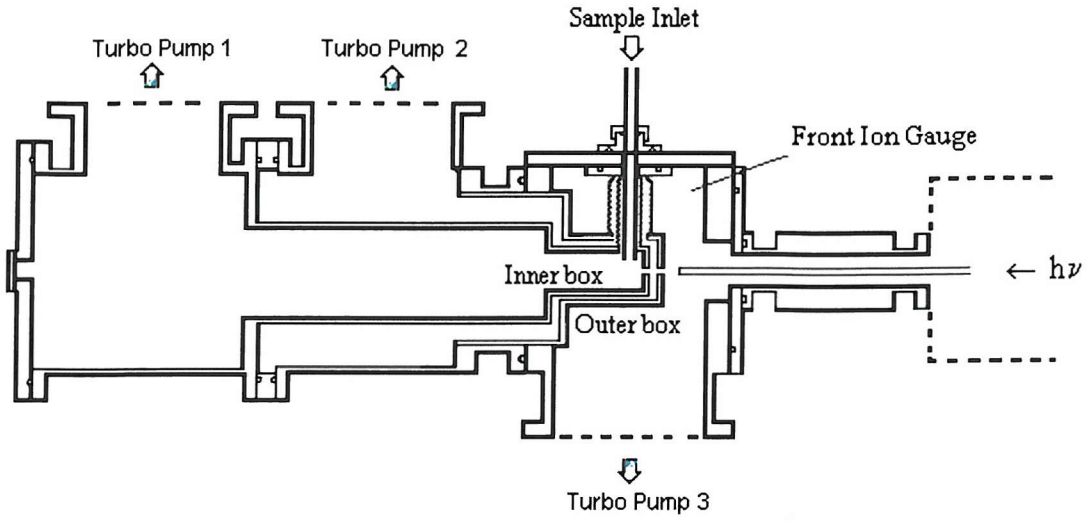

Figure 4.3 *The pumping system of the spectrometer.*

Figure 4.2 shows a cross section of the spectrometer in the plane perpendicular to the photon beam (PB in Figure 4.2).

The sample gases are introduced through an inlet system into the ionization chamber of the spectrometer, where they interact with the photon beam.

In the ionization chamber there are two metallic boxes (B in Figure 4.2) which are differentially pumped in order to prevent contamination of the spectrometer and of the monochromator optics. The inner metal box is earthed and coated with a conductive graphite layer in order to reduce local electric fields that could degrade the spectra. The boxes are connected to two turbomolecular pumps to allow differential pumping, as can be seen in Figure 4.3.

As the electrons leave the boxes they enter a three elements lens system (L in Figure 4.2). The main reasons for using the lens are to use the analyser at constant pass energy and to keep the analyser far away from the photoionization region reducing its contamination. The first lens element (nearest the photon beam PB) is electrically connected to the outer box, the third element is kept at a positive (negative) voltage in order to accelerate (decelerate) the electrons, and the second

element is at a voltage chosen to optimize the focus of the electron beam onto the entrance slit of the analyser.

This voltage depends on the kinetic energy of the electrons and is experimentally pre-determined from a focus voltage curve.

A 180° 100 mm mean radius hemispherical electron energy analyzer (A in Figure 4.2) is used. It is operated at fixed pass energy, usually 5 eV, which should ensure constant resolution and transmission throughout the spectral range.

The ionization and analyzer chamber must be at sufficiently low pressure to ensure that the electrons can travel from the point of production to the detector without undergoing collisions with the background gas. Two turbomolecular pumps, each backed by a rotary pump, evacuate the ionization chamber and the analyzer; typical pressures are in the range 10^{-5} - 10^{-6} mbar.

As local electric and magnetic fields could effect the motion of the electrons, shielding is extremely important. The spectrometer is made entirely of non-magnetic metals and any unwanted local electrostatic fields inside sensitive regions should be avoided. In order to eliminate any magnetic field effects the ionization region, the lens, the analyser and the detector are enclosed in a shielding made by μ-metal (M in Figure 4.2); this is a material especially produced to have a high magnetic permeability to constrain magnetic fields to pass within the metal rather than through the metal.

The electrons are detected by a channeltron (D in Figure 4.2). The final electron signal is transmitted to a standard electronic counting system.

The cross section of the ionization region, depicted in Figure 4.3, shows the differential pumping which has to be used to prevent contamination of the beam-line optics when working at the Synchrotron Radiation Source.

4.1.1 The vacuum system

The spectrometer must be evacuated to low pressures ($P < 10^{-5}$ mbar), otherwise the VUV radiation will be absorbed, photoelectrons will be scattered, and the detector will not operate.

The differential pumping system[10] adopted in the apparatus consists of four turbomolecular pumps, each backed by its own rotary pump. The ionization region is enclosed within two boxes. The boxes are closed, apart from a 2 mm circular aperture at the front to allow the photon beam to pass through, the slits (10 mm × 2 mm) which point towards the electron analyser, and a 12 mm diameter hole at the top for the introduction of the sample gas. Most of the sample gas in the inner box is removed via a 360 ls^{-1} turbo pump (Turbo Pump 1 in Figure 4.3, Leybold Turbovac 361C). The gas that escapes through the slits on the inner box is pumped away by a 360 ls^{-1} turbomolecular pump (Turbo Pump 2 in Figure 4.3, Leybold Turbovac 361C). A third turbomolecular pump, speed 1000 ls^{-1} (Turbo Pump 3 in Figure 4.3, Leybold Turbovac 1000) maintains the vacuum between the spectrometer and the Synchrotron Radiation Source by collecting any gas that enters the ionization chamber. An ionization gauge measures the pressure outside the boxes, whose base value is 8×10^{-8} mbar, rising to 5×10^{-6} mbar when gas is admitted. The pressure inside the inner box is estimated to be at least one order of magnitude higher. No appreciable change in the beamline pressure is observed when gas is admitted. Pressure in the spectrometer in the analyser region is measured by an ionization gauge and read by an Edwards AGC controller. Because Turbo Pumps 1 and 2 receive a heavy load of gases, which are often corrosive, both have corrosion resistant coatings. They are also fitted with purge valves to reduce bearing contamination and extend the operational lifetime when pumping corrosive gases. The electron analyser region is also held under vacuum using a fourth, horizontally mounted tubomolecular pump (Turbo Pump 4 in Figure 4.2, Leybold Turbovac 600). Using this pumping arrangement and a 4 mm diameter stainless steel light-guide to connect the spectrometer to the beamline, contamination of the monochromator optics is kept to a minimum.

4.1.2 The hemispherical electron analyser

The electron analyser, labelled A in Figure 4.2, consists of two concentric 180° hemispherical electrodes. The inner and outer sectors are constructed from aluminium alloy; they have radii R_i and R_o of 80 mm and 120 mm respectively and

an internal separation of 40 mm. In order to select electrons with mean pass energy E_{pass}, the sectors must be at potentials V_i and V_0 given respectively by[11,12]:

$$V_i = E_{pass}\frac{R_0}{R_i} \qquad \text{Eq. 4.1}$$

$$V_0 = E_{pass}\frac{R_i}{R_0} \qquad \text{Eq. 4.2}$$

The contribution of the finite width of the analyser slits to the full width at half maximum (FWHM) of a photoelectron band is approximately[13]:

$$\Delta E_{FWHM} = \frac{\Delta S}{R_i + R_0} E_{pass} \qquad \text{Eq. 4.3}$$

where ΔS is the common width of the entrance and exit slits, $\Delta S = \Delta S_{entrance} = \Delta S_{exit}$. For the analyser geometry used in this work $\Delta S = 1$ mm and the ΔE_{FWHM} is equal to 25 meV for pass energies of $E_{pass} = 5$ eV. This is the contribution from the analyser itself, and neglects the small effect arising from the angular acceptance of the analyser, α[14]. Narrower slits or lower pass energy would give rise to better resolution, but at the expense of a lower electron transmission. Other broadening effects arise from the radiation bandwidth, Doppler broadening in the sample beam and thermal motion of the sample molecules[15]. A further important contribution to the ΔE_{FWHM} arises from local potentials that may deflect the electrons, accelerate them, decelerate them or cause them not to reach the entrance slit of the hemispheres. To minimise these potentials all the inner surfaces of the analyser are coated with a conductive layer of graphite.

The transmission efficiency of the analyser is a linear function of the pass energy, except at very low energies (< 1 eV) as such electrons are more strongly effected by stray fields[16]. Contamination of the electron optics from the reactive gases used usually leads to the resolution and transmission of the spectrometer deteriorating with time so that regular cleaning and replacement of the graphite coating is essential to regenerate the best conditions for recording high quality spectra.

4.1.3 The electron lenses

Usually photoelectron spectrometers record spectra by sweeping the voltages on the hemispheres, so that the kinetic energy of the transmitted electrons is scanned. This procedure has the disadvantage of giving different resolution and transmission for electrons with different kinetic energies. The apparatus used in this work was built in such a way that the spectrometer has an analyser that operates at constant pass energy, E_{pass}, typically of 5 eV. The electrons are accelerated (or decelerated) by a lens, labelled L in Figure 4.2, so that they enter the analyser with the appropriate fixed energy. Hence spectra are recorded with constant transmission and resolution.

The lens is constructed from three electrically isolated, coaxial, cylindrical aluminium elements. The first element is earthed, so that electrons in this segment maintain their initial kinetic energy after ionization. The third element is at a voltage $V_3 = E_{pass} - E_i$, where E_i is the original energy of the electrons, so that when moving from the first to the third element these electrons are accelerated or decelerated to the pass energy E_{pass}. The plate on which the analyser is mounted is in electrical contact with the third element lens.

The second element of the lens is at a potential V_2, and acts as a focusing element. The value of V_2 must be such that the exit slit of the lens becomes the optical image of the entrance slit. A focus curve is generated by plotting $(E_i + V_2)/E_i$ vs E_{pass}/E_i. Focus curves for various lens geometries have been calculated by Harting and Read[17]. In practice, the focus curve was determined empirically in this work. This is performed by optimising V_2 so that the intensity of a particular electron signal is maximized for a range of kinetic energies at the selected analyser pass energy. An example of a focus curve is shown in Figure 4.4 where the red line is the result of a fourth order polynomial fit to the points obtained. The coefficients of the fit are passed to the controlling software which is then able to calculate the optimum focusing voltage V_2 at a particular electron kinetic energy.

In Southampton only the HeI (21.22 eV) discrete line source is available, and different electron kinetic energies are obtained by observing the photoelectron bands of molecular oxygen and applying positive and negative external voltages to the inner boxes to obtain an energetic shift of the bands.

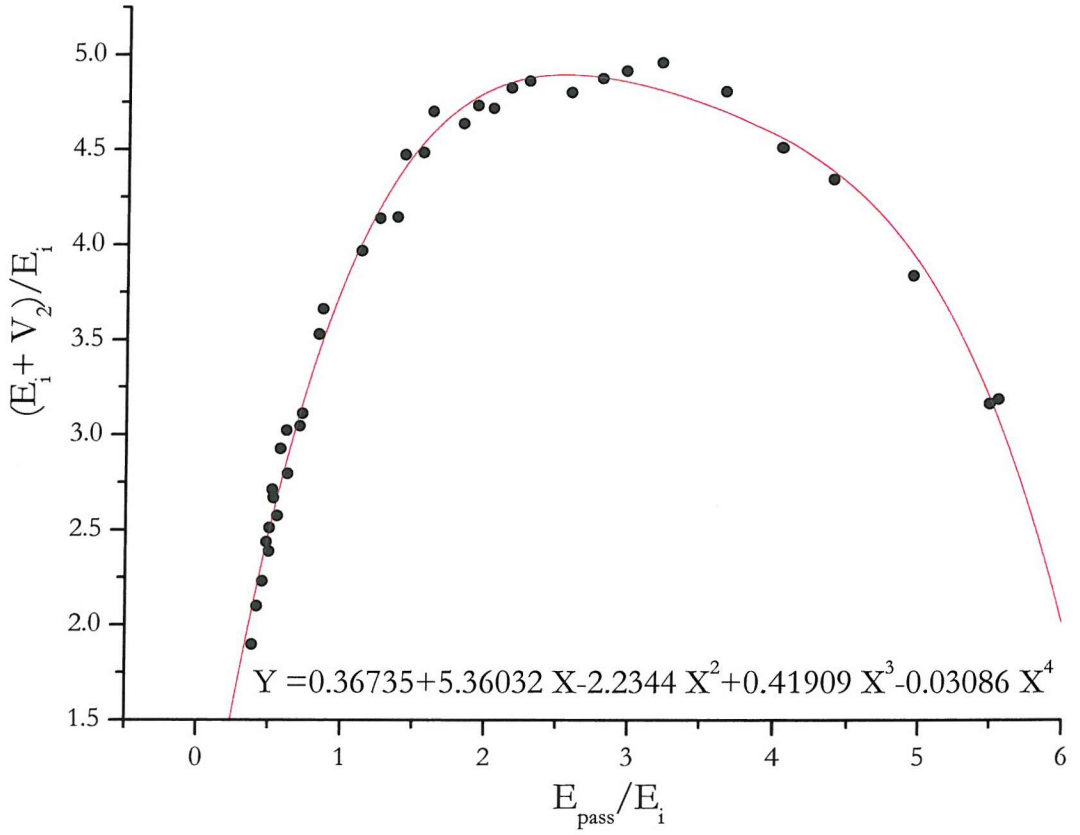

Figure 4.4 *Focus curve obtained with a polynomial fit.*

4.1.4 Shielding

External electric and magnetic fields must be removed since these can affect the paths of the electrons which are to be analysed. Electrostatic fields cannot penetrate the metal frame of the spectrometer, but extra effort must be made to minimize the magnetic fields. One possible way to avoid this problem is by enclosing the spectrometer with three pairs of mutually orthogonal Helmholtz coils, in which the field produced by the current passing in any pair of coils compensates the component of the earth's field in a plane perpendicular to that of the coils. The photoelectron resolution and count-rate can be optimised by adjusting the current through the coils. However space constraints at the Synchrotron Radiation Source do not permit such an arrangement; hence the critical regions of the spectrometer (the ionization region,

the lens, the analyser and the detector) are enclosed by a 2 mm-thick layer of μ-metal, labelled M in Figure 4.2, an alloy with high magnetic permeability that tends to constrain the magnetic field to pass within it rather than through it.

4.1.5 Electron detection and control system

Electrons that traverse the analyser and pass through the exit slit are detected by a single channel electron multiplier (channeltron), labelled D in Figure 4.2. The electron pulses produced by the channeltron are preamplified and passed to an Ortec 590A amplifier, whose output goes to a "General Purpose I/O" National Instrument card plugged into a computer. The potentials for the focussing and retarding elements of the lens are set by Kepco APH500M and BOP100-1M power supplies respectively, controlled by digital-to-analog converters (DACs), supplied by a Keatly board with 2 channels 20 bit analog output plugged into a computer.
The control software written with the programme LABVIEW allows the collection of photoelectron spectra and is interfaced with the beamline control system to record constant ionic state spectra at ELETTRA.

4.1.6 The rotation mechanism

Angle resolved photoelectron and constant ionic state spectra are recorded by rotating the analyser in the plane perpendicular to the linearly polarized photon beam. This spectrometer was built in such a way that the whole apparatus can be rotated, vacuum system included. Figure 4.5 shows the two extreme cases in which the lens axis, that defines the direction of the electrons collected, is positioned at an angle of *(a)* $\theta = 0°$ and *(b)* $\theta = 73.5°$ with respect to the horizontal direction of polarization of the photon beam (at right angles to the direction of propagation of the radiation). A fixed vertical screw-drive is mounted in bearings located at the top and bottom of the fitting. When rotated this moves the threaded block and the attached arm up or down, as shown in Figure 4.5. For the measurements of angular distribution it is important to make sure that the efficiency of the analyser does not change when the spectrometer is rotated. The biggest contribution to the change of

the efficiency of the analyser comes from small misalignments between the axis of rotation and the direction of the photon beam. This contribution is minimised by slight adjustments, after each rotation of the spectrometer, of the direction of the photon beam in such a way as to maximise the signal from the detector and the current measured by the photodiode at the back of the spectrometer, on the opposite side of the ionization chamber from the radiation source. Moreover to minimize this contribution all the experiments related to angle resolved studies were performed at θ values of 0°, 54° 44' and 60°. These three positions were extensively tested to ensure the reliability of this kind of experiment by measuring photoelectrons from gases of known angular distribution parameters at known photon energies.

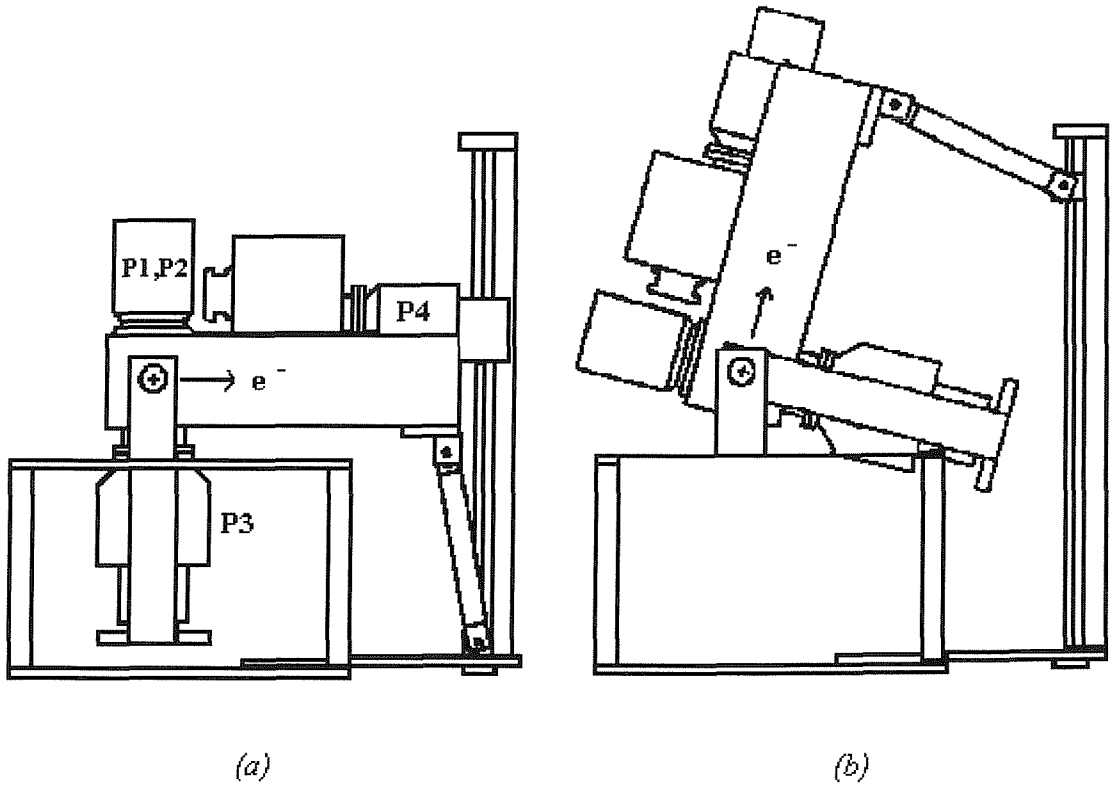

Figure 4.5 *A view in the photon beam direction showing the mechanism for rotating the spectrometer*
(a) $\theta = 0°$ *(b)* $\theta = 73.5°$

4.1.7 The laboratory radiation source

The inert gas discharge lamp is the most common photon source used in gas phase ultraviolet photoelectron spectroscopy[18], and the most widely used photon source is a discharge in pure helium, which gives the HeI α ($He(1s2p\ ^1P) \rightarrow He(1s^2\ ^1S) + h\nu$) resonance line at 584 Å, corresponding to a photon energy of 21.22 eV, as its main output. This radiation is energetic enough to cause ionization of valence electrons in most molecules. The He(I)α line is accompanied by lines of higher energy, e.g. the HeI β ($He(1s3p\ ^1P) \rightarrow He(1s^2\ ^1S) + h\nu$) resonance line at 537 Å, equivalent to a photon energy of 23.08 eV; this is much lower in intensity and approximately 98% of the radiation emitted in the vacuum ultraviolet region is HeI α[11].

In Southampton this kind of discharge lamp (Fisons/VG 232) is fitted to record test photoelectron spectra when beamtime is not available. The radiation from the He lamp is unpolarized. With unpolarized radiation to performed angular resolved experiments the signal must be measured as a function of the angle θ' away from the direction of the radiation beam[11]; for this reason no angle resolved experiments were performed in Southampton.

4.2 Types of spectra

The spectrometer has been designed to allow two different kinds of spectra to be recorded: photoelectron (PE) spectra and constant ionic state (CIS) spectra.

4.2.1 Photoelectron Spectra (PES)

In a PE spectrum the yield of photoelectrons is measured as a function of their kinetic energy, with the wavelength of the incident radiation fixed at a particular value, as explain in Chapter 2.1. This kind of spectrum is recorded in this work by scanning the voltage of the third lens element to obtain a photoelectron spectrum at fixed pass energy. An electron energy spectrum of this type provides a map of the ionic states that are accessed, and allows ionization energies to be measured. The

overall resolution, that is the combination of the resolution of the analyser and the bandwidth of the radiation, is normally of the order of 50 meV. This allows vibrational structure to be resolved in the photoelectron spectra of most light molecules.

4.2.2 Constant Ionic State Spectra (CIS)

In addition to a photoelectron (PE) spectrum, a constant ionic state (CIS) spectrum can also be recorded with a Synchrotron Radiation Source by sweeping the energy of the monochromatized Synchrotron Radiation and monitoring the intensity of a selected photoelectron feature, see Chapter 2.2.

In a CIS spectrum the yield of electrons corresponding to a selected ionization process, normally a vibrational component of a photoelectron band, is measured as a function of the energy of the incident radiation.

In this kind of spectrum the kinetic energy of the electrons to be detected is scanned simultaneously with the energy of the radiation, while maintaining their difference equal to the ionization energy of the process under investigation, i.e. the energy separation between the initial molecular state and the final ionic state does not change. This is possible to perform when using the Synchrotron Radiation Source because the acquisition program is written in such a way that the potential of the third lens is scanned with the monochromator of the beamline, which selects the photon beam energy, in order to keep the electrons of a selected ionization process, focused on the detector.

A CIS spectrum can show discrete structure when the radiation is resonant with an excited neutral state that autoionizes to the ionic state under investigation, as explained extensively in Chapter 2.2.

The resolution in a CIS spectrum depends only on the radiation bandwidth, and not on the analyser resolution, and it allows vibrational and rotational progressions in neutral excited states to be resolved. By recording such a spectrum, a map of autoionizing states, usually Rydberg states, is obtained. The nature of these states may be deduced and new ionization limits may be extrapolated from these spectra.

To run a CIS spectrum it is usual to first acquire a conventional PE spectrum, from which accurate ionization energy to the particular ionic state and vibrational component of interest can be determined.

4.3 Sample production

The short lifetimes (≈ 0.1 msec) of the reactive molecules studied in this work mean that they must be produced *in situ* for spectroscopic investigation and then rapidly pumped into the photon beam[19]. Methods that are commonly used to produce such species are fast atom-molecule reactions, pyrolysis, photolysis and gas-solid reactions, and are based on the safe handling of reactive intermediates in photoelectron spectroscopy[20].

In Figure 4.6 are shown the inlet systems utilized during this work in which the samples under investigation were produced.

As can be seen in Figure 4.6, in order to prevent low energy electrons produced in the discharge from entering the ionization region, the side inlet tube has three 90° bends.

Typically, in these inlet systems atoms are produced in the microwave discharge and subsequently they react with a stable target molecule which is flowed down the central tube, usually the inner inlet system. Depending on the rate constant of the primary reaction and on the lifetime of the reactive molecule of interest, the position of the inner inlet system above the photon beam, which is called the mixing distance, can be adjusted to give the maximum signal of the molecule of interest.

4.3.1 Atoms production

Nitrogen atoms were produced by microwave discharging (2.45 GHz, *P*~50/60 W) a flowing mixture of molecular nitrogen, with helium as carrier, flowing through a phosphoric acid coated inlet system. A schematic drawing of the inlet system is shown in Figure 4.6 *(b)*. This inlet system is the simplest one because both the gas and the carrier are introduced via the same aperture.

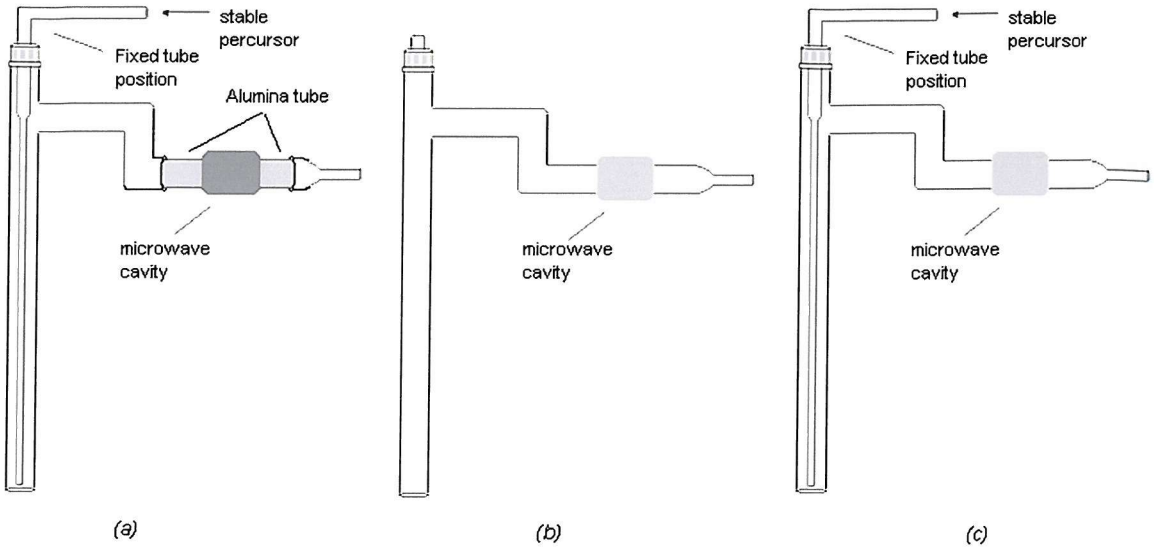

Figure 4.6 *Schematic inlet systems used for producing reactive intermediates by a rapid atom-molecule reaction.*

4.3.2 Radicals production

The fast atom-molecule route was used to produce OH radicals via the rapid reaction:

$$H + NO_2 \rightarrow OH + NO \qquad \text{Eq. 4.4}$$

The rate constant of this reaction is 1.1×10^{-10} $cm^3molecule^{-1}sec^{-1}$ at room temperature[21].

Hydrogen atoms were produced by microwave discharging a flowing mixture of molecular hydrogen and helium through a coated inlet system, Figure 4.6 *(c)*. Helium is added to help sustain the discharge, and the inner surface of the glass tube is coated with phosphoric acid to reduce hydrogen atom recombination. NO_2 is added, as a stable precursor, to the $H/H_2/He$ mixture through a 3 mm inner inlet system which passes down the centre of the main inlet system. At ELETTRA the inner tube should not be moved to adjust the position of the mixing point, but the

optimum mixing distance must be accurately determined during several test experiments performed in Southampton.

The OH radicals produced by the reaction Eq. 4.5 undergo rapid secondary reactions:

$$OH + OH \rightarrow H_2O + O \qquad \text{Eq. 4.5}$$

$$O + O + M \rightarrow O_2 + M \qquad \text{Eq. 4.6}$$

These reduce the yield of OH radicals and also give rise to H_2O bands in the spectra that can overlap with those from OH. This is a common problem when studying the PES of reactive intermediates.

In order to reduce the concentration of secondary products in the ionization region, the precursors must be mixed close to the photon beam, but not so close that an insufficient partial pressure of OH is produced. For OH produced from the H + NO_2 reaction in the apparatus used, the optimum mixing distance was found to be 3 cm above the photon beam. OD was produced via the same method as OH, using D_2 instead of H_2.

The fast atom-molecule route was also used to produce S atoms and SH radicals via the rapid reactions:

$$F + H_2S \rightarrow SH + HF \qquad \text{Eq. 4.7}$$

$$F + HS \rightarrow S + HF \qquad \text{Eq. 4.8}$$

Fluorine atoms were produced by passing a flowing mixture of F_2 in 5% helium through a microwave discharge in a glass inlet tube coated with teflon.

The rate constant of the F + H_2S reaction is 1.33×10^{-10} $cm^3molecule^{-1}s^{-1}$ at room temperature[22]. In order to avoid attack of the glass of the inlet system by the fluorine atoms produced by the discharge, the inner surface of the tube is coated with a thin layer of teflon, while the discharge cavity was positioned on an alumina section of the inlet system to prevent melting of the teflon due to heating from the discharge[19], as shown in Figure 4.6 *(a)*.

The optimum mixing distance for production of both S and SH was found to be 2 cm above the photon beam, with the inner-inlet system longer than the outer inlet system by about 2 mm.

The fast atom-molecule route was also used at ELETTRA to produce the CF radicals. These radicals can be produced by reaction of fluorine atoms with a secondary gas which can be chosen from acetaldehyde, acetone, acetonitrile or acetylene[23,24]. All these reactions produced a low yield of CF and also species as CO (AIE 14.018 eV[25]) which contribute to the region of interest around 13.8 - 14.2 eV. For these reasons the reaction used for producing CF was F + CH_3F. The following species are also produced with CF as reaction products depending on the reaction time and partial pressure of F and CH_3F: C_2H_2, C_2HF and HF. However, they do not contribute any signals within the ionization energy region of interest.

As for the production of S and SH radicals, in order to avoid attack of the glass of the inlet system, the inner surface of the tube is coated with a thin layer of teflon, while the discharge cavity was positioned on an alumina section in the inlet system to prevent melting of the teflon due to heating from the discharge[19], as shown in Figure 4.6 *(a)*. The optimum mixing distance for production of CF was found to be 4 cm above the photon beam.

Some test experiments were also performed at Southampton to produce NH radicals. The fast atom-molecule route was also used to produce these radicals via the rapid reaction:

$$F + NH_3 \rightarrow HF + NH_2 \qquad \text{Eq. 4.9}$$

where fluorine atoms were produced by passing a flowing mixture of F_2 in 5% helium through a microwave discharge in a glass inlet tube coated with teflon. The rate constant of the F + NH_3 reaction is 1.1×10^{-10} $cm^3molecule^{-1}s^{-1}$ at room temperature[22]. NH radicals were produced by the rapid secondary reaction of atomic fluorine with NH_2:

$$F + NH_2 \rightarrow HF + NH \qquad \text{Eq. 4.10}$$

As for all the reactions carried out using fluorine atoms, in order to avoid attack of the glass of the inlet system by the fluorine atoms produced by the discharge, the

inner surface of the tube is coated with a thin layer of teflon, while the discharge cavity was positioned on an alumina section in the inlet system to prevent melting of the teflon due to heating from the discharge[19], as shown in Figure 4.6 *(a)*.

The same conditions for the production of S and SH were found also for the production of both NH_2 and NH: an optimum mixing distance of 2 cm above the photon beam, with the inner-inlet system longer than the outer inlet system by about 2 mm.

4.4 Conclusions

The photoelectron spectrometer used in this thesis for the study of reactive intermediates with a Synchrotron Radiation Source has been fully described in this Chapter. This spectrometer has been used to study the photoionization behaviour of several reactive intermediates (namely N and S atoms, OH, OD, SH, NO and CF radicals) and the results of this work are presented in Chapters 5 to 10.

References

[1] D. C. Frost, S. T. Lee, C. A. McDowell and N. P. C. Westwood
Journal of Electron Spectroscopy and Related Phenomena **12**, 95 (1977).

[2] N. Jonathan, D. J. Smith and K. J. Ross
Chemical Physics Letters **9**, 217 (1971).

[3] J. M. Dyke, L. Golob, N. Jonathan, A. Morris and M. Okuda
Journal of The Chemical Society and Faraday Transactions 2 **70**, 1828 (1974).

[4] J. M. Dyke, N. Jonathan and A. Morris *Electron Spectroscopy: Theory, Techniques and Applications*, edited by C.R. Brundle and A.D. Baker ed.; Academic Press: London, 1979.

[5] A. Morris, N. Jonathan, J. M. Dyke, P. D. Francis, N. Keddar and J. D. Mills
Review of Scientific Instruments **55**, 172 (1984).

[6] J. M. Dyke, A. Morris and N. Jonathan
International Review of Physical Chemistry **2**, 3 (1982).

[7] http://www.dl.ac.uk

[8] www.elettra.trieste.it

[9] J. M. Dyke, S. D. Gamblin, A. Morris, T. G. Wright, A. E. Wright and J. B. West
Journal of Electron Spectroscopy and Related Phenomena **97**, 5 (1998).

[10] D. J. Hucknall and A. Morris *Vacuum technology calculations in chemistry*, Rs C ed.Cambridge, 2003.

[11] J. H. D. Eland *Photoelectron Spectroscopy*, Butterworths & Co ed.Oxford, 1984.

[12] J. W. Rabalais *Principles of Ultraviolet Photoelectron Spectroscopy*, Wiley & Sons ed.New York, 1977.

[13] A. Poulin and D. Roy
Journal of Physics E **11**, 35 (1978).

[14] G. K. Ovrebo and J. L. Erskine
Journal of Electron Spectroscopy and Related Phenomena **24**, 189 (1981).

[15] J. M. Hollas *Modern Spectroscopy*, Wiley & Sons ed.New York, 1996.

[16] J. L. Gardner and J. A. R. Samson
Journal of Electron Spectroscopy and Related Phenomena **8**, 123 (1976).

[17] E. Harting and F. H. Read *Electrostatic Lenses*, Elsevier ed.Amsterdam, 1976.

[18] J. A. R. Samson *Tecniques of Vacuum Ultraviolet Spectroscopy*, Wiley & Sons ed.New York, 1967.

[19] M. C. R. Cockett, J. M. Dyke and H. Zamanpour *Vacuum Ultraviolet Photoionization and Photodissociation of Molecules and Clusters*, edited by C.Y. Ng, World Scientific ed.London, 1991.

[20] A. Morris and J. M. Dyke
Vacuum **53**, 339 (1999).

[21] P. P. Benard and M. A. A. Clyne
Journal of The Chemical Society and Faraday Transactions 2 **73**, 394 (1977).

[22] http://kinetics.nist.gov/index.php

[23] J. M. Dyke, A. E. Lewis and A. Morris
Journal of Chemical Physics **80**, 1382 (1984).

[24] J. M. Dyke, N. Hooper and A. Morris
Journal of Electron Spectroscopy and Related Phenomena **119**, 49 (2001).

[25] K. Kimura, S. Katsumata, Y. Achiba, T. Yamazaki and S. Iwata *Handbook of HeI photoelectron spectra of fundamental organic molecules*, Japan Scientific Societies Press ed.Tokyo, 1981.

Chapter 5

5 PHOTOELECTRON SPECTROSCOPY OF OH AND OD RADICALS

This Chapter reports studies of photoelectron spectroscopy using Synchrotron Radiation on the OH and OD radicals.

The Chapter is organized as follows. In section 5.1 previous spectroscopy investigations on OH and OD that are considered important for the present work are briefly reviewed. Section 5.2 presents the results of the measured CIS spectra, and resonant photoelectron spectra, together with their interpretations. Section 5.3 summarizes the results obtained.

5.1 Previous investigations on OH and OD radicals with photoelectron spectroscopy

Over the past 30 years, the hydroxyl radical, OH, has been one of the most thoroughly studied simple diatomic hydrides due to its importance in the chemistry of the Earth's atmosphere[1], combustion processes[2,3], and the interstellar medium[4]. During this time, OH has been the focus of several different experimental and theoretical studies. Of particular interest has been an investigation of its electronic structure via experimental studies involving its interaction with ultraviolet (UV) and vacuum ultraviolet (VUV) radiation. The low-lying electronic states of the neutral molecule have been extensively studied by experiment[5-15] and theory[16-18].

The ground state electronic configuration of OH and OD is $1\sigma^2 2\sigma^2 3\sigma^2 1\pi^3$,which gives rise to a $^2\Pi$ state.

Photoionization from the valence 1π molecular orbital produces the $X^3\Sigma^-$, $a^1\Delta$ and $b^1\Sigma^+$ ionic states at adiabatic ionization energies (AIEs) of 13.01, 15.17 and 16.61 eV respectively[8]. The potential energy curves of these ionic states are very similar to that of the ground state of the neutral because of the non-bonding character of the 1π orbital. Removal of one electron from the 3σ shell gives rise to the $A^3\Pi$ and $c^1\Pi$ ionic states at AIEs of 16.48 and 18.30 eV respectively[8].

Photoabsorption measurements in the 1830 - 1150 Å region (6.8 - 10.8 eV) have been carried out by Douglas[5], Viney[6] and Nee *et al.*[7].

Photoelectron spectra of OH and OD have been recorded with HeI radiation by Katsumata *et al.*[19] and more recently by van Lonkhuyzen *et al.*[8]. In the first study[19] the H (D) + NO_2 reaction was used to produce OH (OD), and the first and second PE bands were observed, while bands at higher ionization energies could not be observed because of overlap with bands from secondary reaction products. In the second PE investigation[8], where OH and OD were produced by the F + H_2O and the F + D_2O reactions, four of the five expected OH (OD) bands could be observed.

Little information is available concerning autoionization of OH and OD. The UV absorption spectrum at wavelengths shorter than 1200 Å (10 eV) is poorly resolved and resonant states above the first ionization energy have only been observed by

photoionization mass spectrometry (PIMS)[9,15]. In the work of Dehmer[9], performed with a high-intensity VUV helium continuum radiation source and a near-normal incidence monochromator over the photon energy region 13.0 - 16.5 eV, only one Rydberg series was identified converging to the second ionization limit ($a^1\Delta$). Most bands associated with excitation to Rydberg states were unassigned.

In an attempt to assign these Rydberg bands to particular Rydberg series, Cutler *et al.*[15] repeated this work, on both OH and OD. They performed a higher resolution study at the Aladdin Synchrotron Radiation Source[20] in Wisconsin, over the photon energy range 13.0 - 18.2 eV. Two additional Rydberg series were observed, converging to the fourth and third ionization limits, $b^1\Sigma^+$ and $A^3\Pi$ respectively. Rotational structure associated with the transition $OH^*(a^1\Delta, 3d) \leftarrow OH(X^2\Pi, v''=0)$ was recorded, although no analysis of this structure was presented. Also, for the $OH^*(A^3\Pi, 3d) \leftarrow OH(X^2\Pi, v''=0)$ absorption, components were observed with $v' = 0$, 1 and 2. For higher values of principal quantum number ($n = 4$ - 8), only the $v'=0 \leftarrow v''=0$ components could be identified but positions of the other vibronic transitions (i.e. $v'=1, 2 \leftarrow v''=0$ for each n) were suggested based on results of the earlier PES work.

The Southampton PES group has previously carried out an investigation into the photoelectron spectroscopy of OH and OD radicals[21] using Synchrotron Radiation at the SRS in Daresbury[22]. Rydberg states which are parts of series which converge to the second and third ionization limits, $a^1\Delta$ and $A^3\Pi$ respectively, were observed in the CIS spectra of the first and second PE bands of both OH and OD. These were confidently assigned by comparison with previous work as autoionizations via Rydberg states.

To evaluate the viability of further synchrotron studies on small radicals using the third generation Synchrotron Radiation Source ELETTRA[23], a selection of the measurements previously made at SRS[22] were repeated. The $OH^*(a^1\Delta, nd)$ Rydberg series observed previously was re-investigated, to try to take advantage of the increased flux and improved narrow bandwidth available at ELETTRA[23], with the aim of obtaining assignments of the observed bands.

5.2 Results and discussion

As already discussed, a natural extension of the previous work made by the Southampton PES group was to repeat some of the PES and CIS measurements made at the SRS in Daresbury[22] using the third generation Synchrotron Radiation Source ELETTRA[23]. Moreover evidence for different states that arise from the different coupling of the angular momentum of the Rydberg orbital with the ionic core has been found[21], and this issue has been investigated in more depth using the high resolution radiation available from ELETTRA[23].

As described in the previous instrumental section (see Chapter 4.4.2), OH (OD) radicals were produced by the fast reaction of atomic hydrogen (deuterium) with nitrogen dioxide:

$$H(D) + NO_2 \rightarrow OH(OD) + NO \qquad \text{Eq. 5-1}$$

Hydrogen (deuterium) atoms were produced by passing a flowing mixture of H_2 (D_2) and He through a microwave discharge at 2.45 GHz in a glass inlet tube coated with phosphoric acid[21]. NO_2 was introduced into the $H_2(D_2)$/H(D)/He mixture, about 3 cm above the photon beam, through an inner inlet tube, 3 mm internal diameter, see Figure 4.10 *(c)*. Test experiments were carried out in Southampton in order to find out the optimum pressures and mixing distance above the photon beam which maximise the intensities of OH bands with respect to the bands from the secondary reactions:

$$OH + OH \rightarrow H_2O + O \qquad \text{and} \qquad O + O + M \rightarrow O_2 + M \qquad \text{Eq. 5-2}$$

CIS spectra were then recorded for the $OH^+(X^3\Sigma^+, v^+=0) \leftarrow OH(X^2\Pi, v''=0)$ and $OD^+(X^3\Sigma^+, v^+=0) \leftarrow OD(X^2\Pi, v''=0)$ vibrational components, in the photon energy range 13.1 - 15.1 eV, where structure is expected to be observed.

Figure 5.1 shows the photoelectron spectra acquired in ELETTRA at $h\nu = 21.22$ eV for the $H + NO_2$ reaction with the H_2/He discharge on and off and at a mixing distance above the photon beam of 3 cm.

The spectra obtained are in good agreement with those previously recorded by Katsumata *et al.*[19] and by the Southampton PES group[21].

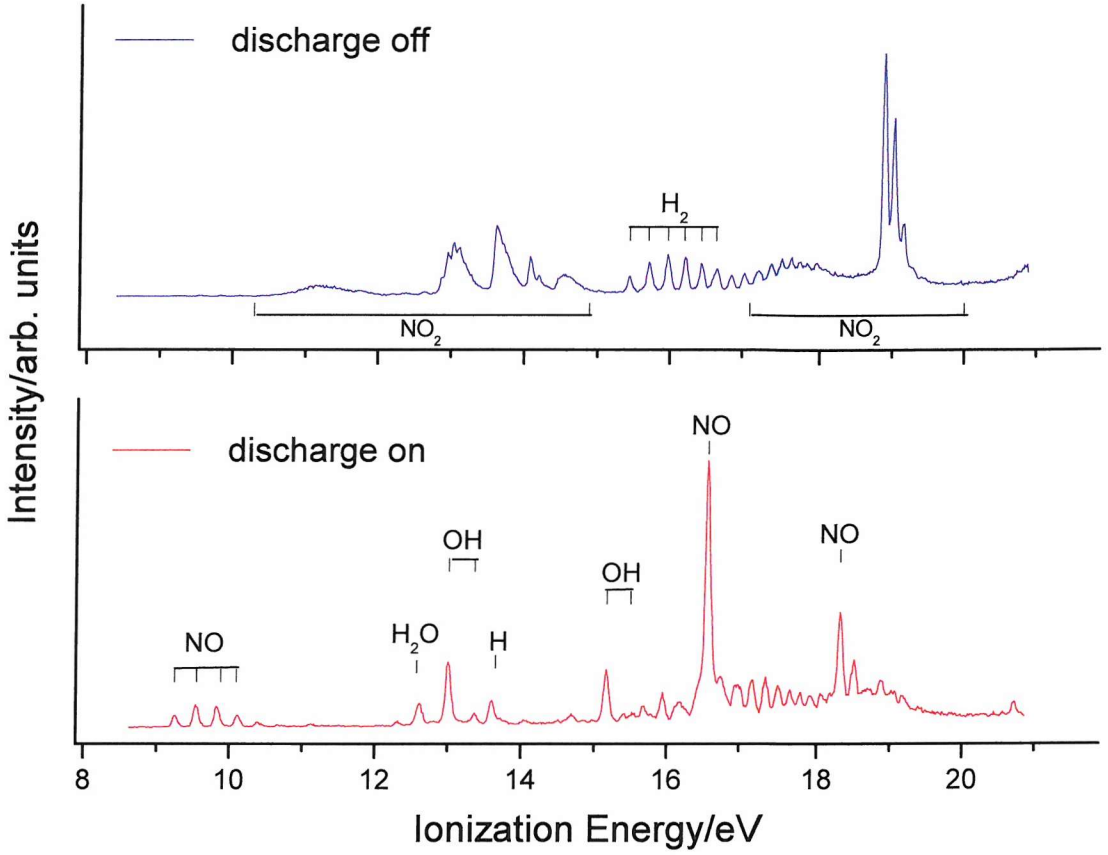

Figure 5.1 *Photoelectron spectrum recorded at $h\nu = 21.22$ eV of the reaction $H + NO_2 \rightarrow OH + NO$ with discharge off (blue trace) and discharge on (red trace).*

As can be seen from Figure 5.1, there is almost a complete reaction of the NO_2 in the discharge-on spectrum. This was the first objective, to use sufficient H atoms to remove all the NO_2 and observe bands of OH.

The first two photoelectron bands of OH at 13.01 eV and 15.17 eV AIEs corresponding to the ionizations $OH^+(X^3\Sigma^-, v^+=0) \leftarrow OH(X^2\Pi, v''=0)$ and $OH^+(a^1\Delta, v^+=0) \leftarrow OH(X^2\Pi, v''=0)$ have been maximized with respect to the H_2O band at 12.62 eV (by optimizing the mixing distance and reagent partial pressures, in Southampton) and the first vibrational component of each OH band can be observed. Bands associated with H_2, H and NO were observed in the discharge on spectrum, along with signals arising from H_2O produced by secondary reactions.

In this study the most intense vibrational component of the first band of OH $OH^+(X^3\Sigma^-, v^+=0) \leftarrow OH(X^2\Pi, v''=0)$ was selected for CIS studies.

Figure 5.2 shows the photoelectron spectrum acquired in ELETTRA at $h\nu$=21.22 eV for the D + NO_2 reaction with the D_2/He discharge on and at a mixing distance above the photon beam of 3 cm.

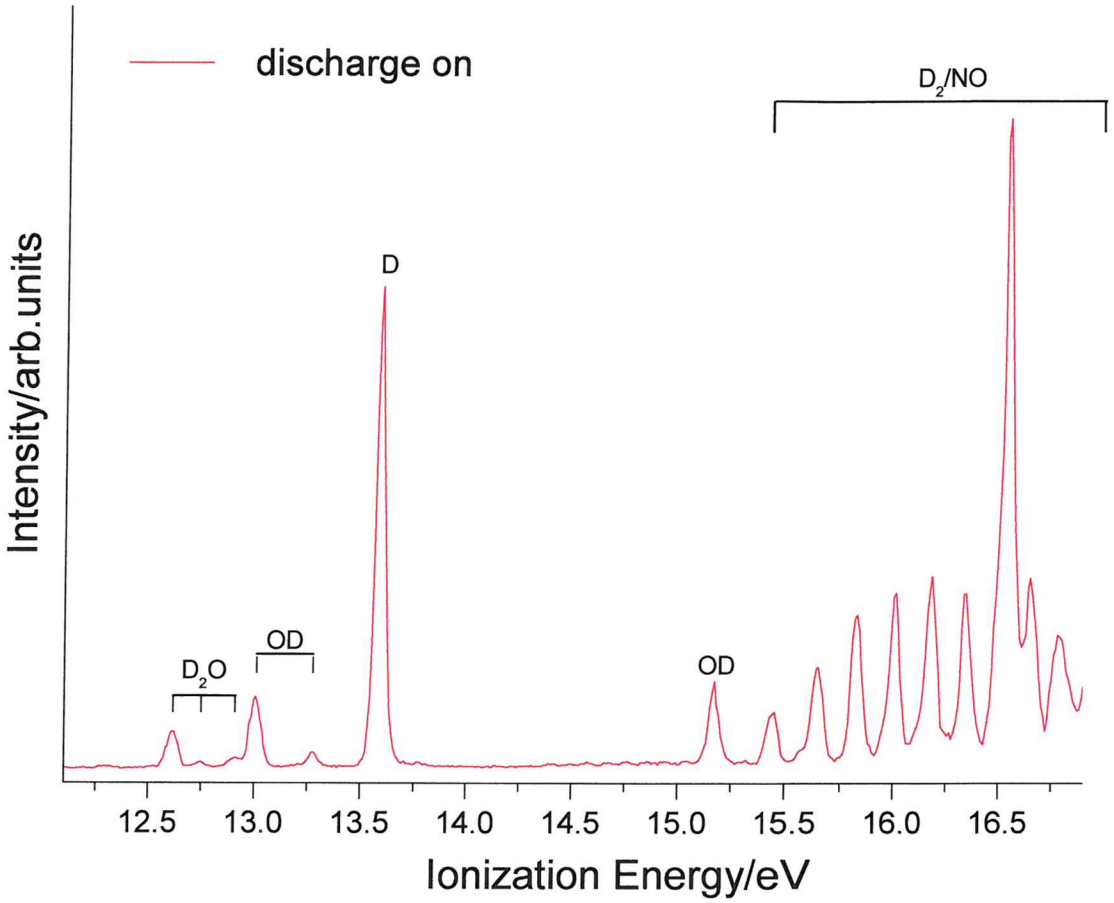

Figure 5.2 *Photoelectron spectrum of the reactions D + NO_2 → OH + NO with discharge on at $h\nu$ = 21.22 eV.*

The photoelectron spectrum of the D_2/He + NO_2 mixture recorded in ELETTRA, shown in Figure 5.2 is very similar to the spectrum shown in Figure 5.1. The main difference is that the vibrational separations in the D_2, D_2O and OD bands are

smaller than in the corresponding bands of H_2, H_2O and OH. The measured vibrational separations for the first photoelectron bands of OH and OD are 366 and 266 meV respectively and they are compatible with the ionic state values known from other spectroscopic investigations[19] (366 and 280 meV).

5.2.1 CIS spectra for the ($X^3\Sigma^-$, v^+=0) ← ($X^2\Pi$, v''=0) ionizations of OH and OD in the photon energy range hν = 13.10 - 15.10 eV

CIS spectra have been recorded for the ($X^3\Sigma^-$, v^+=0) ← ($X^2\Pi$, v''=0) ionizations of OH and OD in the photon energy range 13.10 - 15.10 eV, and the spectrum obtained for $OH^+(X^3\Sigma^-, v^+=0) \leftarrow OH(X^2\Pi, v''=0)$ has been compared with the spectrum of reference (21) previously recorded at the SRS[22]. The CIS technique cannot distinguish between different photoionization processes with the same ionization energy. Potential contaminants from this reaction at this binding energy (13.01 eV) are NO_2, H_2O and NO. CIS spectra of these molecules at the ionization energy used to record spectra of OH and OD (13.01 eV) have been previously recorded[21] by the Southampton PES group and the conclusion is that only NO contributes to peaks in the CIS spectra of OH and OD. A peak due to NO is marked with an asterisk (*) in the following CIS spectra.

In Figures 5.3 - 5.8 the CIS spectra recorded for the ($X^3\Sigma^-$, v^+=0) ← ($X^2\Pi$, v''=0) ionization of both OH and OD in the photon energy range 13.10 - 15.10 eV and at θ = 60° with respect to the major polarization axis of the photon source, are shown.

The spectrum shown in Figure 5.3 is in good agreement with the spectrum from reference (21) recorded at the SRS[22]; however, a much higher resolution is obtained in this present work and rotational structure can be observed in the vibrational components as can be better seen in Figure 5.5 where the photon energy range 13.45 - 14.00 eV has been expanded. In Figures 5.5 and 5.6 rotationally resolved features are shown for autoionization via $OH/OD^*(a^1\Delta, 3d)$ Rydberg states, recorded in the ($X^3\Sigma^-$,v^+=0) ← ($X^2\Pi$,v''=0) CIS spectrum. In Figures 5.7 and 5.8 the results of this investigation are compared with the results obtained in the PIMS studies of references (9) and (15).

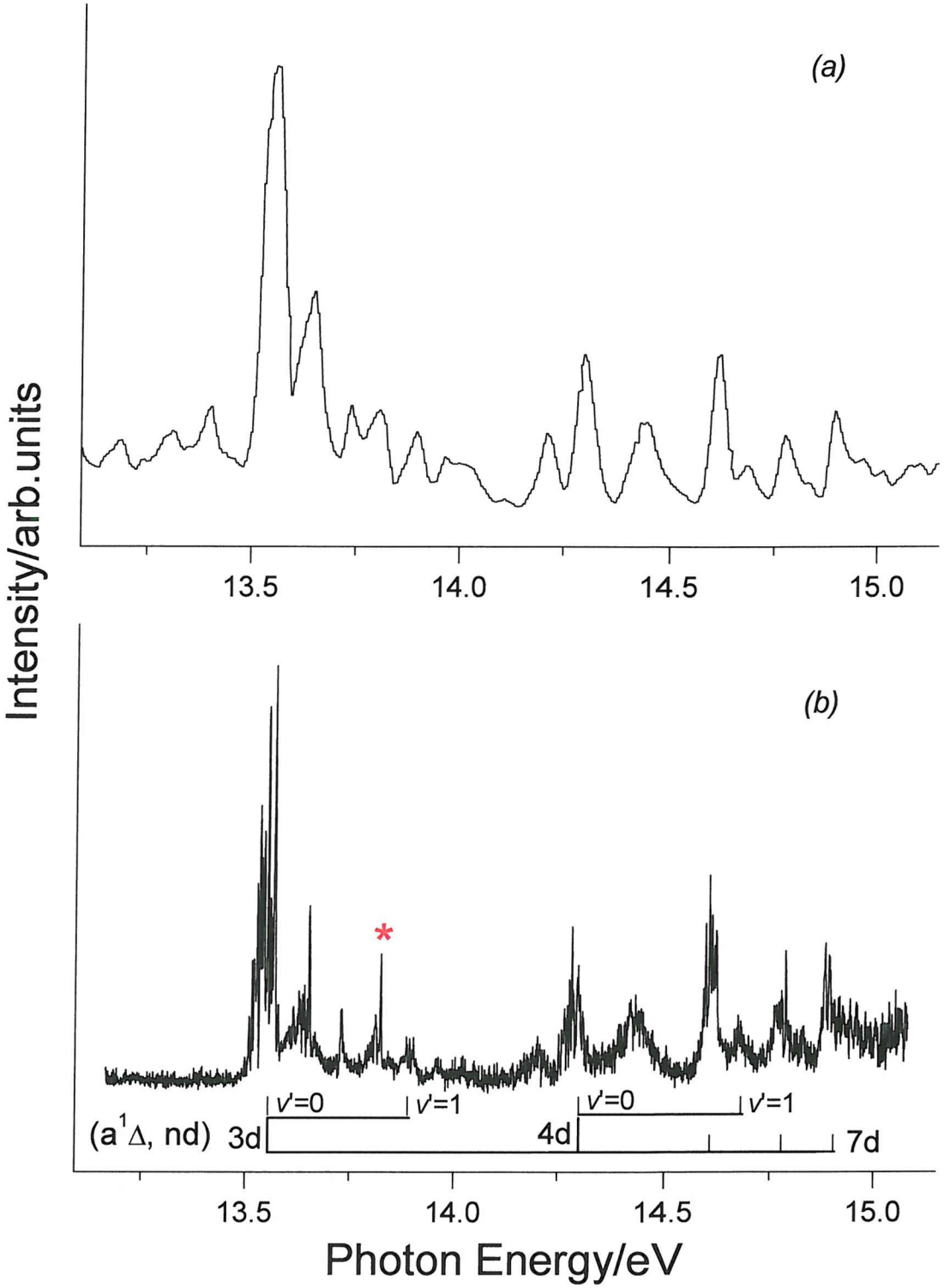

Figure 5.3 *CIS spectrum for the $OH^+(X^3\Sigma^-, v^+=0) \leftarrow OH(X^2\Pi, v''=0)$ ionization in the photon energy range 13.05 - 15.05 eV recorded at $\theta = 60°$ (a) at Daresbury on BL 3.2 and (b) at ELETTRA on BL 4.2. The peak due to NO is marked with an asterisk (*) in the CIS spectrum. Positions of $OH^*(a^1\Delta, nd)$ Rydberg states are indicated.*

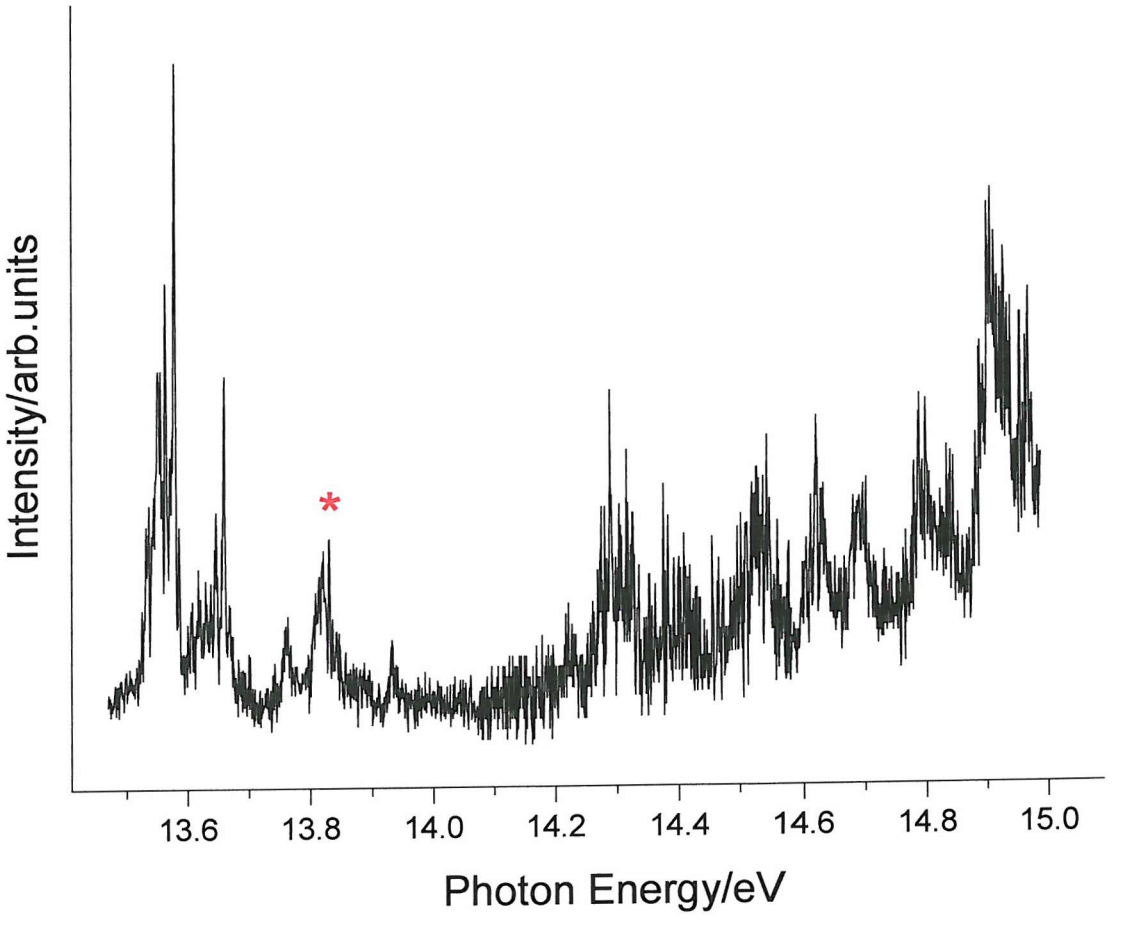

Figure 5.4 *CIS spectrum for the $OD^+(X^3\Sigma^-, v^+=0) \leftarrow OD(X^2\Pi, v''=0)$ ionization in the photon energy range 13.10 - 15.10 eV. The peak due to NO is marked with an asterisk (*) in the CIS spectrum.*

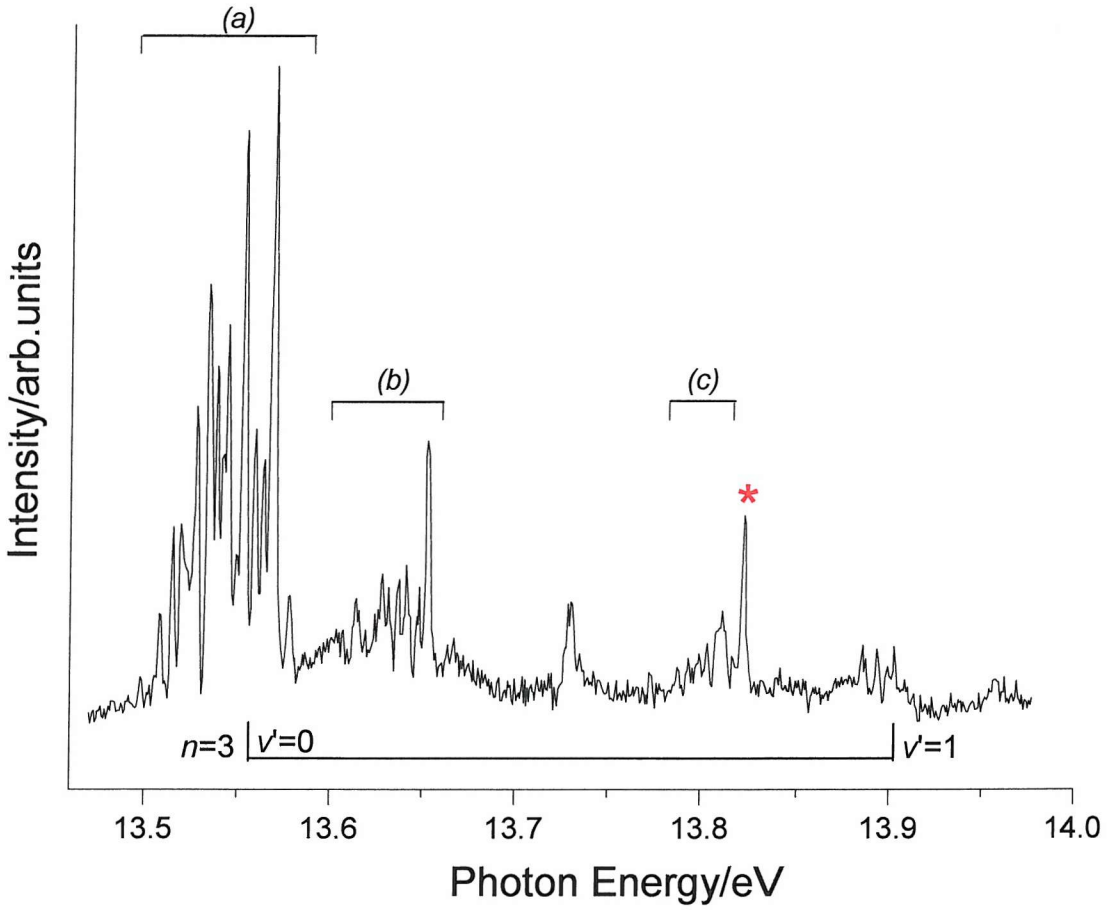

Figure 5.5 *CIS spectrum of the $OH^+(X^3\Sigma, v^+=0) \leftarrow OH(X^2\Pi, v''=0)$ ionization in the photon energy range 13.45 - 14.00 eV. The peak due to NO is marked with an asterisk (*) in the CIS spectrum.*

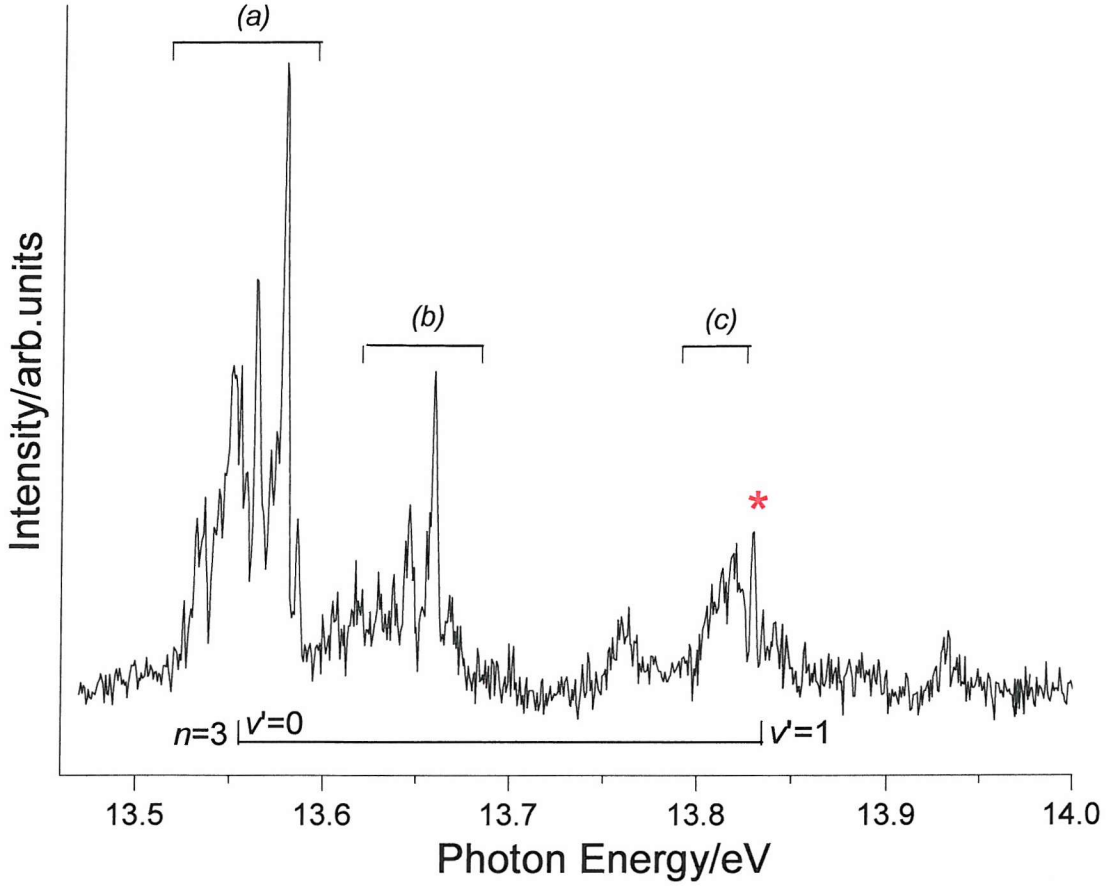

Figure 5.6 *CIS spectrum of the $OD^+(X^3\Sigma, v^+=0) \leftarrow OD(X^2\Pi, v''=0)$ ionization in the photon energy range 13.45 - 14.00 eV. The peak due to NO is marked with an asterisk (*) in the CIS spectrum.*

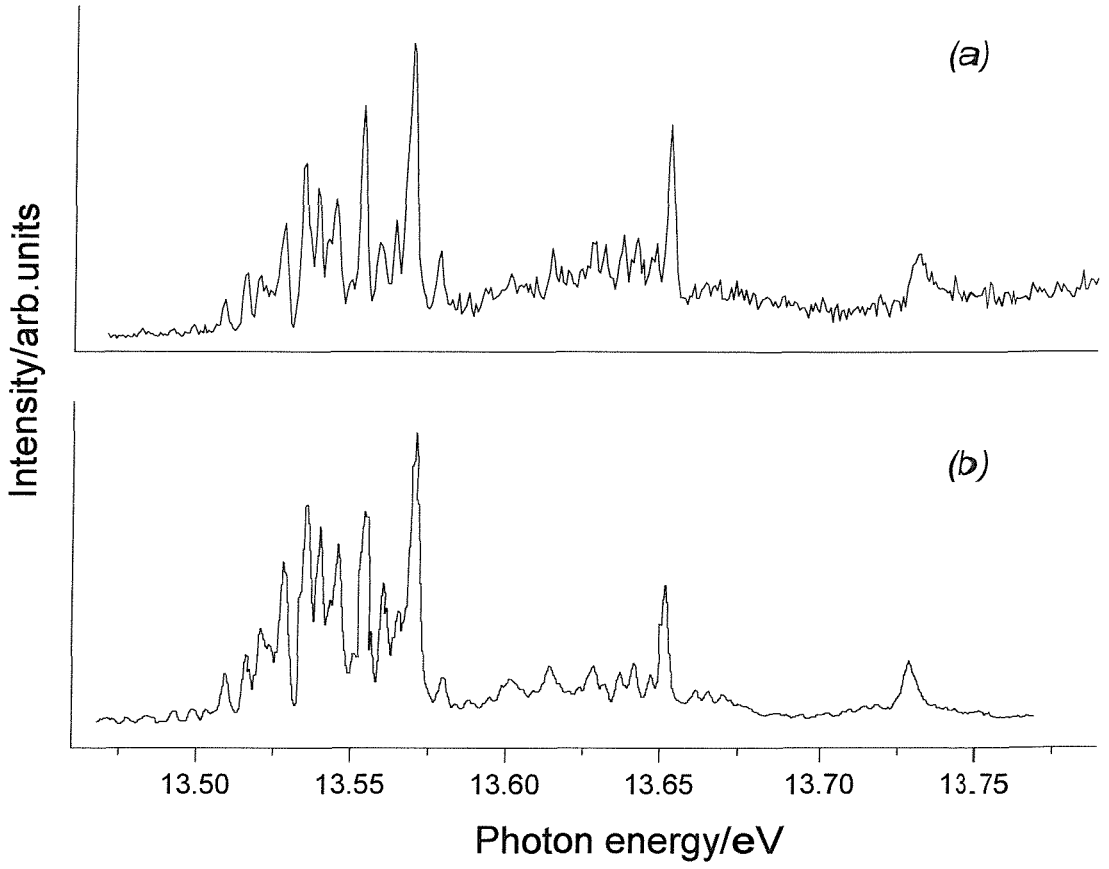

Figure 5.7 *Comparison of:*
(a) a CIS spectrum of the $OH^+(X^3\Sigma, v^+=0) \leftarrow OH(X^2\Pi, v''=0)$ *ionization in the photon energy range 13.45 - 13.80 eV obtained in this work with*
(b) a PIMS spectrum obtained by Dehmer[9].

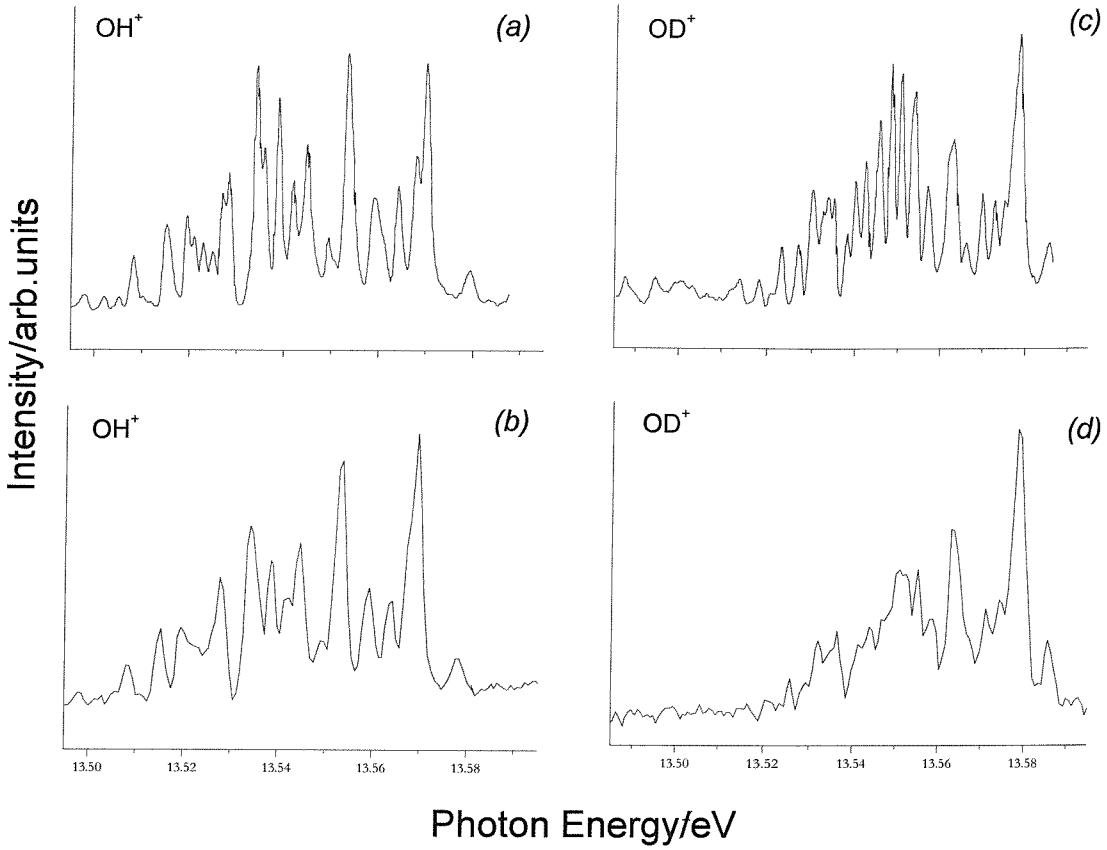

Figure 5.8 *Comparison of:*
(a) a PIMS spectrum of OH obtained in Ref. (15) with
(b) a CIS spectrum of the $OH^+(X^3\Sigma, v^+=0) \leftarrow OH(X^2\Pi, v''=0)$ *ionization in the photon energy range 13.50 - 13.60 eV, this work*
(c) a PIMS spectrum of OD obtained in Ref. (15) with
(d) a CIS spectrum of the $OD^+(X^3\Sigma, v^+=0) \leftarrow OD(X^2\Pi, v''=0)$ *ionization in the photon energy range 13.50 - 13.60 eV, this work.*

Figure 5.7 shows good agreement with the previously recorded PIMS spectrum recorded by Dehmer[9], with features with linewidths of ~ 2meV.

Figure 5.8 shows good agreement of the results of this work for both OH and OD with the previously recorded PIMS spectra recorded by Cutler *et al.*[15], with features with linewidths of ~ 2 meV.

From the spectra in references (9) and (15) and the spectra obtained in the present work, all the rotationally resolved features in this region can be assigned to autoionization via $OH^*(a^1\Delta, 3d)$ Rydberg states.

The rotational structure shown in Figures 5.5 and 5.6 has not yet been assigned. The spin-orbit splitting in the $X^2\Pi$ state (139.1 cm^{-1}, 0.017 eV)[24] means that the $^2\Pi_{1/2}$ state will be 139.1 cm^{-1} above the $^2\Pi_{3/2}$ state with a relative population of 51% at 300 K. From the method used to make OH, ionization will occur from both spin-orbit components with a Boltzmann population of the rotational levels at ≈ 300 K.

In the CIS experiments, the $OH^+(X^3\Sigma^-, v^+=0) \leftarrow OH(X^2\Pi, v''=0)$ ionization is selected and the structure shown in Figure 5.5 must arise from $OH^*(a^1\Delta, 3d, v'=0, J') \leftarrow OH(X^2\Pi_{1/2, 3/2}, v''=0, J'')$ transitions.

The $OH^*(a^1\Delta, 3d)$ Rydberg state is expected to give the $(a^1\Delta, 3d\sigma)$, $(a^1\Delta, 3d\pi)$ and $(a^1\Delta, 3d\delta)$ components in $C_{\infty v}$ symmetry. These give rise to the following states:

$OH^*[a^1\Delta, 3d\sigma]$ $(^2\Delta)$

$OH^*[a^1\Delta, 3d\pi]$ $(^2\Pi)/(^2\Phi)$

$OH^*[a^1\Delta, 3d\delta]$ $(^2\Sigma)/(^2\Gamma)$

According to the selection rules for an electric dipole transition (see Chapters 2.2), only the $^2\Sigma \leftarrow {}^2\Pi$, $^2\Pi \leftarrow {}^2\Pi$ and $^2\Delta \leftarrow {}^2\Pi$ transitions are allowed.

Bearing in mind that the 3d and 4s Rydberg orbitals in OH and OD are oxygen in character and considering the value of the quantum defects for molecular oxygen[25,26] [$n s\sigma = 1.06$, $n d\sigma = 0.18$, $n d\pi = 0.11$, $n d\delta = 0.02$], then using the known second AIE of OH as 15.17 eV, excitation energies can be calculated from the $OH(X^2\Pi)$ state as follows:

the excitation energy (ExEn) of the $[\sigma^2\pi^2\ ^1\Delta, 4s\sigma]$ $(^2\Delta)$ state is 13.595 eV

the ExEn of the $[\sigma^2\pi^2\ ^1\Delta, 3d\delta]$ $(^2\Sigma)$ state is 13.639 eV

the ExEn of the $[\sigma^2\pi^2\ ^1\Delta, 3d\pi]$ $(^2\Pi)$ state is 13.542 eV

the ExEn of the $[\sigma^2\pi^2\ ^1\Delta, 3d\sigma]$ $(^2\Delta)$ state is 13.460 eV

For these reasons the suggested assignment of the 3d bands is $^2\Delta < ^2\Pi < ^2\Sigma$, corresponding to *(a) < (b) < (c)* as shown in Figure 5.5. However, these values should only be used as a guide as to where the actual values are as they were obtained for molecular oxygen and do not apply to OH. However, the transitions to the 3d states are expected to be more intense than the transitions to the 4s Rydberg state. This is due to the fact that the s Rydberg states are more prone to predissociation than the d Rydberg state because of their bigger electron densities close to the core, and the transition moments to *n*s Rydberg states are smaller than those to (*n* - 1)d Rydberg states.

Attempts have been made to simulate this structure using computed one-photon Rotational Line Strengths[27-30] (RLS). In Figure 5.9 the experimental first band envelope at ≈ 13.55 eV (left hand side) is compared with results of rotational line strength calculations for the $^2\Pi \leftarrow ^2\Pi$, $^2\Delta \leftarrow ^2\Pi$ and $^2\Sigma \leftarrow ^2\Pi$ transitions (right hand side). These calculations were performed assuming a rotational temperature T = 300 K, a resolution of 15 cm^{-1} and using *Hund's case a* for the $^2\Pi$ and $^2\Delta$ states, and *Hund's case b* for the $^2\Sigma$ state.

Comparison of the RLS envelopes with the experimental envelope in Figure 5.9 shows that the range covered by the experimental envelope (0.08 eV) is approximately the same as the range covered by the simulations. Although the comparison of the computed envelopes with the experimental one is only moderate, it appears that the experimental envelope at ≈ 13.55eV excitation energy fits best with a $^2\Pi \leftarrow ^2\Pi$ transition. The second band at ≈ 13.66 eV would then fit best as a $^2\Delta \leftarrow ^2\Pi$ transition and the third band at ≈ 13.81 eV would fit best as a $^2\Sigma \leftarrow ^2\Pi$ transition. With this assignment the quantum defects can be calculated as $n\mathrm{d}\sigma = 0.006$, $n\mathrm{d}\pi = 0.085$, $n\mathrm{d}\delta = -0.165$ with a relative excited state order $^2\Pi < ^2\Delta < ^2\Sigma$. (The envelopes of bands (b) and (c) in Figure 5.5 were not sufficiently well resolved to be included in this comparison).

The β parameter was also measured across this region. No detailed structure was discernible, although there was a gradual rise in β from -0.7 to -0.1 (see Figure 5.10), consistent with different assignments of the three bands arising from the $OH^*(a^1\Delta, 3d) \leftarrow OH(X^2\Pi)$ transitions.

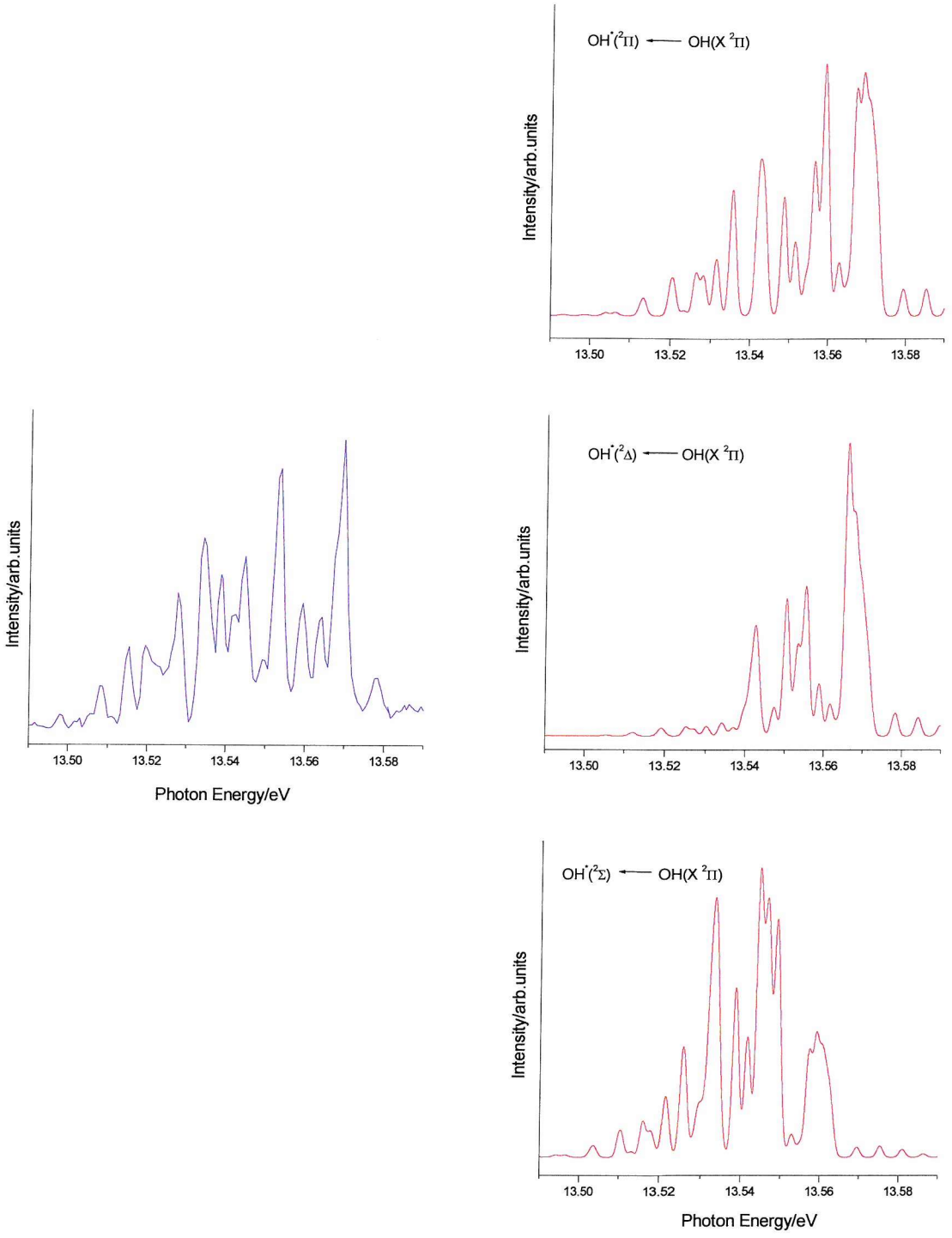

Figure 5.9 *Result of rotational line strength calculations, right hand red trace, compared to the experimental band at ≈ 13.55 eV, left hand blue trace.*

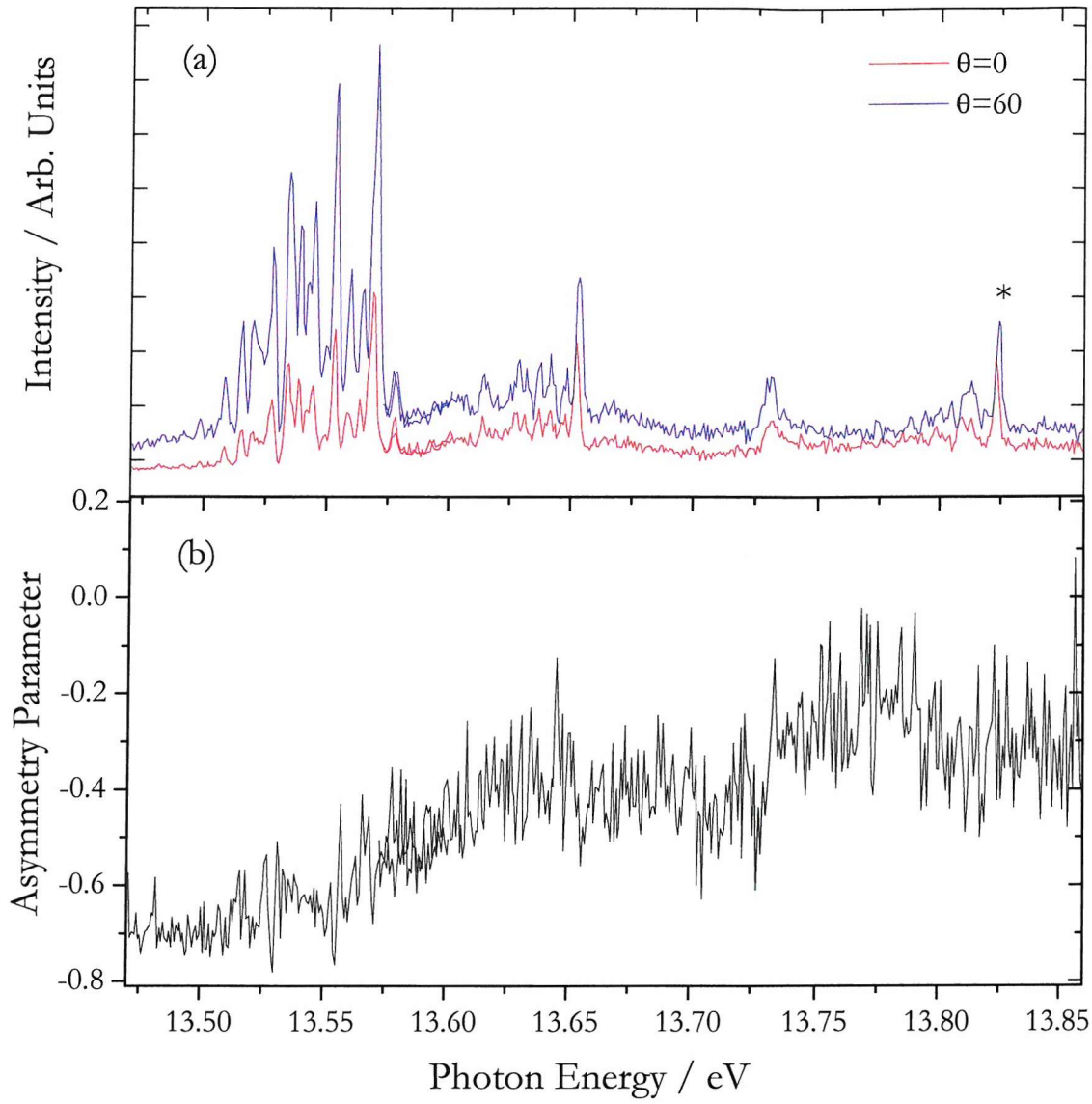

Figure 5.10 *(a) CIS spectrum at $\theta = 0°$ and $60°$ and (b) the asymmetry parameter β of the $OH^+(X^3\Sigma, v^+=0) \leftarrow OH(X^2\Pi, v''=0)$ ionization in the photon energy range 13.48 - 13.85 eV.*

Inspection of published papers[31-36] on NO reveals why the simulated rotational envelopes of the first observed 3d band in the $OH^+(X^3\Sigma^+, v^+=0) \leftarrow OH(X^2\Pi, v''=0)$ CIS spectrum cannot be adequately simulated using one-photon rotational line strengths. The reason is that there is l-mixing between the 3dσ and 4sσ states (both give rise to $^2\Delta$ excited states and interact) and l-uncoupling between close lying 3dσ

and 3dπ components (l-uncoupling causes mixing between the $^2\Delta$ and $^2\Pi$ states). Any further simulation of the rotational envelopes in the observed CIS spectra would have to take these effects into account.

However the spectra obtained in this work were felt to be not sufficiently well resolved to warrant attempting simulations which include these effects (although interaction with the Orsay group of Prof. D. Gauyacq[37] was considered to achieve this).

The [$a^1\Delta$, 3dδ] ($^2\Sigma$) states are unaffected by the 3d - 4s interaction and l-uncoupling (there are no orbitals of 3dδ symmetry in the core) and hence the $OH^*(a^1\Delta,3d\delta)$ ($^2\Sigma$) ← $OH(X^2\Pi)$ band should be well represented by *Hund's case a/b* RLS calculations. Unfortunately, the band at ≈ 13.81 eV is only poorly observed in our spectra and hence a meaningful comparison with the RLS calculations cannot be made because of its low intensity. Nevertheless, with these caveats, it is believed that the assignment of the bands shown in Figure 5.5, and labelled as (a), (b) and (c), is $OH^*(a^1\Delta,3d,)$ ($^2\Pi$) ← $OH(X^2\Pi)$, $OH^*(a^1\Delta,3d,$ ($^2\Delta$) ← $OH(X^2\Pi)$, and $OH^*(a^1\Delta,3d)$ ($^2\Sigma^-$) ← $OH(X^2\Pi)$ respectively.

5.3 Conclusions

The work in this Chapter on OH and OD is presented to demonstrate the feasibility of synchrotron studies on short-lived radicals. It is clear that the increased photon flux and improvement in spectral resolution available at the ELETTRA[23] third generation Synchrotron Radiation Source, makes the study of short-lived molecules possible with PES, CIS and angle-resolved measurements.

References

[1] R. P. Wayne *Chemistry of Atmospheres*, Claredon Press ed.; Oxford Science Publications: Oxford, 1991.

[2] G. J. Mintoff and C. F. H. Tipper *Chemistry of Combustion Reactions*, Butterworths ed.London, 1962.

[3] D. J. Hucknall *Chemistry of Hydrocarbon Combustion Reactions*, Chapman Hall ed.London, 1985.

[4] W. D. Watson
Review of Modern Physics **48**, 513 (1976).

[5] A. E. Douglas
Canadian Journal of Physics **52**, 318 (1974).

[6] J. C. Viney
Journal of Molecular Spectroscopy **83**, 465 (1980).

[7] J. B. Nee and L. C. Lee
Journal of Chemical Physics **81**, 31 (1984).

[8] H. van Lonkhuyzen and C. A. De Lange
Molecular Physics **51**, 551 (1984).

[9] P. M. Dehmer
Chemical Physics Letters **110**, 79 (1984).

[10] R. J. Cody, C. Maralejo and J. E. Allen
Journal of Chemical Physics **95**, 2491 (1991).

[11] M. Collard, P. Kerwin and A. Hodgson
Chemical Physics Letters **179**, 422 (1991).

[12] E. De Beer, M. P. Koopmans, C. A. De Lange, Y. Wang and W. A. Chupka
Journal of Chemical Physics **94**, 7634 (1991).

[13] E. De Beer, C. A. De Lange, J. A. Stephens, Y. Wang and V. McKoy
Journal of Chemical Physics **95**, 714 (1991).

[14] C. A. De Lange *High Resolution Laser Photoionization and Photoelectron Studies*, edited by I. Powis, T. Baer and C.Y. Ng, Wiley ed.Chichester, 1995.

[15] J. N. Cutler, Z. X. He and J. A. R. Samson
Journal of Physics B **28**, 4577 (1995).

[16] E. F. van Dishoeck, S. R. Langhoff and A. Dalgarno
Journal of Chemical Physics **78**, 4552 (1983).

[17] E. F. van Dishoeck and A. Dalgarno
Journal of Chemical Physics **79**, 873 (1983).

[18] A. V. Nemukhin and B. L. Grigorenko
Chemical Physics Letters **276**, 171 (1997).

[19] S. Katsumata and D. R. Lloyd
Chemical Physics Letters **45**, 519 (1977).

[20] http://www.src.wisc.edu/facilities/default.html.

[21] J. D. Barr, A. DeFanis, J. M. Dyke, S. D. Gamblin, N. Hooper, A. Morris, S. Stranges, J. B. West and T. G. Wright
Journal of Chemical Physics **110**, 345 (1999).

[22] http://www.dl.ac.uk/.

[23] http://www.elettra.trieste.it

[24] H. Herzberg *Molecular Spectra and Molecular Structure*, D. van Nostrand Company Inc. ed.New York, 1966; Vol. IV.

[25] E. Lindholm
Arkiv för Fysik **9**, 117 (1968).

[26] C. Y. R. Wu
Journal of Quantitative Spectroscopy Radiative Transfer **37**, 1 (1987).

[27] J. Baker *Ph.D Thesis*, University of Southampton ed., 1991.

[28] D. L. Andrews and W. A. Ghoul
Journal of Chemical Physics **75**, 530 (1981).

[29] M. N. R. Ashfold
Molecular Physics **58**, 1 (1986).

[30] C. Mainos, M. C. Castex and H. Nkwawo
Journal of Chemical Physics **93**, 5370 (1990).

[31] C. Jungen
Journal of Chemical Physics **53**, 4168 (1970).

[32] E. Miescher
Canadian Journal of Physics **54**, 2074 (1976).

[33] S. Fredin, D. Gauyacq, M. Horani, C. Jungen, G. Lefevre and F. Masnou-Seeuws
Molecular Physics **60**, 825 (1987).

[34] S. T. Pratt, C. Jungen and E. Miescher
Journal of Chemical Physics **90**, 5971 (1989).

[35] D. Gauyacq, A. L. Roche, M. Seaver, S. D. Colson and W. A. Chupka
Molecular Physics **71**, 1311 (1990).

[36] A. Vient, N. Shafizadeh, J. H. Fillion, D. Gauyacq, M. Horani and J. L. Lemaire
Journal of Physical Chemistry **99**, 1666 (1995).

[37] http://www.chem.uva.nl/imc/reactive_intermediates.html

Chapter 6

6 PHOTOELECTRON SPECTROSCOPY OF N ATOMS

This Chapter reports studies on N atoms with ultraviolet photoelectron spectroscopy using Synchrotron Radiation.

The Chapter is organized as follows. In section 6.1 previous spectroscopic investigations on N atoms that are considered important for the present work are briefly reviewed. Section 6.2 presents experimental constant ionic state (CIS) spectra, and photoelectron spectra of N atoms, together with their interpretations. Section 6.3 summarizes the results obtained.

6.1 Previous investigations on N atoms with photoelectron spectroscopy

Photoionization of atomic nitrogen is an important process in the physics and chemistry of the ionosphere[1]. There has been considerable theoretical work carried out on the photoionization cross section of N atoms from threshold at 14.54 eV to energies greater than 40 eV[1-5]. An accurate calculation of the photoionization cross section is difficult due to the open-shell electronic structure and consequent high degree of electron correlation in this atom. Henry[2] computed the photoionization cross section for N atoms over the energy range 14.6 - 20.6 eV using the continuum Hartree-Fock approximation. Later Henry[3] extended these calculations to higher energies (19 - 130 eV). Le Dourneuf *et al.*[4] and Bell *et al.*[5], in their work with R-matrix calculations, calculated the photoionization cross section of ground state of atomic nitrogen from threshold up to 95 eV. Experimentally, the total photoionization cross section of atomic nitrogen was measured in photoabsorption by Ehler *et al.*[6] and by Comes *et al.*[7]. The first measurements of the photoionization cross section were reported by Ehler *et al.*[6] in the region 17 - 31 eV; later Comes *et al.*[7] carried out measurements in the range 14 - 31 eV. Recently, Samson *et al.*[8] have made measurements of the absolute photoionization cross section for single and double ionization of atomic nitrogen in the range from 45 eV to 280 eV and from 14 eV to 24 eV performing ion mass spectrometry at the Synchrotron Radiation Center at the University of Wisconsin[9]. Carroll *et al.*[10] recorded the absorption spectrum of atomic nitrogen and observed for the first time Rydberg series which have been attributed to excitation to $[2s2p^3\ (^5S)\ np]\ ^4P$ autoionizing states. The shape of the line of an autoionizing resonance is a sharp feature and it can be observed as a decrease, an increase or an asymmetric profile in the cross section. The reason for this is the interference between the amplitudes of the direct and indirect processes resulting in a characteristic Fano profile[11].

Near the ionization threshold the asymmetry parameter β may vary with electron kinetic energy, but it is normally constant within a particular photoelectron band since it is determined mainly by the character of the ionised orbital. The asymmetry

parameter may vary sharply as resonant states are accessed due to the enhancement of electron interactions[12].

The line-shape parameters Γ, q and ρ^2 characterize the autoionizing resonances revealing information on the dynamics of the photoionization process and they are expected to have certain characteristics[13]. The relative photoionization cross section for atomic nitrogen from 14 eV to 21 eV and, for the first time, the line-shape parameters and oscillator strengths for the $N^*[2s2p^3\ (^5S), 3p]\ (^4P) \leftarrow N(^4S)$ and $N^*[2s2p^3\ (^5S), 4p]\ (^4P) \leftarrow N(^4S)$ resonances were measured by Dehmer *et al.*[14] using a photoionization mass spectrometer coupled with the helium Hopfield continuum as incident radiation.

The Dehmer work has been extended by Schaphorst *et al.*[15], who performed electron spectroscopy at the Synchrotron Radiation Center at the University of Wisconsin[9], to the $N^*[2s2p^3\ (^5S), np]\ (^4P) \leftarrow N(^4S)$ resonances with $n = 5$ and they reported for the first time the angular distribution of photoelectrons for the $n = 3$ and $n = 4$ resonances.

6.2 Results and discussion

The purpose of the work presented in this Chapter was to extend the data analysis of Schaphorst *et al.*[15], in particular to evaluate the line-shape parameters and oscillator strengths for the $N^*[2s2p^3\ (^5S), np]\ (^4P) \leftarrow N(^4S)$ resonances for $n \geq 5$, using the ELETTRA Synchrotron Radiation Source on the BL 4.2 Circular Polarized Beamline[16] as described in Chapter 3.4.1.

The constant ionic state (CIS) spectra obtained were of higher resolution than previous measurements[15] and this allowed the data analysis to be extend to higher resonances.

Nitrogen atoms were produced by passing a flowing mixture of molecular nitrogen mixed with helium as a carrier, through a microwave discharge (2.45 GHz) in a glass

inlet tube, coated with phosphoric acid[17], attached to the ionization chamber of the spectrometer, as described in Chapter 4.4.1.

The photon energy was calibrated against the energy values of the N autoionizing resonances obtained from the study of Schaphorst *et al.*[15].

The intensities of the bands in the experimental PE and CIS spectra were normalized by the photon flux and then by the transmission correction of the spectrometer. The photon flux was estimated as a function of photon energy from the current measured on an aluminium photodiode placed on the opposite side of the spectrometer ionization chamber from the photon source. The transmission function of the spectrometer, for electrons of different initial electron kinetic energy, was determined by measuring the intensity of the helium $(1s)^{-1}$ photoelectron band at different photon energies. The intensity of the helium $(1s)^{-1}$ band was measured in the VUV photon energy range used and then it was normalized using the absolute photoionization cross section of helium in this range[18]; finally the normalized intensity was plotted as function of the kinetic energy. This curve was used to correct the experimental PE and CIS spectra for the transmission of the spectrometer.

The degree of linear polarization ($P = 1$) of the radiation was well established[19]. The asymmetry parameter (β) was measured for nitrogen atoms at selected photon energies and over a photon energy range, by recording CIS spectra at two different θ angles (0° and 54° 44') at each photon energy (at 54° 44' the measured intensity is proportional to the total photoionization cross section, independent of β).

The β parameter was then calculated from the expression (see Chapter 2.2.6):

$$\beta = (R - 1) \qquad \text{Eq. 6-1}$$

where $R = I_0 / I_{54°44'}$ is the ratio of the experimental intensities at these two angles, after applying the above corrections.

For the measurements of angular distribution it is important that the efficiency of the analyser does not change when the spectrometer is rotated. The change of the efficiency of the analyser on rotation arises from small misalignments between the axis of rotation and the direction of the photon beam. In order to quantify this contribution a correction factor is evaluated by measuring the intensity of bands at

$\theta = 0°$ and at $\theta = 54°\ 44'$, usually at 21.22 eV photon energy, from a sample (usually Ar) where the asymmetry parameter is well established. From the comparisons between the calculated asymmetry parameter and the known asymmetry parameter, the correction factor was determined.

Test experiments were carried out in Southampton in order to determine the optimum nitrogen and helium pressures to be used in the experiments at ELETTRA, which maximise the intensities of the atomic nitrogen bands. Figure 6.1 shows the photoelectron spectrum recorded at $h\nu = 21.22$ eV with the following partial pressures measured on an ionization gauge positioned on the wall of the ionization chamber with respect to the background pressure: $\Delta p(N_2) = 2.52\times10^{-7}$ mbar and $\Delta p(He) = 1.55\times10^{-7}$ mbar.

The ground state configuration of N is $1s^2 2s^2 2p^3$; three ionic states should arise from ionization from the 2p level corresponding to the ionization: $N^+(^3P) \leftarrow N(^4S)$, $N^+(^1D) \leftarrow N(^4S)$ and $N^+(^1S) \leftarrow N(^4S)$. The first ionization is clearly observed in Figure 6.1 at 14.54 eV[17] ionization energy. The second and third ionizations, expected at 16.44 eV and 18.59 eV ionization energies respectively, can only be observed if Russell-Saunders selection rules are broken[17], as the $N^+(^1D) \leftarrow N(^4S)$ and the $N^+(^1S) \leftarrow N(^4S)$ ionizations are both spin forbidden (see Chapter 2.2.5).

The small band labelled (*) in Figure 6.1 at 16.45 eV is believed to result from the ionization $N_2^+(A^2\Pi_u, v^+=0) \leftarrow N_2(X^1\Sigma_g^+, v''=1)$[15,20].

For the $(2s)^{-1}$ ionization of $N(^4S)$, bands are expected at 20.39 eV $[N^+(^5S) \leftarrow N(^4S)]$, 25.98 eV $[N^+(^3D) \leftarrow N(^4S)]$, 28.08 eV $[N^+(^3P) \leftarrow N(^4S)]$, and 33.77 eV $[N^+(^3S) \leftarrow N(^4S)]$ respectively[21].

In Figure 6.2 PE spectra recorded at $h\nu = 29.99$ eV with and without discharge are shown.

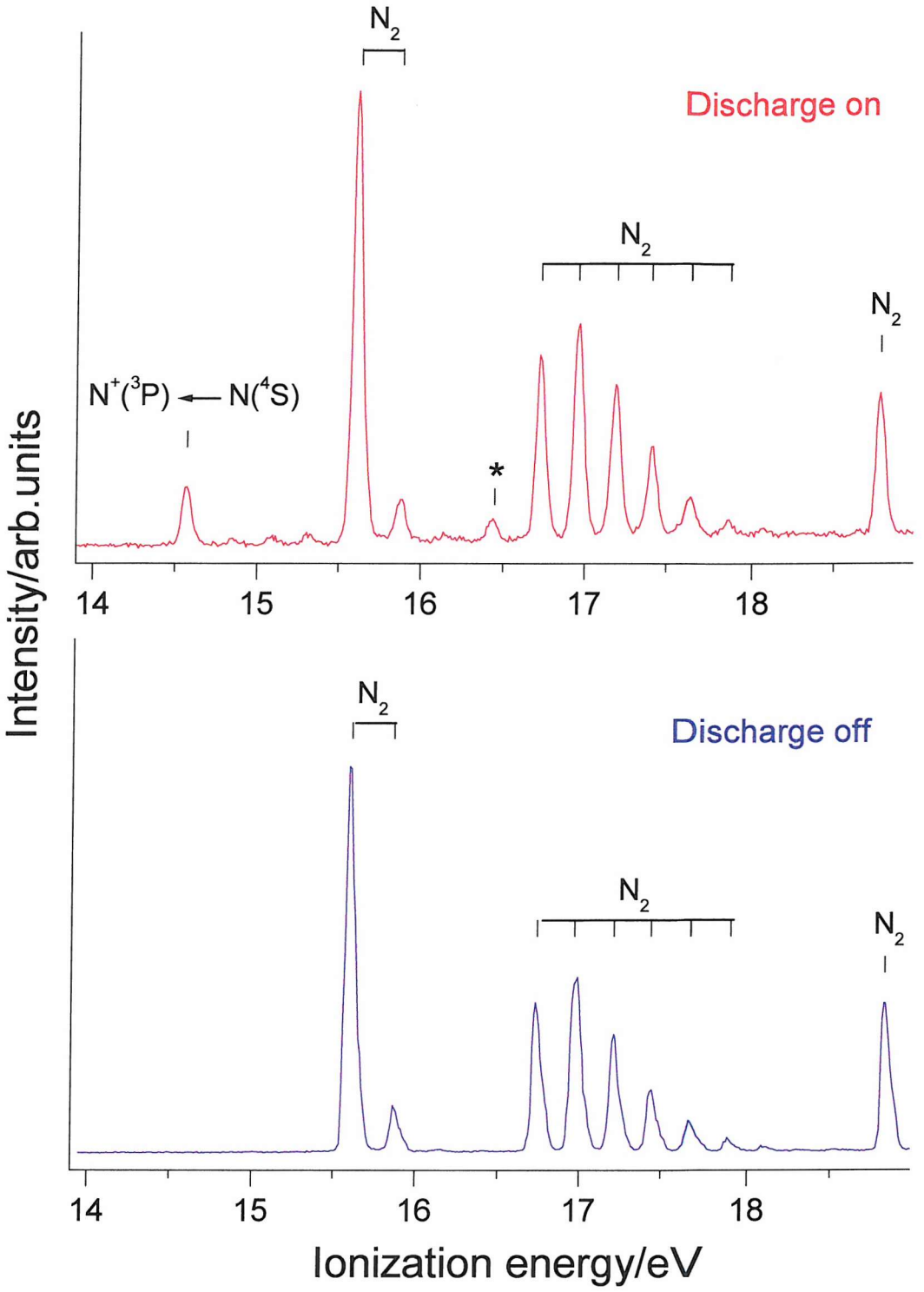

Figure 6.1 *PE spectrum recorded at photon energy $h\nu = 21.22$ eV with the microwave discharge on (upper panel) and off (lower panel) of a He/N_2 mixture.*
The peak labelled with (*) at 16.44 eV is believed to result from the ionization $N_2^+(A^2\Pi_u, v^+=0) \leftarrow N_2(X^1\Sigma_g^+, v''=1)$.

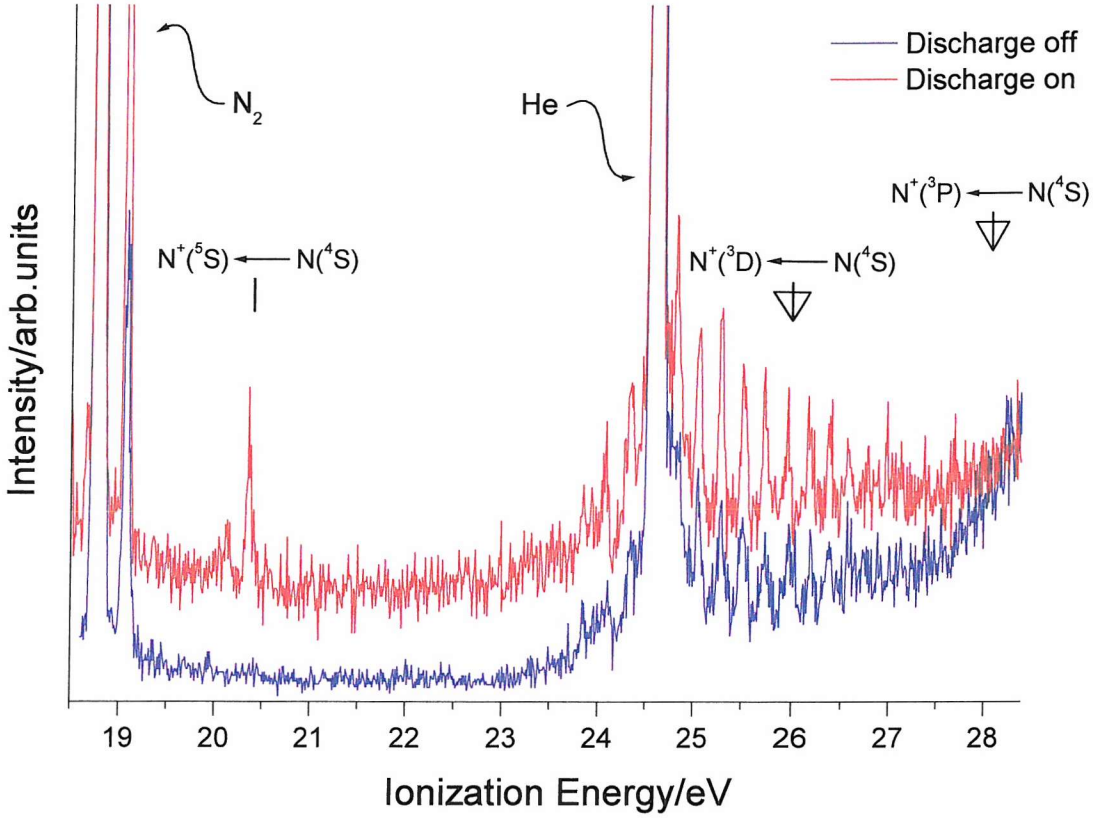

Figure 6.2 *PE spectrum recorded at photon energy $h\nu = 29.99\ eV$ with the microwave discharge on (red line) and off (blue line) of a He/N_2 mixture.*
The expected positions of the $N^+(^5S) \leftarrow N(^4S)$, $N^+(^3D) \leftarrow N(^4S)$ and $N^+(^3P) \leftarrow (^4S)$ ionizations are indicated as well as N_2 and He features.

In Figure 6.2 the band at 20.39 eV corresponding with the ionization $N^+(^5S) \leftarrow N(^4S)$, is clearly observed, while the bands arising from the ionizations $N^+(^3D) \leftarrow N(^4S)$ and $N^+(^3P) \leftarrow N(^4S)$ are completely overlapped by the molecular features. Moreover the $N^+(^3D)$ and $N^+(^3P)$ states are expected to be less intense than the $N^+(^5S)$ state because they are not one-electron process; one electron is removed from 2s subshell and the electrons in the 2p subshell are reorganized.

These molecular features arise from the $N_2^+(C^2\Sigma_u^+) \leftarrow N_2(X^1\Sigma_g^+)$ ionization and are in good agreement with the study of Asbrink *et al.*[22], where the photoelectron spectrum of N_2 was recorded between 23.50 and 28.00 eV ionization energy using a HeII lamp. The vertical ionization energy (VIE) for this ionization is measured in the spectrum in Figure 6.2 at 25.29 eV, while the adiabatic energy is not observed due to low intensity at the band onset. Also the vibrational spacings of the band at 25.29 eV are in agreement with those of Asbrink *et al.*[22].

Due to an intrinsic limitation of the normal incidence monochromator used, the photon flux at energies above the 30.00 eV is not sufficient to record PE spectra. For this reason it was not possible to check for the presence of the atomic nitrogen band at 33.77 eV.

6.2.1 CIS of $N^+(^3P) \leftarrow N(^4S)$, $h\nu = 19.4 - 20.5$ eV

Constant ionic state spectra have been recorded for the first atomic nitrogen band, $N^+(^3P) \leftarrow N(^4S)$, at the ionization energy of 14.54 eV with a 1 meV/channel stepwidth. All spectra were recorded at two angles, $\theta = 0°$ and $\theta = 54° 44'$, with respect to the polarization axis of the photon source.

The relative integrated cross section and the β parameter as a function of photon energy are shown in Figures 6.3 and 6.4. The asymmetry parameter has been evaluated as a function of photon energy applying Eq. 6.1. The β parameter across the 5p and 6p resonances varies sharply between +2 and -0.3. Similar behaviour was reported by Schaphorst *et al.*[15] for the 3p and 4p resonances. The variation of the β parameter across the autoionizing resonances for $n \geq 7$ shows smoother behaviour.

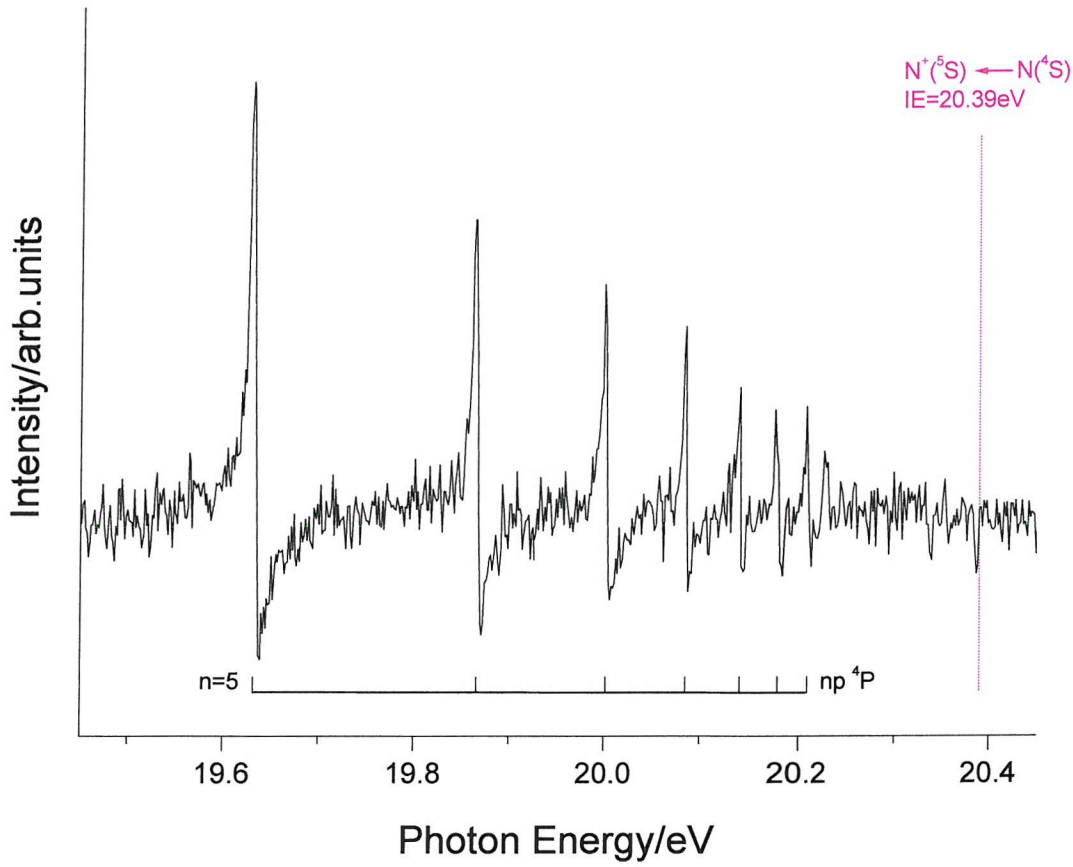

Figure 6.3 *Relative integrated cross section of atomic nitrogen across the* $N^+(^3P) \leftarrow N^* \leftarrow N(^4S)$ *autoionizing resonances for* $n \geq 5$*, over the photon energy range 19.4 - 20.5 eV.*
The spectrum was recorded at $\theta = 54° 44'$ *and 1 meV/channel stepwidth.*

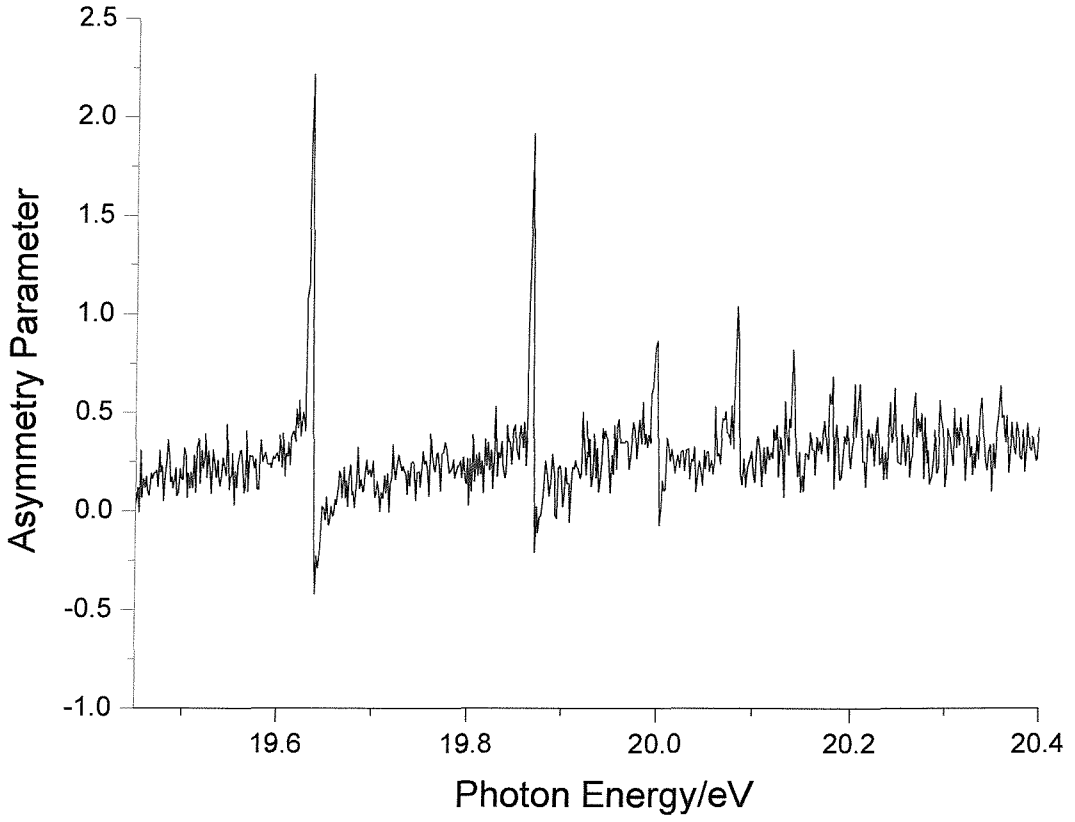

Figure 6.4 *Asymmetry parameter for atomic nitrogen across the $N^*[2s2p^3\,(^5S),\,np]\,(^4P) \leftarrow N(^4S)$ autoionizing resonances for $n \geq 5$, over the photon energy range 19.4 – 20.4 eV.*

The lines shown in Figure 6.3 have a characteristic asymmetric profile due to the interference between the amplitudes of the direct and indirect processes resulting in a characteristic Fano profile[11,23] where the cross section can be expressed as (see Chapter 2.2.3):

$$\sigma(E) = \sigma_a \frac{(q+\varepsilon)^2}{1+\varepsilon^2} + \sigma_b \qquad \text{Eq. 6-2}$$

In this equation σ_a and σ_b represent two portions of the cross section which correspond respectively to transitions to states of the continuum that do and do not interact with the discrete autoionizing state. The reduced energy ε is defined as:

$$\varepsilon = \frac{E - E_r}{\frac{1}{2}\Gamma} \qquad \text{Eq. 6-3}$$

where E_r is the resonance energy and Γ is the natural width of the autoionizing state which represents the bound-continuum mixing of the resonance state[11].

The q parameter characterises the line profile: neglecting the background cross section, the resonance has a maximum at $\varepsilon_{max} = 1/q$ and is zero at $\varepsilon_0 = -q$. The sign of q thus determines whether the maximum occurs before or after the minimum. The magnitude of q indicates qualitatively the relative probabilities of the transition to the Rydberg state and direct ionization[11].

Another parameterization of Eq. 6.2 that is frequently used defines a correlation index ρ^2 and a cross section for photon energies outside of the resonance region σ_c as:

$$\rho^2 = \frac{\sigma_a}{\sigma_a + \sigma_b} \qquad \text{Eq. 6-4}$$

In this case Eq. 7.2 can then be rewritten as:

$$\sigma(E) = \sigma_c \left[\frac{(q+\varepsilon)^2}{1+\varepsilon^2} \rho^2 + (1-\rho^2) \right] \qquad \text{Eq. 6-5}$$

A direct numerical fit of the observed spectrum to the Fano formula of Eq. 6.5 may become unreliable for an atomic transition involving a narrow resonance[24]. The fitting function used in this work is the convolution of the Fano profile in Eq. 6.5 and the instrumental function $F(E,\Omega)$ where Ω is the energy resolution measured by the full width at half maximum (FWHM):

$$\sigma(E,\Omega) = \int_{-\infty}^{\infty} \sigma(E - E') \cdot F(E', \Omega) dE' \qquad \text{Eq. 6-6}$$

It is often a good approximation to assume a Gaussian distribution as the instrumental function; alternatively a weighted combination of a Gaussian and Lorentzian distributions can be used[24]. In order to evaluate the Fano profile parameters of the autoionizing resonances for $n \geq 5$, several fits have been performed

using either a Gaussian distribution or a weighted combination of a Gaussian and Lorentzian distribution as the instrumental function and varying the CIS energy resolution Ω from 1 to 7 meV.

The fits with the best χ^2 values have been obtained using a pure Gaussian distribution as the instrumental function and an energy resolution of 3 meV. Figure 6.5 shows the Fano profile fits compared with the experimental data for the $n = 6, 7, 8, 9$ and 10 resonances.

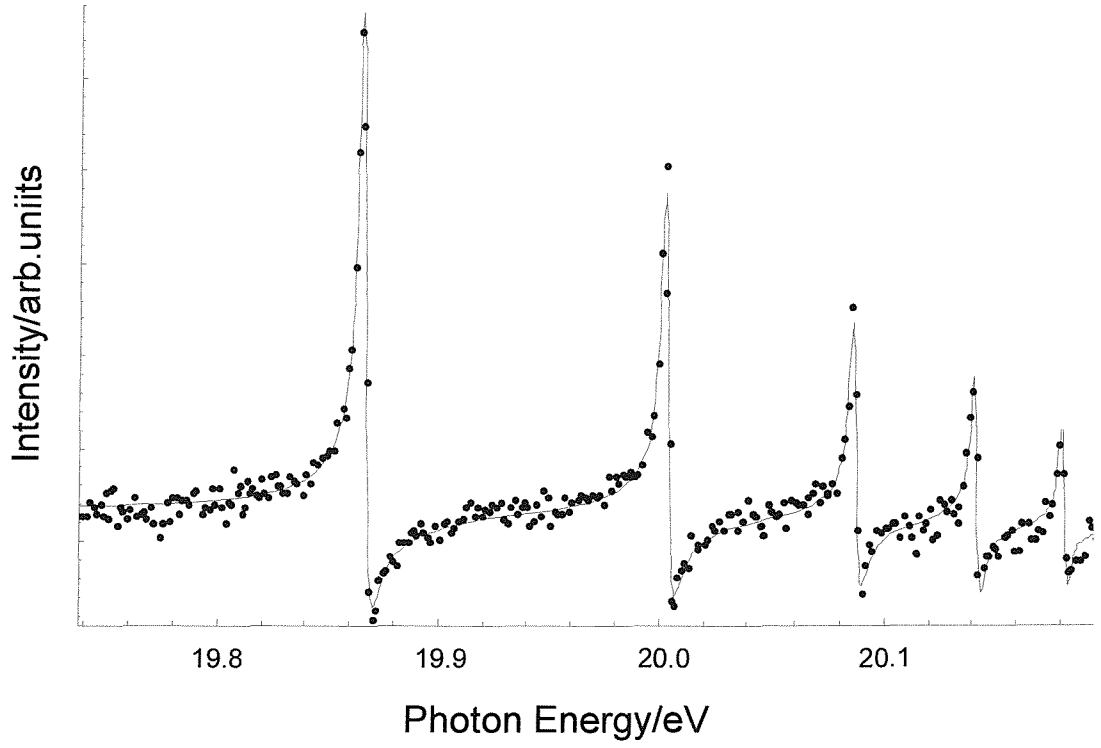

Figure 6.5 *The solid line is the Fano profile fit to the data (dots) for the n = 6, 7, 8, 9 and 10 autoionizing resonances.*

The discrete oscillator strengths for the resonances have been calculated from the expression[13]:

$$f = \frac{mc^2}{2e^2}\sigma_c \rho^2 \Gamma q^2 \qquad \text{Eq. 6-7}$$

where c is the speed of the light, e and m are the charge and the mass of the electron, respectively. To express the oscillator strengths on an absolute scale and for comparison with the value for $n = 5$ obtained by Schaphorst *et al.*[15], the cross section σ_c has been set to 11 Mb in agreement with the results of the multiconfiguration Hartree-Fock calculation at a photon energy of 18.6 eV obtained in reference (15).

Values of Γ, q, ρ^2 and f are reported in Table 6-1 for the autoionizing resonances from $n = 5$ to $n = 10$. The present results for the 5p resonance agree with those of Schaphorst *et al.*[15] within experimental error. The ρ^2 value is nearly equal for the autoionizing resonances, as expected for the members of a Rydberg series with an approximately constant quantum defect δ[13,23]. The same behaviour is expected for the q value. Experimentally the q value becomes more negative from $n = 3$ to $n = 7$, taking in account the values of -1.60 and -1.70 obtained by Shaphorst *et al.*[15] for the 3p and 4p resonances respectively. For autoionizing resonances for $n > 7$ the q value becomes less negative although it can be considered constant within experimental error.

If the mean separation of the energy levels N_n adjacent to the energy level E_n is considered[23]:

$$N_n^2 = \frac{1}{2}(E_{n+1} - E_{n-1}) = R\frac{2(n-\delta_n)}{\left((n-\delta_n)^2 - 1\right)^2} \qquad \text{Eq. 6-8}$$

the dependence of N_n on the quantum number n is:

$$N_n \propto \frac{1}{n^3} \qquad \text{Eq. 6-9}$$

The same procedure yields a relationship for the widths of successive lines of a Rydberg series, namely:

$$\Gamma_n = R\frac{2(n-\delta_n)}{\left((n-\delta_n)^2 - 1\right)^2}\overline{\Gamma} \qquad \text{Eq. 6-10}$$

where $\overline{\Gamma} = \Gamma(n-\delta_n)^3$ represents the ratio of each line width to the average separation of the adjacent lines; this ratio is constant for the whole series and it is called "reduced linewidth"[23]. However for $n > 250$ the presence of weak electric

fields inevitably present in the ionization region are sufficient to causes l as well as m_l mixing (l and m_l represent the Rydberg electron orbital angular momentum and magnetic quantum numbers, respectively) both of which contribute to the lengthening of the lifetime (≡ drop in $\overline{\Gamma}$)[25].

In Table 6-1 are reported the value of $\overline{\Gamma} = \Gamma n^{*3}$ where $n^* = (n - \delta_n)$. In the calculations the quantum defect parameters, δ_n, obtained by Schaphorst *et al.*[15] from the expression:

$$E_n = E_\infty - \frac{R}{(n-\delta_n)^2} \qquad \text{Eq. 6-11}$$

have been used, where E_∞ is the adiabatic ionization energy of the atom and R is the Rydberg constant. This choice is justified by the fact the photon energy source has been calibrated using the resonance energies obtained by Schaphorst *et al.*[15] and the resonance positions determined by the fit. For all the resonances the $\overline{\Gamma}$ values are approximately constant, within experimental error, as expected[13,23], as the n values are well below the high values where lengthening of Rydberg state lifetime occurs through l and m_l mixing.

Table 6-1: *Widths (Γ), line-shape parameters (q and ρ^2) and oscillator strengths (f) for the $N^*[2s2p^3(^5S), np](^4P) \leftarrow N(^4S)$ autoionizing resonances for $n \geq 5$.*

		Γ(meV)	q	ρ^2 (×10²)	f(×10³)	Γn^{*3} (×10²)
5p	Ref. (15)	4.4 ± 0.3	-1.9 ± 0.3	65 ± 15	1.6 ± 0.6	37.3 ± 2.5
5p	Present work	4.77 ± 0.15	-1.85 ± 0.08	62.1 ± 1.9	1.59 ± 0.15	40.1 ± 1.3
6p	Present work	2.60 ± 0.15	-2.07 ± 0.10	56.5 ± 3.0	0.99 ± 0.12	40.5 ± 2.4
7p	Present work	1.80 ± 0.15	-2.22 ± 0.10	61.6 ± 4.9	0.86 ± 0.13	47.1 ± 3.9
8p	Present work	1.19 ± 0.27	-1.84 ± 0.14	55.8 ± 12.0	0.35 ± 0.12	47.9 ± 10.9
9p	Present work	0.89 ± 0.39	-1.58 ± 0.16	61.9 ± 25.1	0.22 ± 0.14	52.0 ± 22.8
10p	Present work	0.62 ± 0.59	-1.31 ± 0.19	81.0 ± 66.6	0.14 ± 0.17	51.2 ± 48.7

In practice the experimental error increases as n increases. This is because of a lower signal-to-noise and a decrease in the number of experimental points for each resonance as n increase. This is particularly noticeable for the errors in Γn^{*3} for the 9p and 10p resonances.

As can be seen in Table 6-1, and from the results presented for n = 3, 4 and 5 in reference (15), the oscillator strengths (f) for the autoionizing resonances decrease from n = 3 to 10. The q value however becomes more negative from -1.60 ± 0.24 at n = 3 to -2.22 ± 0.10 at n = 7 and then less negative from n = 7 to n = 10. The overall trend of decreasing f values is due to the fact that the probability of autoionization relative to direct ionisation decreases from n = 3 to 10.

The parameter q can be written as (see also Chapter 2.2.3, Eq. 2-16):

$$q = \sqrt{\frac{2}{\pi \cdot \Gamma}} \frac{\langle \gamma_i | D | \Phi \rangle}{\langle \gamma_d | D | \Phi \rangle} \qquad \text{Eq. 6-12}$$

where γ_d and γ_i are the final state wavefunctions for the direct and indirect processes respectively, D is the electric dipole moment operator and Φ is the wavefunction for the initial sate. The first term in this expression is inversely proportional to $\sqrt{\Gamma}$ and hence increases with n, as Γ decreases with n (see Table 6-1). From Eq. 6-7, assuming ρ^2 is constant (see Table 6-1), the second term in Eq. 6-12 is proportional to $\sqrt{f}$ and hence decreases with n (see Table 6-1). This gives rise to a change of slope of q with n. The second term is dominant up to $n = 7$ explaining the decrease of q up to $n = 7$ while after $n = 7$ the first term becomes dominant, explaining the increase of q after $n = 7$.

6.3 Conclusions

The natural width Γ, line shape parameters q and ρ^2 and discrete oscillator strengths f have been measured for the members of the $N^*[2s2p^3\ (^5S), np]\ (^4P) \leftarrow N(^4S)$ autoionizing resonances for $n \geq 5$. The 5p parameters calculated in this work are in good agreement with the values obtained by previous experiment. The constancy of the parameters ρ^2 and Γn^{*3} for the whole series of autoionizing resonances has been demonstrated while the parameter q shows a non constant behaviour.

References

[1] J. U. Koppel
Journal of Chemical Physics **55**, 123 (1971).

[2] R. J. W. Henry
Journal of Chemical Physics **44**, 4357 (1966).

[3] R. J. W. Henry
Journal of Chemical Physics **48**, 3635 (1968).

[4] M. Le Dourneuf, L. Vo Ky and A. Hibbert
Journal of Physics B **9**, L359 (1976).

[5] K. L. Bell and K. A. Berrington
Journal of Physics B **24**, 933 (1991).

[6] A. W. Ehler and G. L. Weissler
Journal of the Optical Society of America **45**, 1035 (1955).

[7] F. J. Comes and A. Elzer
Physics Letters A **25**, 334 (1967).

[8] J. A. R. Samson and G. C. Angel
Physical Review A **42**, 1307 (1990).

[9] http://www.src.wisc.edu/default.html.

[10] P. K. Carroll, R. E. Huffman, J. C. Larrabee and Y. Tanaka
Astrophysical Journal **146**, 553 (1966).

[11] U. Fano
Physics Review **124**, 1866 (1961).

[12] D. Dill
Physical Review A **7**, 1976 (1973).

[13] U. Fano and J. W. Cooper
Review of Modern Physics **40**, 441 (1968).

[14] P. M. Dehmer, J. Berkowitz and W. A. Chupka
Journal of Chemical Physics **60**, 2676 (1974).

[15] S. J. Schaphorst, S. B. Whitfield, H. P. Saha, C. D. Caldwell and Y. Azuma
Physical Review A **47**, 3007 (1993).

[16] http://www.elettra.trieste.it

[17] J. M. Dyke, N. Jonathan, A. Morris and T. Sears
Journal of The Chemical Society and Faraday Transition 2 **72**, 597 (1976).

[18] J. B. West and G. V. Marr
Atomic Data and Nuclear Data Tables **18**, 497 (1976).

[19] J. B. West, J. M. Dyke, A. Morris, T. G. Wright and S. D. Gamblin
Journal of Physics B **32**, 276 (1999).

[20] J. M. Dyke, N. Jonathan and A. Morris *Electron Spectroscopy: Theory, Techniques and Applications*, edited by C.R. Brundle and A.D. Baker ed.; Academic Press: London, 1979.

[21] C. E. Moore *Atomic Energy Levels*, U.S. Government Printing Office ed.Washington DC, 1952; Vol. 1.

[22] L. Asbrink and C. Fridh
Physica Scripta **9**, 338 (1974).

[23] U. Fano and J. W. Cooper
Physics Review **137**, 1364 (1965).

[24] T. K. Fang and T. N. Chang
Physical Review A **57**, 4407 (1998).

[25] W. A. Chupka
Journal of Chemical Physics **98**, 4520 (1993).

Chapter 7

7 AN INITIAL STUDY OF S ATOMS AND SH RADICALS BY PHOTOELECTRON SPECTROSCOPY

This Chapter reports a preliminary study of photoelectron spectroscopy using Synchrotron Radiation on the S atoms and SH radicals.

The Chapter is organized as follows. In section 7.1 previous spectroscopy investigations on S atoms and SH radicals that are considered important for the present work are briefly reviewed. Section 7.2 presents the results of the measured photoelectron spectra at different photon energies and at two different angles with respect to the major polarization axis of the photon source, together with their interpretations. The results have been obtained with the photoelectron (PE) spectroscopy technique. Section 7.3 summarizes the results obtained.

This Chapter describes results obtained from a single visit to ELETTRA. Chapter 8, also on S and SH, describes results from a later visit to ELETTRA.

7.1 Previous investigations on S atoms and SH radicals with photoelectron spectroscopy

In the extreme ultraviolet wavelength region, absorption, photoionization and autoionization of sulphur atoms are of fundamental interest for understanding the spectroscopy and photoionization dynamics of open-shell atoms. Moreover, due to its relatively high solar abundance, sulphur plays an important role in determining solar and stellar opacities[1-3] and interaction of S atoms with ultraviolet radiation is important in the solar atmosphere[4].

The ground state configuration of S atoms is $1s^2 2s^2 2p^6 3s^2 3p^4$, ^3P. Three ionic states arise on $(3p)^{-1}$ ionization from this state: the ^4S, ^2D and ^2P states at ionization energies of 10.35, 12.21 and 13.40 eV respectively[5].

There has been considerable theoretical work carried out on the photoionization cross section of S atoms over a wide photon energy range. Conneelly *et al.*[6] computed photoionization cross sections for atomic systems with incomplete outer 3p subshells using the continuum Hartree-Fock approximation, and Dill et al.[7] derived expressions for the angular distribution of photoelectrons produced by ionization of open shell atoms including sulphur. The asymmetry parameter, β, as function of photon energy was calculated for each of the three ionic channels resulting from the $(3p)^{-1}$ ionization of sulphur atoms using both Hartree-Fock and Herman-Skillman wavefunctions for the atom, ion and free electron from threshold up to 60 eV.

Later, Manson et al.[8] presented results of calculations of the photoionization cross sections and angular distributions of the outer p sub-shell of chalcogen and halogen atoms from 13 to 100 eV photon energy, using the continuum Hartree-Fock approximation. In the theoretical work on S atoms[7,8], the general shape of the cross section for each of the three ionic channels shows a clearly observable Cooper minimum around 40 eV. The calculated asymmetry parameters as a function of photon energy have a small value near threshold, rise rapidly to a maximum then fall to a minimum with negative β values at the Cooper minimum of the cross section; they subsequently increase smoothly (the S 3p orbital is expected to show a Cooper minimum since the number of nodes in the atomic wavefunction, $n - l - 1$, is greater

than zero). The $(3p)^{-1}$ photoionization cross section of S atoms has also been calculated at a number of photon energies by Yeh *et al.*[9] using Hartree-Fock-Slater calculations.

Experimentally, a number of studies have been made on S atoms[10-13]. Tondello[10] measured and analysed the absorption spectrum of S in the vacuum ultraviolet region 1830 - 900 Å (6.77 - 13.77 eV), below and above the ionization threshold. An attempt to derive the absolute value of the photoionization cross section from the ground state in the 1197 - 940 Å region (10.36 - 13.19 eV) was made in this work. Modifications and additions to this spectrum have been made using a similar technique by Sarma *et al.*[11] and, more recently, by Joshi *et al.*[12].

Subsequently, Gibson *et al.*[13] studied the photoionization spectrum of atomic sulphur using photoionization mass spectrometry from the ionization threshold, 10.35 to 13.40 eV.

The SH radical is a molecule of environmental importance which plays a role in the ultraviolet photochemistry of several small sulphur-containing compounds which are released into the earth's atmosphere from natural and anthropogenic sources[14]. For example, hydrogen sulphide, carbonyl sulphide and carbon disulphide are released from the earth and its oceans as a consequence of microbiological processes. They react with the hydroxyl radical in the atmosphere to yield SH, which is then oxidized by O_2 and O_3 to SO_2.

Although SH has been studied with various spectroscopic techniques[15-18] and theoretical methods[19,20], information on its electronic states is still somewhat limited. A multiphoton ionization study of the SH radical in the single photon energy range 4.68 - 3.91 eV has been performed by Ashfold *et al.*[15] The observation and partial characterization of three Rydberg states of SD and SH, accessed via 2-photon resonances from the ground state was achieved in this work. More recently, thirteen Rydberg states converging to the second and third ionic state have been observed and characterised by two-photon resonance enhanced multiphoton ionization spectroscopy and multiphoton ionization photoelectron spectroscopy[21]. Also, the electronic absorption spectrum of SH has been investigated from the near ultraviolet into the vacuum ultraviolet region and several electronic transitions have been identified[16,17].

The adiabatic ionization energies of $SH(X^2\Pi)$ to the first five ionic states have been established from HeI vacuum ultraviolet (VUV) photoelectron spectroscopy measurements to an accuracy of ± 0.01 eV[5]. Recently a more accurate determination of the ionization energies to the $X^3\Sigma^-$ state[22] and $a^1\Delta$ ionic state[23] from $SH(X^2\Pi)$ have been achieved by the pulsed field ionization zero electron kinetic energy method.

The ground state electronic configuration of the SH radical is $1\sigma^2 2\sigma^2 3\sigma^2 1\pi^4 4\sigma^2 5\sigma^2 2\pi^3$; photoionization from the valence 2π molecular orbital produces the $X^3\Sigma^-$, $a^1\Delta$ and $b^1\Sigma^+$ ionic states at adiabatic ionization energies (AIEs), equal to the vertical ionization energies (VIEs), of 10.42, 11.64 and 12.76 eV respectively[5,22,23]. The potential energy curves of these ionic states are very similar to that of the ground state of the neutral because of the non-bonding S 3p character of the 2π orbital. The removal of one electron from the 5σ shell gives rise to the $SH^+(A^3\Pi) \leftarrow SH(X^2\Pi)$ and $SH^+(c^1\Pi) \leftarrow SH(X^2\Pi)$ bands which are broad and vibrationally resolved, with the AIE equal to the VIE for both bands. AIE values for these bands are 14.11 eV and 15.69 eV respectively[5].

Until now no attempts have been made to measure asymmetry parameters (β) and photoionization cross sections (σ) of either S or SH. The purpose of this present work was to measure angular distribution parameters and relative photoionization cross sections for the $S^+(^4S) \leftarrow S(^3P)$, $S^+(^2D) \leftarrow S(^3P)$ and $S^+(^2P) \leftarrow S(^3P)$ bands and the $SH^+(X^3\Sigma^-, v^+=0) \leftarrow SH(X^2\Pi, v''=0)$, $SH^+(a^1\Delta, v^+=0) \leftarrow SH(X^2\Pi, v''=0)$ and $SH^+(b^1\Sigma^+, v^+=0) \leftarrow SH(X^2\Pi, v''=0)$ bands as a function of photon energy from threshold (~10.3 eV) to 21.64 eV with the ELETTRA Synchrotron Radiation Source. This should allow comparison to be made with available calculations.

7.2 Results and discussion

Photoelectron (PE) spectra were recorded in the constant pass energy mode; by scanning the voltage on a lens which accelerates (or decelerates) the photoelectrons before they enter the analyser (see Chapter 4.2.1).

In this work, S atoms and the SH radicals were produced by the following consecutive reactions (see also Chapter 4.4.2):

$$F + H_2S \rightarrow SH + HF \qquad \text{Eq. 7-1}$$

$$F + HS \rightarrow S + HF \qquad \text{Eq. 7-2}$$

The room temperature rate constants for the above reactions are 1.33×10^{-10} and 2.01×10^{-10} $cm^3molecule^{-1}s^{-1}$ respectively[24]. To obtain a high F-atom yield, fluorine atoms were produced by flowing 5% F_2 in helium through a microwave discharge at 2.45 GHz in the side arm of a glass inlet system[25], with an inner inlet system which is the inlet used for the target molecules (in this case H_2S). In order to avoid attack of the glass system by the fluorine atoms produced by the discharge, the inner surface of the tube was coated with a thin layer of teflon, while the discharge cavity was positioned on an alumina section of the inlet system to prevent melting of the teflon due to heating from the discharge[25], as explained in Chapter 4.4. The intensities of the bands in the experimental PE spectra were normalized by the photon flux and then by the transmission correction of the spectrometer. The transmission function of the spectrometer, for electrons of different initial electron kinetic energy, was determined by measuring the intensity of the helium $(1s)^{-1}$ photoelectron band at different photon energies. The intensity of the helium $(1s)^{-1}$ band was measured in the VUV photon energy range used and then it was normalised using the absolute photoionization cross section of helium in this range[26]; finally the normalized intensity was plotted as function of the electron kinetic energy. This curve was used to correct the experimental PE spectra for the transmission of the spectrometer.

The degree of linear polarisation ($P = 1$) of the radiation was well established[27,28]. The asymmetry parameter (β) was measured for S and SH radicals at selected photon energies and over a photon energy range, by recording PE spectra at two different θ angles (0° and 54° 44') at each photon energy (at 54° 44′ the measured intensity is proportional to the total photoionization cross section, independent of β); the β parameter was then calculated from:

$$\beta = (R - 1) \qquad \text{Eq. 7-3}$$

where $R = I_0 / I_{54°44'}$ is the ratio of the experimental intensities at these two angles, after applying the above corrections.

The photon energy was calibrated in the 11.5 - 29.0 eV region against the energies of the Ar $3s3p^6(^2S_{1/2})np \leftarrow 3s^23p^6(^1S_0)$ resonances[29] and He $1s^1np \leftarrow 1s^2$ absorption lines[30]. The Ar resonances were obtained recording ClS spectra of the first band (first component) of the $(3p^{-1})$ ionization of argon in the photon energy region 26.0 - 29.0 eV. The absorption spectra of He were recorded measuring the current on the aluminium plate at the back of the spectrometer in the photon energy ranges 21.0 - 24.0 eV using first order radiation and 11.5 - 12.3 eV using second order radiation.

Test experiments were carried out in Southampton in order to determine the optimum pressures and mixing distance above the photon beam to be used in the experiments at ELETTRA which maximise the intensities of the second and third photoelectron bands of SH at 11.64 eV and 12.76 eV AIE respectively, corresponding to the ionizations $SH^+(a^1\Delta, v^+=0) \leftarrow SH(X^2\Pi, v''=0)$ and $SH^+(b^1\Sigma^+, v^+=0) \leftarrow SH(X^2\Pi, v''=0)$, and the second and third ionizations of S at 12.21 eV and 13.40 eV IE respectively, corresponding to the ionizations $S^+(^2D) \leftarrow S(^3P)$ and $S^+(^2P) \leftarrow S(^3P)$[5]. The following conditions were found to be the optimum for production of both S and SH: a mixing distance above the photon beam of 2 cm, with the inner-inlet system used for H_2S longer than the outer inlet system by about 2 mm, and the partial pressures measured on an ionization gauge positioned on the wall of the ionization chamber of $\Delta p(H_2S) = 2.4\times10^{-7}$ mbar and $\Delta p(F_2/He) = 4.6\times10^{-6}$ mbar.

The PE spectra recorded at a photon energy of $h\nu = 21.64$ eV with Synchrotron Radiation and at two different angles with respect to the polarization axis of the photon source ($\theta = 0°$ and $\theta = 54° 44'$) of the products of the F + H_2S reaction are shown in Figures 7.1 and 7.2 with the assignment of the major features indicated.

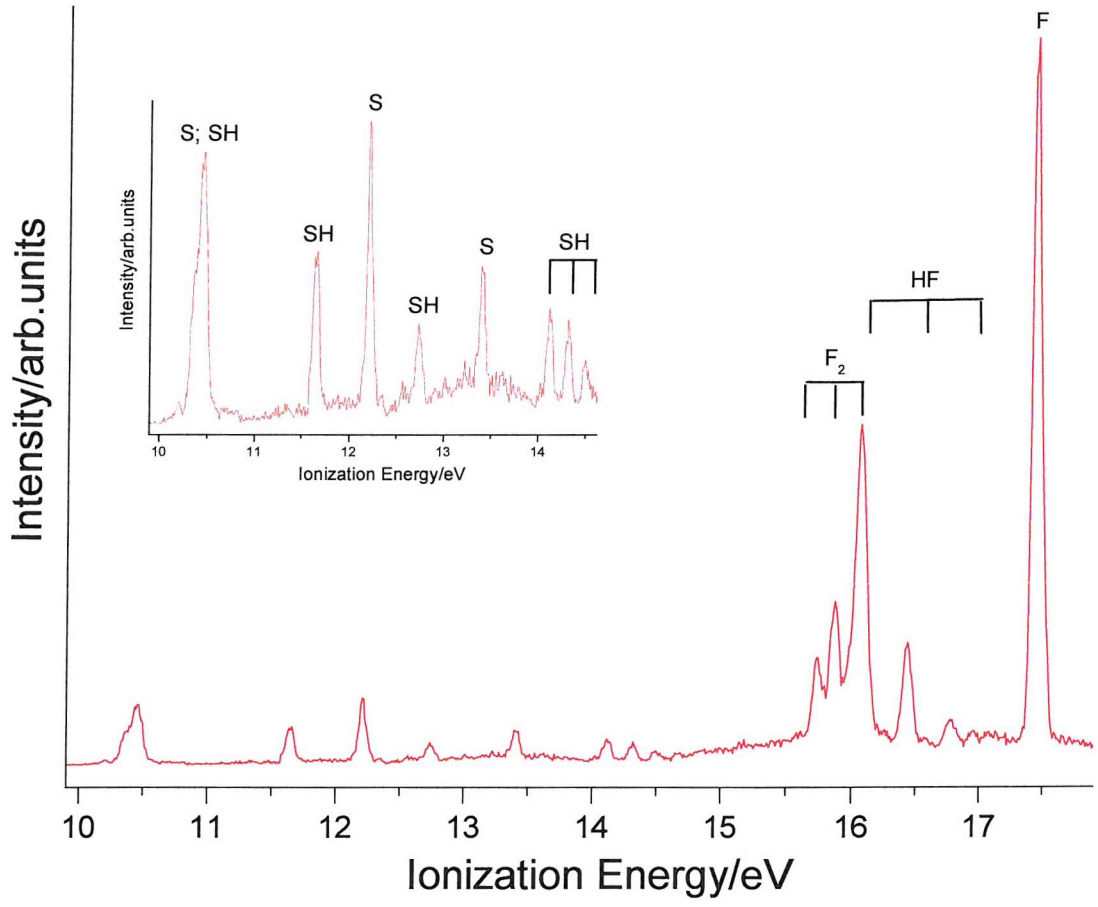

Figure 7.1 *Photoelectron spectrum at $h\nu = 21.64$ eV of the reactions*
$F + H_2S \rightarrow SH + HF$
$F + HS \rightarrow S + HF$
measured at the angle with respect to the major polarization axis of the photon source $\theta = 0°$. In the inset a magnification of the region of interest is presented.

These spectra show sharp bands at 11.64 and 12.76 eV, which are the second and third bands of SH, and sharp bands at 12.21 and 13.40 eV which are the second and third bands of S atoms. The sharp band at ≈ 10.5 eV arises from overlap of the first band of S atoms at 10.35 eV, and the first band of SH at 10.42 eV as well as a small contribution from the first band of residual H_2S at 10.48 eV[5]. Bands associated with F and F_2 were also observed in the spectra[31,32], as well as a small contribution from SF_2 which is a secondary reaction product[33] (see Figure 7.3).

The vibrationally resolved band of SH at 14.11 eV AIE is the fourth band of SH, the $SH^+(A^3\Pi) \leftarrow SH(X^2\Pi)$ ionization. Unfortunately, the fifth band of SH, the $SH^+(c^1\Pi) \leftarrow SH(X^2\Pi)$ ionization AIE 15.69 eV, was not observed because it was too weak and overlapped with the first band of F_2.

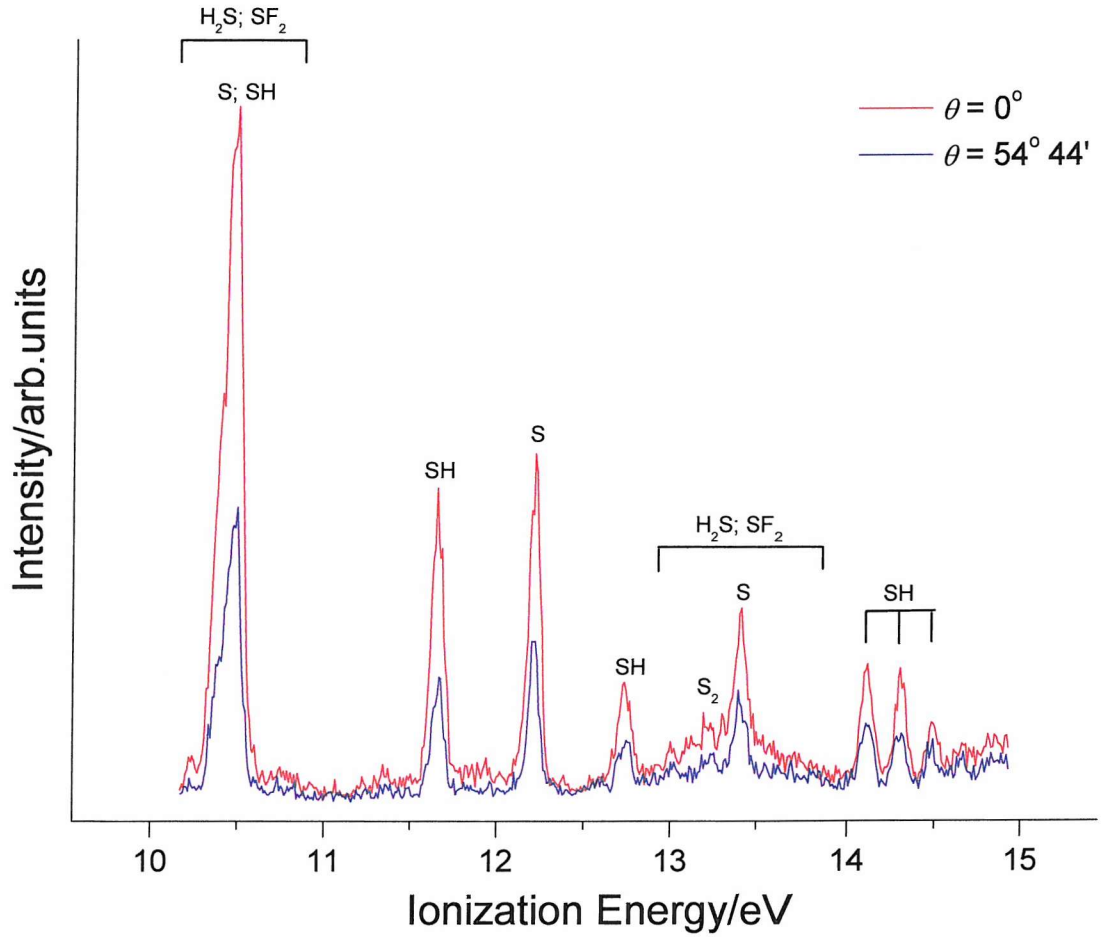

Figure 7.2 *Photoelectron spectrum at $h\nu$ =21.64 eV of the reactions*
$F + H_2S \rightarrow SH + HF$
$F + HS \rightarrow S + HF$
measured at two different angles $\theta = 0°$ (red trace) and $\theta = 54°44'$ (blue trace) with respect to the major polarization axis of the photon source in the 10 - 15 eV ionization energy region.

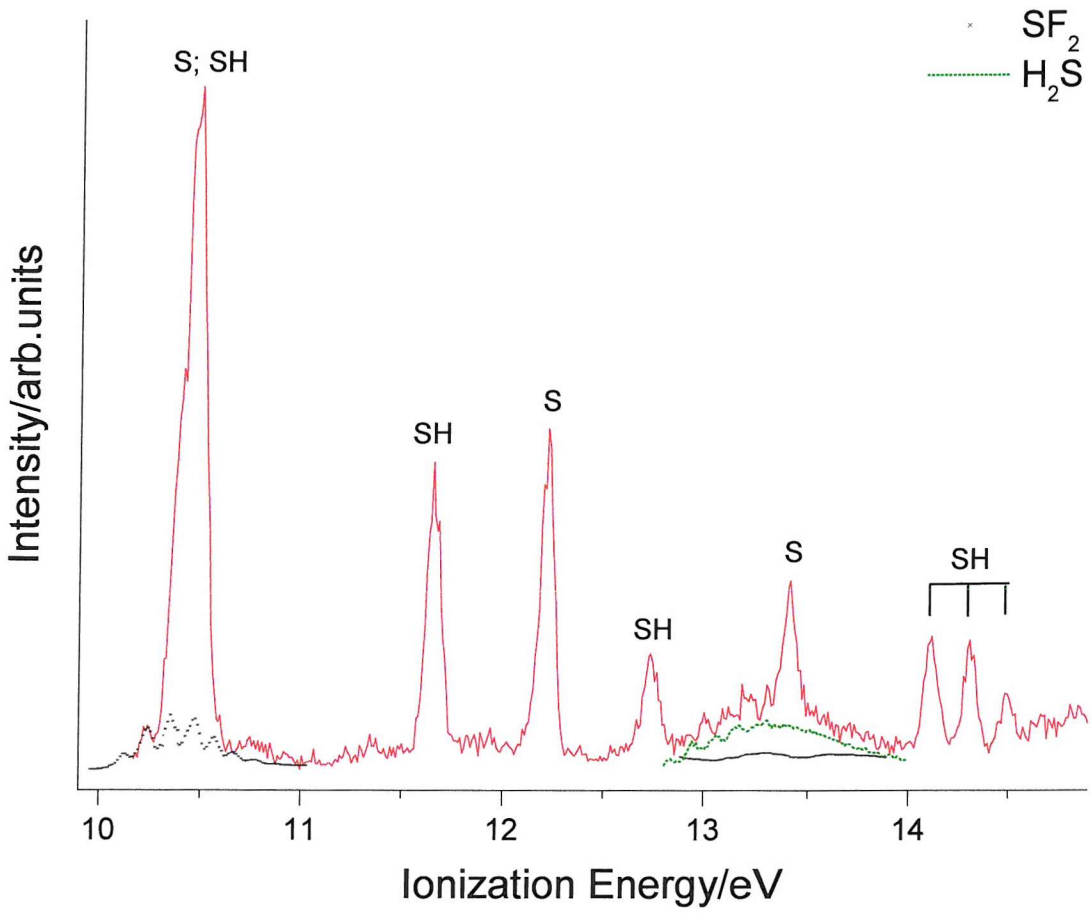

Figure 7.3 *Photoelectron spectrum recorded at $h\nu = 21.64$ eV at $\theta = 0°$ for the reaction $F + H_2S$ at a mixing distance of 2 cm above the photon beam. Estimated contributions from SF_2 (first and second bands) and H_2S (second band) are shown. The asymmetry parameter of the first vibrational component of the 4th band of SH at IE of 14.11 eV has been measured as $\beta = 1.04 \pm 0.39$ at this photon energy.*

The broad band on the low energy side of the $S^+(^2P) \leftarrow S(^3P)$ ionization at 13.40 eV ionization energy in Figure 7.3 is mainly due to the presence of unreacted H_2S, along with SF_2 produced by secondary reactions. Confirmation of the presence of SF_2 can be easily obtained from the observation of the first two vibrational components of the first band of SF_2 on the low ionization energy side of the sharp band at $\approx$ 10.5 eV

(1^{st} AIE of SF_2 10.08 eV)[33], see Figure 7.3. The spectra obtained are in good agreement with those previously recorded in Southampton by Dunlavey *et al.*[5] with a HeI radiation source.

In Figure 7.4, an expanded version of the composite band at ≈ 10.5 eV is shown.

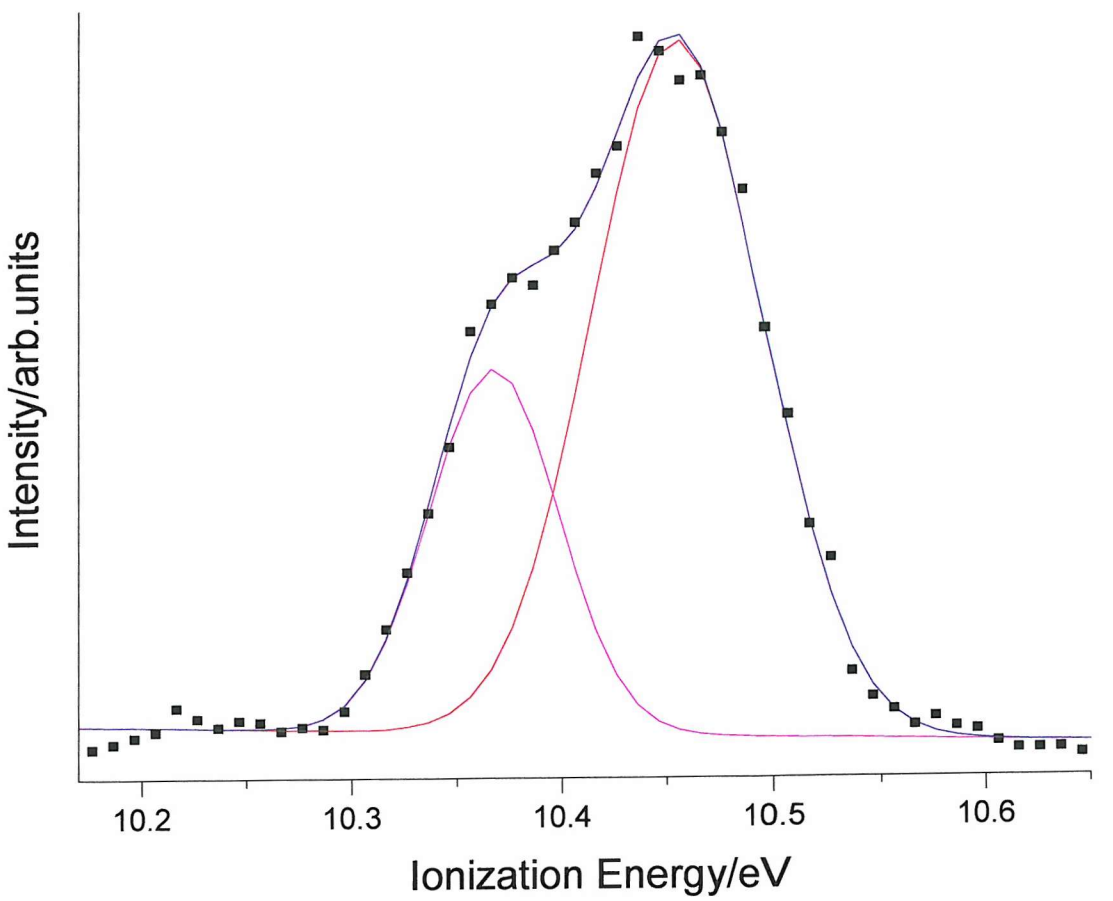

Figure 7.4 *Deconvolution of the band shown in Figure 7.3 at ≈10.4 eV ionization energy into two Gaussian components. The band centred at 10.36 eV is the first band of S atoms, $S^+(^4S) \leftarrow S(^3P)$, whereas the band at 10.45 eV contains contributions from the first band of SH, $SH^+(X^3\Sigma^-) \leftarrow SH(X^2\Pi)$, and from the first band of H_2S (see text for further details).*

Figure 7.4 clearly shows two maxima. Deconvolution of this band into two Gaussians was performed and the fitted Gaussians were centred at 10.36 ± 0.02 and 10.45 ± 0.03 eV. These energies are in agreement with the known energies of the $S^+(^4S) \leftarrow S(^3P)$ and $SH^+(X^3\Sigma^-) \leftarrow SH(X^2\Pi)$ ionizations at 10.35 eV and 10.42 eV respectively. The small contribution of the $H_2S^+(X^2B_1) \leftarrow H_2S(X^1A_1)$ ionization at 10.48 eV is included in the band centred at 10.45 eV. This is consistent with a slightly larger full width at half maximum (FWHM) of the second fitted Gaussian compared to the first Gaussian. The values obtained from the fit are $FWHM_1 = 72 \pm 3$ meV and $FWHM_2 = 95 \pm 3$ meV for the first and second Gaussian, respectively.

7.2.1 The preliminary studies by PES

The ionization energy region 9.600 - 15.200 eV was recorded using 23 different photon energies from 13.205 to 21.640 eV. A step size of 0.20 eV was used from $h\nu = 13.205$ eV to $h\nu = 16.420$ eV and a step size of 0.40 eV was used from $h\nu = 16.420$ eV to $h\nu = 18.494$ eV; PE spectra were also recorded at $h\nu = 21.640$ eV. In Figures 7.5 and 7.6 the renormalized PE spectra recorded at $\theta = 0°$ at $\theta = 54°\ 44'$ with respect to the major polarization axis of the photon source are shown.

Due to significant variations in the intensities of the 12.21 eV band (second band of S) and the 11.64 eV band (second band of SH) with photon energy, the ionization energy region 11.500 - 12.400 eV was re-examined by recording a new series of 21 PE spectra with photon energies from $h\nu = 13.205$ eV to $h\nu = 13.411$ eV, with a smaller step size of 0.01 eV.

In Figure 7.7 the re-examined sections are shown for the two different angles.

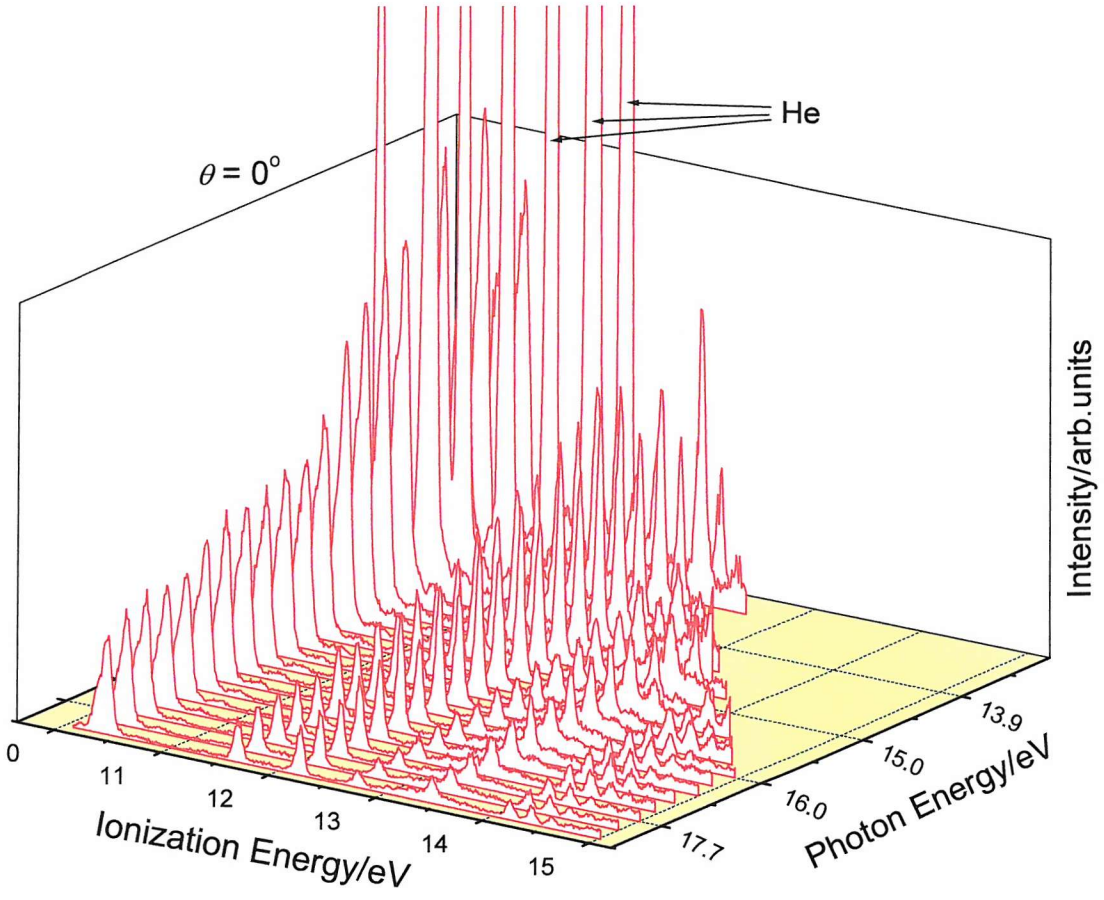

Figure 7.5 *PE spectra recorded at 22 different photon energy from $h\nu = 13.2$ eV to $h\nu = 18.5$ eV (with $a \sim 200$ meV of stepwidth in the photon energy region 13.2 - 16.4 eV; with $a \sim 400$ meV of stepwidth in the photon energy region 16.4 - 18.5 eV) in the ionization energy region 9.6 - 15.2 eV, at $\theta = 0°$.*

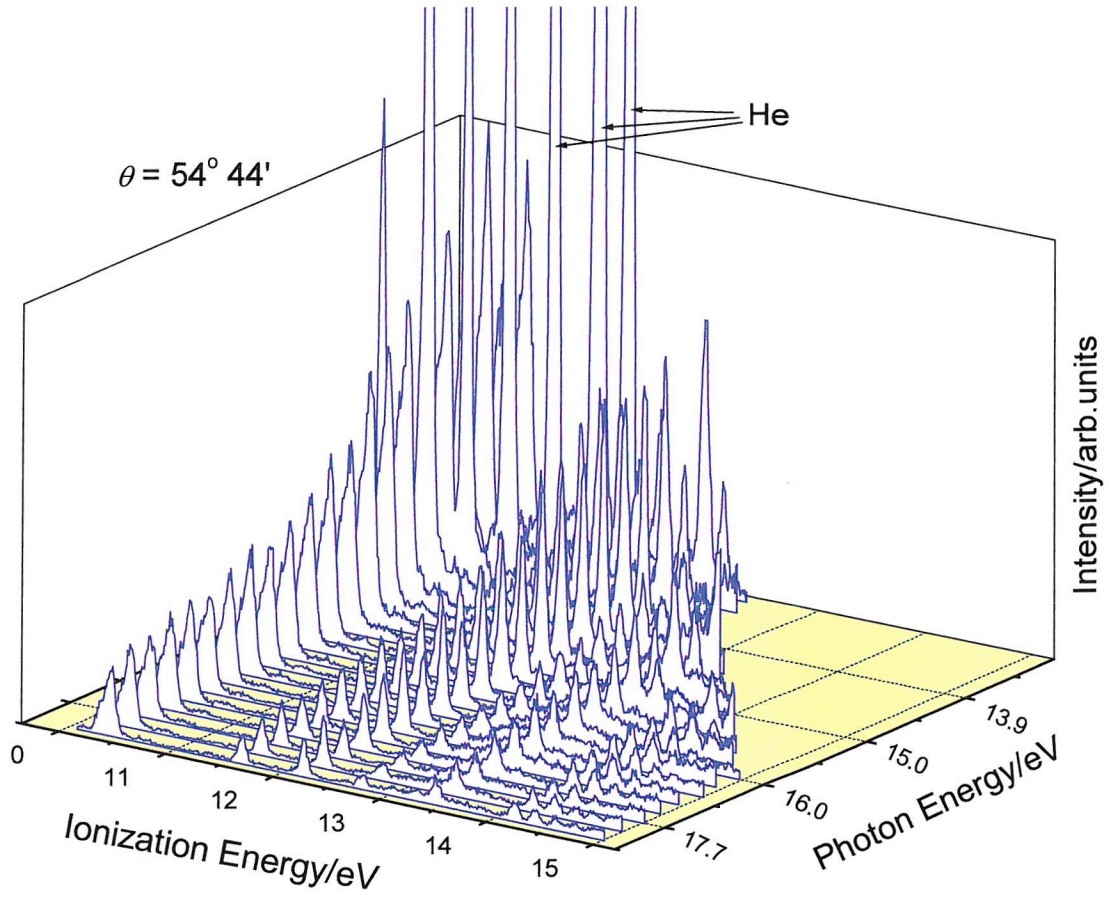

Figure 7.6 *PE spectra recorded at 22 different photon energy from $h\nu = 13.2$ eV to $h\nu = 18.5$ eV (with $a \sim 200$ meV of stepwidth in the photon energy region 13.2 - 16.4 eV; with $a \sim 400$ meV of stepwidth in the photon energy region 16.4 - 18.5 eV) in the ionization energy region 9.6 - 15.2 eV, at $\theta = 54°44'$.*

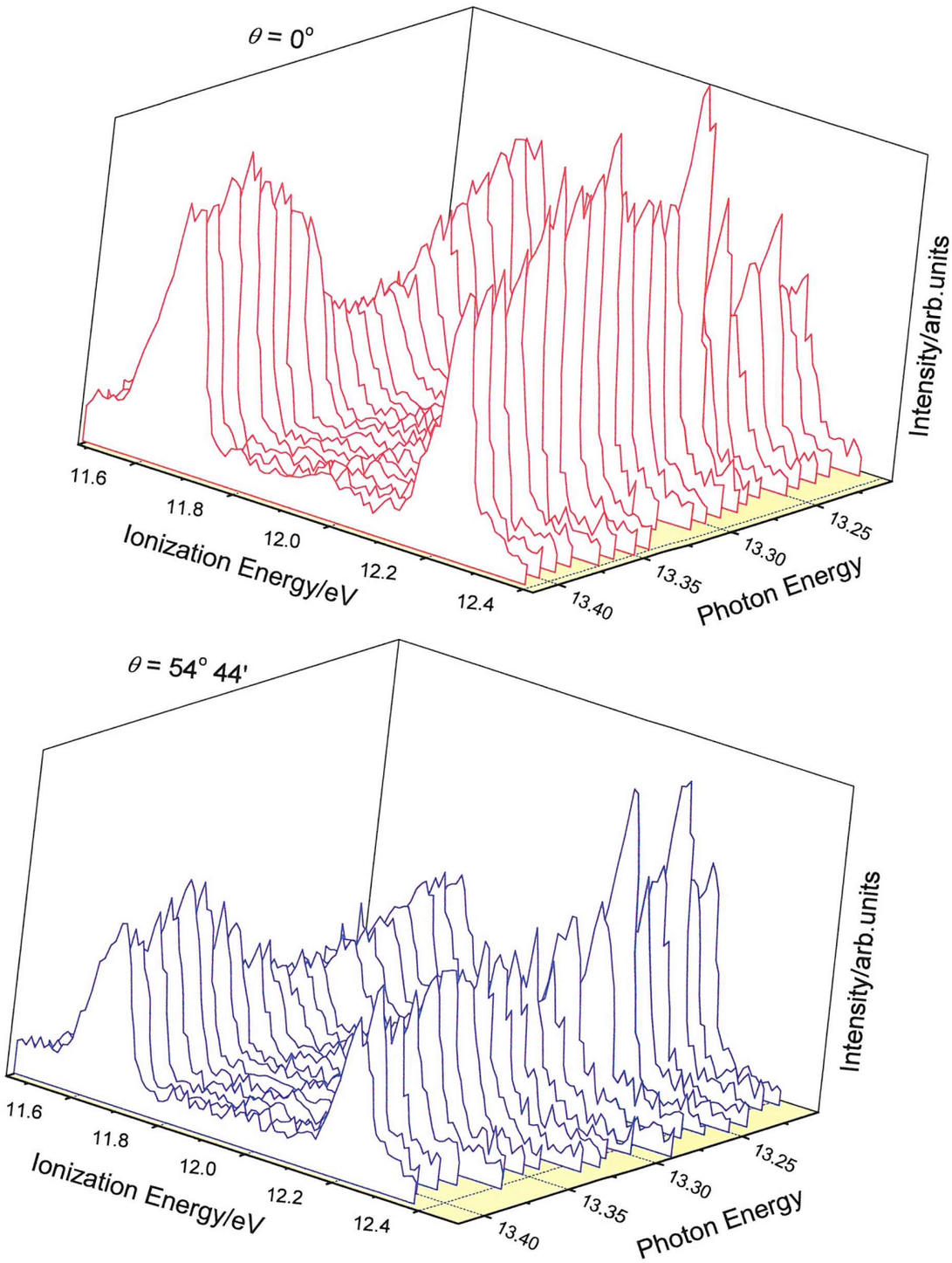

Figure 7.7 *PE spectra recorded at 21 different photon energy from $h\nu = 13.20$ eV to $h\nu = 13.41$ eV (with $a \sim 10$ meV of stepwidth) in the ionization energy region 11.5 - 12.4 eV; at $\theta = 0°$ (higher panel) and at $\theta = 54°44'$ (lower panel).*

The strong band present in the PE spectra of Figures 7.5 and 7.6 at photon energy between 13.20 eV and 14.30 eV, shown by arrows in these diagrams, is due to ionization of helium by the second order radiation. In this photon energy region second order radiation can ionize helium (IE = 24.58 eV[34]) with consequent emission of electrons. This helium $(1s)^{-1}$ band was used as an internal check for the correction factor applied for the evaluation of the asymmetry parameter for the observed bands of S and SH. Indeed, with the procedure used, β was always obtained as 2.00, within experimental error, for this helium $(1s)^{-1}$ band. In practice, for the measurements of angular distribution it is important to make sure that the efficiency of the analyser does not change when the spectrometer is rotated. The biggest contribution to the change of the efficiency of the analyser comes from small misalignments between the axis of rotation and the direction of the photon beam. This contribution is minimized by adjusting, after each rotation of the spectrometer, the direction of the photon beam in such a way as to maximize the signal coming from the detector and the current measured by the photodiode on the opposite side of the ionization chamber of the spectrometer from the direction of the photon beam. However, to quantify this contribution for all the angle resolved experiments, a correction factor is evaluated at each set of experiments by measuring the intensity of bands at $\theta = 0°$ and at $\theta = 54° 44'$, usually at 21.22 eV photon energy, from a sample (usually Ar) where the asymmetry parameter is well established. From the comparisons between the calculated asymmetry parameter and the known asymmetry parameter, the correction factor was determined. Then, at each photon energy, the asymmetry parameter can be calculated for an S or SH band using Eq. 7-3 with this correction factor. This has been carried out to give the plots shown in Figures 7.8 to 7.12.

The relative photoionization cross sections can be evaluated by integrating the area of the bands at $\theta = 54° 44'$, the results are shown in Figures 7.13 to 7.16

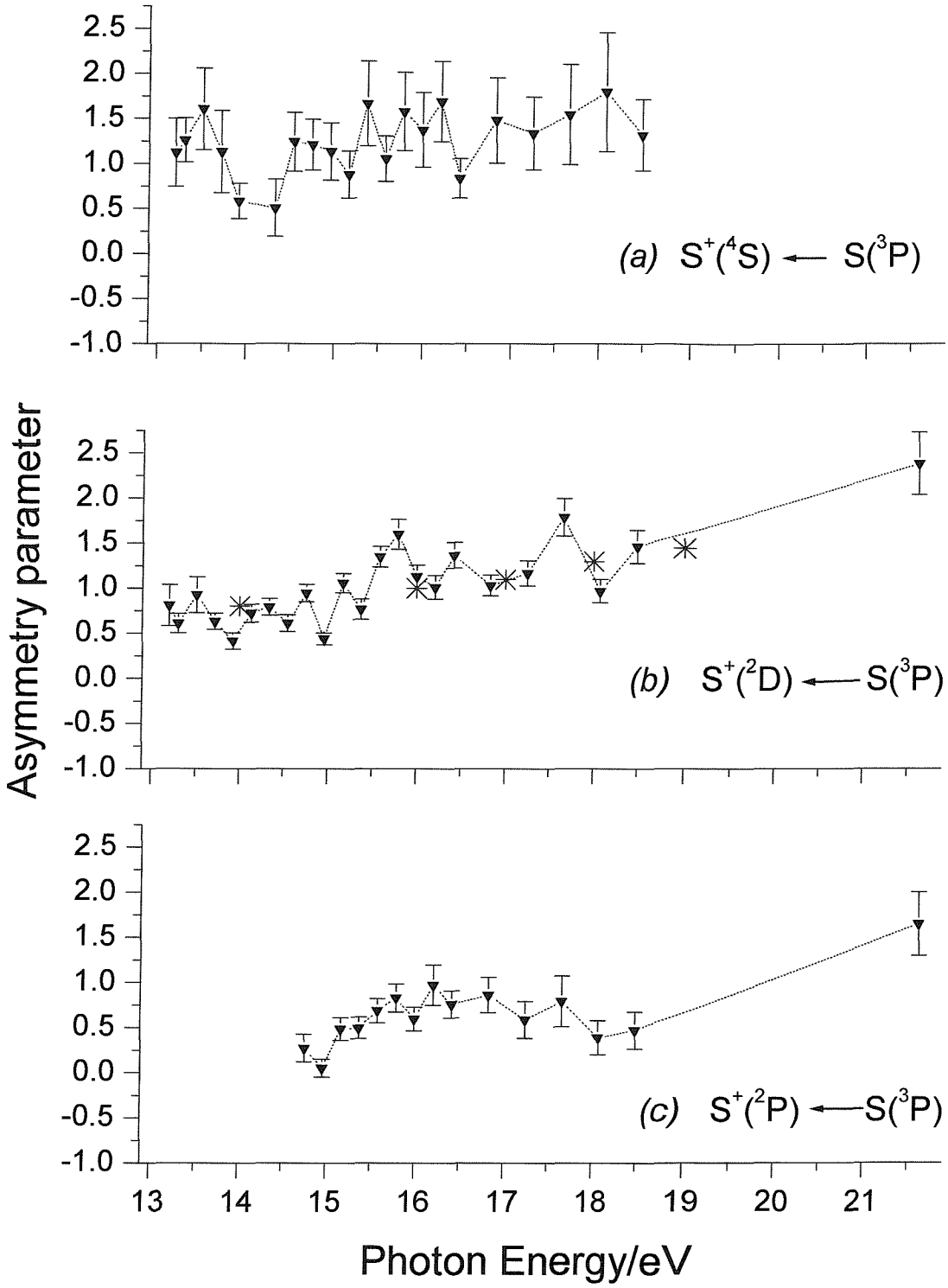

Figure 7.8 *Plots of the asymmetry parameter (β) as a function of photon energy over the range hν = 13.0 - 22.0 eV, for the first three photoelectron bands of S atoms.*
Plot (b) includes β values for the first band of H_2S measured at different photon energies in Ref. (35), denoted with the symbol (*).

Inspection of existing angular distribution and relative cross section (σ) measurements for H_2S[35-37], indicates that for the S photoelectron bands arising from a $(3p)^{-1}$ ionization, the angular distribution parameter (β) plotted as function of photon energy is expected to show an initial increase, a maximum at $\approx$ 25 eV and a minimum at $\approx$ 40 eV, the Cooper minimum, whereas the σ plot is expected to show a regular decrease from threshold, the shallow Cooper minimum at $\approx$ 40 eV and then a slow increase. The first, second and third bands of S, SH and the first band of H_2S are expected to be very similar in their β and σ plots as they all correspond to ionization from a S 3p lone-pair orbital. Comparisons of the measured asymmetry parameters as a function of photon energy for the three ionization channels resulting from the $(3p)^{-1}$ photoionization of S derived from this work with results of the angular distribution Hartree-Fock calculations of Dill *et al.*[7] have been made over the photon energy range 10 - 22 eV. These calculations[7] used Russell-Saunders coupling and were based on an angular momentum transfer expansion for the differential photoionization cross section. Dill *et al.*[7] showed that the three ionic channels resulting from photoionization of $S(^3P)$ should show significantly different behaviour from each other when plotted as function of photon energy, in contrast to identical behaviour expected in the Cooper-Zare model[38,39]. In Figure 7.8, the three different angular distribution plots are shown as a function of photon energy and comparisons with the results of Dill *et al.*[7] are presented in Figures 7.9 - 7.11.

Figure 7.8 *(b)* also shows data points taken from reference (35) for the first band of H_2S. This shows reasonable agreement with the S atom results of this work but again more H_2S data points are required for a more meaningful comparison.

As can be seen in Figures 7.9 - 7.11, the experimental results obtained in this work are in reasonable agreement with the results of the calculations[7] for the $S^+(^4S) \leftarrow S(^3P)$ and $S^+(^2D) \leftarrow S(^3P)$ ionization channels, Figures 7.9 and 7.10 respectively, but are in poorer agreement for the $S^+(^2P) \leftarrow S(^3P)$ ionization, Figure 7.11. However, for all three ionizations data points are required to higher photon energy than the range covered in this work for a more detailed comparison between experiment and theory.

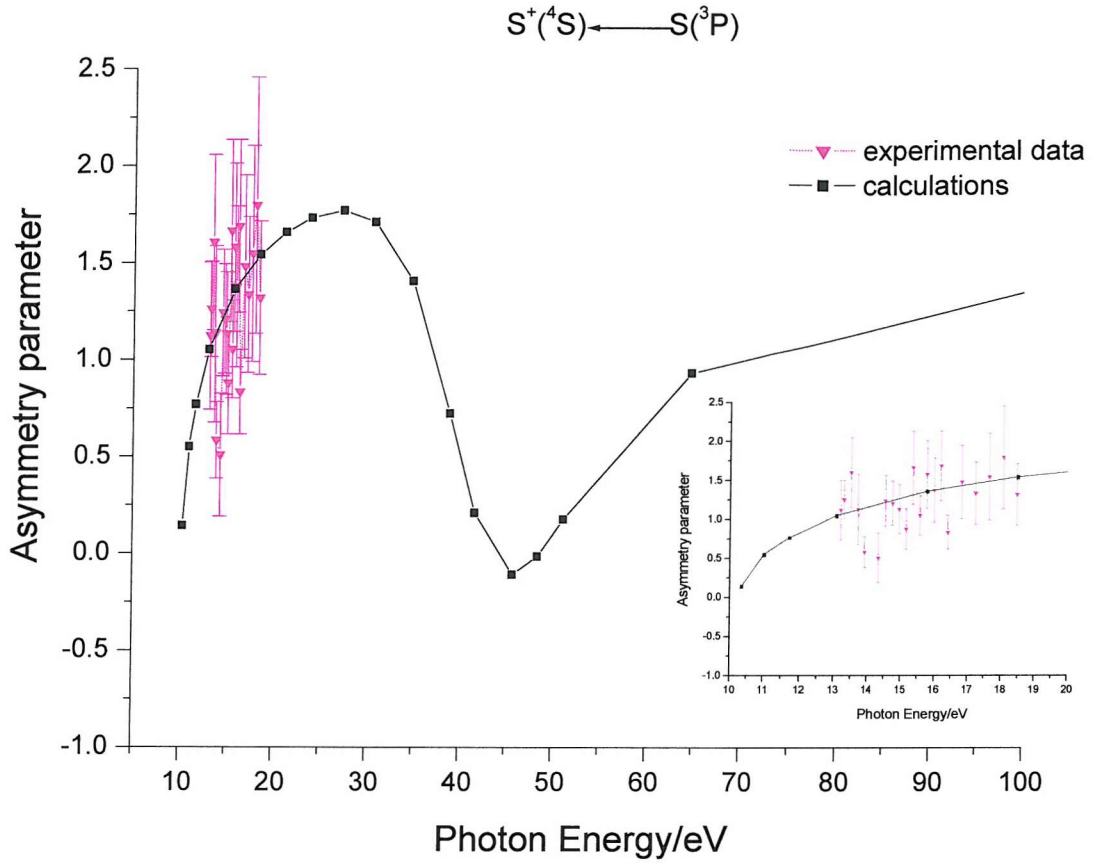

Figure 7.9 *Asymmetry parameters for S atoms plotted as a function of photon energy and compared with the results of Dill et al.*[7]*, for the first S atom band* $S^+(^4S) \leftarrow S(^3P)$.

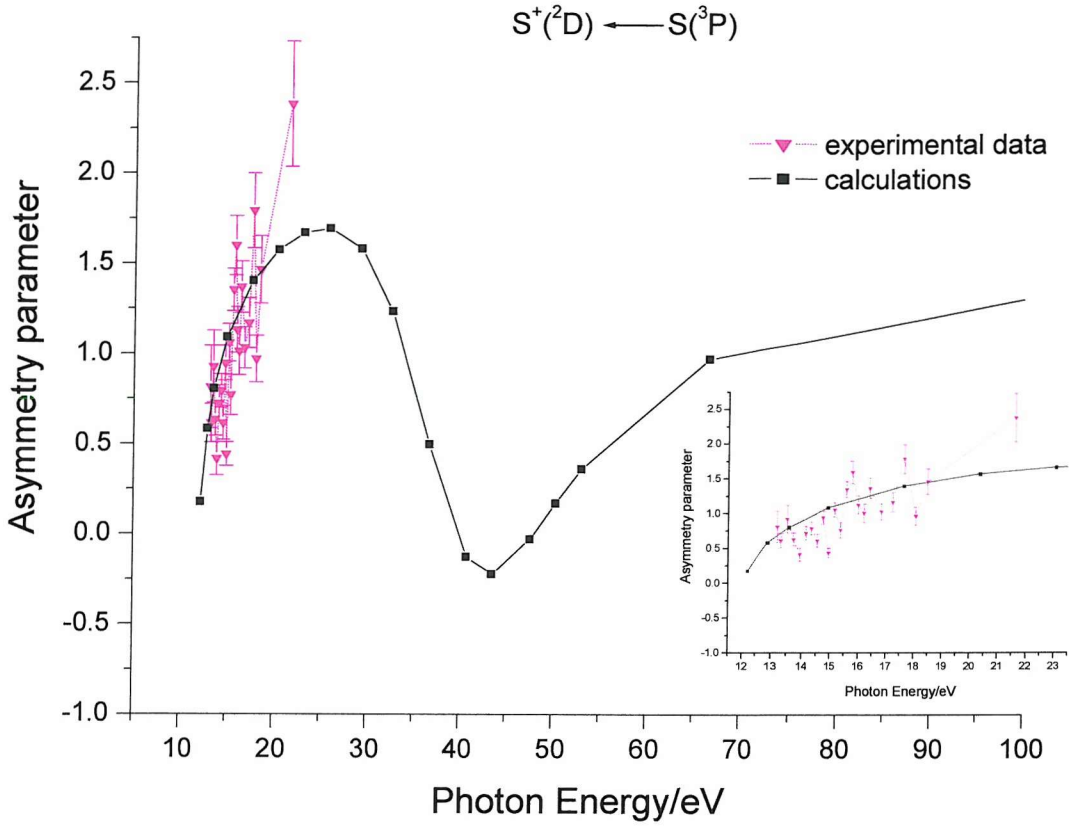

Figure 7.10 *Asymmetry parameters for S atoms plotted as a function of photon energy and compared with the results of Dill et al.*[7]*, for the second S atom band* $S^+(^2D) \leftarrow S(^3P)$.

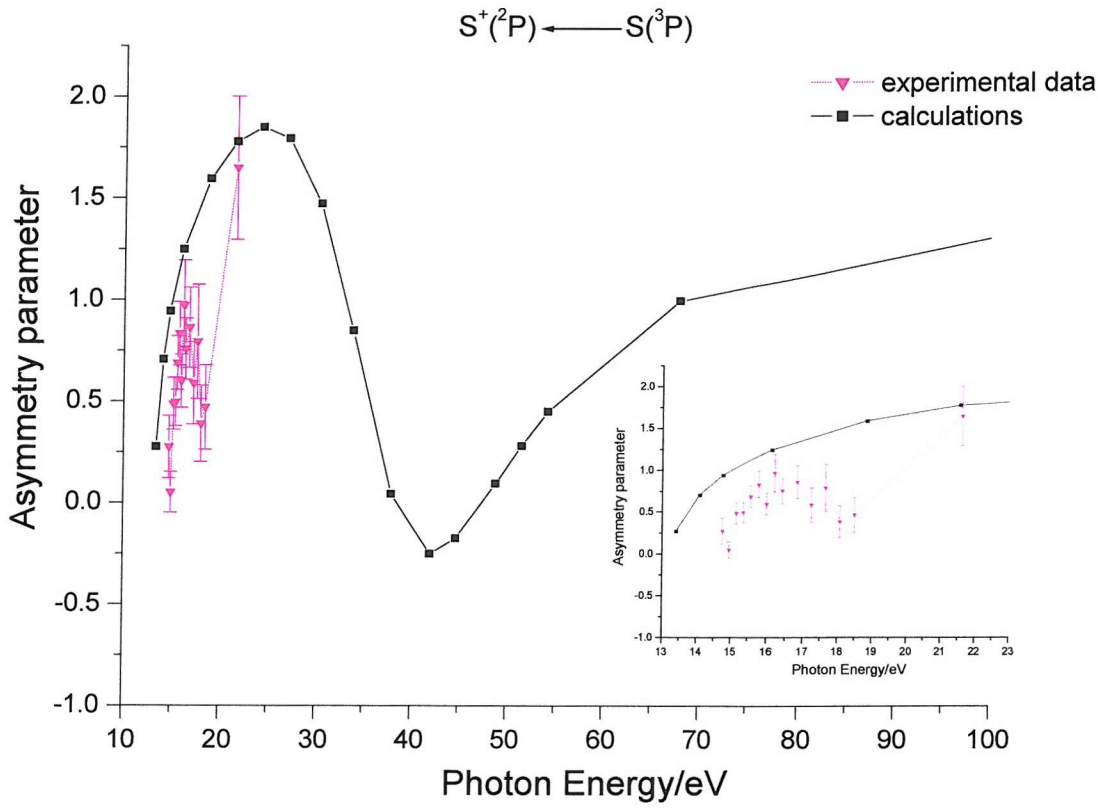

Figure 7.11 *Asymmetry parameters for S atoms plotted as a function of photon energy and compared with the results of Dill et al.*[7] *for the third S atom band* $S^+(^2P) \leftarrow S(^3P)$.

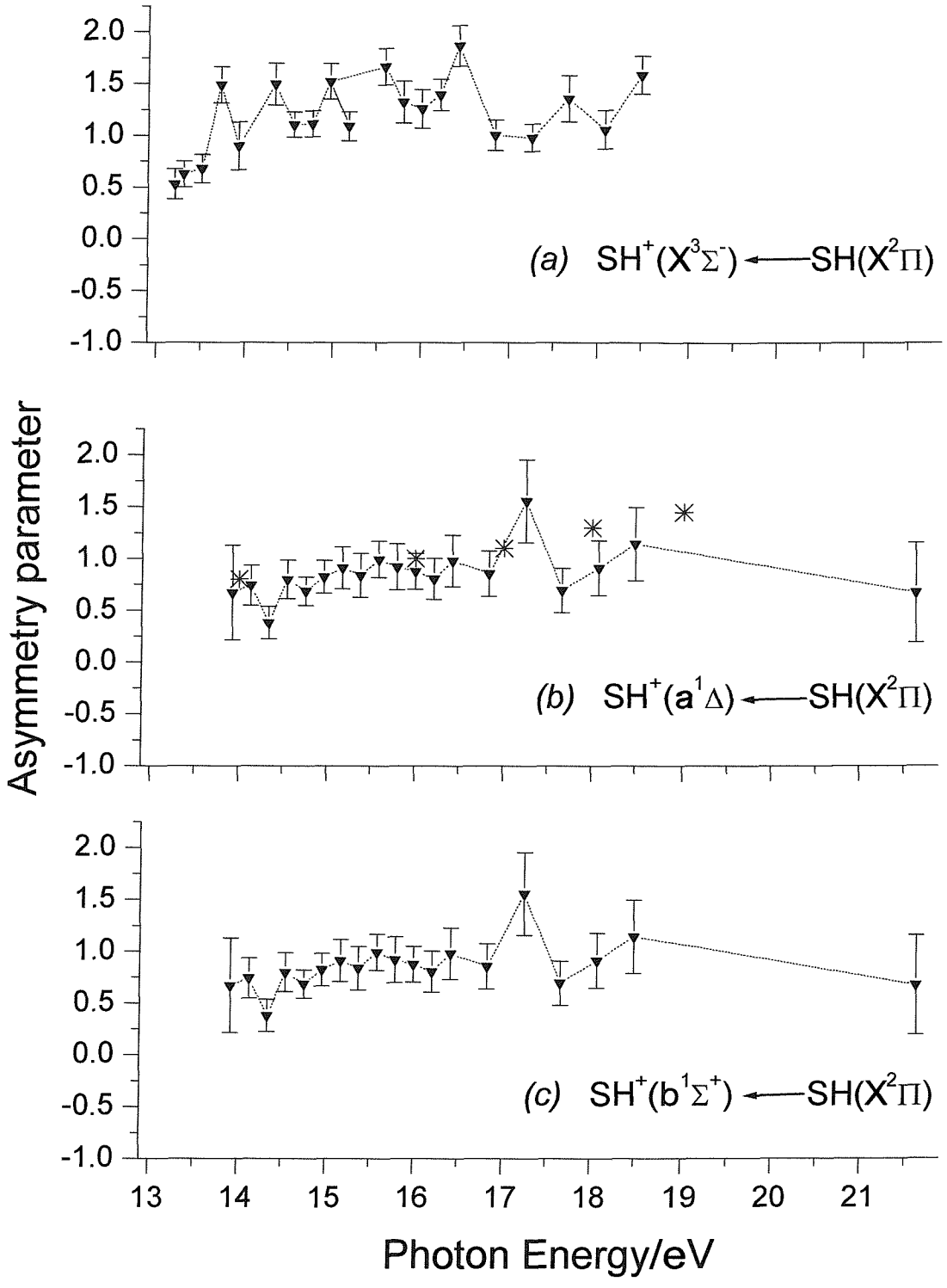

Figure 7.12 *Plots of the asymmetry parameter (β) as a function of photon energy over the range hν = 13.0 - 22.0 eV, for the first three photoelectron bands of SH.*
Plot (b) includes β values for the first band of H_2S measured at different photon energies in Ref. (35), denoted with the symbol (*).

Figure 7.12 shows similar β plots for the first three bands of SH, with Figure 7.12 *(b)* again showing the available data for the first band of H_2S from reference (35). No previous measurements or calculations of the β parameter as a function of photon energy have been made for SH. However, as with the S atom data, more data points are required notably at higher photon energy. Also, it should be borne in mind that, as stated earlier, the first band of SH contains a small contribution from H_2S and this will contribute to Figure 7.12 *(a)*.

In Figures 7.13 and 7.14 the relative photoionization cross sections for the second S atom band and for the first three S atom bands are plotted as a function of photon energy in the energy region 13.2 - 13.8 eV and 13.0 - 21.5 eV respectively.

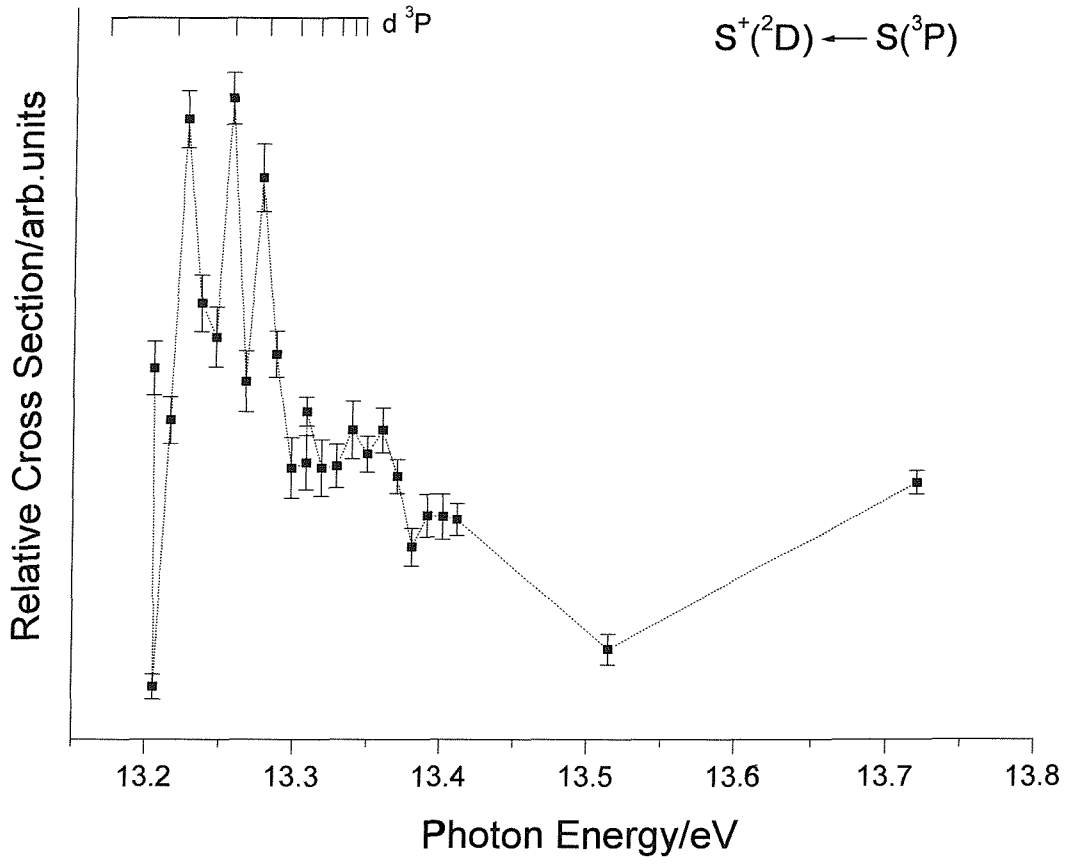

Figure 7.13 *Relative cross sections for the $S^+(^2D) \leftarrow S(^3P)$ band in the photon energy region 13.205 - 13.800 eV.*
The resonances present in the region 13.20 - 13.75 eV have been assigned to excitations to $[3s^2 3p^3(^2P)\, nd]^3P$ Rydberg states which are part of a series which converges to the third ionization limit at 13.400 eV.

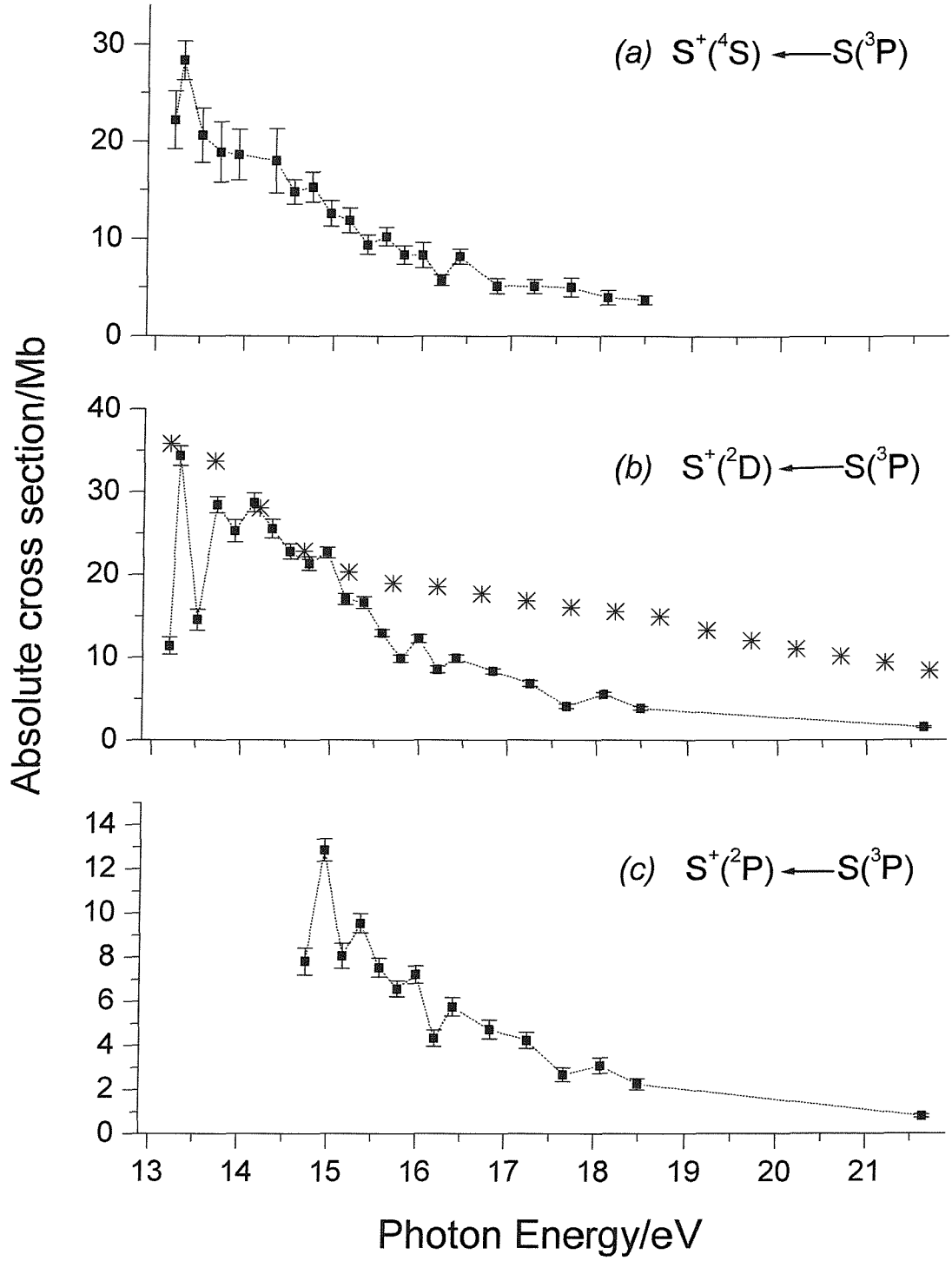

Figure 7.14 *Absolute photoionization cross sections for the first three bands of S atoms in the photon energy region 13.0 - 21.5 eV.*
In plot (a) the maximum observed at 13.30 eV corresponds to excitation to unresolved [$3s^2 3p^3 (^2P)$ nd]^3P Rydberg states.
Plot (b) includes σ values for the first band of H_2S measured at different photon energies in Ref. (40), denoted with the symbol (*).

In Figure 7.13, the relative cross section of the second S atom band, the $S^+(^2D) \leftarrow S(^3P)$ ionization, is plotted as function of the photon energy in the interval 13.20 - 13.80 eV. As can be seen, this plot shows clear structure in the region 13.205 - 13.350 eV. The observed maxima can be assigned to excitation to ^3P Rydberg states derived from $3s^23p^3$ *n*d configurations accessed from the $3s^23p^4\ ^3P$ ground state. These Rydberg states are parts of a series which converges to the third ionization limit at 13.400 eV[12,13].

To estimate the behaviour of the absolute photoionization cross section for the three ionic states of sulphur, the integrated area of each band was estimated at a photon energy of 16.7 eV, an energy at which the total photoionization cross section has been calculated by Yeh *et al.*[9] as 18.2 Mb, using Hartree-Fock-Slater calculations. While for the second and third bands, corresponding to the $S^+(^2D) \leftarrow S(^3P)$ and the $S^+(^2P) \leftarrow S(^3P)$ ionizations, the integrated areas could be easily measured, for the first S atom band, the $S^+(^4S) \leftarrow S(^3P)$ ionization, that strongly overlaps with the first band of SH, the result of the double-Gaussian deconvolution shown in Figure 7.4 was used. The contribution of the first H_2S band at 10.48 eV is included with the first band of SH in the second Gaussian band and it does not affect the calculated intensity of the first S band, which corresponds to the first fitted band.

As a result, the intensity ratios of the first three bands of S atoms, were measured at an angle of 54° 44′, as $(6.2 \pm 1.0):10:(5.7 \pm 0.5)$ at 16.7 eV. The relatively high experimental uncertainty of the first band relative intensity is due to overlap of the first S atom band with the first bands of SH and H_2S, as stated earlier. In order to estimate the absolute cross sections for these ionizations at 16.7 eV, the total areas of these bands were normalized to the total cross section of the $(3p)^{-1}$ ionization of 18.2 Mb, calculated by Yeh *et al.*[9].

Once this had been done, the experimental results could be used to estimate the photoionization cross section at 13.8 eV, an energy at which the total photoionization cross section has been determined in an experimental study of the absorption spectrum of S atoms. In this investigation, Tondello[10] determined the photoionization cross section over the energy region investigated, 10.3 to 13.8 eV. In the photon energy region 12.8 to 13.8 eV, which overlaps with the photon energy

region investigated in the present work, the photoionization cross section decreases regularly from 90 to 79 Mb. At 13.8 eV, values for the photoionization cross sections of the first two bands of atomic S could be obtained from the plots made in the present study, whereas the photoionization cross section for the third band was obtained by extrapolation of the plot shown in Figure 7.14 *(c)* to lower energy. This gave estimates of the photoionization cross section for the first three bands of S atoms at 13.8 eV, which when summed gave a total photoionization cross section of 58 Mb, which can be compared with the photoionization cross section value determined in Tondello's work of 79 Mb[10]. Given the approximations involved, most notably that the total photoionization cross section in the present work has been referenced to the photoionization cross section calculated at 16.7 eV by Hartree-Fock-Slater calculations[9], it is not surprising that only moderate agreement is obtained. Nevertheless, this comparison indicates there is a clear need for a direct measurement of the photoionization cross section of atomic sulphur in the vacuum ultraviolet region, most notably above the third ionization energy of 13.4 eV i.e. at photon energies which include all three ionic states arising from the $(3p)^{-1}$ ionization.

The general behaviour of the photoionization cross sections for the first three ionizations of sulphur atoms are shown in Figure 7.14. In Figure 7.14 *(a)* the relative photoionization cross section of the first S atom band is plotted as a function of the photon energy in the interval 13.205 - 18.494 eV. In this figure the maximum at 13.30 eV corresponds to excitation to the $[3s^23p^3\ (^2P)\ nd]\ ^3P$ Rydberg states seen in Figure 7.13, recorded with a smaller photon energy increment.

In Figure 7.14 it can be seen that except for the resonance at 13.30 eV, already assigned to excitation to $[3s^23p^3\ (^2P)\ nd]\ ^3P$ Rydberg states, at least two other small maxima are seen at 14.96 eV and 15.37 eV. These probably correspond to excitation to $[3s^13p^4\ (^4P)\ np]\ ^3D/\ ^3P/\ ^3S$ or $[3s^13p^4\ (^2P)\ np]\ ^3D/\ ^3P/\ ^3S$ states accessed from the $3s^23p^4\ (^3P)$ state. However, because of the stepwidth used to record these spectra (0.20 eV) and the limited number of data points, assignment of these features will only be achieved when spectra of the type shown in Figures 7.13 and 7.14 are recorded over a wider photon energy range and with a smaller stepwidth.

Figures 7.15 and 7.16 show plots of relative photoionization cross sections for the first three bands of SH. They show similar overall behaviour to that observed for the

equivalent plots for S atoms (Figure 7.14) and H_2S[35], but, as with the S atom plots, need to be recorded over a wider photon energy range with a smaller stepwidth. Figures 7.14 *(b)* and 7.16 *(b)* also include the experimental photoionization cross section for the first band of H_2S as a function of photon energy, taken from Feng *et al.*[40], for comparison.

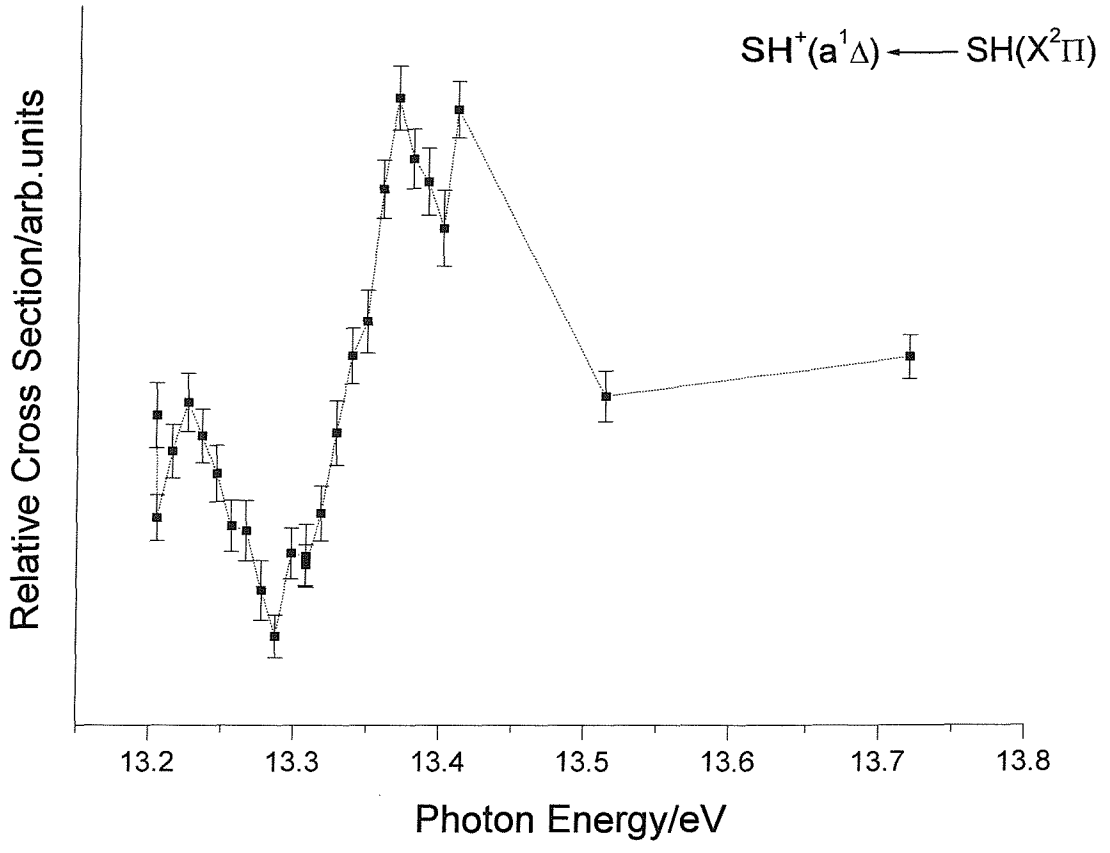

Figure 7.15 *Relative photon ionization cross sections for SH plotted as a function of photon energy for the second band of SH in the photon energy region 13.2 - 13.8 eV.*

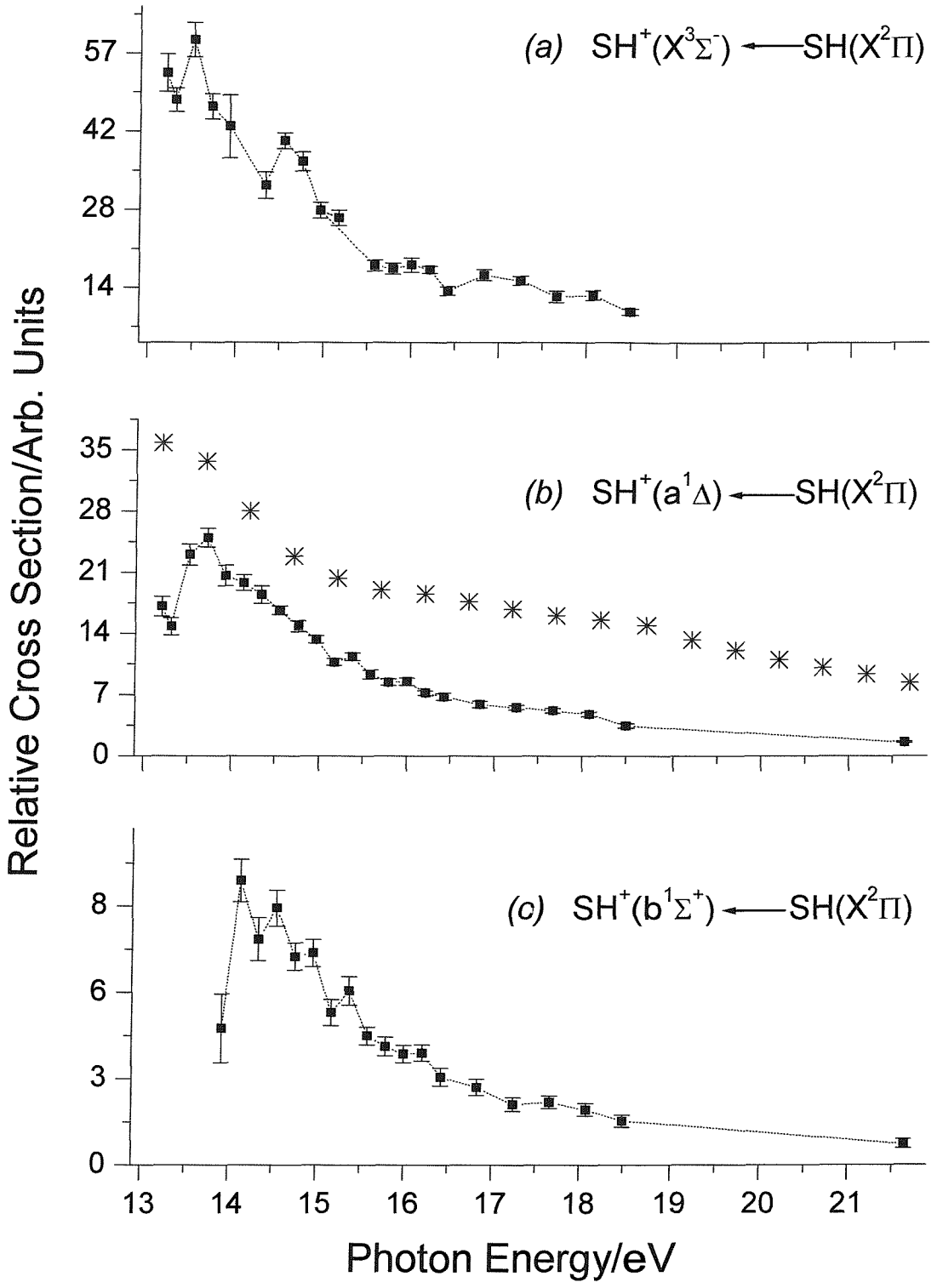

Figure 7.16 *Relative photon ionization cross sections for SH plotted as a function of photon energy for the first three bands of SH in the photon energy region 13.0 - 21.5 eV.*
Plot (b) includes σ values for the first band of H_2S measured at different photon energies in Ref. (40), denoted with the symbol (*).

7.3 Conclusion

This initial study of S and SH has shown that PES studies on short lived species of this type are possible using Synchrotron Radiation, and angular distribution and relative cross section measurements can be made. For SH, the results obtained are new and no calculations of σ or β as a function of photon energy are available with which the results obtained can be compared. For S atoms no previous measurements of this type have been made but, calculations are available of σ and β as a function of photon energy[6-8]; however the measurements need to be extended over a wider photon energy range and should be recorded with a smaller stepwidth to allow a more detailed comparison to be made. Results of these experiments are presented in the next chapter, Chapter 8.

References

[1] G. G. Lombardi, B. L. Cardon and R. L. Kurucz
Astrophysical Journal **248**, 1208 (1981).

[2] J. E. Vernazza, E. H. Averett and R. Loeset
Astrophysical Journal Supplement **45**, 635 (1981).

[3] M. L. Meeks, M. A. Gordon and M. M. Litvak
Science **163**, 173 (1969).

[4] K. Sinha
Proceedings of the Astronomical Society of Australia **9**, 32 (1991).

[5] S. J. Dunlavey, J. M. Dyke, N. K. Fayad, N. Jonathan and A. Morris
Molecular Physics **38**, 729 (1979).

[6] M. J. Conneelly, K. Smith and L. Lipsky
Journal of Physics B **3**, 493 (1970).

[7] D. Dill, A. F. Starace and S. T. Manson
Physical Review A **11**, 1596 (1975).

[8] S. T. Manson, A. Msezane, A. F. Starace and S. Shahabi
Physical Review A **20**, 1005 (1979).

[9] J. J. Yeh and I. Lindau
Atomic Data and Nuclear Data Tables **32**, 1 (1985).

[10] G. Tondello
Astrophysical Journal **172**, 771 (1972).

[11] V. N. Sarma and Y. N. Joshi
Physica **123 C**, 349 (1984).

[12] Y. N. Joshi, M. Mazzoni, A. Nencioni, W. H. Parkinson and A. Cantu
Journal of Physics B **20**, 1203 (1987).

[13] S. T. Gibson, J. P. Green, B. Ruscic and J. Berkowitz
Journal of Physics B **19**, 2825 (1986).

[14] G. W. vanLoon and S. J. Duffy *Enviromental Chemistry a global perspective*, University Press ed.Oxford, 2000.

[15] M. N. R. Ashfold, B. Tutcher and C. M. Western
Molecular Physics **66**, 981 (1989).

[16] G. Herzberg and K. P. Huber *Molecular Spectra and Molecular Structure*, D. VAN NOSTRAND COMPANY Inc. ed., 1966; Vol. IV.

[17] B. A. Morrow
Canadian Journal of Physics **44**, 2447 (1966).

[18] J. Brzozowski, N. Elander, P. Erman and M. Lyyra
Physica Scripta **10**, 241 (1974).

[19] P. E. Cade and W. M. Huo
Journal of Chemical Physics **47**, 649 (1967).

[20] M. Horani, J. Rostas and H. Lefebvre-Brion
Canadian Journal of Physics **45**, 3319 (1967).

[21] J. B. Milan, W. J. Buma and C. A. deLange
Journal of Chemical Physics **105**, 6688 (1996).

[22] C. W. Hsu, D. P. Baldwin, C. L. Liao and C. Y. Ng
Journal of Chemical Physics **100**, 8047 (1994).

[23] J. B. Milan, W. J. Buma and C. A. deLange
Journal of Chemical Physics **104**, 521 (1996).

[24] http://kinetics.nist.gov/index.php

[25] M. C. R. Cockett, J. M. Dyke and H. Zamanpour *Vacuum Ultraviolet Photoionization and Photodissociation of Molecules and Clusters*, edited by C.Y. Ng, World Scientific ed., 1991.

[26] J. B. West and G. V. Marr
Atomic Data and Nuclear Data Tables **18**, 497 (1976).

[27] A. Derossi, F. Lama, M. Piacentini, T. Prosperi and N. Zema
Review of Scientific Instrumentation **66**, 1718 (1995).

[28] D. Desiderio, S. DiFonzo, B. Diviacco, W. Jark, J. Krempasky, R. Krempaska, F. Lama, M. Luce, H. C. Mertins, M. Piacentini, T. Prosperi, S. Rinaldi, F. Schefers, F. Schmolla, G. Soulle, L. Stichauer, S. Turchini, R. P. Walker and N. Zema
Synchrotron Radiation News **12**, 34 (1999).

[29] W. F. Chan, G. Cooper, X. Guo, G. R. Burton and C. E. Brion
Physical Review A: Atomic, Molecular, and Optical Physics **46**, 149 (1992).

[30] http://physics.nist.gov/PhysRefData

[31] A. B. Cornford, D. C. Frost, C. A. McDowell, J. L. Ragle and I. A. Stenhouse
Journal of Chemical Physics **54**, 2651 (1971).

[32] P. M. Guyon, R. Spohr, W. A. Chupka and J. Berkowitz
Journal of Chemical Physics **65**, 1650 (1976).

[33] D. M. deLeeuw, R. Mooyman and C. A. deLange
Chemical Physics **34**, 287 (1978).

[34] C. E. Moore *Atomic Energy Levels*, U.S. Government Printing Office ed.Washington DC, 1952; Vol. 1.

[35] P. Baltzer, L. Karlsson, M. Lundqvist, B. Wannberg, D. M. P. Holland and M. A. MacDonald
Chemical Physics **195**, 403 (1995).

[36] M. Y. Adam, P. Morin, C. Cauletti and M. N. Piancastelli
Journal of Electron Spectroscopy and Related Phenomena **36**, 377 (1985).

[37] K. Watanabe and A. S. Jursa
Journal of Chemical Physics **41**, 1650 (1964).

[38] J. Cooper
Physical Review **128**, 681 (1962).

[39] J. Cooper and R. N. Zare *Lectures in Theoretical Physics*, edited by S. Geltman, K.T. Mahanthappa and W.E. Brittin ed.New York, 1967; Vol. XI-C.

[40] R. Feng, G. Cooper and C. E. Brion
Chemical Physics **249**, 223 (1999).

Chapter 8

8 FURTHER STUDY OF S ATOMS AND SH RADICALS BY PHOTOELECTRON SPECTROSCOPY

This Chapter reports a second study by photoelectron spectroscopy on S atoms and SH radicals using Synchrotron Radiation.

These results follow the previous investigation presented in Chapter 7. They have been obtained during a second beamtime at ELETTRA[1] and the constant ionic state (CIS) spectroscopy technique has been used to study S and SH. The results obtained are presented from Section 8.1

Because of the large number of plots presented in this Chapter, all the Figures have been grouped at the end of the Chapter.

8.1 Results and discussion

Photoelectron (PE) spectra were recorded in the constant pass energy mode, by scanning the voltage on a lens which accelerates (or decelerates) the photoelectrons before they enter the analyser, as explained in Chapter 4.2.1.

In this work, S atoms and the SH radicals were produced by the following consecutive reactions (see also Chapter 4.4.2 and Chapter 7.2):

$$F + H_2S \rightarrow SH + HF \qquad \text{Eq. 8-1}$$

$$F + HS \rightarrow S + HF \qquad \text{Eq. 8-2}$$

The room temperature rate constants for the above reactions are 1.33×10^{-10} and 2.01×10^{-10} $cm^3molecule^{-1}s^{-1}$ respectively[2]. To obtain a high F-atom yield, fluorine atoms were produced by flowing 5% F_2 in helium through a microwave discharge at 2.45 GHz in the side arm of a glass inlet system[3], with an inner inlet system which is the inlet used for the target molecules (in this case H_2S). The intensities of the bands in the experimental PE and CIS spectra were normalized by the photon flux and then by the transmission correction of the spectrometer as explained in Chapter 7.

The degree of linear polarization ($P = 1$) of the radiation was well established[4,5]. The asymmetry parameter (β) was measured for S and SH at selected photon energies and over a photon energy range, by recording CIS spectra at two different θ angles (0° and 54° 44') at each photon energy (at 54° 44' the measured intensity is proportional to the total photoionization cross section, independent of β); the β parameter was then calculated from:

$$\beta = (R - 1) \qquad \text{Eq. 8-3}$$

where $R = I_0 / I_{54°44'}$ is the ratio of the experimental intensities at these two angles, after applying the above corrections.

The photon energy was calibrated in the 11.5 - 29.0 eV region against the energies of the Ar $3s3p^6(^2S_{1/2})np \leftarrow 3s^23p^6(^1S_0)$ resonances[6] and He $1s^1np \leftarrow 1s^2$ absorption lines[7]. The Ar resonances were obtained recording CIS spectra of the first band (first component) of the $(3p^{-1})$ ionization of Argon in the photon energy region

26.0 - 29.0 eV. The absorption spectra of He were recorded measuring the current on the aluminium plate at the back of the spectrometer in the photon energy ranges 21.0 - 24.0 eV using first order radiation and 11.5 - 12.3 eV using second order radiation.

Test experiments were carried out in Southampton in order to determine the optimum pressures and mixing distance above the photon beam to be used in the experiments at ELETTRA which maximise the intensities of the second and third photoelectron bands of SH at 11.64 eV and 12.76 eV AIE respectively, corresponding to the ionizations $SH^+(a^1\Delta, v^+=0) \leftarrow SH(X^2\Pi, v''=0)$ and $SH^+(b^1\Sigma^+, v^+=0) \leftarrow SH(X^2\Pi, v''=0)$, and the second and third ionizations of S at 12.21 eV and 13.40 eV IE respectively, corresponding to the ionizations $S^+(^2D) \leftarrow S(^3P)$ and $S^+(^2P) \leftarrow S(^3P)$[8]. The following conditions were found to be the optimum for production of both S and SH: a mixing distance above the photon beam of 2 cm, with the inner-inlet system used for H_2S longer than the outer inlet system by about 2 mm, and the partial pressures measured on an ionization gauge positioned on the wall of the ionization chamber of $\Delta p(H_2S) = 2.4\times10^{-7}$ mbar and $\Delta p(F_2/He) = 4.6\times10^{-6}$ mbar.

8.1.1 CIS spectroscopy studies

During this beamtime, better experimental conditions allowed studies to be performed on S and SH over wider photon energy. This was because new software was written to allow PES and CIS spectra to be acquired and the experimental resolution was better, which allowed the first bands of S and SH to be resolved. In Figure 8.1, PE spectra recorded at ELETTRA of the products of the F + H_2S reaction at a photon energy of $h\nu = 21.26$ eV and at two different angles with respect to the polarization axis of the photon source ($\theta = 0°$ and $\theta = 54°\ 44'$) are shown with the assignment of the major features indicated. These spectra show sharp bands at 11.64 and 12.76 eV, which are the second and third bands of SH, and sharp bands at 12.21 and 13.40 eV which are the second and third bands of S atoms. Also, observed is the first bands of O atoms (13.62 eV[9]) and H_2O (12.62 eV[9]). The H_2O arises from

residual water in the inlet system and O atoms probably arise from reaction of F atoms with H_2O. Compared with Figure 7.2, in Figure 8.1 the bands at ≈ 10.5 eV arising from the first bands of S and SH/H_2S could be resolved. As can be seen in the expanded plot of the 10.0 - 11.0 eV IE region in Figure 8.2, the first band of S atoms at 10.35 eV is resolved from the first band of SH at 10.42 eV, and the small contribution from the first band of residual H_2S at 10.48 eV[8].

The vibrationally resolved band of SH at 14.11 eV AIE is the fourth band of SH, the $SH^+(A^3\Pi) \leftarrow SH(X^2\Pi)$ ionization.

CIS spectra, recorded as described in Chapter 4.2.2, could be successfully recorded for the $S^+(^4S) \leftarrow S(^3P)$ ionization at 10.35 eV, for the $S^+(^2D) \leftarrow S(^3P)$ ionization at 12.21 eV and for the $S^+(^2P) \leftarrow S(^3P)$ ionization at 13.40 eV. All spectra were recorded at two angles, $\theta = 0°$ and $\theta = 54° 44'$, with respect to the polarization axis of the photon source and with a 1 meV/channel stepwidth. In Figures 8.3 - 8.16 the CIS spectra for the $S^+(^4S) \leftarrow S(^3P)$, $S^+(^2D) \leftarrow S(^3P)$ and $S^+(^2P) \leftarrow S(^3P)$ ionizations are shown. Figure 8.3 shows the $S^+(^4S) \leftarrow S(^3P)$ CIS spectrum in the photon energy region 11.5 - 30.0 eV, Figure 8.10 shows the $S^+(^2D) \leftarrow S(^3P)$ CIS spectrum in the photon energy region 13.5 - 30.5 eV and Figure 8.14 shows the $S^+(^2P) \leftarrow S(^3P)$ CIS spectrum in the photon energy region 14.5-30.5 eV. These spectra were recorded at $\theta = 54° 44'$ (at this angle the measured intensity is proportional to the total photoionization cross section, independent of the asymmetry parameter).

To estimate the behaviour of the absolute cross sections for the three ionic states of sulphur, the relative cross sections off resonance for the atomic sulphur CIS bands were estimated at a photon energy of 14.76 eV, an energy at which the total photoionization cross section has been obtained by extrapolation of Tondello's absolute measurements[10] as 82 Mb, based on the linewidths of Tondello's lines and the absorption oscillator strength measured in emission by Muller[11].

In order to estimate the absolute cross section for these ionizations at 14.76 eV, the sum of the relative cross sections of these bands were normalized to the total cross section of 82 Mb, determined by Tondello[10].

Once this had been done, the experimental results could be used to estimates of the photoionization cross section for the first three bands of S atoms at 16.7 eV, which

when summed gave a total photoionization cross section of 68.7 Mb, which can be compared with the total photoionization cross section calculated by Yeh *et al.*[12] as 18.2 Mb, using Hartree-Fock-Slater calculations.

Bearing in mind that values of absolute cross sections can be obtained only if all the parameters are measured simultaneously, or consecutively in the same experiment and under experimental conditions, values of "absolute cross sections" using data extrapolations from other work, both experimental and theoretical, can be used only as a relative indication. Therefore, given the approximations involved, most notably that the total photoionization cross section in the present work has been referenced to the extrapolated photoionization cross section at 14.76 eV determined by Tondello's measurements[10], it is not surprising that an unsatisfactory agreement is obtained with the computed value of Yeh *et al.*[12]. Nevertheless, this comparison indicates there is a clear need for a direct measurement of the absolute photoionization cross section of atomic sulphur in the vacuum ultraviolet region.

The results of the above relative-absolute normalization obtained from Tondello results[10] have been applied in Figures 8.3 - 8.16. In this Chapter this normalization has been preferred over the one carried out in Chapter 7 using the value by Yeh *et al.*[12] from Hartree-Fock-Slater calculations, because it is obtained from experimental measurements.

The $S^+(^4S) \leftarrow S^* \leftarrow S(^3P)$ and $S^+(^2D) \leftarrow S^* \leftarrow S(^3P)$ CIS spectra in the photon energy region 11.60 - 13.45 eV with the second and third ionization limits marked in, are shown in Figures 8.4 - 8.6 and 8.11, recorded at $\theta = 54° 44'$.

The bands observed in these Figures can be readily assigned to known $S^* \leftarrow S(^3P)$ transitions by comparison with known S^* term values[10,13,14]. The energy positions of the resonances have been fitted using the Rydberg formula and good agreement has been found with the results of previous studies of Joshi *et al.*[13] and Gibson *et al.*[14]. Examples of the results obtained for the $n = 7$ ns' ^3D, nd' ^3D and nd' ^3S Rydberg states by these fits have been summarized in Table 8-1 using the band maxima shown, where they are compared with the results obtained by Joshi *et al.*[13] and Gibson *et al.*[14] for the Rydberg series which converges to the second ionization limit shown in Figure 8.4.

Inspection of the CIS spectrum recorded for the first PE band of S atoms shows that in the photon energy region 11.60 - 12.20 eV, all the bands can be assigned to excitation to Rydberg states which are members of series which converge to the second ionization energy, apart from a couple of bands associated with Rydberg states which are part of series converging to the third ionization energy, see Figure 8.5. On expanding a section of the first band CIS spectrum for the photon energy range 12.30 - 13.42 eV (see Figure 8.6), the structures observed in Figure 8.5 in the region 12.205 - 13.350 eV were investigated and assigned to the $[3s^2 3p^3 (^2P) ns]\ ^3P$, $[3s^2 3p^3 (^2P) nd]\ ^3P$ and $[3s^2 3p^3 (^2P) nd]\ ^3D$ Rydberg series accessed from the $3s^2 3p^4\ ^3P$ ground state. These Rydberg states are parts of series which converge to the third ionization limit at 13.400 eV[13,14].

Table 8-1 *Examples for n = 7 ns' ^3D, nd' ^3D and nd' ^3S Rydberg states which are parts of a Rydberg series converging to the second ionization limit listing the fitted quantum defects and fitted ionization limits obtained in this work compared with the results of ref. (13, 14).*
The weighted average of the $^2D_{3/2}$ and $^2D_{5/2}$ limits has been used in ref. (13, 14) to calculate the quantum defects.

		Present work		Results of ref. (13, 14)	
Excitation energy/eV	Rydberg series	Quantum defect δ	Ionization limit IE/eV	Quantum defect δ	Ionization limit IE/eV
11.907	nd' ^3D	0.313	12.204	0.272	12.204
11.633	ns' ^3D	2.134	12.204	2.118	12.204
11.929	nd' ^3S	0.039	12.204	-0.030	12.204

Figures 8.6 and 8.11 show CIS spectra of the first PE band and second PE band of S atoms recorded in the photon energy region 12.30 - 13.42 eV and 13.10 - 13.42 eV respectively. Resonances are observed which are consistent with excitations to Rydberg states which are part of series converging to the third ionization limit. The position and

assignment of these states has been established previously by Joshi *et al.*[13], using an absorption technique, and by Gibson *et al.*[14], using photoionization mass spectrometry. Examples of the results obtained for the $n = 9$ *n*d" ^{3}P and *n*d" ^{3}D Rydberg states by these fits have been summarized in Table 8-2 using the band maxima shown, where they are compared with the results obtained by Joshi *et al.*[13] and Gibson *et al.*[14] for the Rydberg series which converge to the third ionization limit shown in Figure 8.6.

Table 8-2 *Examples for $n = 9$ nd" ^3P and nd" ^3D Rydberg states which are parts of a Rydberg series converging to the third ionization limit listing the fitted quantum defects and fitted ionization limits obtained in this work compared with the results of ref. (13, 14).*
The weighted average of the $^2P_{1/2}$ and $^2P_{3/2}$ limits has been used in ref. (13, 14) to calculate the quantum defects.

		Present work		Results of ref. (13, 14)	
Excitation energy/eV	Rydberg series	Quantum defect δ	Ionization limit IE/eV	Quantum defect δ	Ionization limit IE/eV
13.226	*n*d" ^{3}P	0.296	13.441	0.264	13.404
13.229	*n*d" ^{3}D	0.340	13.410	0.194	13.404

Comparing Figure 7.13 with Figure 8.11, it can be seen that in the CIS scan several structures are present in the energy region 13.3 - 13.4 eV. These resonances could be easily misunderstood in the PES study as background noise due to the low count rate and big stepwidth while the CIS study confirms the presence of real structures converging to the third ionization limit.

The structure observed in Figure 7.14 *(c)* of the relative cross section for the $S^+(^2P) \leftarrow S(^3P)$ ionization in the 14.00 - 16.00 eV photon energy region have been investigated again to see if the small maxima presented (at 14.96 eV and 15.37 eV) are really part of excitation to $[3s^13p^4\ (^4P)\ np]\ ^3D/\ ^3P/\ ^3S$ or $[3s^13p^4\ (^2D)\ np]\ ^3D/\ ^3P/\ ^3S$ states accessed from the $3s^23p^4\ (^3P)$ state as proposed in the PE study. In Figure 8.14,

where the $S^+(^2P) \leftarrow S(^3P)$ CIS spectrum in the photon energy region 14.5 - 30.5 eV is presented, no consistent structures were observed in these positions. Also, no maxima were seen in CIS scans of the first and second bands at these photon energies (see Figures 8.7 and 8.10). Unfortunately the results of the CIS investigation of this region (14 - 16 eV) are less reliable than CIS results obtained in other regions due to several problems that occurred during the acquisition (*viz.* instability of the reaction followed by switch-off of the discharge caused by an electrical shutdown of the entire synchrotron facility due to a thunderstorm). However, in this region the cross section for the $S^+(^2P) \leftarrow S(^3P)$ ionization is increasing with increasing photon energy and an incorrect maximum could have been inferred from the previous PE study especially because the data points were taken with big stepwidth.

In Figures 8.8, 8.12 and 8.15, Rydberg series converging to the fourth ionization limit at 20.204 eV are presented. This is the first time that a Rydberg series converging to this limit has been observed.

Photoabsorption cross sections in regions of autoionization can be parameterized with a lineshape formula based on multichannel quantum defect theory (MQDT) analogous to Fano's resonance formula[15,16] as described in Chapter 2.2.4.

In this work, codes for fitting the experimental data to Eq. 2-25, 26 and 27 have been written using the program Mathematica.

In Figures 8.8, 8.12 and 8.15, the $S^+(^4S) \leftarrow S^* \leftarrow (^3P)$, $S^+(^2D) \leftarrow S^* \leftarrow (^3P)$ and $S^+(^2P) \leftarrow S^* \leftarrow (^3P)$ CIS spectra are shown. Ejection of a 3s electron from the ground state of atomic sulphur gives rise to $3s3p^4$ (^4P), $3s3p^4$ (^2D), $3s3p^4$ (^2S) ionic states at ionization energies of 20.204 eV, 22.497 eV and 25.211 eV, respectively[17]. The $S^+(^2D)$ and $S^+(^2P)$ states are expected to be less intense than the $S^+(^4S)$ state because they are not one-electron process; one electron is removed from 3s subshell and the electrons in the 3p subshell are reorganized.

In order to attempt to assign the bands in Figures 8.8, 8.12 and 8.15, it is helpful to determine the energy levels to which transitions are allowed from the ground state $3s^23p^4\ ^3P$. The upper level can be restricted to triplet terms, since the spin selection rule[18,19], $\Delta S = 0$, should be strictly obeyed for a light atom such as sulphur. The most

likely transitions will be those with $\Delta l = \pm 1$, or $p \leftarrow s$ in this case[18,19]. The terms involved may be considered to be the result of adding a p electron to the term of S^+ resulting from the electronic configuration $3s3p^4$.

The lowest $S^+(3s^13p^4)$ core state is ^4P, and the resulting terms are obtained by combining the angular momentum of the p electron with the core-state angular momentum. From these term symbols the selection rule[18,19] $\Delta L = 0, \pm 1$ reduces the possible transitions to the allowed states given in Table 8-3.

Table 8-3 *Energy levels to which transitions are allowed from the ground state $3s^23p^4\ ^3P$ assuming Russell-Saunders coupling is valid. Transition (a) requires a configuration where εp is the free electron, which is not allowed from parity rules.*

Excited State	Ionic State after Autoionization
$[3s3p^4(^4P)\ np]\ ^3D$	$S^+(^4S)$, εd
$[3s3p^4(^4P)\ np]\ ^3P$	(a)
$[3s3p^4(^4P)\ np]\ ^3S$	$S^+(^4S)$, εs
$[3s3p^4(^4P)\ np]\ ^3D$	$S^+(^2D)$, εs; $S^+(^2D)$, εd
$[3s3p^4(^4P)\ np]\ ^3P$	$S^+(^2D)$, εd
$[3s3p^4(^4P)\ np]\ ^3S$	$S^+(^2D)$, εd
$[3s3p^4(^4P)\ np]\ ^3D$	$S^+(^2P)$, εd
$[3s3p^4(^4P)\ np]\ ^3P$	$S^+(^2P)$, εs; $S^+(^2P)$, εd
$[3s3p^4(^4P)\ np]\ ^3S$	(a)

The ^4P core state of S^+ is spin-orbit split into three states $^4P_{5/2}$, $^4P_{3/2}$ and $^4P_{1/2}$ at ionization energies from $S(^3P)$ of 20.204, 20.249 and 20.274 eV, respectively[17]. The ground state of S, ^3P, is spin-orbit split into three states as well, $^3P_{2,1,0}$. The energy differences between the $^3P_2$ ground state and $^3P_1$, and $^3P_2$ and $^3P_0$ are 49 meV and

71 meV respectively. The $^3P_2$ state will be the most populated at room temperature. Therefore it should be possible to observe nine series for the $S^+(^2D) \leftarrow S^* \leftarrow (^3P)$ process (i.e. 3 Rydberg series each converging to 3 ionic limits, ignoring the population of the $^3P_1$ and $^3P_0$ states which are expected to be small relative to $^3P_2$) and six series for the $S^+(^4S) \leftarrow S^* \leftarrow (^3P)$ and $S^+(^2P) \leftarrow S^* \leftarrow (^3P)$ processes (i.e. in each case two Rydberg series each converging to three ionic limits).

Several fits of the experimental data to Eq. 2-26 have been performed for the case of many open and closed channels, varying the number k of the closed channels.

The best results for all the three experimental spectra have been obtained fitting the data with a function with only two closed channels ($k = 2$). For $k = 1$ it is impossible to fit the spectra where there are clearly at least two Rydberg series. The fits with three Rydberg series ($k = 3$) gave the same two series obtained with $k = 2$ and physically unrealistic parameter values for the third series. In Figures 8.17 - 8.19 are shown the fits for the three CIS spectra shown in Figures 8.8, 8.12 and 8.15 and recorded at $\theta = 54° 44'$.

Figure 8.20 shows the experimental CIS spectra for the three different ionic channels and the resonance energies obtained by fitting them. These values are also reported in Table 8-4 for each final ionic state.

Table 8-4 *Energy resonance positions, expressed in eV, from the fits of the CIS spectra on the three different ionic states.*

n	4	5	6	7	∞
$S^+(^4S)$ *Series 1*	17.844 ± 0.006	19.053 ± 0.002	19.521 ± 0.001	19.753 ± 0.001	20.212
$S^+(^4S)$ *Series 2*	17.876 ± 0.011	19.064 ± 0.002	19.525 ± 0.001	19.755 ± 0.001	20.212
$S^+(^2D)$ *Series 1*	17.962 ± 0.011	19.077 ± 0.003	19.527 ± 0.001	19.753 ± 0.001	20.212
$S^+(^2D)$ *Series 2*	18.093 ± 0.034	19.122 ± 0.009	19.566 ± 0.004	19.793 ± 0.003	20.255
$S^+(^2P)$ *Series 1*	17.867 ± 0.008	19.058 ± 0.002	19.523 ± 0.001	19.753 ± 0.001	20.212
$S^+(^2P)$ *Series 2*	17.944 ± 0.011	19.077 ± 0.003	19.551 ± 0.002	19.789 ± 0.001	20.255

For the $S^+(^4S) \leftarrow S^* \leftarrow S(^3P)$ process, the fit showed that there are two series converging to the same limit at 20.212 eV while for the $S^+(^2D) \leftarrow S^* \leftarrow S(^3P)$ and $S^+(^2P) \leftarrow S^* \leftarrow S(^3P)$ processes the fits showed that there are two series converging to two different limits at 20.212 eV and 20.255 eV. These two limits are near to the energy values founded in literature for the ionization energies from $S(^3P_2)$ to the $S^+(^4P_{5/2})$ and $S^+(^4P_{3/2})$ states of 20.204 eV and 20.249 eV respectively[17].

According to Table 8-3, the $S^+(^4S) \leftarrow S^* \leftarrow S(^3P)$ CIS spectrum has a ^3S and a ^3D Rydberg series while the $S^+(^2P) \leftarrow S^* \leftarrow S(^3P)$ CIS spectrum has a ^3P and a ^3D Rydberg series.

Series 1 of the $S^+(^2P) \leftarrow S^* \leftarrow S(^3P)$ CIS spectrum has the resonance energies values which are similar to the values of both Rydberg series of the $S^+(^4S) \leftarrow S^* \leftarrow S(^3P)$ CIS spectrum and the same limit. This means that S*eries 1* of the $S^+(^2P) \leftarrow S^* \leftarrow S(^3P)$ CIS spectrum should be ^3D Rydberg series but it is not sure which of S*eries 1* and *2* of the $S^+(^4S) \leftarrow S^* \leftarrow S(^3P)$ CIS spectrum is the ^3D Rydberg series; once this assignment is made the other series is a ^3S Rydberg series.

Series 1 of the $S^+(^2D) \leftarrow S^* \leftarrow S(^3P)$ CIS spectrum should be a ^3P Rydberg series converging to the $^4P_{5/2}$ limit since the ^3S and a ^3D Rydberg series have already been assigned at different resonance energies.

Series 2 of the $S^+(^2D) \leftarrow S^* \leftarrow S(^3P)$ CIS spectrum converges to the $^4P_{3/2}$ limit at 20.255 eV and it could be a ^3S, ^3P and ^3D Rydberg series. If it is a ^3P Rydberg series, the resonance energy difference between the two $n = 4$ ^3P Rydberg states converging to the $^4P_{5/2}$ and $^4P_{3/2}$ limits is about 130 meV. If it is a ^3S or a ^3D Rydberg series, the resonance energy differences between the two $n = 4$ ^3S or ^3D Rydberg states converging to the $^4P_{5/2}$ and $^4P_{3/2}$ limits are 217 and 249 meV (i.e. the differences in Table 8.4 between $S^+(^2D)$ *Series 2* and $S^+(^4S)$ S*eries 2* and *1*, respectively).

Series 2 of the $S^+(^2P) \leftarrow S^* \leftarrow S(^3P)$ CIS spectrum converges to the $^4P_{3/2}$ limit at 20.255 eV and it could be a ^3P and ^3D Rydberg series. If it is ^3P series, its energy position for $n = 4$ would be higher than the corresponding ^3P resonance converging to the $^4P_{5/2}$ limit, which is not the case. It is therefore possible to identify this series as a ^3D Rydberg series. At $n = 4$, the resonance energy difference between the two ^3D Rydberg states converging to the $^4P_{5/2}$ and $^4P_{3/2}$ limits is about 80 meV. It is likely

then that *Series 2* of the $S^+(^2D) \leftarrow S^* \leftarrow S(^3P)$ CIS spectrum is a ^3P Rydberg series since at $n = 4$ the resonance energy difference between the two ^3P Rydberg series, converging to the $^4P_{5/2}$ and $^4P_{3/2}$ limits, is 130 meV.

In this way, the only series that are not unequivocally identified are the two in the $S^+(^4S) \leftarrow S^* \leftarrow S(^3P)$ CIS spectrum. In order to obtain more information, a study of the asymmetry parameter has been performed (see later in this Chapter).

As was done in the previous PES study of Chapter 7.2.1, at each photon energy, the asymmetry parameter can be calculated for an S band using Eq. 8-3 . Comparisons of the measured asymmetry parameters as a function of photon energy for the three ionization channels resulting from the $(3p)^{-1}$ photoionization of S derived from this work with results of the angular distribution Hartree-Fock calculations of Dill *et al.*[20] have been made over the photon energy range 10 - 30 eV. This has been carried out to give the plots shown in Figures 8.21 to 8.24.

Figure 8.21 the three different angular distribution plots are shown as a function of photon energy and comparisons with the results of Dill *et al.*[20] are presented in Figures 8.22 - 8.24.

As can be seen in Figures 8.22 - 8.24, the experimental results obtained in this work are in reasonable agreement with the results of the calculations[20] for all three ionization channels. However, the high resolution obtained with the ELETTRA synchrotron and the abundance of resonances resolved make a comparison difficult. Indeed, the calculations made by Dill *et al.*[20] were intended to provide a theoretical framework that allows angular distribution calculations comparable to calculations of total photoionization cross sections, without taking into account resonances in the β-results.

Figures 8.25 to 8.27 show the measured asymmetry parameters as a function of photon energy over the photon energy range 16.5 - 20.5 eV for the three ionization channels resulting from the $(3p)^{-1}$ photoionization of S.

Fits of the experimental spectra recorded at $\theta = 0°$ to Eq. 2-26 have been performed as well. It was then possible to calculate the asymmetry parameters for each ionization channel from the two fitted spectra at $\theta = 0°$ and $\theta = 54° 44'$. The asymmetry

parameters evaluated in this way as a function of the photon energy are shown in Figures 8.28 - 8.30.

The agreement between the experimental and calculated asymmetry parameters is good although at higher n resonances there are more spikes in the calculated spectra. This is principally due to a small misalignment of the resonance positions between the fitted spectra at $\theta = 0°$ and $\theta = 54° 44'$. A small misalignment of 0.5 meV becomes important at higher n where the width of the resonances is small and gives a spike effect. This effect is increased by the fact that the fits are performed without deconvoluting the data with the instrumental resolution[21]. A fit without instrumental deconvolution may become unreliable for an atomic transition involving narrow resonances[22].

Nevertheless, a qualitative agreement for $n = 4$, 5 and 6 is good for the purpose of this work.

The behaviour of the total asymmetry parameters as a function of photon energy in Figures 8.28 - 8.30 cannot help the assignment of the Rydberg series. More information could be obtained from the asymmetry parameter plot of each Rydberg series. To calculate them, the parameters of the fits at $\theta = 0°$ and $\theta = 54° 44'$ are separated for the two series of each ionization process.

The asymmetry parameters so obtained are plotted in Figures 8.31 to 8.36.

The asymmetry parameters of the two series in each of the two $S^+(^2D) \leftarrow S^* \leftarrow S(^3P)$ and $S^+(^2P) \leftarrow S^* \leftarrow S(^3P)$ CIS spectra have very similar behaviour in proximity of the resonances as can be observed in Figures 8.33 - 8.36. Crossing a resonance, the asymmetry parameter firstly increases its value then decreases to its value out of resonance. According to these observations and Table 8-3, the free electron of all the four series has a pure d character; therefore similar behaviour of all the four asymmetry parameters is expected.

The asymmetry parameter of the Rydberg *Series 2* of the $S^+(^4S) \leftarrow S^* \leftarrow S(^3P)$ CIS spectrum has a behaviour similar to the four series previously analysed. This means the free electron should have a d character. This property, as can be seen in Table 8-3, is satisfied by the ^3D Rydberg series. By elimination, the Rydberg *Series 1* of the $S^+(^4S) \leftarrow S^* \leftarrow S(^3P)$ CIS spectrum is a ^3S Rydberg series with a s

wavefunction free electron. Indeed, Figure 8.31 shows the asymmetry parameter decreasing and then increasing while crossing a resonance.

Table 8-5 shows the six Rydberg series observed with the assignments made in this work.

Table 8-5 *Summary of the assignment made for the six Rydberg series observed.*

Final CIS Ionic State	Fitted Limit	Ionic Limit	Excited State	Free Electron
$(3s^2 3p^3)$ $S^+(^4S)$ *Series 1*	20.212 eV	$^4P_{5/2}$	$[3s3p^4(^4P)\ np]\ ^3S$	εs
$(3s^2 3p^3)$ $S^+(^4S)$ *Series 2*	20.212 eV	$^4P_{5/2}$	$[3s3p^4(^4P)\ np]\ ^3D$	εd
$(3s^2 3p^3)$ $S^+(^2D)$ *Series 1*	20.212 eV	$^4P_{5/2}$	$[3s3p^4(^4P)\ np]\ ^3P$	εd
$(3s^2 3p^3)$ $S^+(^2D)$ *Series 2*	20.255 eV	$^4P_{3/2}$	$[3s3p^4(^4P)\ np]\ ^3P$	εd
$(3s^2 3p^3)$ $S^+(^2P)$ *Series 1*	20.212 eV	$^4P_{5/2}$	$[3s3p^4(^4P)\ np]\ ^3D$	εd
$(3s^2 3p^3)$ $S^+(^2P)$ *Series 2*	20.255 eV	$^4P_{3/2}$	$[3s3p^4(^4P)\ np]\ ^3D$	εd

In summary, for the first time Rydberg series converging to the fourth ionization limit have been observed for the $S^+(^4S) \leftarrow S^*[3s3p^4\ (^4P)\ np] \leftarrow S(^3P)$, $S^+(^2D) \leftarrow S^*[3s3p^4\ (^4P)\ np] \leftarrow S(^3P)$ and $S^+(^2P) \leftarrow S^*[3s3p^4\ (^4P)\ np] \leftarrow S(^3P)$ ionization processes. The ionic core of the excited S^* atom is split into three spin-orbit states $^4P_{5/2}$, $^4P_{3/2}$ and $^4P_{1/2}$. A total of six Rydberg series have been observed experimentally. Using MQDT it has been possible to fit the experimental spectra with parameterized lineshape formula and to assign the Rydberg series.

^3S, ^3P and ^3D Rydberg series converging to the $^4P_{5/2}$ limit have been identified as well as ^3P and ^3D Rydberg series converging to the higher $^4P_{3/2}$ limit.

For the $S^+(^4S) \leftarrow S^* \leftarrow S(^3P)$ CIS spectrum, two of the possible six series were observed and these two series both converge to the $S^+(^4P_{5/2}) \leftarrow S(^3P)$ limit, see

Figure 8.37. *Series 1* (the series with lower resonance energies for a given *n*) arises from ^{3}S excited states whereas S*eries 2* corresponds to ^{3}D excited states.

For the $S^+(^2D) \leftarrow S^* \leftarrow S(^3P)$ CIS spectrum, two of the nine possible series were observed and these converge to the $S^+(^4P_{5/2}) \leftarrow S(^3P)$ and $S^+(^4P_{3/2}) \leftarrow S(^3P)$ limits, see Figure 8.38. Both the series correspond to ^{3}P excited states.

For the $S^+(^2P) \leftarrow S^* \leftarrow S(^3P)$ CIS spectrum, two of the six possible series were observed and these converge to the $S^+(^4P_{5/2}) \leftarrow S(^3P)$ and $S^+(^4P_{3/2}) \leftarrow S(^3P)$ limits, see Figure 8.39. Both the series correspond to ^{3}D excited states.

Each ionic channel has a clear propensity (intensity preference) for production of certain excited states. Of the series observed, those going to the $^4P_{5/2}$ limit seem to be favoured.

Inspection of Figures 8.37 - 8.39 shows that the $S^+(^4S) \leftarrow S^* \leftarrow S(^3P)$ *Series 2* and $S^+(^2P) \leftarrow S^* \leftarrow S(^3P)$ *Series 1* should be the same. Inspection of Table 8-4 shows that within experimental error this is the case. The angular distributions from these process, Figures 8.32 and 8.35, should also be the same. This is also true within experimental error, given by the errors involved in the fitting of the experimental CIS spectra recorded $\theta = 0°$ and $\theta = 54° 44'$.

8.1.2 CIS spectra for the second and third bands of SH

The CIS spectra recorded for the $SH^+(a^1\Delta, v^+=0) \leftarrow SH(X^2\Pi, v''=0)$ and $SH^+(b^1\Sigma^-, v^+=0) \leftarrow SH(X^2\Pi, v''=0)$ ionizations at $\theta = 54° 44'$ with respect to the polarization axis of the photon source are presented in Figures 8.40 to 8.43.

In the CIS of the second band $SH^+(a^1\Delta, v^+=0) \leftarrow SH(X^2\Pi, v''=0)$ shown in Figures 8.41 and 8.42, the expected position of the $SH^*(b^1\Sigma, nd)$, $SH^*(A^3\Pi, nd)$ and $SH^*(c^1\Pi, nd)$ Rydberg states, which are parts of series converging to the third, fourth and fifth ionization limits, are indicated. The excitation energies have been obtained applying the Rydberg formula with the 3d quantum defect values $\delta = 0.17$ obtained by Gibson *et al.*[14] for S atoms. These spectra are only poorly resolved and hence a positive identification of resonances cannot be made. However, the structures seen in Figure 8.42 in the energetic region 13.0 - 14.5 eV look to be part of a series

converging to a limit at 14.5 eV, but unfortunately there is no SH ionization limit at this energy and attempts to fit some of the components to a series converging to a limit at 14.11 eV (the fourth AIE of SH) proved unsuccessful. In view of these results, CIS measurements were not made at $\theta = 0°$, hence β as a function of the photon energy was not obtained for SH.

8.2 Conclusions

In this second investigation on S atoms with Synchrotron Radiation, the angular distribution parameters and relative photoionization cross section for the $S^+(^4S) \leftarrow S(^3P)$, $S^+(^2D) \leftarrow S(^3P)$ and $S^+(^2P) \leftarrow S(^3P)$ ionizations have been evaluated as a function of photon energy from threshold to 31 eV, with the CIS spectroscopy technique. All spectra were recorded at two angles, $\theta = 0°$ and $\theta = 54° 44'$, with respect to the polarization axis of the photon source. CIS spectra were successfully recorded for the $S^+(^4S) \leftarrow S(^3P)$ ionization at 10.35 eV, for the $S^+(^2D) \leftarrow S(^3P)$ ionization at 12.21 eV and for the $S^+(^2P) \leftarrow S(^3P)$ ionization at 13.40 eV. This second study, compared with the one presented in Chapter 7, has highlighted the presence of several structures that were not observed in the previous PE investigation. Inspections of the CIS spectra have shown that all the bands converging to the second and third ionization limits can be assigned to excitation to known Rydberg states. For the first time Rydberg series converging to the fourth ionization limit have been observed and assignments have been proposed in accordance with Russell-Saunders selection rules[18,19].

The results obtained have been compared, where available, with previous experiments and calculations.

Also the $SH^+(X^3\Sigma^-, v^+=0) \leftarrow SH(X^2\Pi, v''=0)$, $SH^+(a^1\Delta, v^+=0) \leftarrow SH(X^2\Pi, v''=0)$ and $SH^+(b^1\Sigma^-, v^+=0) \leftarrow SH(X\,^2\Pi, v''=0)$ ionizations have been investigated as a function of photon energy from threshold to 21.64 eV by the PE and CIS spectroscopy techniques.

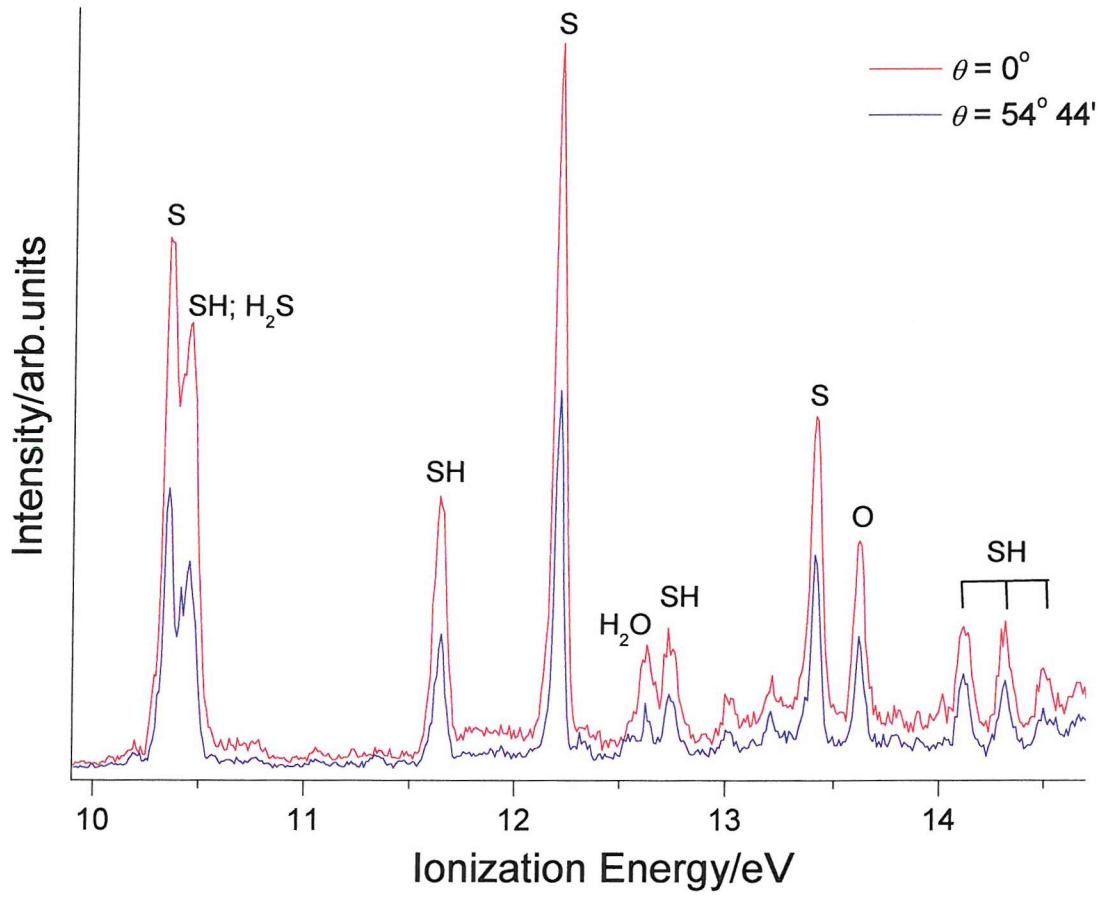

Figure 8.1 *Photoelectron spectrum at $h\nu$ =21.264 eV of the reactions*
$F + H_2S \rightarrow SH + HF$
$F + HS \rightarrow S + HF$
measured at two different angles $\theta = 0°$ (red trace) and $\theta = 54°44'$ (blue trace) with respect to the major polarization axis of the photon source in the 10.0 - 15.0 eV ionization region.

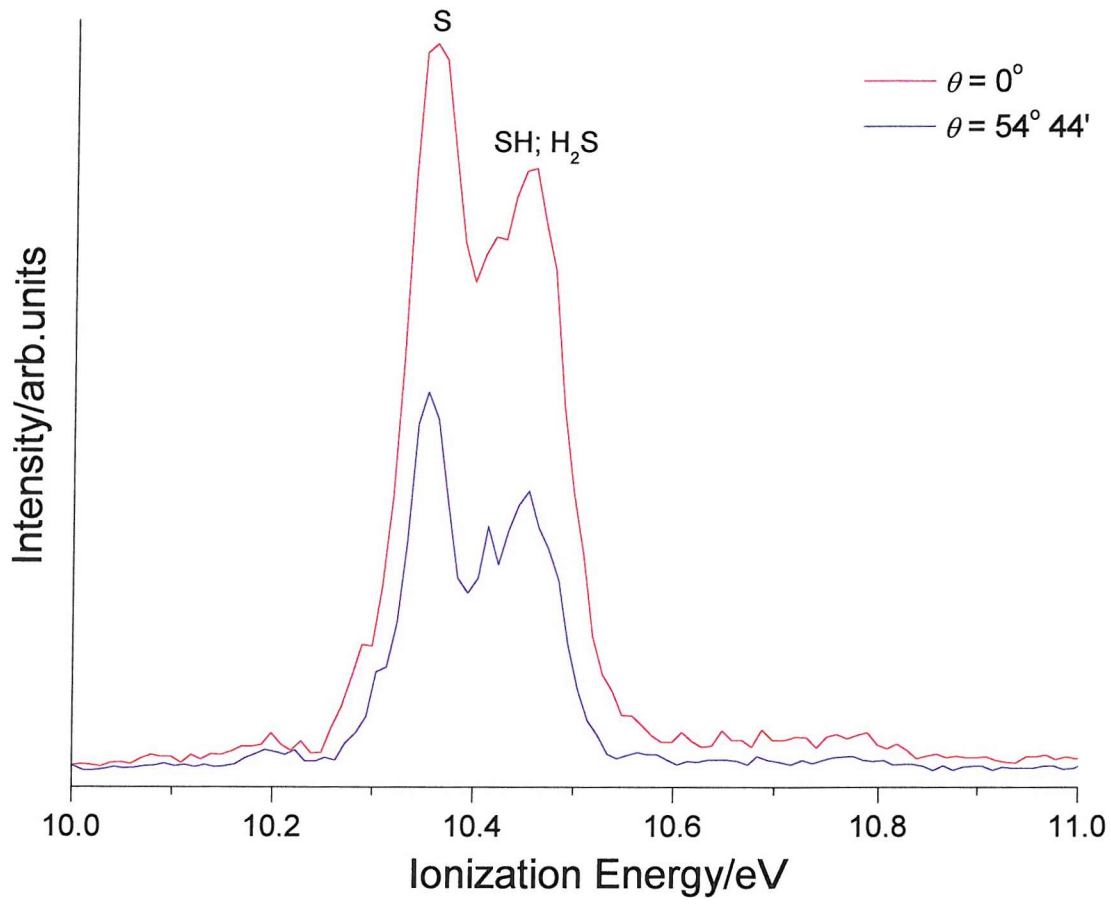

Figure 8.2 *Band shown in Figure 8.1 at ≈10.4 eV ionization energy. The band centred at 10.35 eV IE is the first band of S atoms, $S^+(^4S) \leftarrow S(^3P)$, whereas the band at 10.45 eV contains contributions from the first band of SH, $SH^+(X^3\Sigma^-) \leftarrow SH(X^2\Pi)$) at 10.42 eV IE, and from the first band of H_2S at 10.48 eV IE*[8].

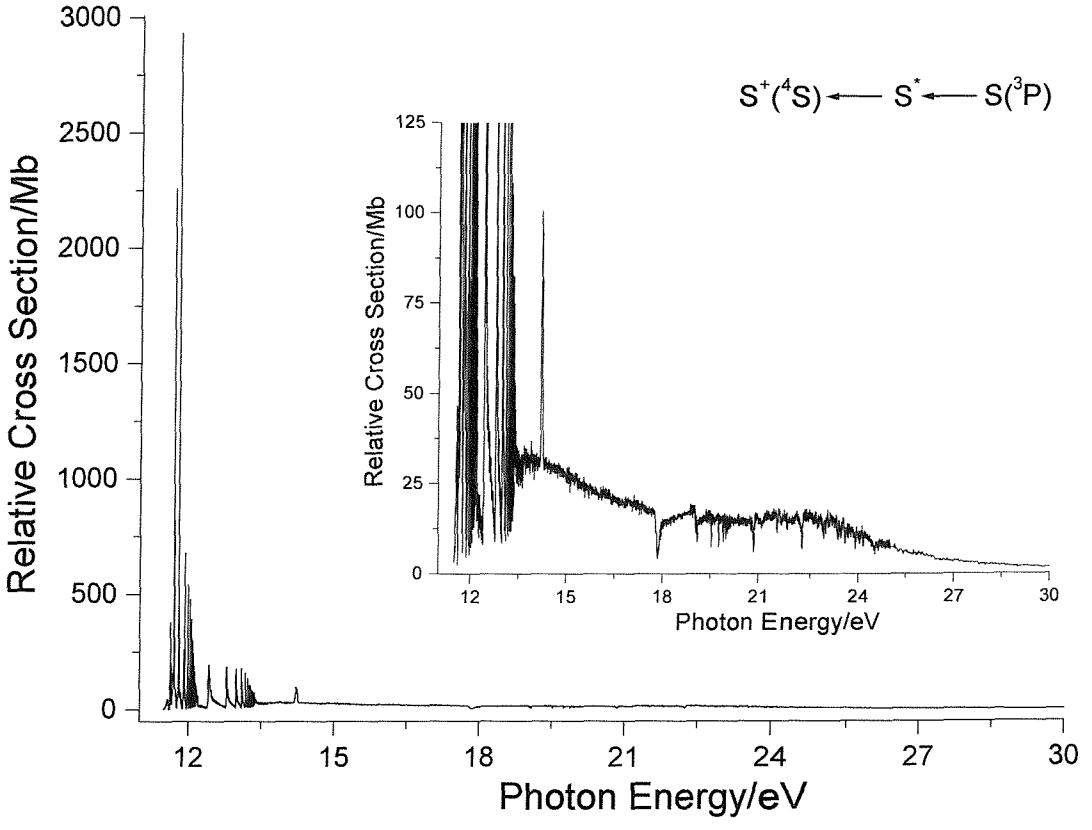

Figure 8.3 *CIS spectrum recorded for the $S^+(^4S) \leftarrow S^* \leftarrow S(^3P)$ process in the 11.5 - 30.0 eV photon energy region, at $\theta = 54^\circ 44'$ detection angle.*

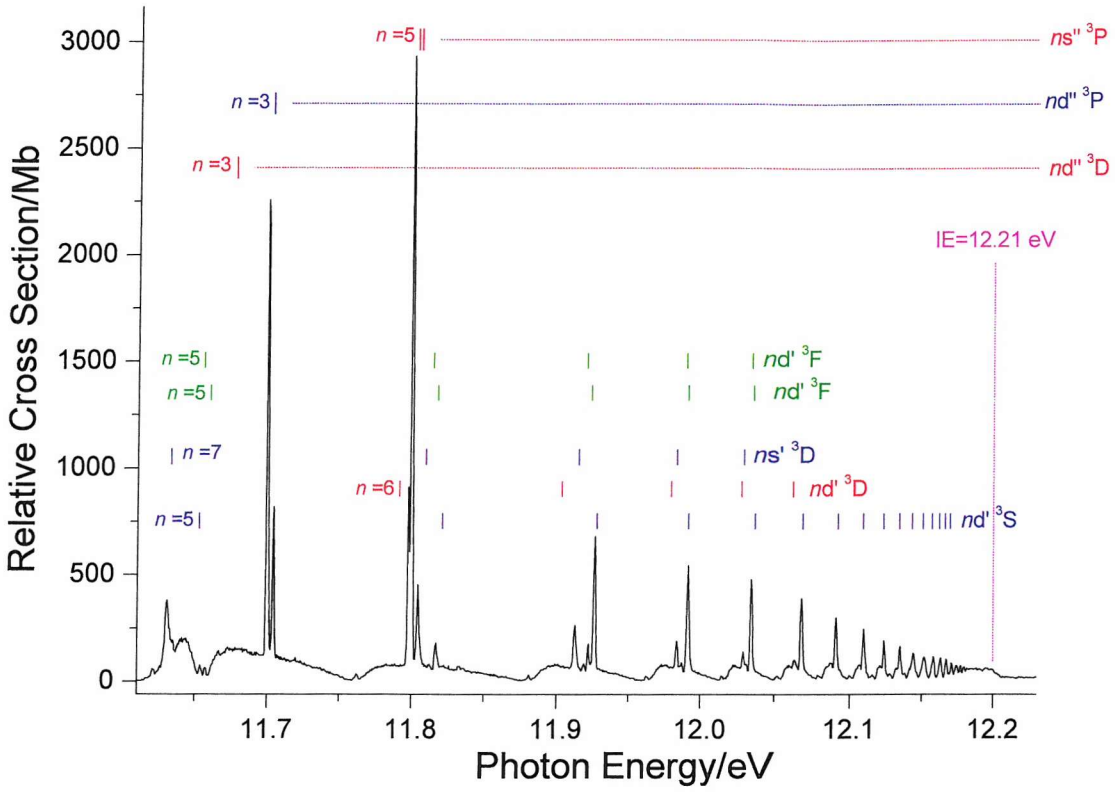

Figure 8.4 *CIS spectrum recorded for the $S^+(^4S) \leftarrow S^* \leftarrow S(^3P)$ process in the 11.50 - 12.25 eV photon energy region, at $\theta = 54°44'$ detection angle, with the second ionization limit marked (magenta trace) $S^* \leftarrow S$ transitions are indicated according with references (13) and (14), single prime on the Rydberg electron in the excited state (e.g. nd') designates terms converging to the second ionization limit.*

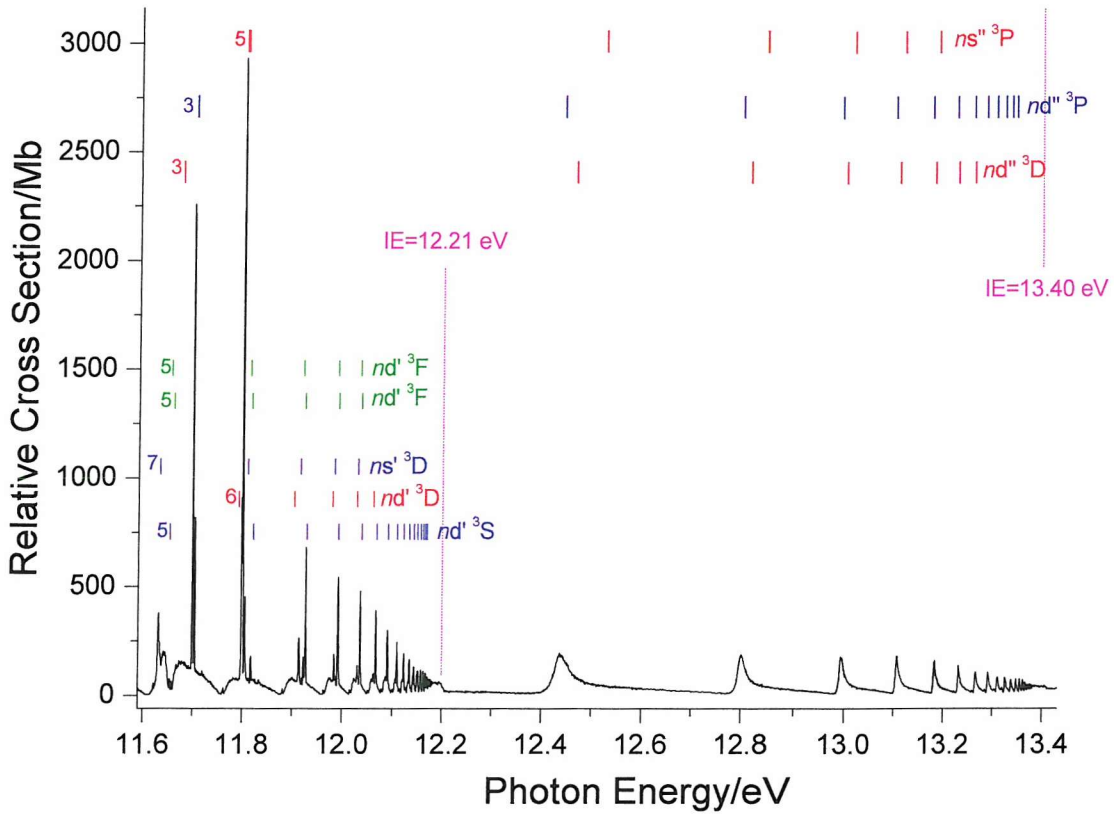

Figure 8.5 *CIS spectrum recorded for the $S^+(^4S) \leftarrow S^* \leftarrow S(^3P)$ process in the 11.60 - 13.45 eV photon energy region, at θ =54° 44' detection angle, with the second and third ionization limits marked (magenta trace) $S^* \leftarrow S$ transitions are indicated according with references (13) and (14), single and double prime on the Rydberg electron in the excited state designates terms converging to the second (IE = 12.21 eV) and to the third (IE = 13.40 eV) ionization limit respectively.*

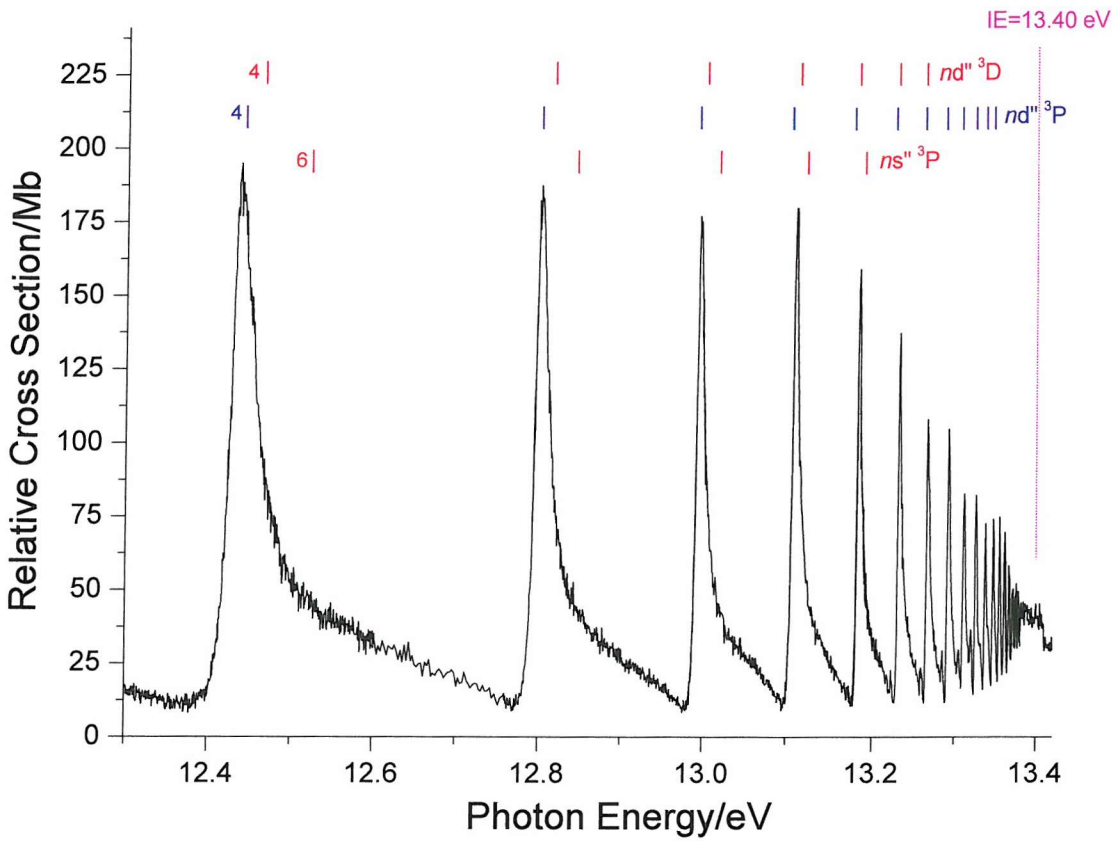

Figure 8.6 *CIS spectrum recorded for the $S^+(^4S) \leftarrow S^* \leftarrow S(^3P)$ process in the 12.30 - 13.42 eV photon energy region, at $\theta = 54°44'$ detection angle, with the third ionization limits marked (magenta trace) $S^* \leftarrow S$ transitions are indicated according with references (13) and (14), double prime on the Rydberg electron in the excited state designates terms converging to the third ionization limit.*

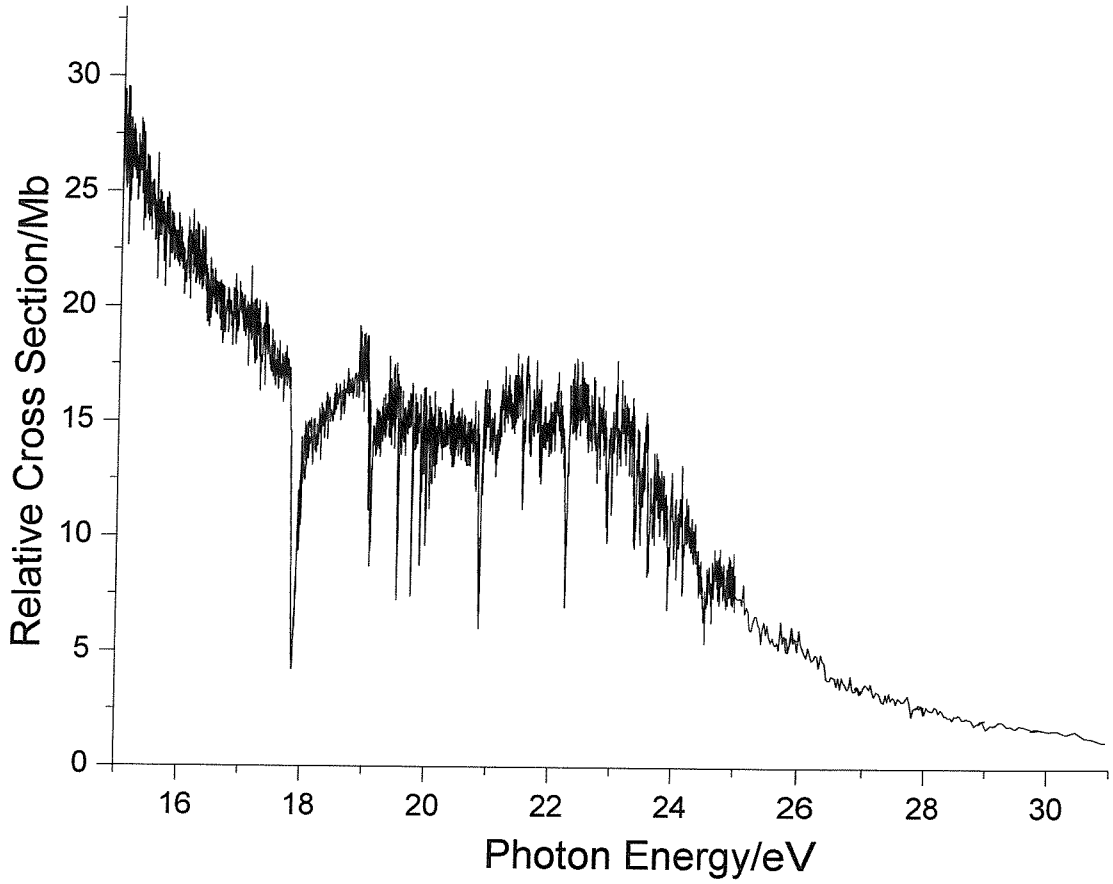

Figure 8.7 *CIS spectrum recorded for the $S^{+}(^{4}S) \leftarrow S^{*} \leftarrow S(^{3}P)$ process in the 15.0 - 31.0 eV photon energy region, at $\theta = 54^{\circ}44'$ detection angle.*

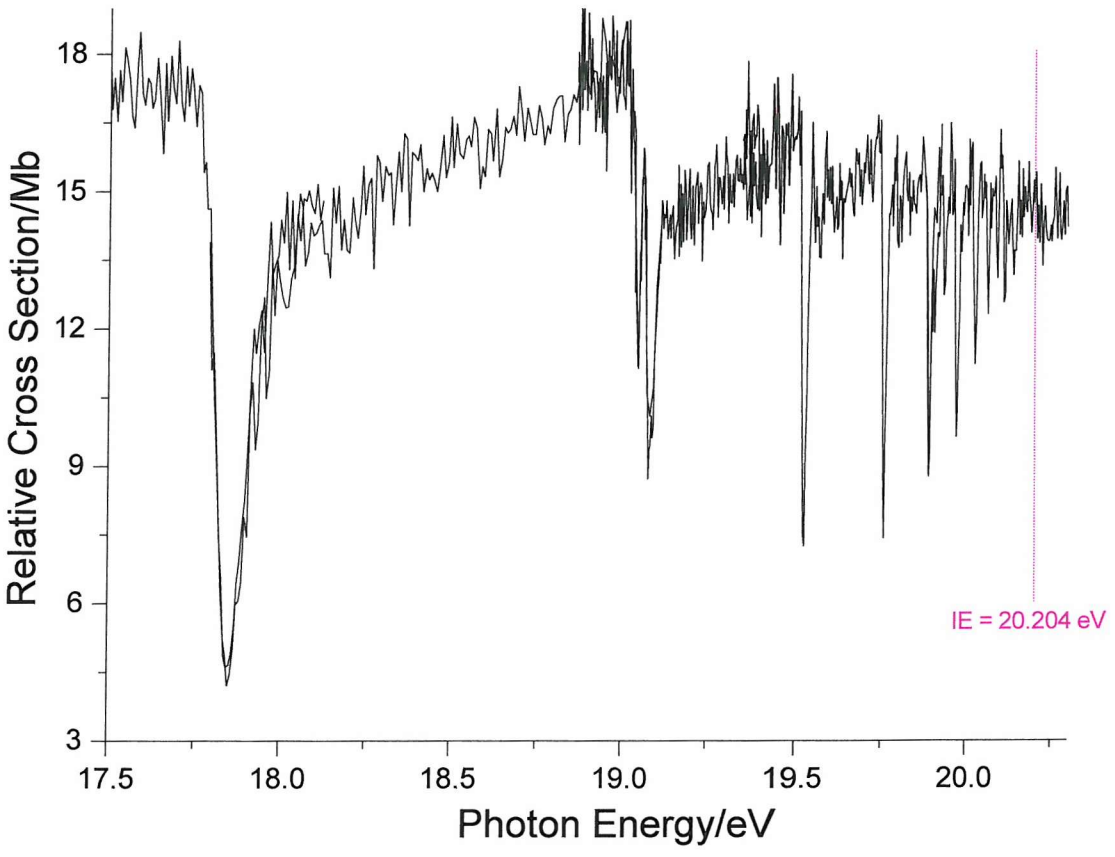

Figure 8.8 *CIS spectrum recorded for the $S^{+}(^{4}S) \leftarrow S^{*} \leftarrow S(^{3}P)$ process in the 17.50 - 20.55 eV photon energy region, at $\theta = 54°44'$ detection angle, with the fourth ionization limit marked (magenta trace).*

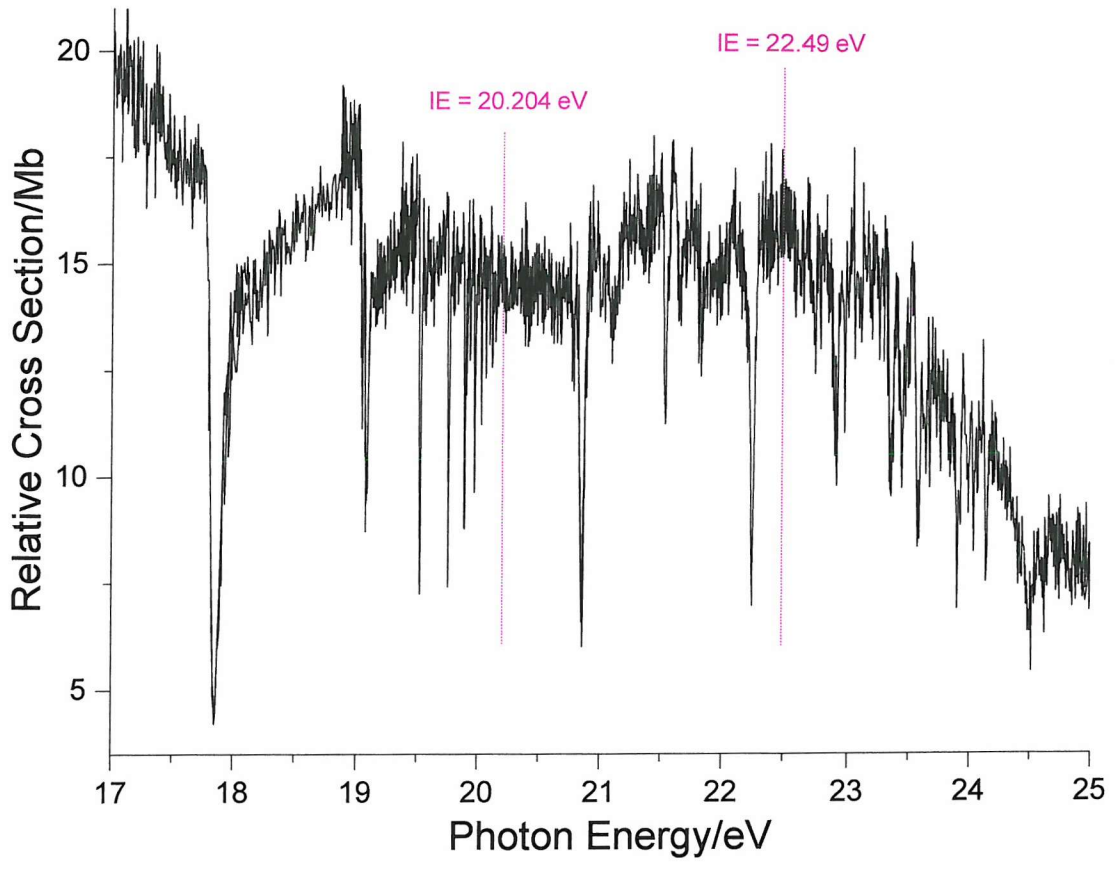

Figure 8.9 *CIS spectrum recorded for the* $S^+(^4S) \leftarrow S^* \leftarrow S(^3P)$ *process in the 17.0 - 25.0 eV photon energy region, at* $\theta = 54°44'$ *with the fourth (IE = 20.204 eV) and fifth (IE =22.49 eV) ionization limits marked (magenta trace).*

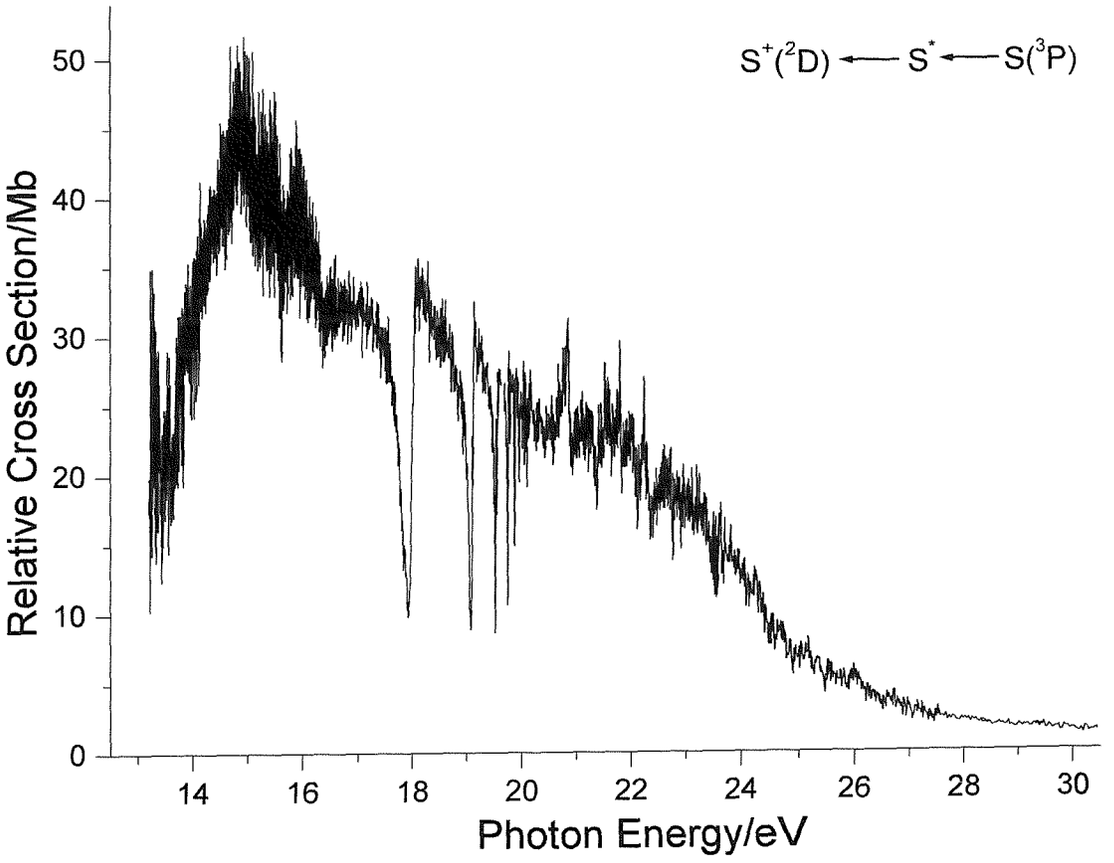

Figure 8.10 *CIS spectrum recorded for the $S^+(^2D) \leftarrow S^* \leftarrow S(^3P)$ process in the 13.5 - 30.5 eV photon energy region, at $\theta = 54°44'$ detection angle.*

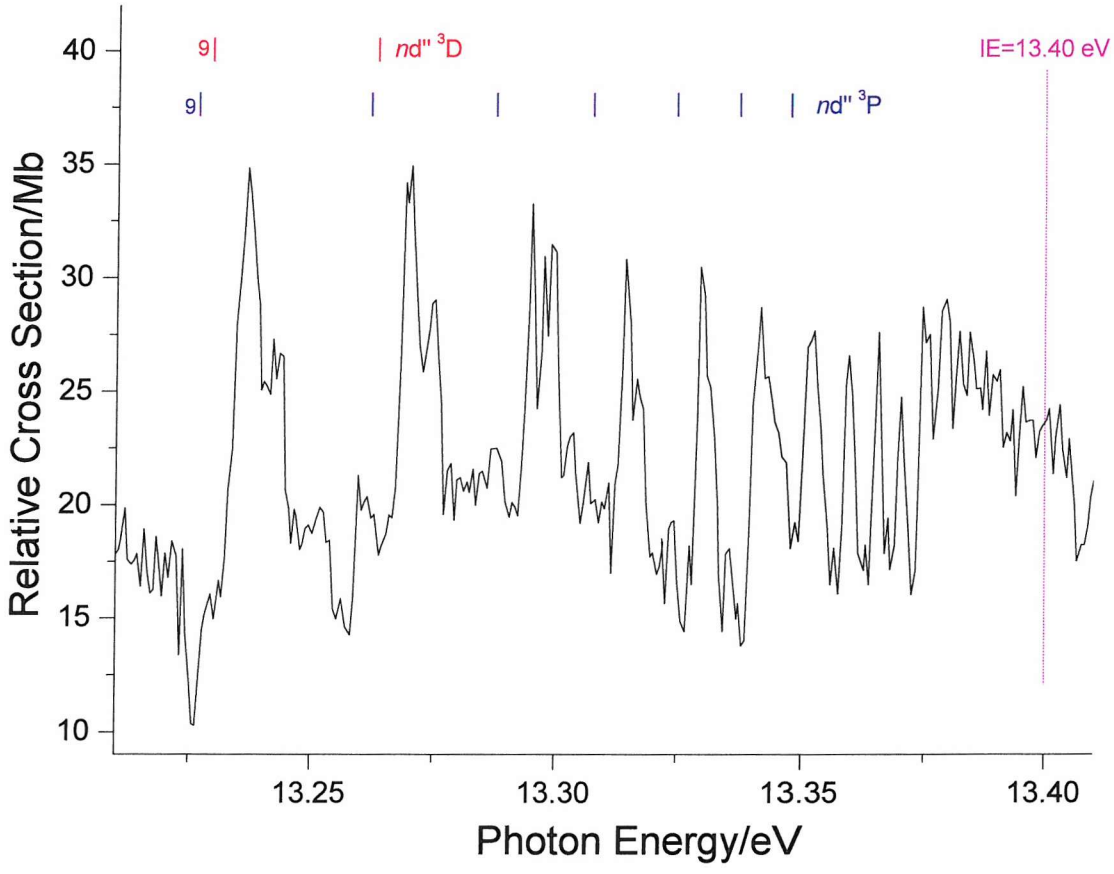

Figure 8.11 *CIS spectrum recorded for the $S^+(^2D) \leftarrow S^* \leftarrow S(^3P)$ process in the 13.10 - 13.42 eV photon energy region, at $\theta = 54°44'$ detection angle with the third ionization limits marked (magenta trace) $S^* \leftarrow S$ transitions are indicated according with references (13) and (14), double prime on the Rydberg electron in the excited state designates terms converging to the third ionization limit.*

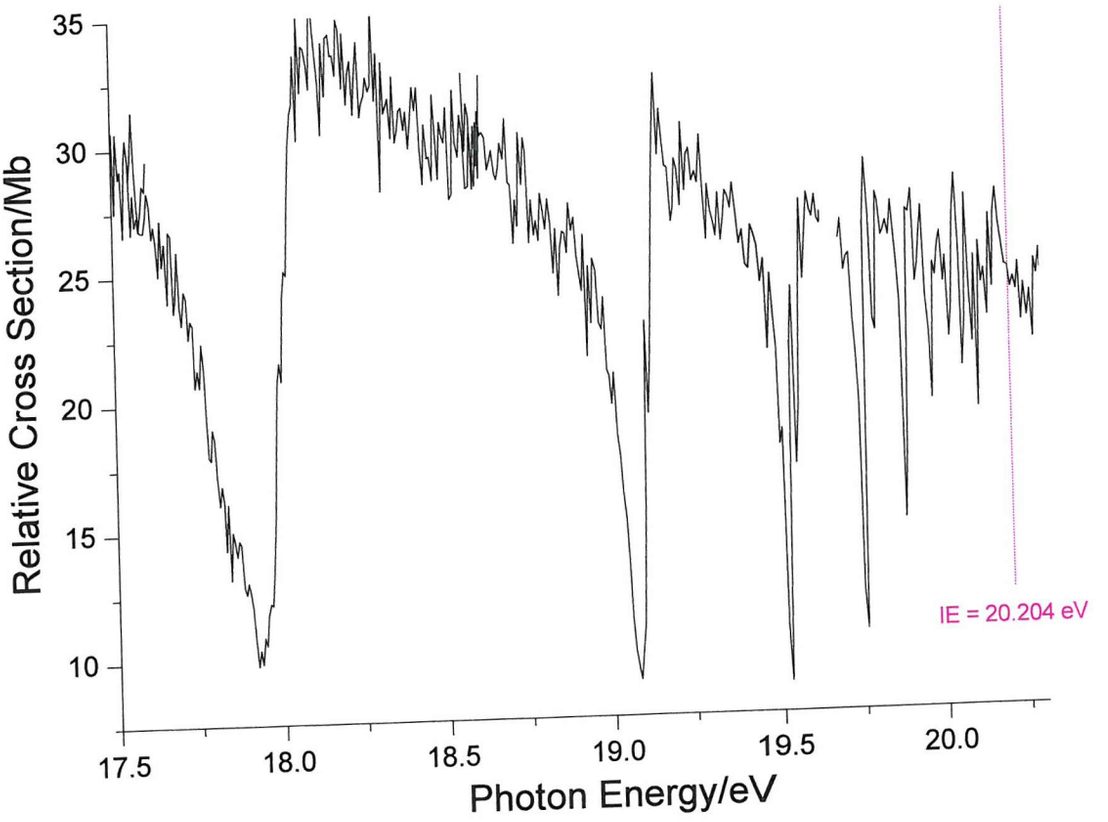

Figure 8.12 *CIS spectrum recorded for the $S^{+}(^{2}D) \leftarrow S^{*} \leftarrow S(\,^{3}P)$ process in the 17.5 - 20.3 eV photon energy region, at $\theta = 54°44'$ detection angle with the fourth ionization limit marked (magenta trace).*

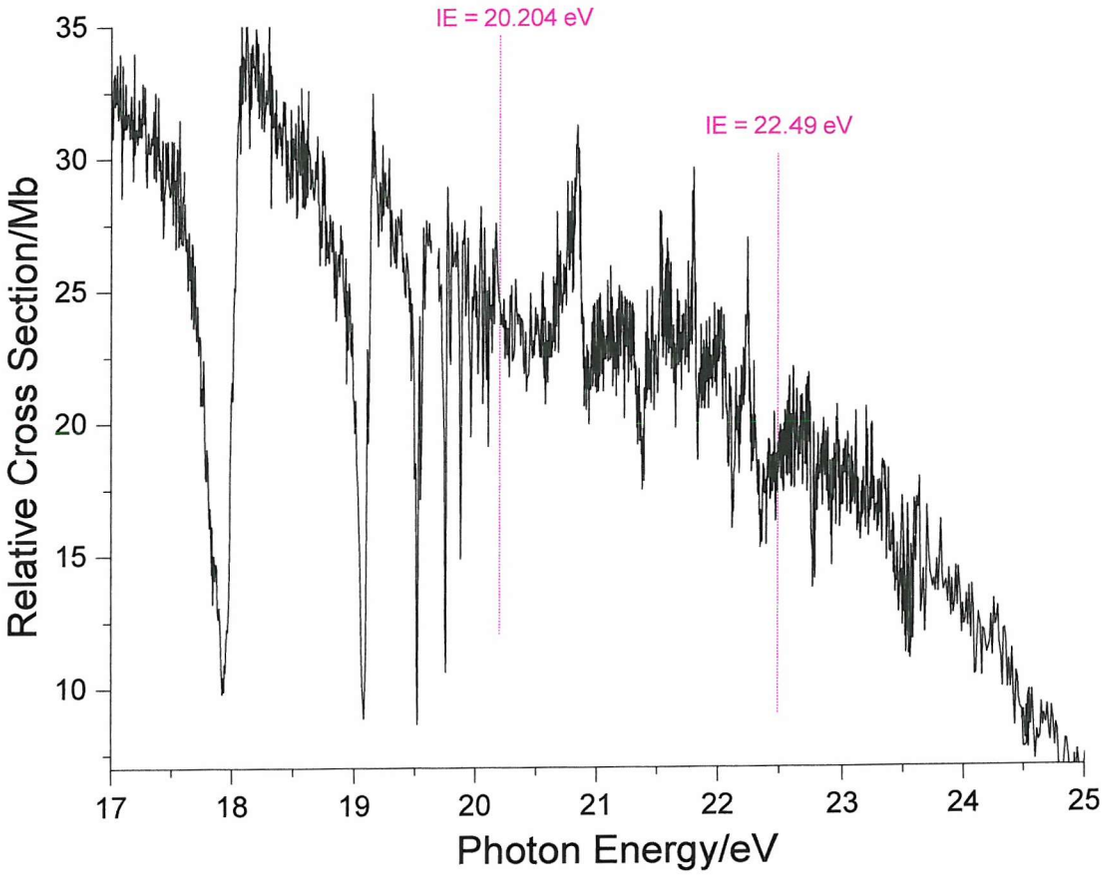

Figure 8.13 *CIS spectrum recorded for the $S^+(^2D) \leftarrow S^* \leftarrow S(^3P)$ process in the 17.0 - 25.0 eV photon energy region, at $\theta = 54°44'$ with the fourth (IE = 20.204 eV) and fifth (IE = 22.49 eV) ionization limits marked (magenta trace).*

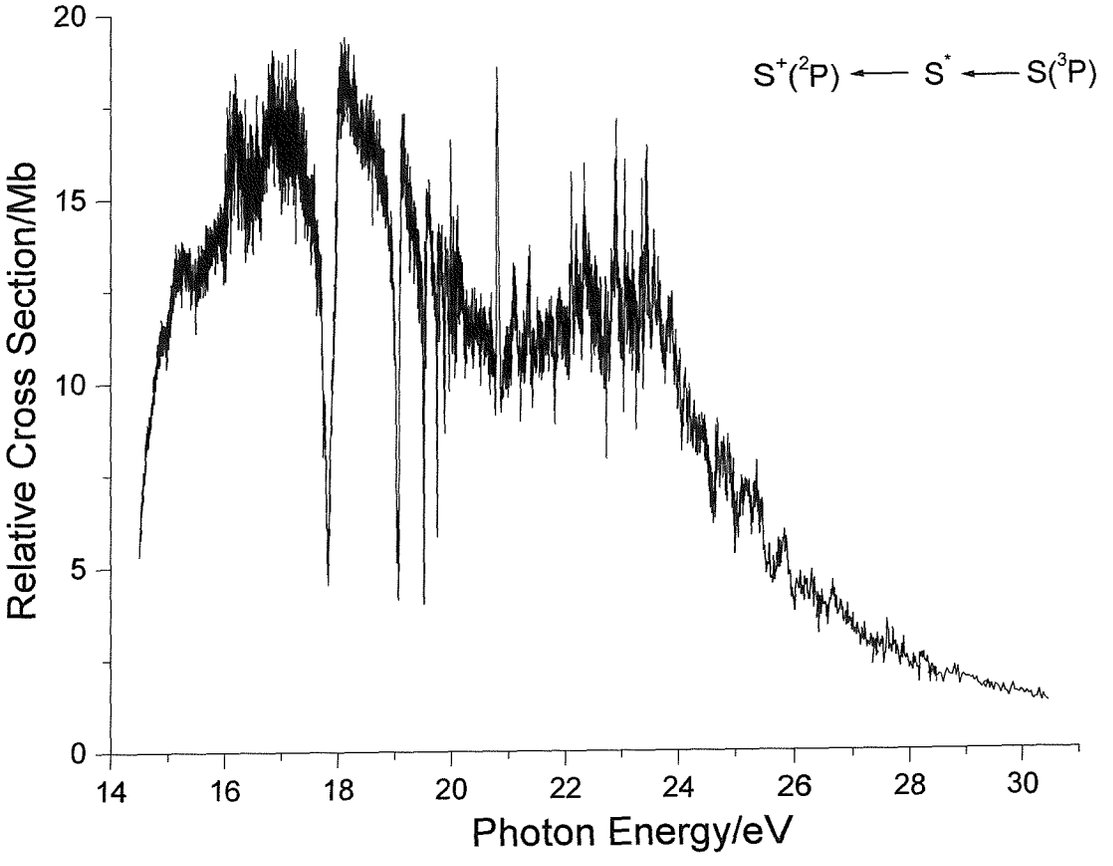

Figure 8.14 *CIS spectrum recorded for the $S^{+}(^{2}P) \leftarrow S^{*} \leftarrow S(^{3}P)$ process in the 14.0 - 31.0 eV photon energy region, at $\theta = 54^{\circ}44'$ detection angle.*

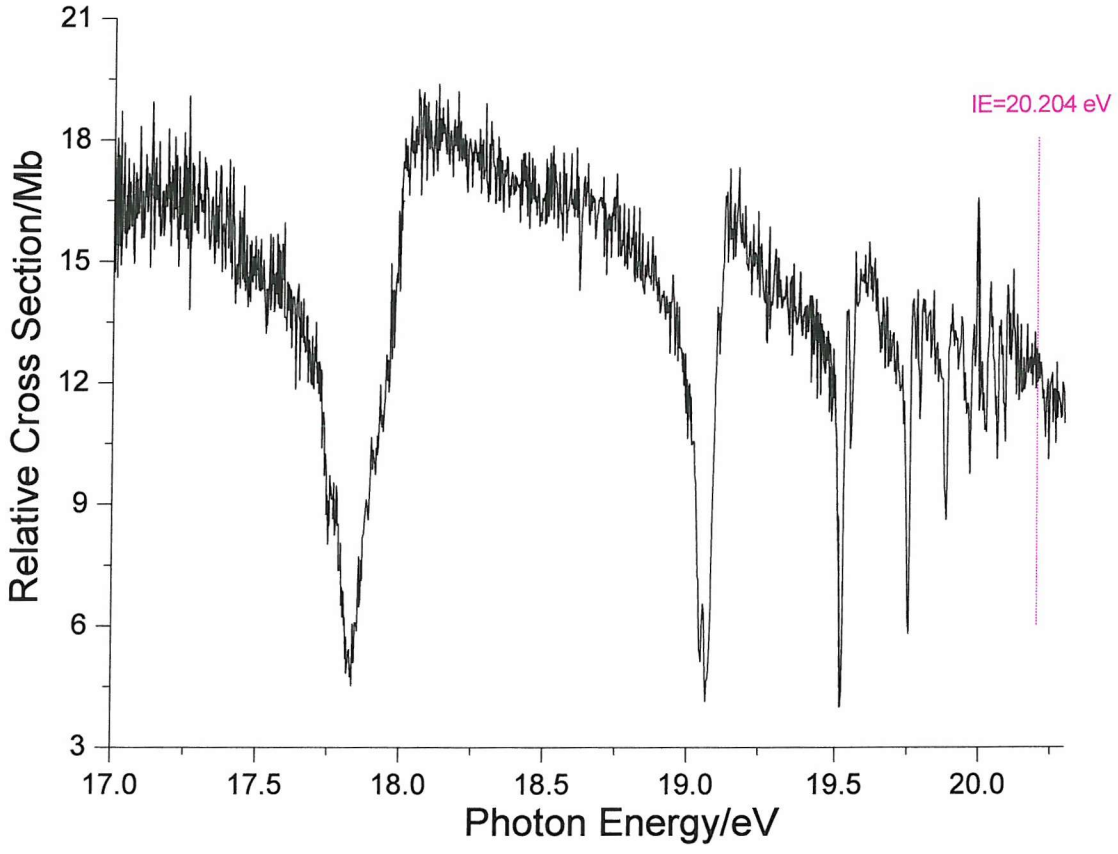

Figure 8.15 *CIS spectrum recorded for the $S^+(^2P) \leftarrow S^* \leftarrow S(^3P)$ process in the 17.0 - 20.3 eV photon energy region, at $\theta = 54°44'$ detection angle with the fourth ionization limit marked (magenta trace).*

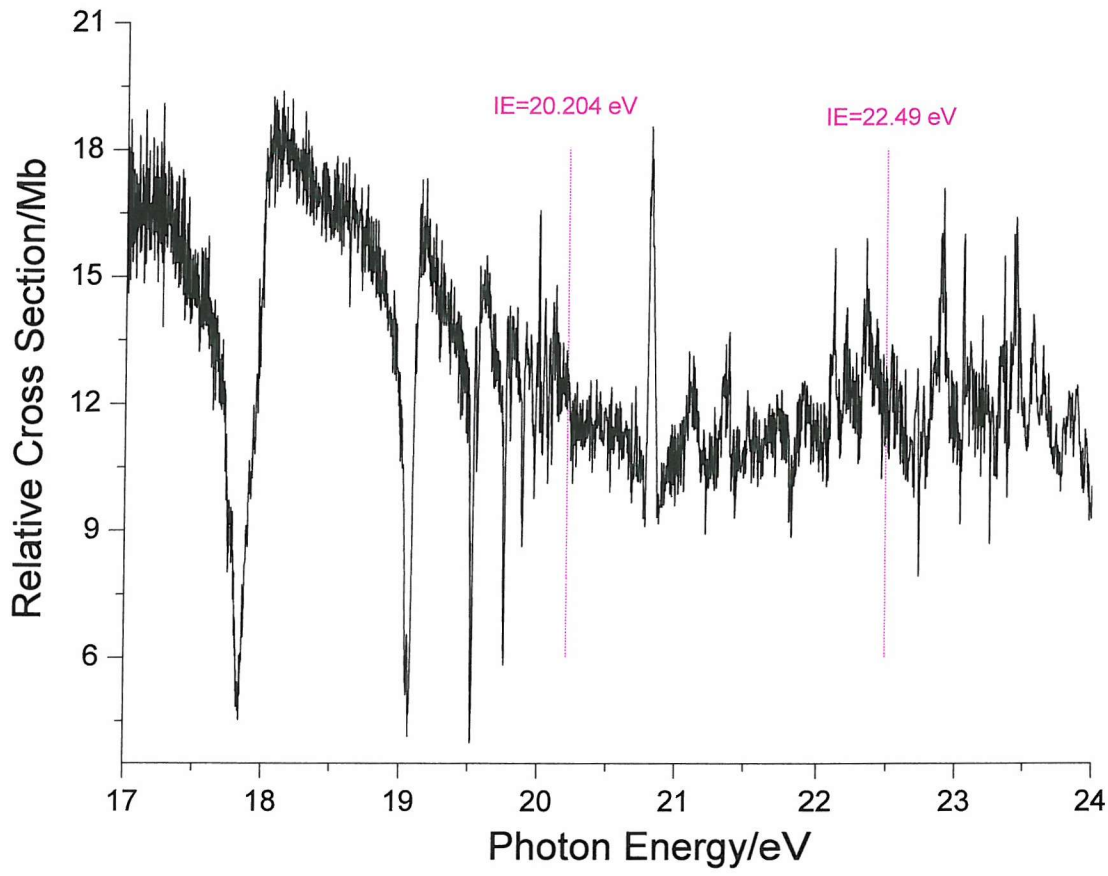

Figure 8.16 *CIS spectrum recorded for the $S^{+}(^{2}P) \leftarrow S^{*} \leftarrow S(^{3}P)$ process in the 17.0 – 24.0 eV photon energy region, at $\theta = 54°44'$ with the fourth (IE = 20.204 eV) and fifth (IE = 22.49 eV) ionization limits marked (magenta trace).*

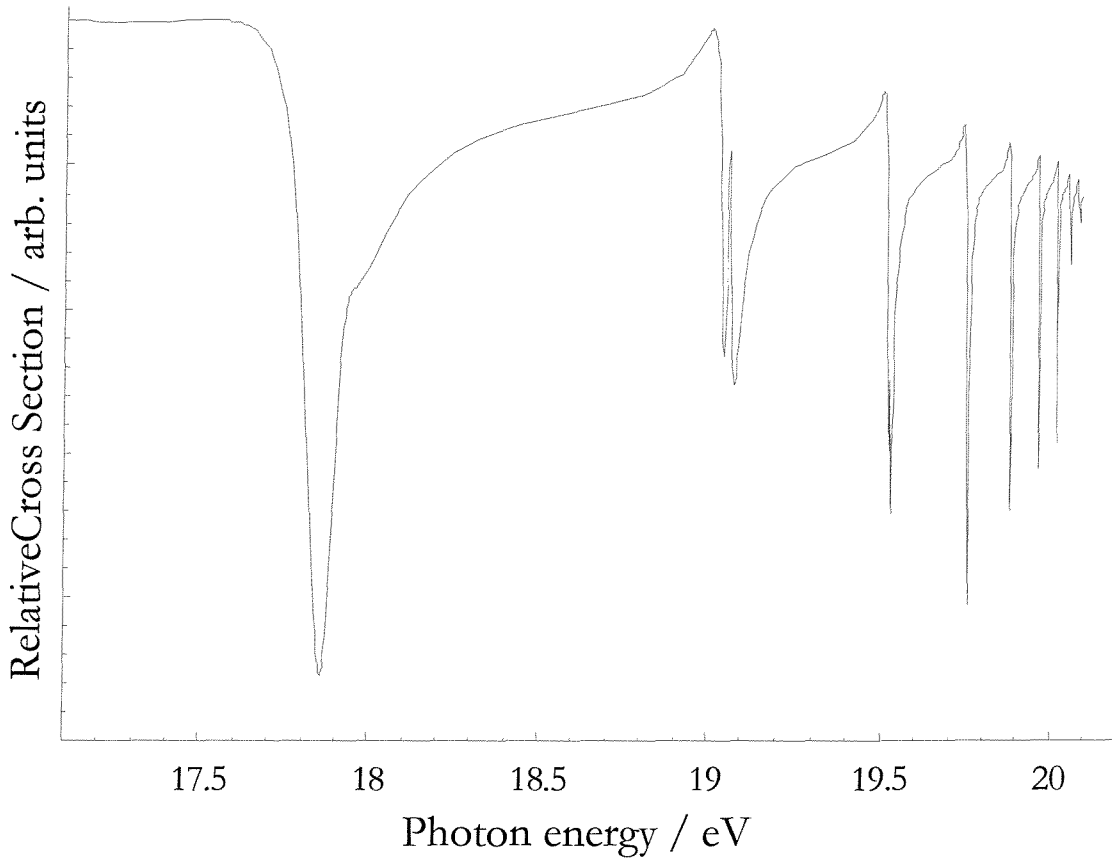

Figure 8.17 *Fit of the data recorded for the $S^+(^4S) \leftarrow S^* \leftarrow S(^3P)$ process in the 17.0 - 20.3 eV photon energy region, at $\theta = 54°44'$ detection angle. This should be compared with the experimental spectrum in Figure 8.8.*

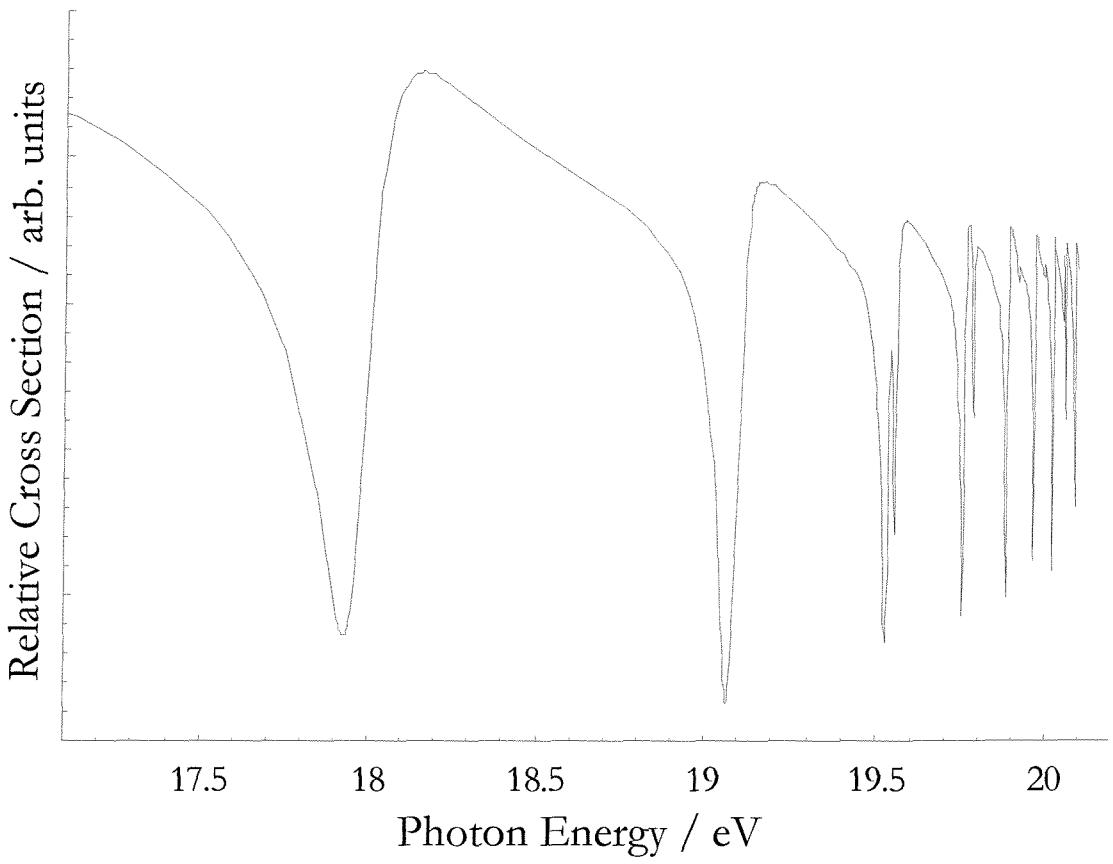

Figure 8.18 *Fit of the data recorded for the $S^+(^2D) \leftarrow S^* \leftarrow S(^3P)$ process in the 17.5 - 20.3 eV photon energy region, at $\theta = 54°44'$ detection angle. This should be compared with the experimental spectrum in Figure 8.12.*

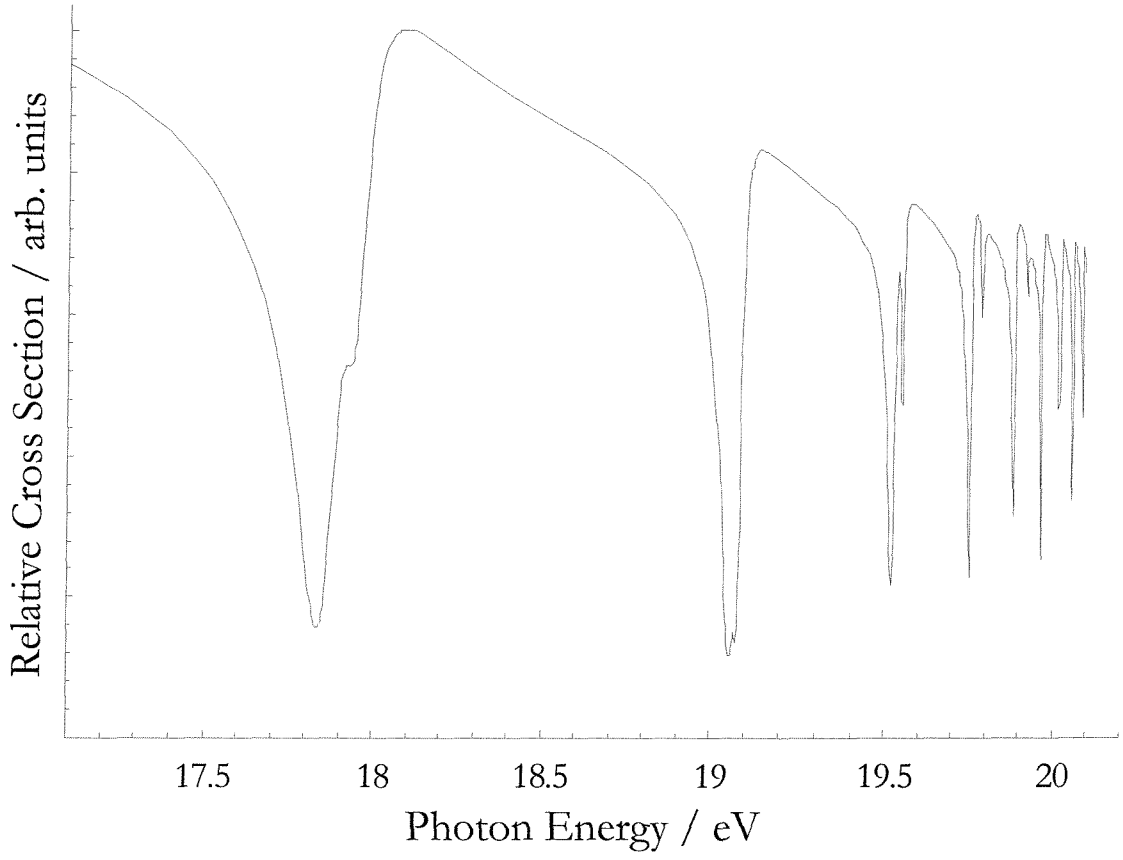

Figure 8.19 *Fit of the data recorded for the $S^+(^2P) \leftarrow S^* \leftarrow S(^3P)$ process in the 17.0 - 20.3 eV photon energy region, at $\theta = 54°44'$ detection angle. This should be compared with the experimental spectrum in Figure 8.15.*

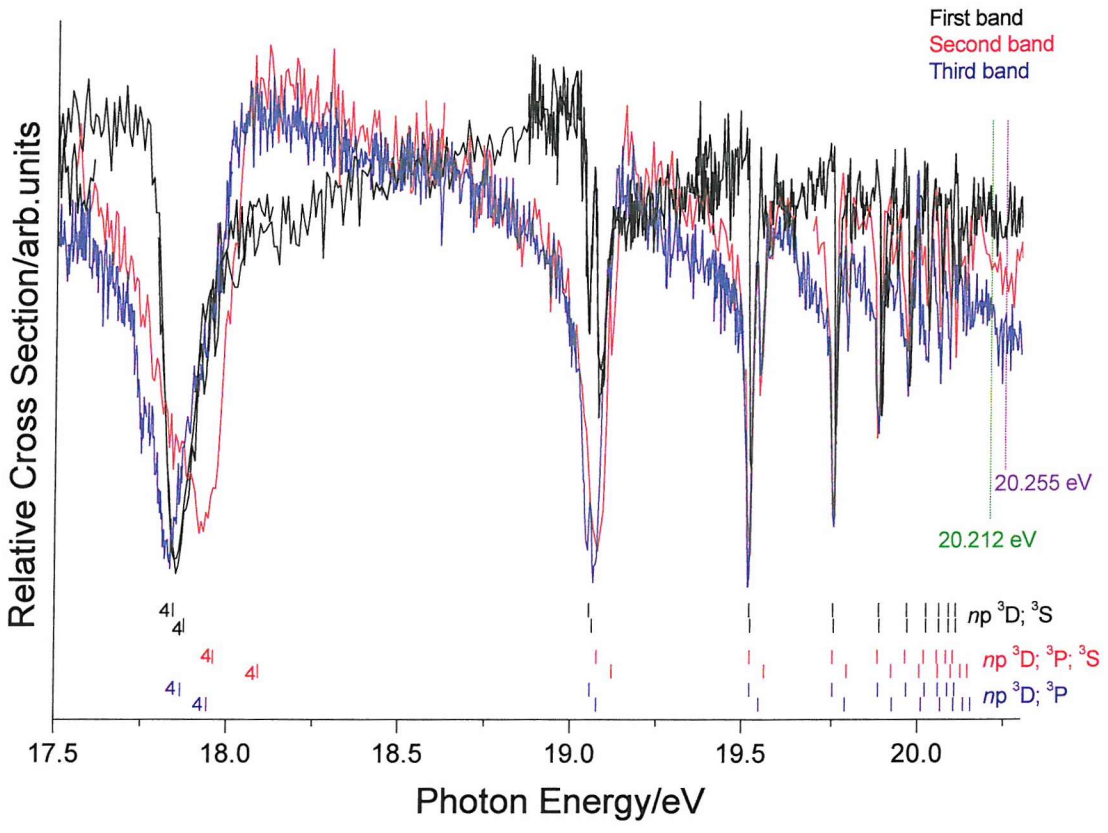

Figure 8.20 *CIS spectra recorded for the $S^+(^4S) \leftarrow S^* \leftarrow S(^3P)$, $S^+(^2D) \leftarrow S^* \leftarrow S(^3P)$ and $S^+(^2P) \leftarrow S^* \leftarrow S(^3P)$ processes in the 17.5 - 20.3 eV photon energy region, at $\theta = 54°44'$ detection angle, with the fourth ionization limit at 20.204 eV marked (magenta trace).*
The tentative assignment of the Rydberg series is presented according to the Russell-Saunders selection rules[18,19] (see text for further details).

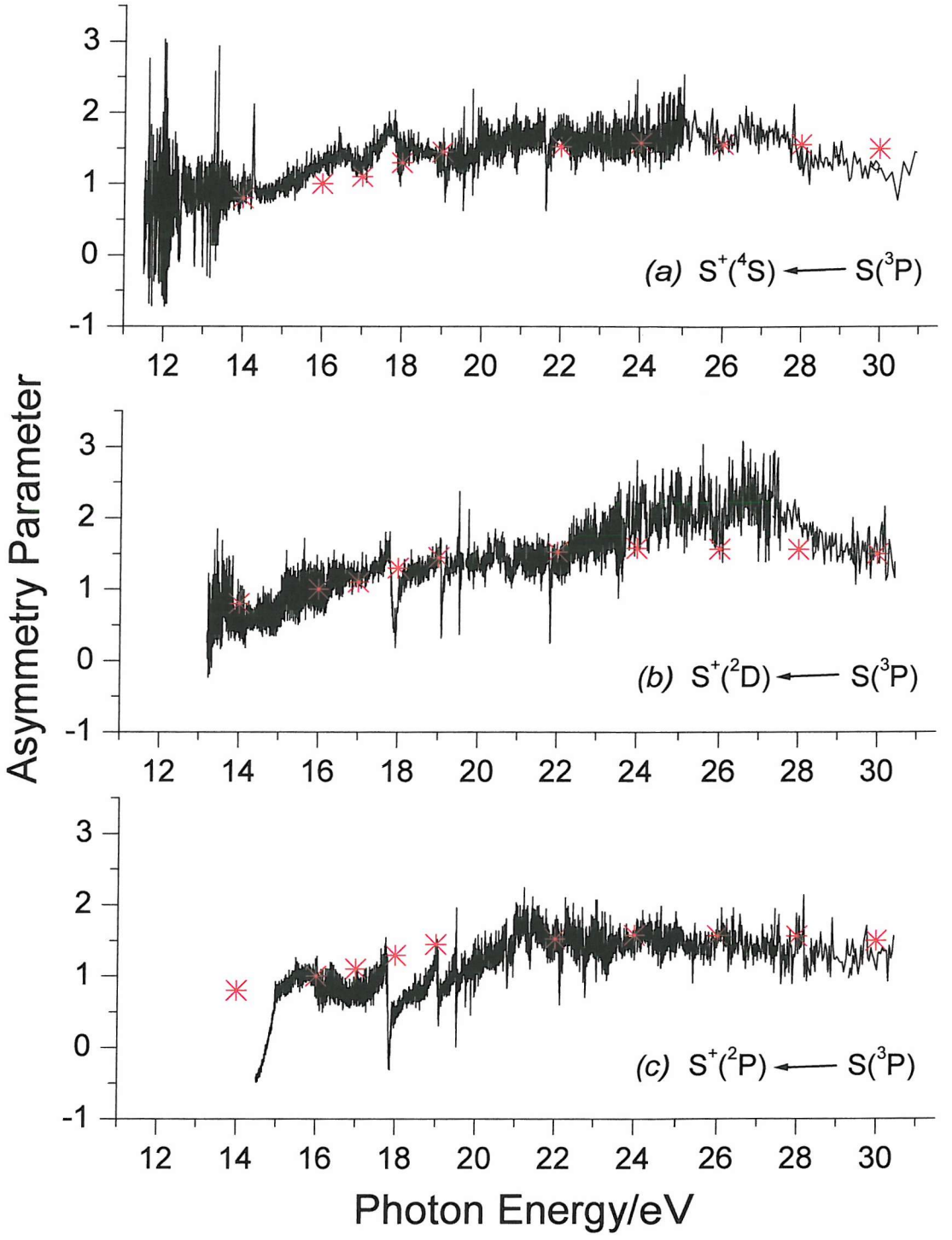

Figure 8.21 *Plots of the asymmetry parameter (β) as a function of photon energy over the range hν =10.0 - 30.0 eV, for the first three photoelectron bands of S atoms. All the plots includes β values for the first band of H_2S measured at different photon energies in Ref.(23), denoted with the symbol (*).*

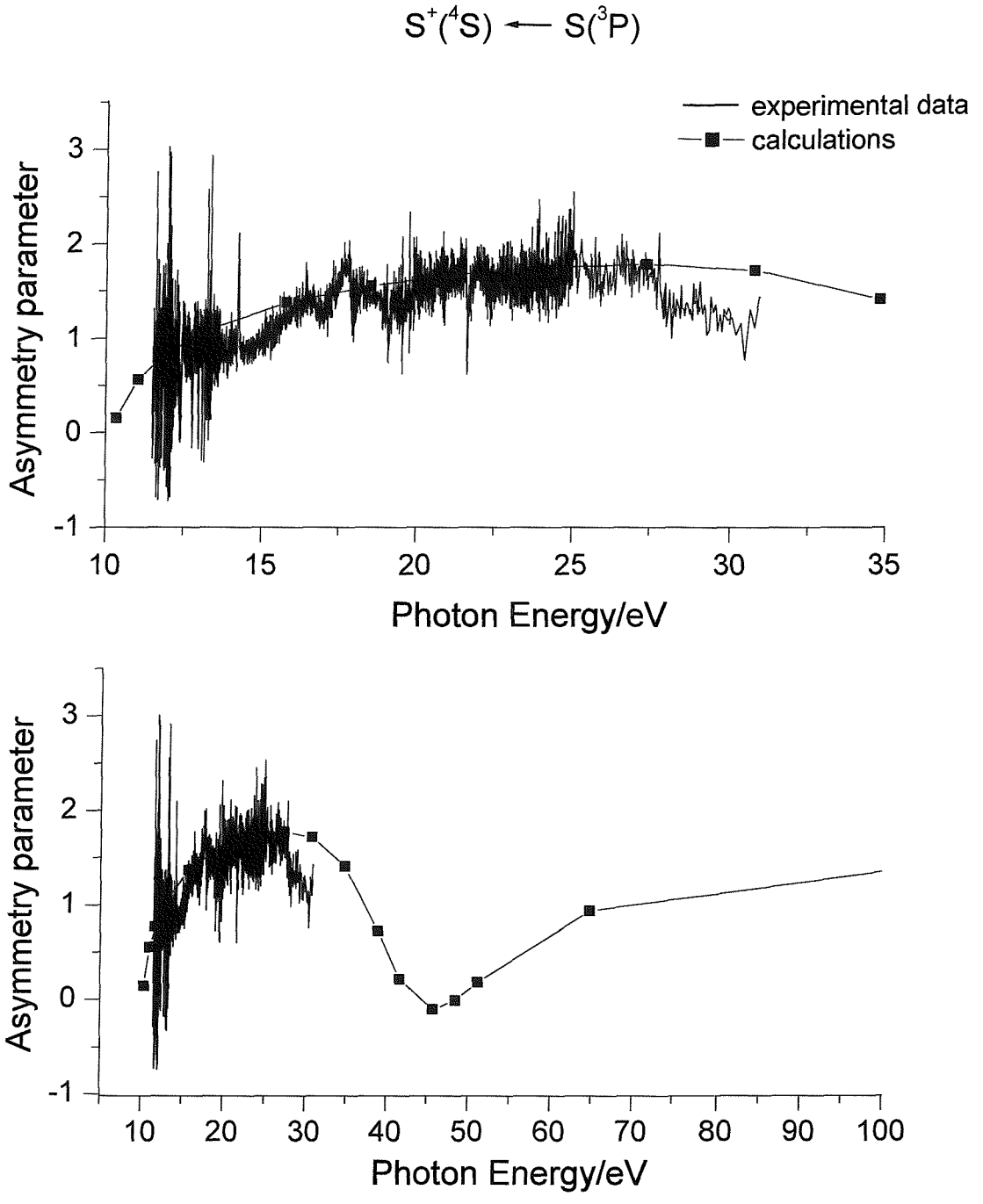

Figure 8.22 *Asymmetry parameters for S atoms plotted as a function of photon energy and compared with the results of Dill et al.*[7]*, for the first S atom band* $S^+(^4S) \leftarrow S(^3P)$.

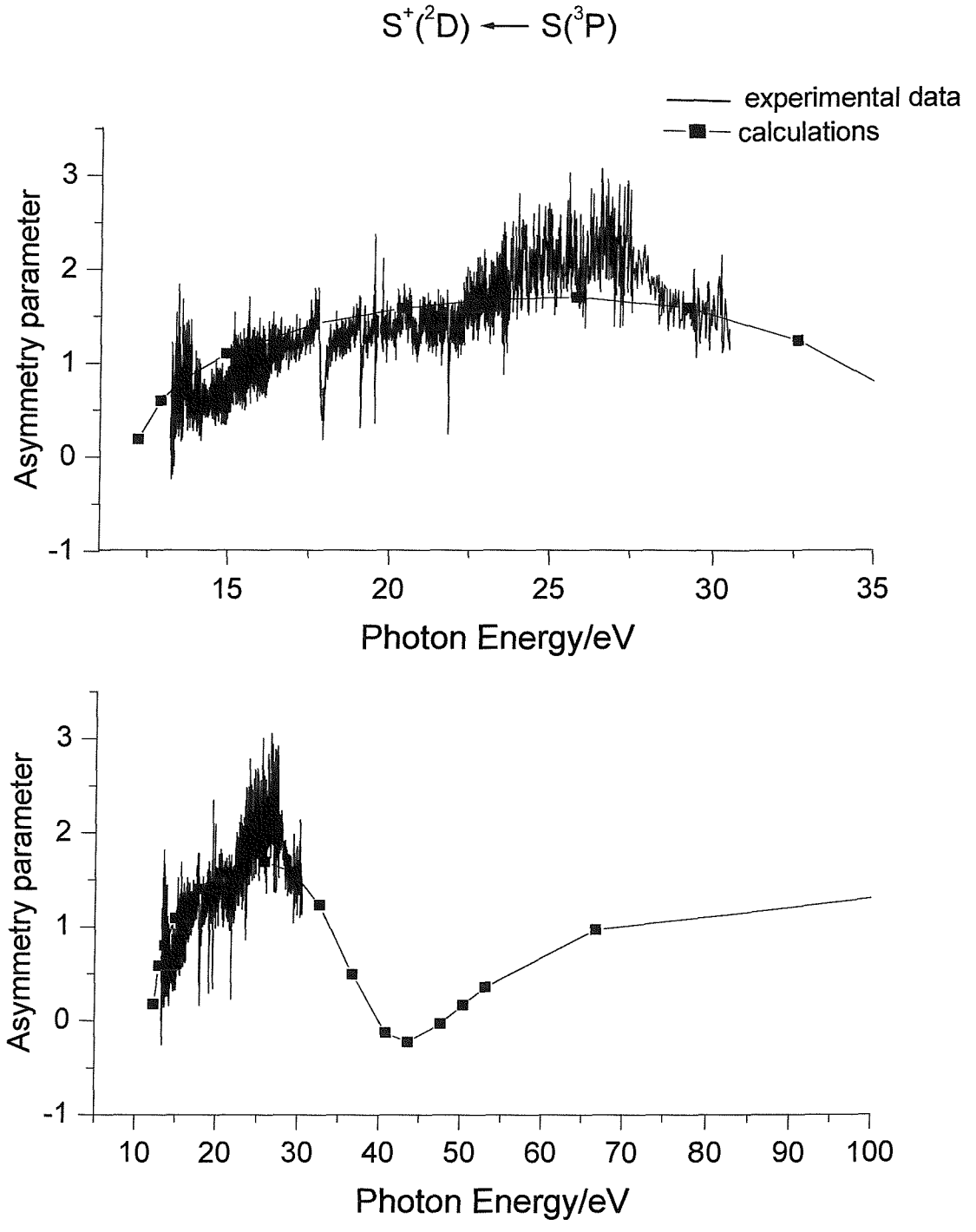

Figure 8.23 *Asymmetry parameters for S atoms plotted as a function of photon energy and compared with the results of Dill et al.*[7]*, for the second S atom band* $S^+(^2D) \leftarrow S(^3P)$.

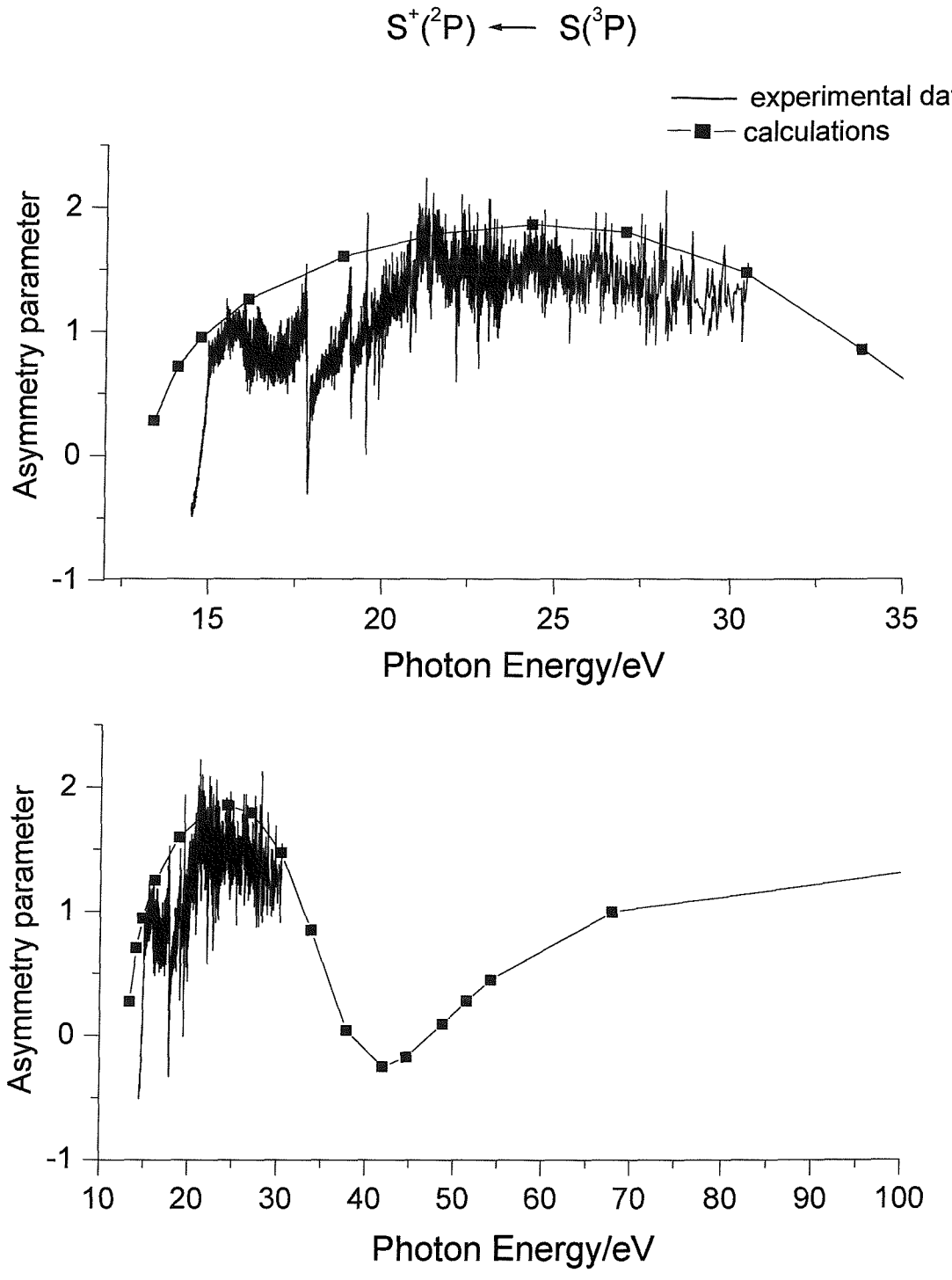

Figure 8.24 *Asymmetry parameters for S atoms plotted as a function of photon energy and compared with the results of Dill et al.*[7] *for the third S atom band* $S^+(^2P) \leftarrow S(^3P)$.

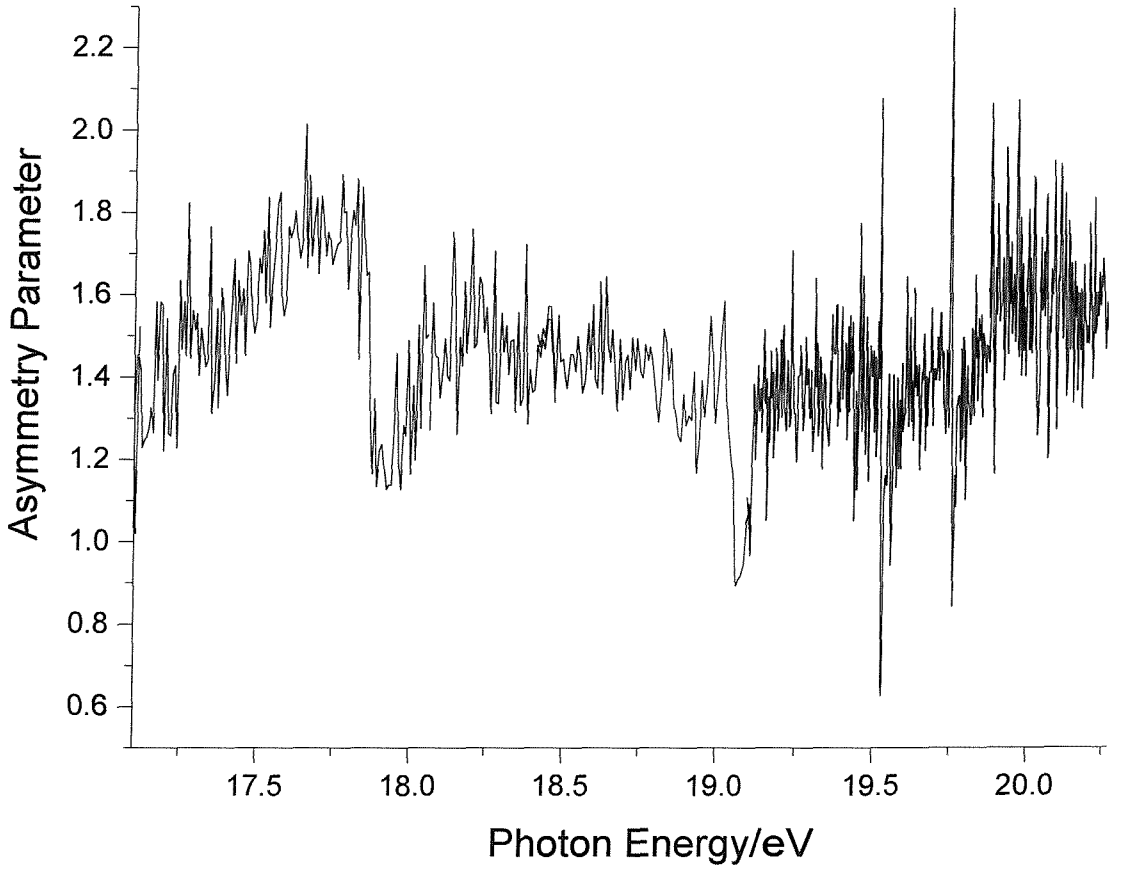

Figure 8.25 *Spectrum of the experimental asymmetry parameter (β) for the $S^{+}(^{4}S) \leftarrow S^{*} \leftarrow S(^{3}P)$ ionization process as a function of the photon energy over the range $h\nu$ = 16.5 - 20.5 eV.*

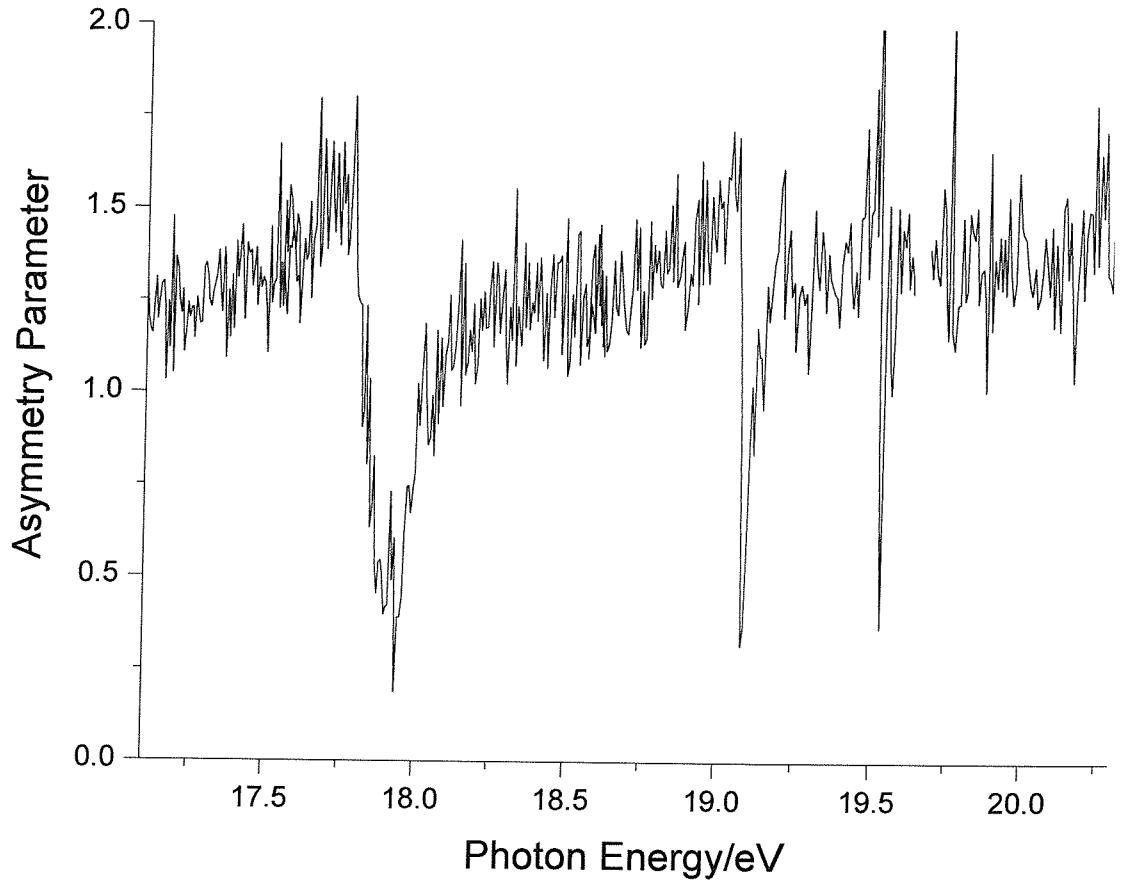

Figure 8.26 *Spectrum of the experimental asymmetry parameter (β) for the $S^{+}(^{2}D) \leftarrow S^{*} \leftarrow S(^{3}P)$ ionization process as a function of photon energy over the range $h\nu$ = 16.5 - 20.5 eV.*

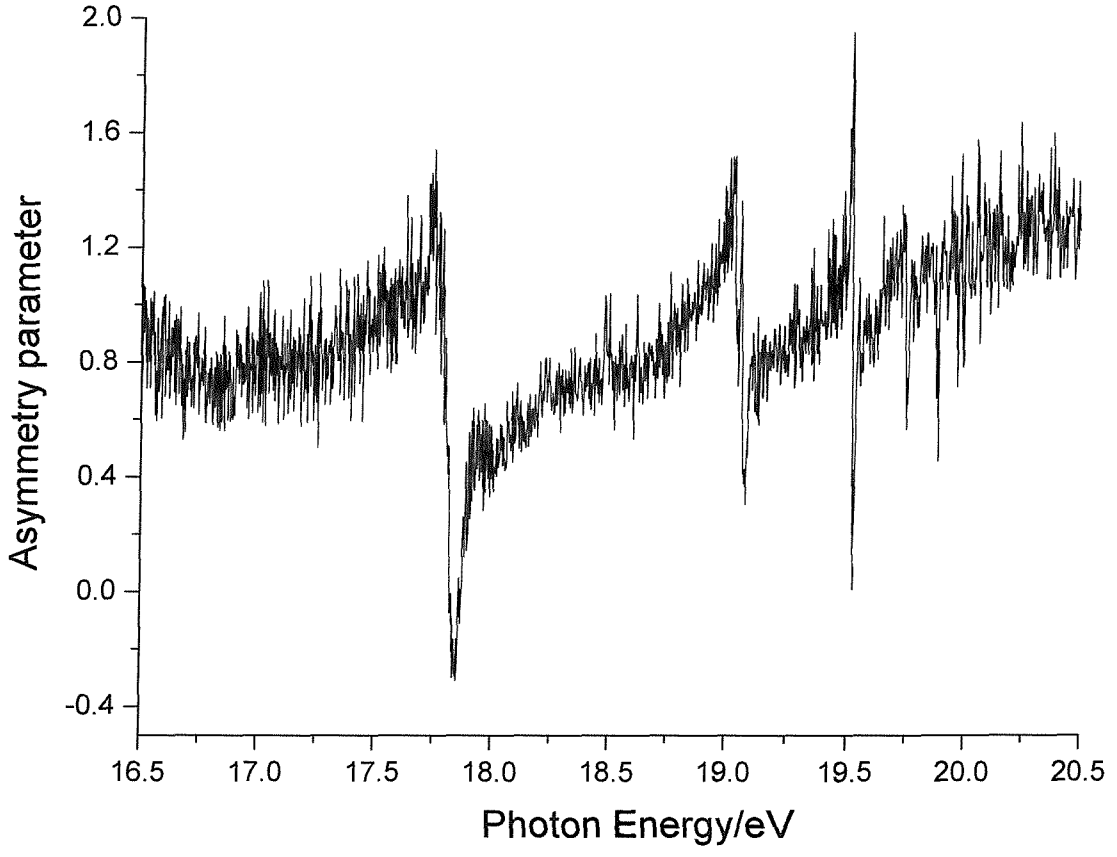

Figure 8.27 *Spectrum of the experimental asymmetry parameter (β) for the $S^{+}(^{2}P) \leftarrow S^{*} \leftarrow S(^{3}P)$ ionization process as a function of photon energy over the range $h\nu$ = 16.5 - 20.5 eV.*

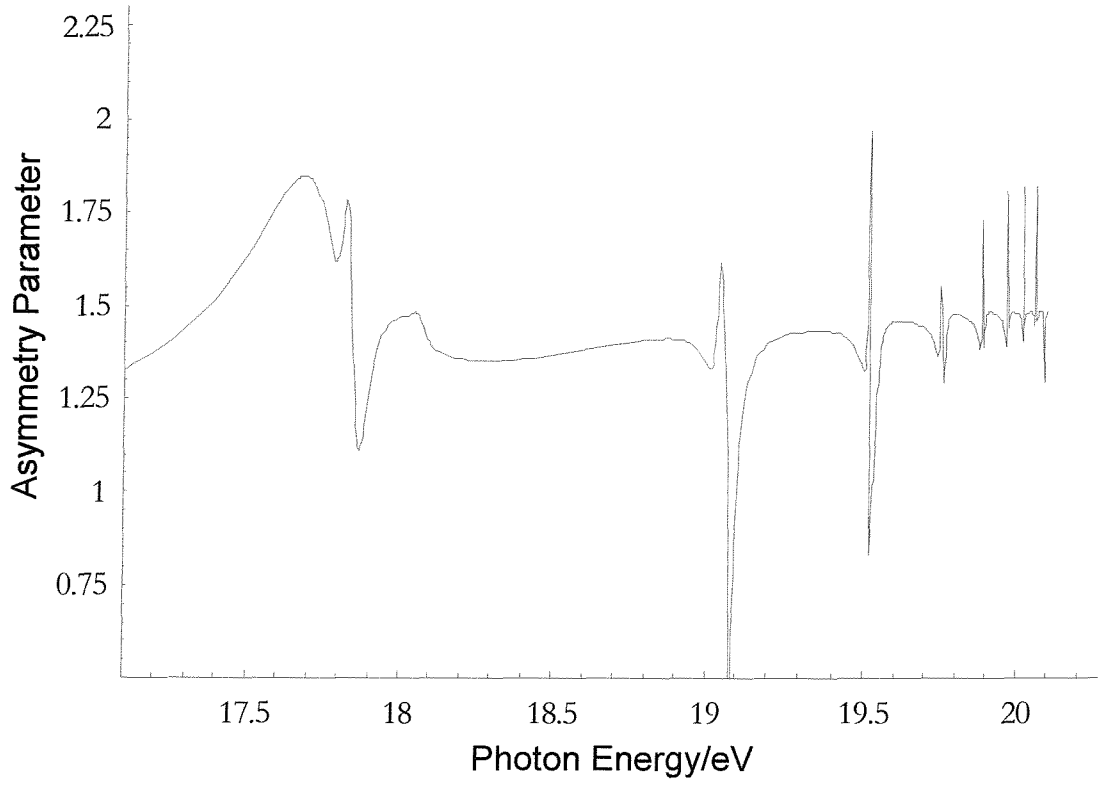

Figure 8.28 *Spectrum of the calculated asymmetry parameter (β) for the* $S^+(^4S) \leftarrow S^* \leftarrow S(^2P)$ *ionization process as a function of photon energy over the range* $h\nu = 17.0 - 20.5$ *eV. This should be compared with the experimental spectrum in Figure 8.25.*

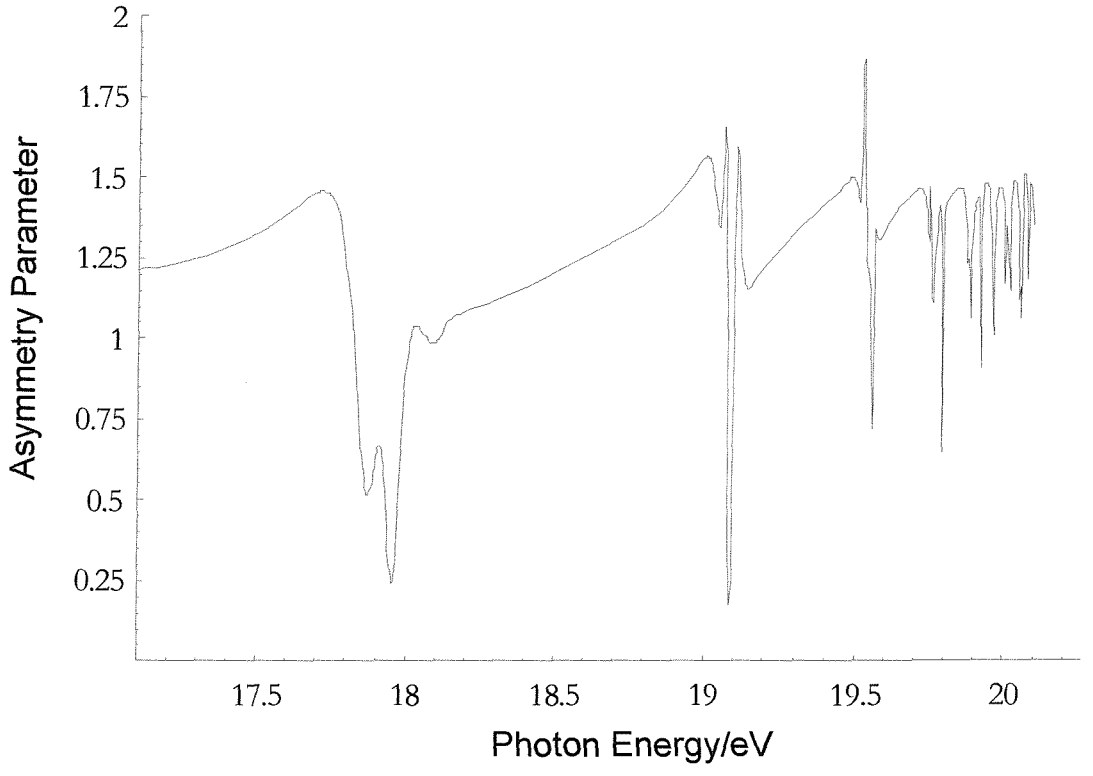

Figure 8.29 *Spectrum of the calculated asymmetry parameter (β) for the* $S^+(^2D) \leftarrow S^* \leftarrow S(^3P)$ *ionization process as a function of photon energy over the range* $h\nu = 17.0 - 20.5$ *eV. This should be compared with the experimental spectrum in Figure 8.26.*

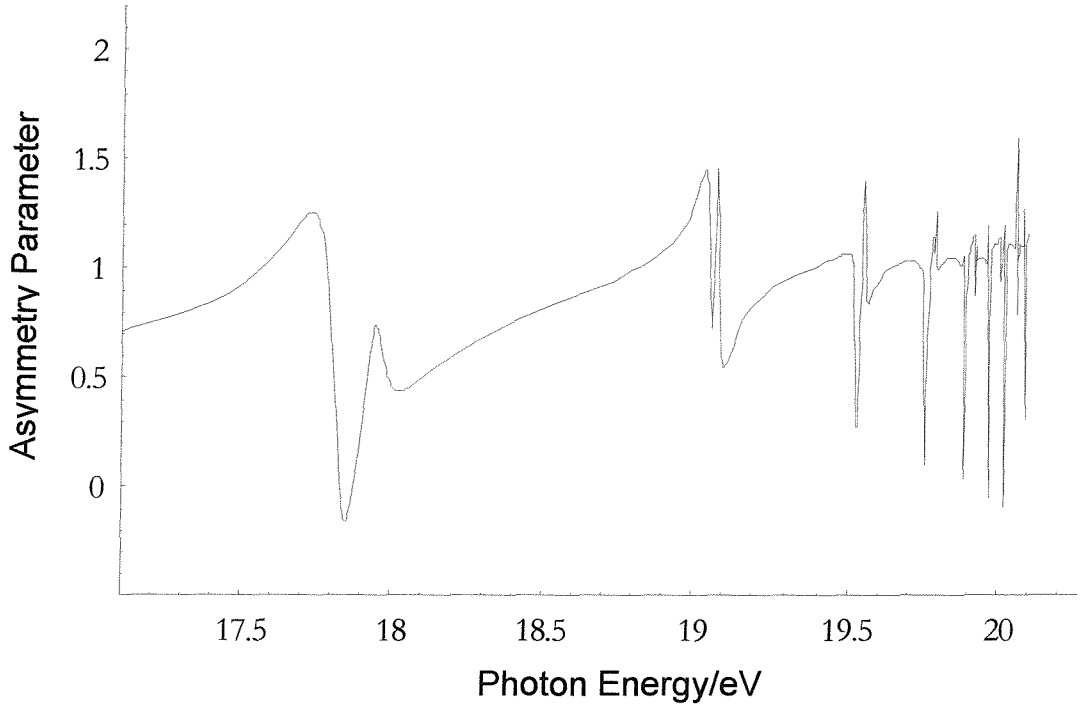

Figure 8.30 *Spectrum of the calculated asymmetry parameter (β) for the $S^+(^2P) \leftarrow S^* \leftarrow S(^3P)$ ionization process as a function of photon energy over the range $h\nu$ = 17.0 - 20.5 eV. This should be compared with the experimental spectrum in Figure 8.27.*

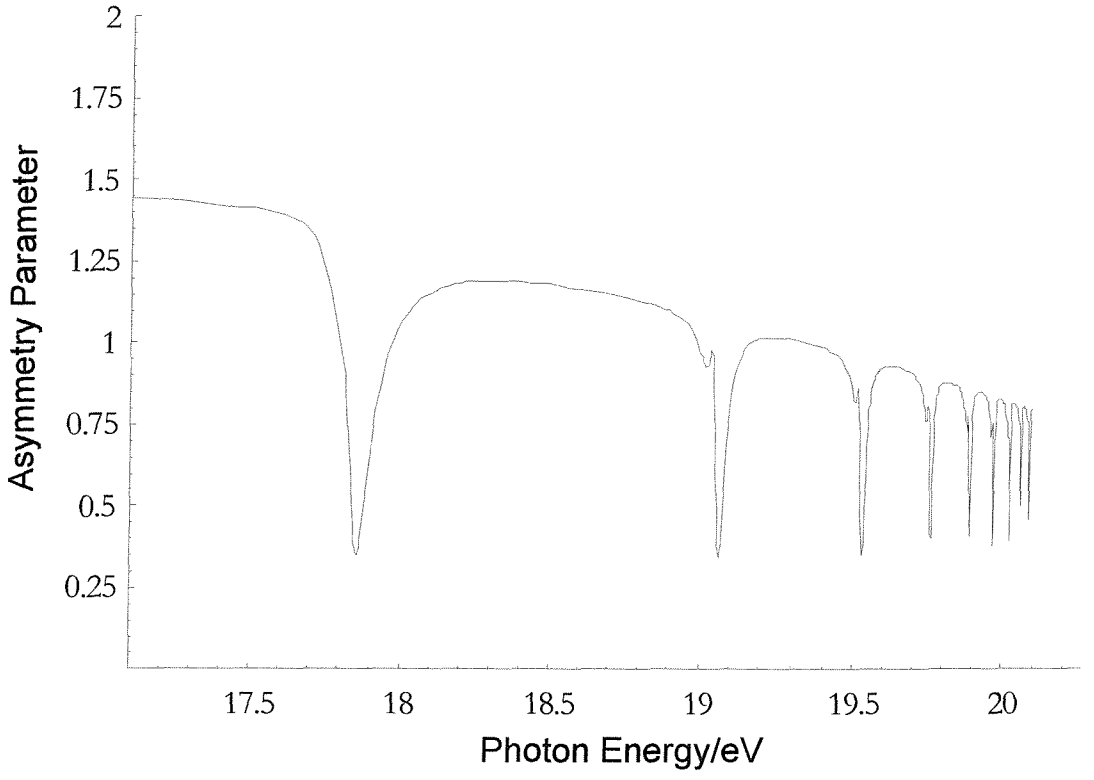

Figure 8.31 *Spectrum of the calculated asymmetry parameter (β) for the Rydberg Series 1 of the* $S^+(^4S) \leftarrow S^* \leftarrow S(^3P)$ *ionization process as a function of the photon energy over the range* $h\nu = 17.0 - 20.5$ *eV.*

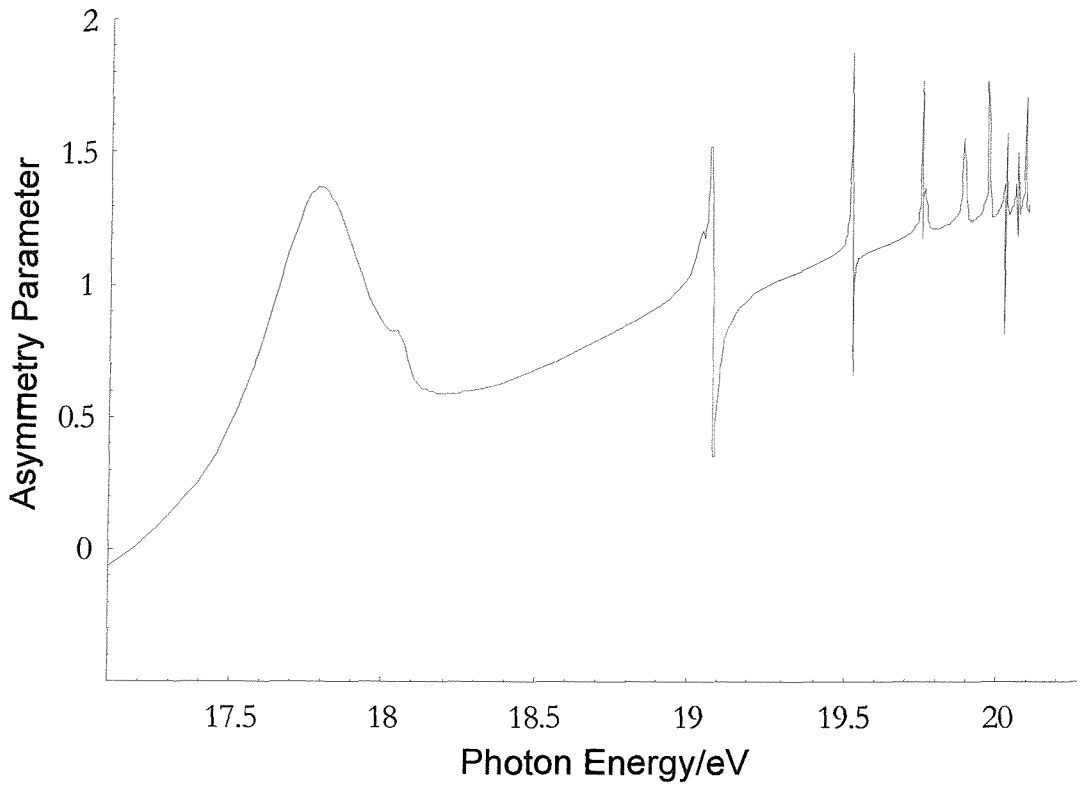

Figure 8.32 *Spectrum of the calculated asymmetry parameter (β) for the Rydberg Series 2 of the $S^+(^4S) \leftarrow S^* \leftarrow S(^3P)$ ionization process as a function of the photon energy over the range $h\nu$ = 17.0 - 20.5 eV.*

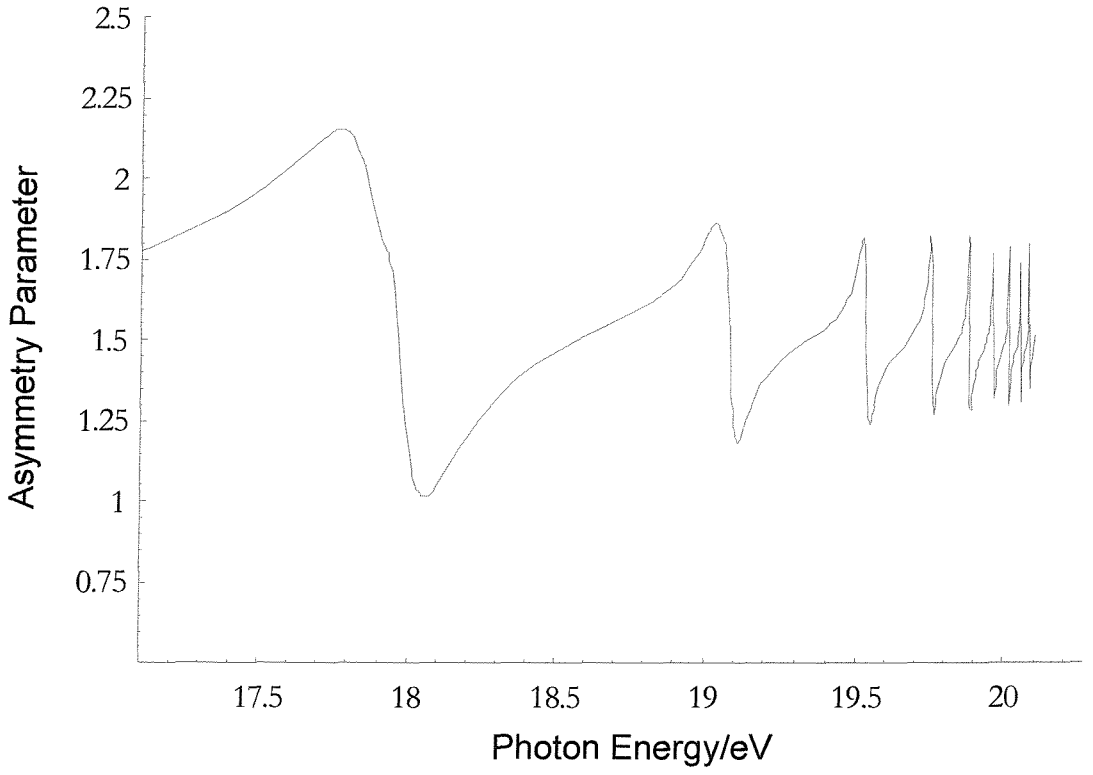

Figure 8.33 *Spectrum of the calculated asymmetry parameter (β) for the Rydberg Series 1 of the $S^+(^2D) \leftarrow S^* \leftarrow S(^3P)$ ionization process as a function of the photon energy over the range $h\nu$ = 17.0 - 20.5 eV.*

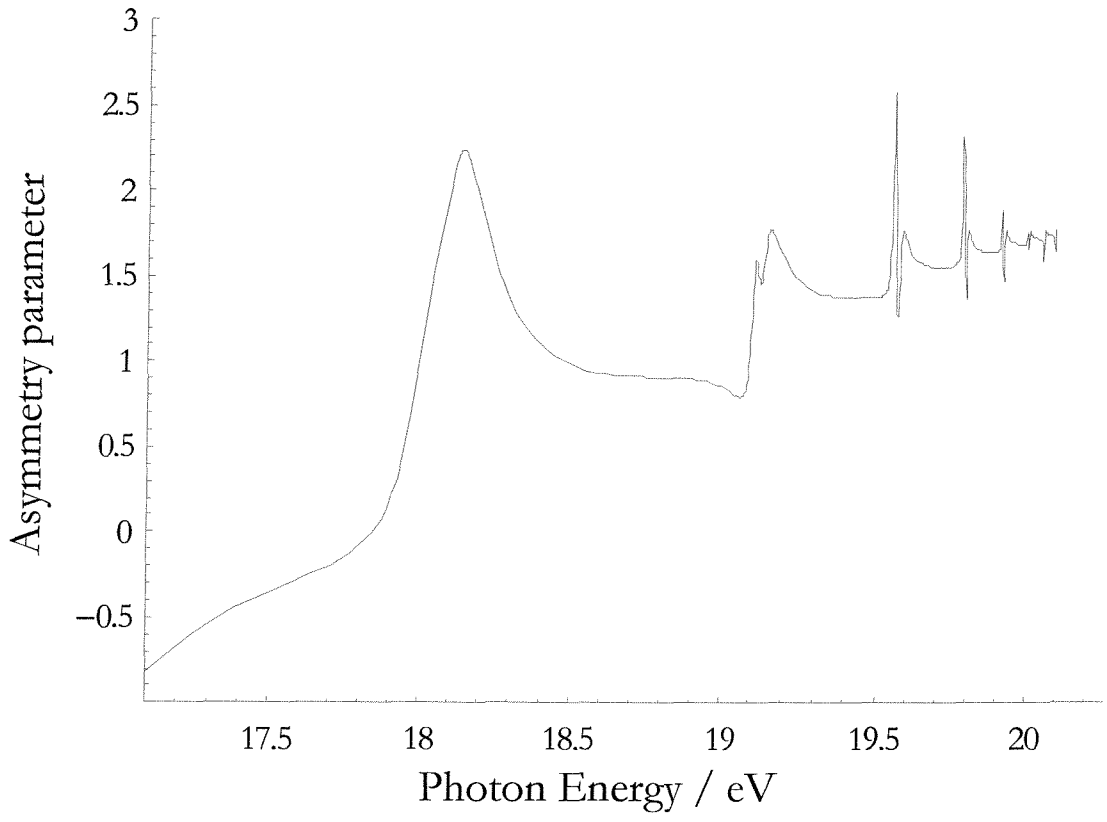

Figure 8.34 *Spectrum of the calculated asymmetry parameter (β) for the Rydberg Series 2 of the $S^+(^2D) \leftarrow S^* \leftarrow S(^3P)$ ionization process as a function of the photon energy over the range $h\nu$ = 17.0 - 20.5 eV.*

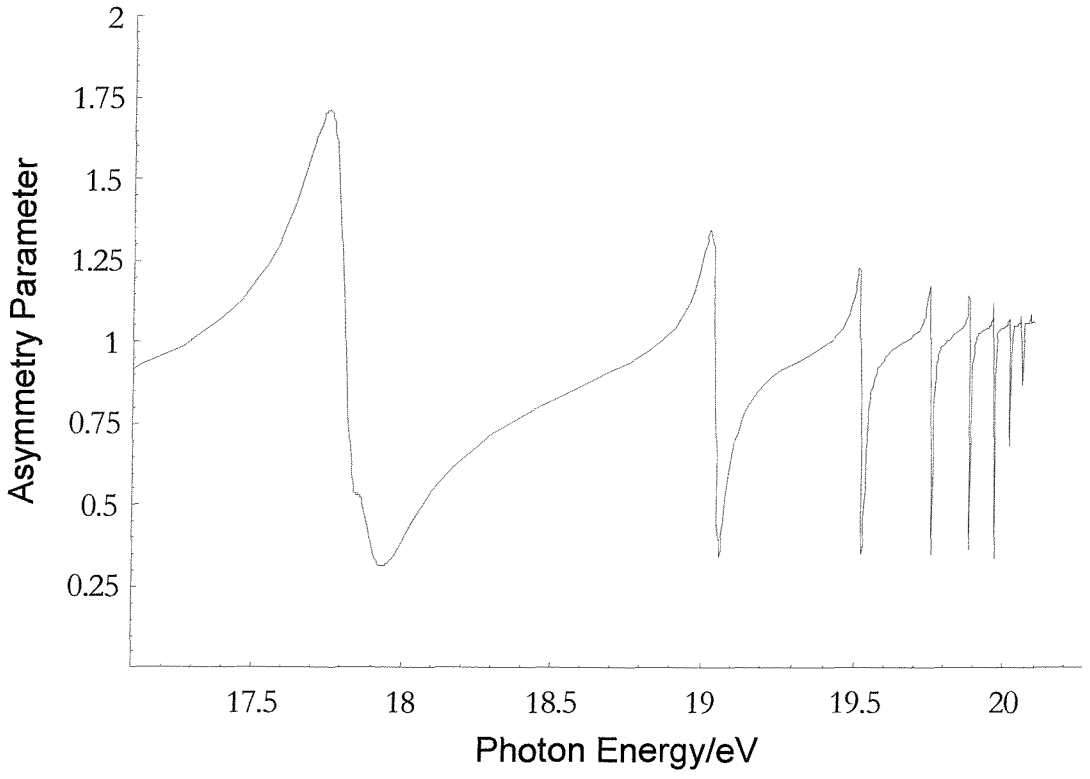

Figure 8.35 *Spectrum of the calculated asymmetry parameter (β) for the Rydberg Series 1 of the $S^+(^2P) \leftarrow S^* \leftarrow S(^3P)$ ionization process as a function of the photon energy over the range $h\nu$ = 17.0 - 20.5 eV.*

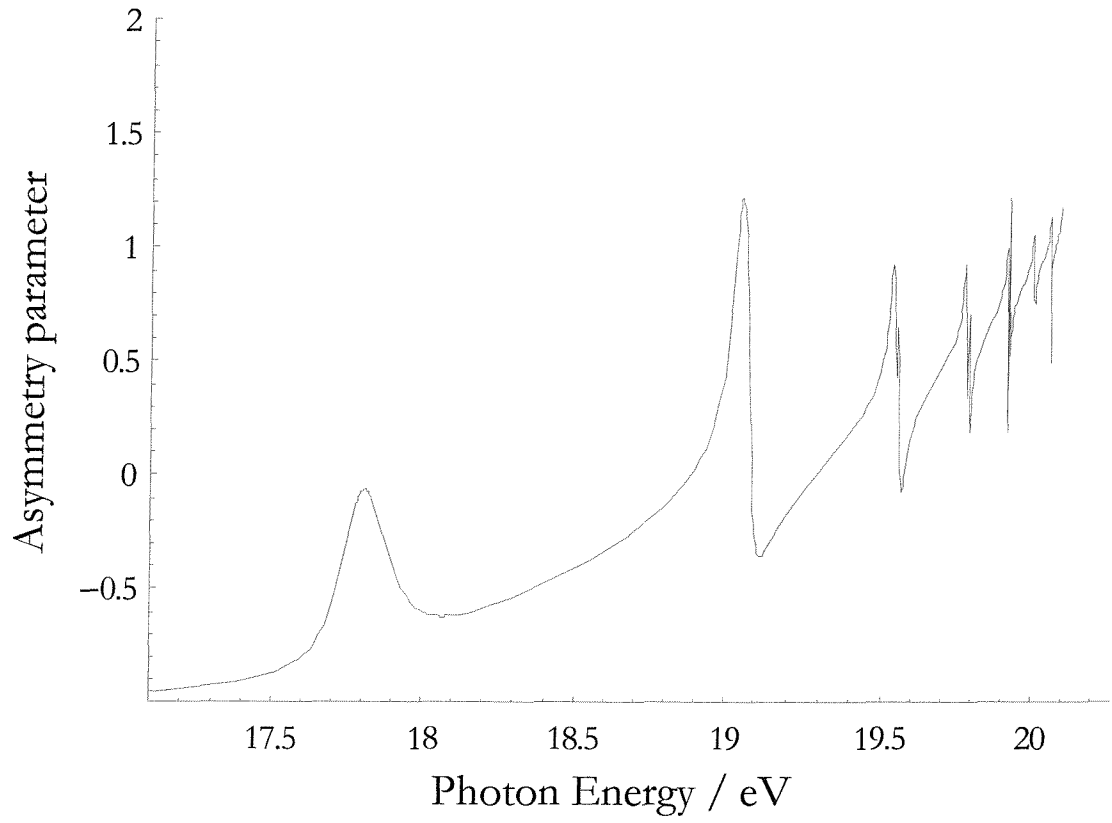

Figure 8.36 *Spectrum of the calculated asymmetry parameter (β) for the Rydberg Series 2 of the $S^+(^2P) \leftarrow S^* \leftarrow S(^3P)$ ionization process as a function of the photon energy over the range $h\nu$ = 17.0 - 20.5 eV.*

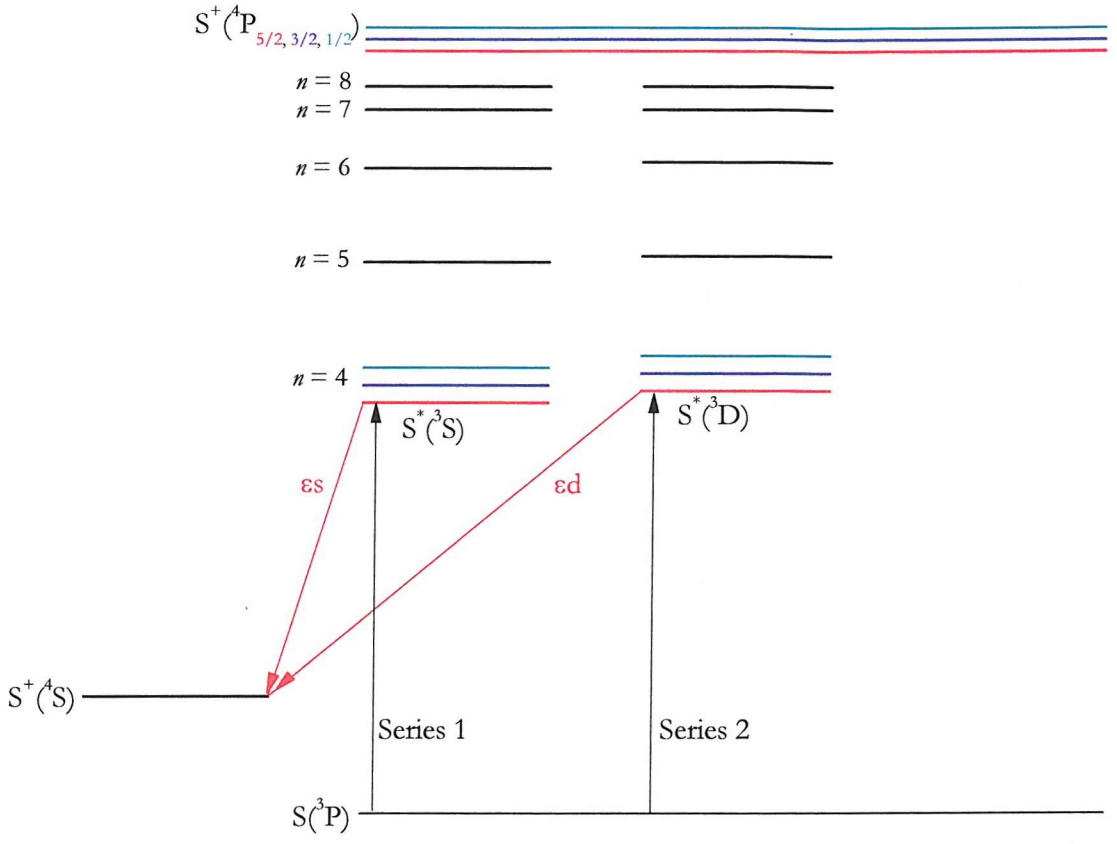

Figure 8.37 *Diagram for the $S^+(^4S) \leftarrow S^* \leftarrow S(^3P)$ ionization process. $S^*(^3S)$ and $S^*(^3D)$ are the two states allowed from the $S(^3P)$ ground state assuming Russell-Saunders coupling valid. The ionic core of the excited S^* atom is split into three spin-orbit states $^4P_{5/2}$ (red line), $^4P_{3/2}$ (blue line) and $^4P_{1/2}$ (green line). For n = 4 the states converging to the three different limits are drawn (for higher n only one state is drawn for convenience). Of the six possible Rydberg series only two are observed in the experimental CIS spectrum going to the $^4P_{5/2}$ limit of the $S^*(^3S)$ and $S^*(^3D)$ states.*

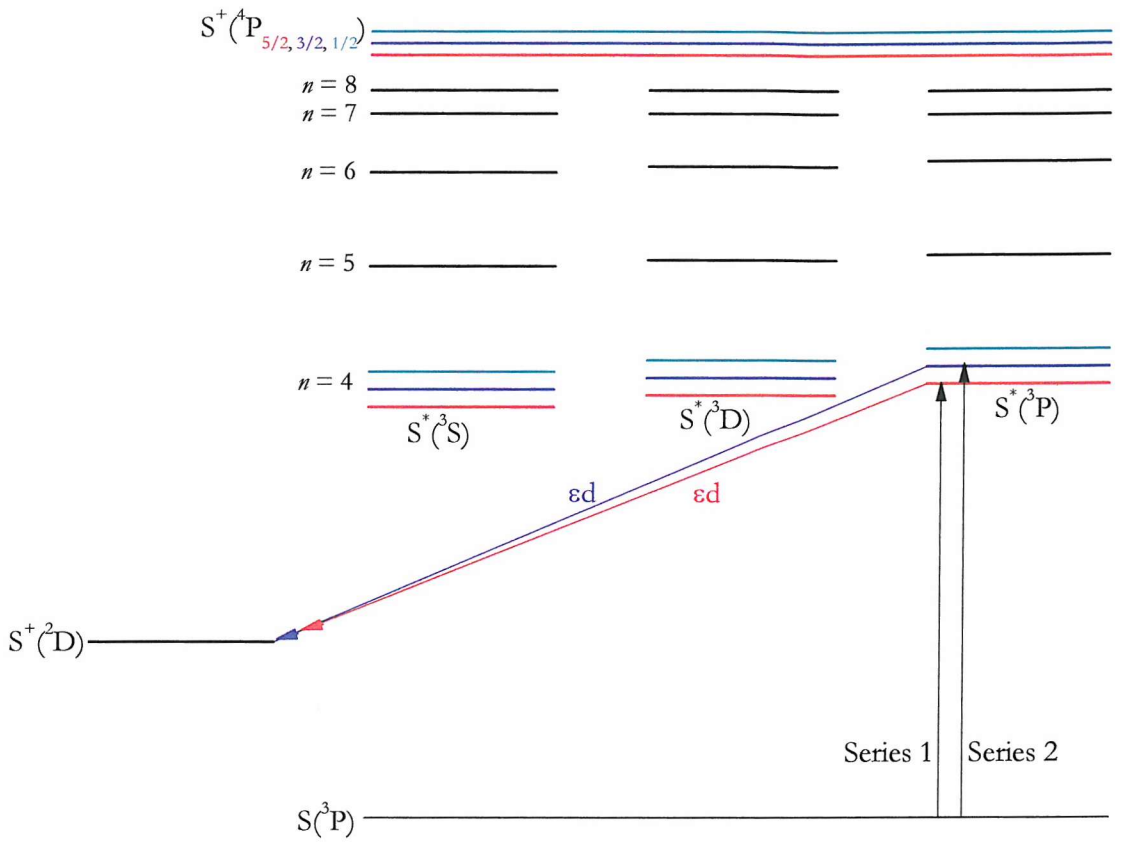

Figure 8.38 *Diagram for the $S^+(^2D) \leftarrow S^* \leftarrow S(^3P)$ ionization process. $S^*(^3S)$, $S^*(^3D)$ and $S^*(^3P)$ are the three states allowed from the $S(^3P)$ ground state assuming Russell-Saunders coupling valid. The ionic core of the excited S^* atom is split into three spin-orbit states $^4P_{5/2}$ (red line), $^4P_{3/2}$ (blue line) and $^4P_{1/2}$ (green line). For n = 4 the states converging to the three different limits are drawn (for higher n only one state is drawn for convenience). Of the nine possible Rydberg series only two are observed in the experimental CIS spectrum going to the $^4P_{5/2}$ and $^4P_{3/2}$ limits of the $S^*(^3P)$ state.*

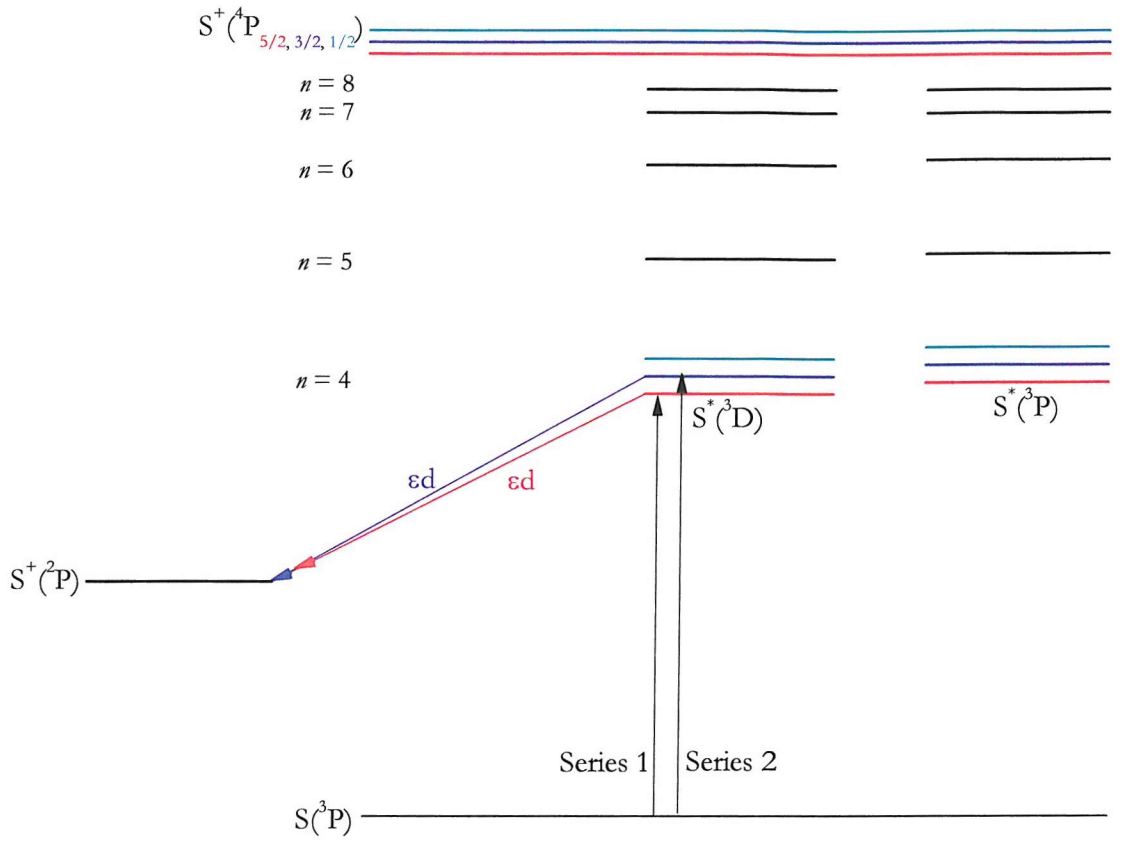

Figure 8.39 *Diagram for the $S^+(^2P) \leftarrow S^* \leftarrow S(^3P)$ ionization process. $S^*(^3D)$ and $S^*(^3P)$ are the two states allowed from the $S(^3P)$ ground state assuming Russell-Saunders coupling valid. The ionic core of the excited S^* atom is split into three spin-orbit states $^4P_{5/2}$ (red line), $^4P_{3/2}$ (blue line) and $^4P_{1/2}$ (green line). For n = 4 the states converging to the three different limits are drawn (for higher n only one state is drawn for convenience). Of the six possible Rydberg series only two are observed in the experimental CIS spectrum going to the $^4P_{5/2}$ and $^4P_{3/2}$ limits of the $S^*(^3D)$ state.*

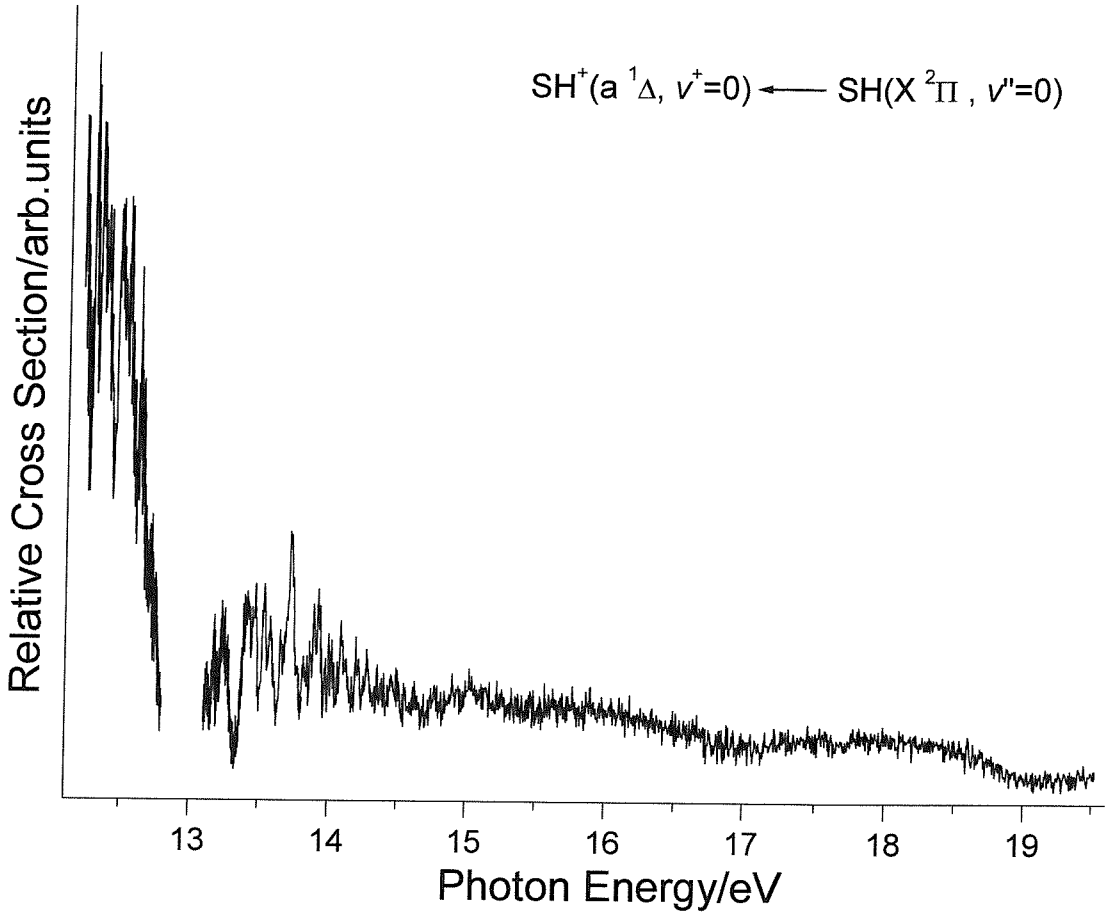

Figure 8.40 *CIS spectra recorded for the $SH^+(a^1\Delta) \leftarrow SH(X^2\Pi)$ process in the 12.1 - 19.6 eV photon energy region, at $\theta = 54°44'$ detection angle.*

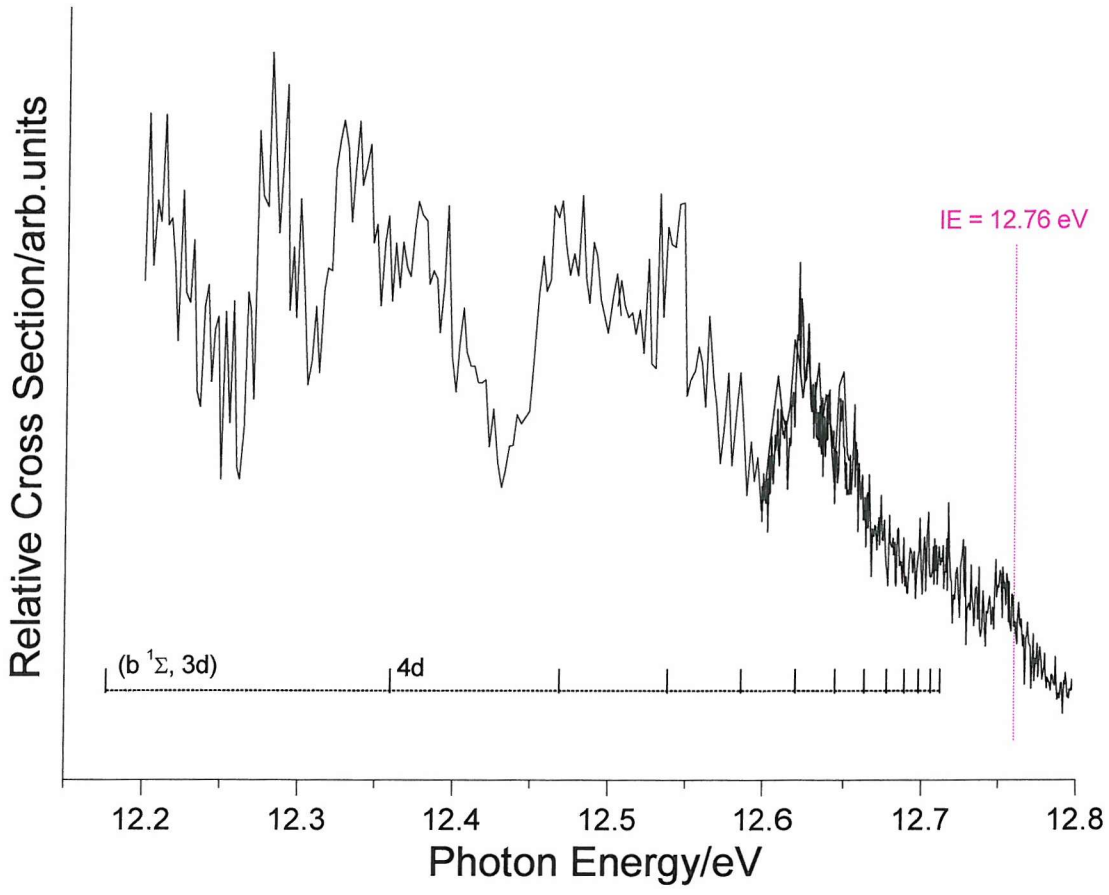

Figure 8.41 *CIS spectra recorded for the $SH^+(a^1\Delta) \leftarrow SH(X^2\Pi)$ process in the 12.2 - 12.8 eV photon energy region, at $\theta = 54°44'$ detection angle, with the third ionization limit marked (magenta trace). Expected positions of $SH^*(b^1\Sigma, nd)$ Rydberg states are indicated.*

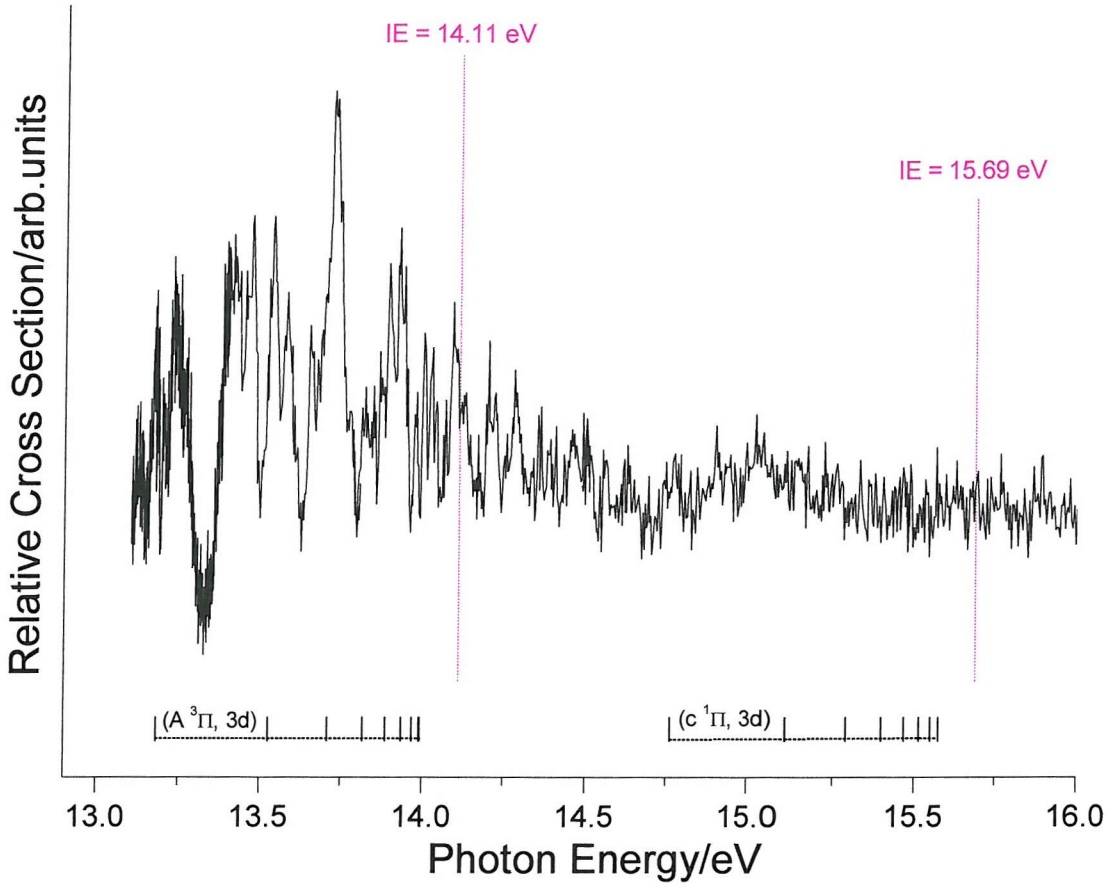

Figure 8.42 *CIS spectra recorded for the $SH^+(a^1\Delta) \leftarrow SH(X^2\Pi)$ process in the 13 - 16 eV photon energy region, at $\theta = 54°44'$ detection angle, with the fourth (IE = 14.11 eV) and fifth (IE = 15.69 eV) ionization limits marked (magenta trace). Expected positions of $SH^*(A^3\Pi, nd)$ Rydberg states and $SH^*(c^1\Pi, nd)$ Rydberg states are indicated.*

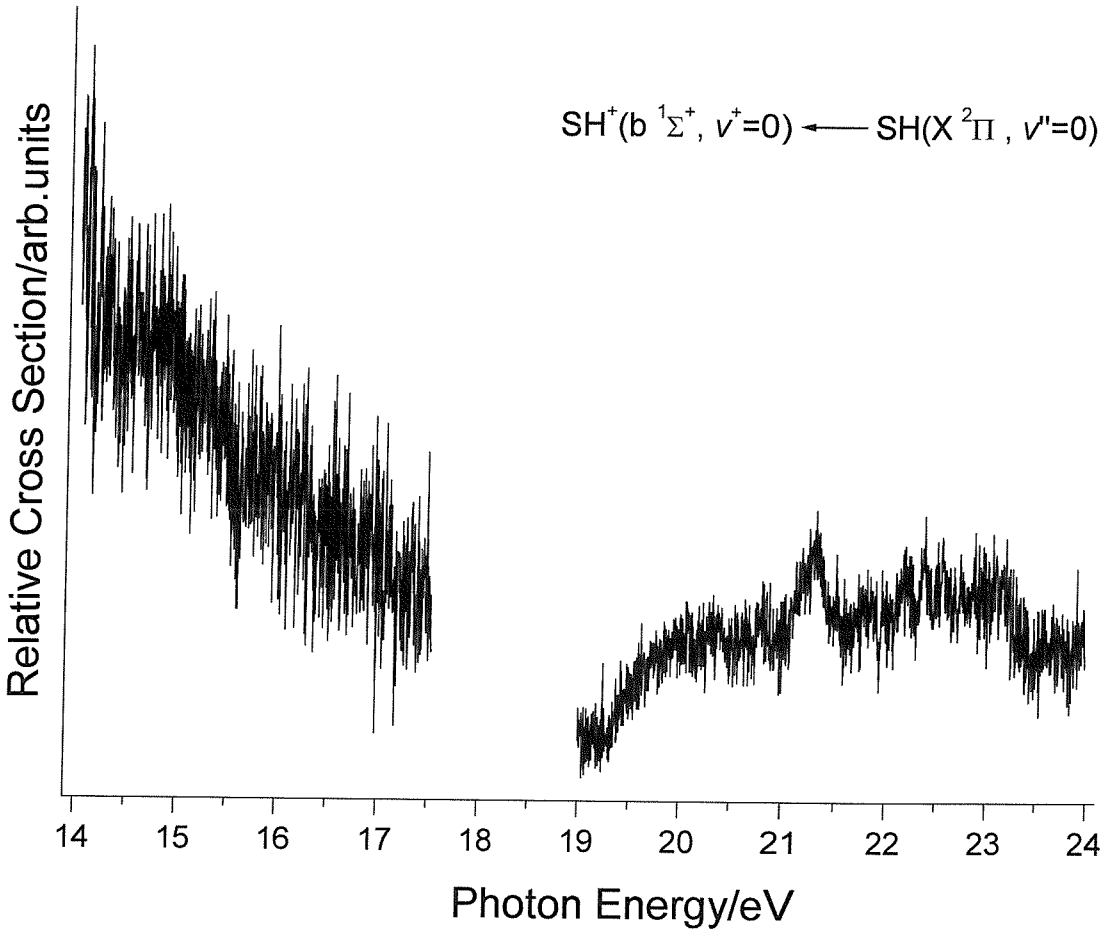

Figure 8.43 *CIS spectra recorded for the $SH^+(b^1\Sigma^+) \leftarrow SH(X^2\Pi)$ process in the 14 - 24 eV photon energy region, at $\theta = 54°44'$ detection angle.*

References

[1] http://www.elettra.trieste.it

[2] http://kinetics.nist.gov/index.php

[3] M. C. R. Cockett, J. M. Dyke and H. Zamanpour *Vacuum Ultraviolet Photoionization and Photodissociation of Molecules and Clusters*, edited by C.Y. Ng, World Scientific ed., 1991.

[4] A. Derossi, F. Lama, M. Piacentini, T. Prosperi and N. Zema
Review of Scientific Instrumentation **66**, 1718 (1995).

[5] D. Desiderio, S. DiFonzo, B. Diviacco, W. Jark, J. Krempasky, R. Krempaska, F. Lama, M. Luce, H. C. Mertins, M. Piacentini, T. Prosperi, S. Rinaldi, F. Schefers, F. Schmolla, G. Soulle, L. Stichauer, S. Turchini, R. P. Walker and N. Zema
Synchrotron Radiation News **12**, 34 (1999).

[6] W. F. Chan, G. Cooper, X. Guo, G. R. Burton and C. E. Brion
Physical Review A: Atomic, Molecular, and Optical Physics **46**, 149 (1992).

[7] http://physics.nist.gov/PhysRefData

[8] S. J. Dunlavey, J. M. Dyke, N. K. Fayad, N. Jonathan and A. Morris
Molecular Physics **38**, 729 (1979).

[9] K. Kimura, S. Katsumata, Y. Achiba, T. Yamazaki and S. Iwata *Handbook of HeI photoelectron spectra of fundamental organic molecules*, Japan Scientific Societies Press ed.Tokyo, 1981.

[10] G. Tondello
Astrophysical Journal **172**, 771 (1972).

[11] D. Muller
Zeitschrift fur Naturforschung **23 A**, 1707 (1968).

[12] J. J. Yeh and I. Lindau
Atomic Data and Nuclear Data Tables **32**, 1 (1985).

[13] Y. N. Joshi, M. Mazzoni, A. Nencioni, W. H. Parkinson and A. Cantu
Journal of Physics B **20**, 1203 (1987).

[14] S. T. Gibson, J. P. Green, B. Ruscic and J. Berkowitz
Journal of Physics B **19**, 2825 (1986).

[15] U. Fano
Physics Review **124**, 1866 (1961).

[16] U. Fano and J. W. Cooper
Physics Review **137**, 1364 (1965).

[17] C. E. Moore *Atomic Energy Levels*, U.S. Government Printing Office ed.Washington DC, 1952; Vol. 1.

[18] H. G. Kuhn *Atomic Spectra*, Longmans ed.London, 1964.

[19] J. M. Hollas *Modern Spectroscopy*, Wiley & Sons ed.Chichester, 1996.

[20] D. Dill, A. F. Starace and S. T. Manson
Physical Review A **11**, 1596 (1975).

[21] K. Maeda, K. Ueda and K. Ito
Journal of Physics B **26**, 1541 (1993).

[22] T. K. Fang and T. N. Chang
Physical Review A **57**, 4407 (1998).

[23] P. Baltzer, L. Karlsson, M. Lundqvist, B. Wannberg, D. M. P. Holland and M. A. MacDonald
Chemical Physics **195**, 403 (1995).

Chapter 9

9 PHOTOELECTRON SPECTROSCOPY OF THE NO RADICAL

This Chapter reports studies on NO($X^2\Pi$) with ultraviolet photoelectron spectroscopy using Synchrotron Radiation.

The Chapter is organized as follows. In section 9.1 previous spectroscopic investigations on NO that are considered important for the present work are briefly reviewed. Section 9.2 presents experimental CIS spectra and resonant photoelectron spectra, together with their interpretations. Section 9.3 summarizes the results obtained.

Because to the large number of plots presented in this Chapter, all the Figures have been grouped at the end of the Chapter.

9.1 Previous investigations on NO($X^2\Pi$) with electron spectroscopy

Of the species present in the earth's atmosphere, NO^+ formed by photoionization of neutral nitric oxide by solar radiation or charge transfer is the major primary ion in the upper atmosphere[1]. Therefore photoionization processes of nitric oxide are of considerable interest to the chemistry of the upper atmosphere. NO is also present in the lower unpolluted atmosphere from reaction of NO_2 with excited atomic oxygen. Many anthropogenic emissions also contribute to the amount of NO in the atmosphere, such as fuel combustion and the burning of biomass[1]. NO also plays an important role in the development of lasers[2]. In addition there is an increasing interest because of its importance in biology and physiology[3].

Furthermore, the open shell nature of the ground state of NO represents a formidable challenge to theorists in the calculation of partial photoionization oscillator strengths[4].

There have been a considerable number of experimental studies carried out on NO using techniques such as photoelectron spectroscopy (PES)[5-13], absorption spectroscopy[14-25], mass analyzed photoion excitation (PIE)[26-31], inelastic electron scattering[32-36], fluorescence emission spectroscopy (FES)[37-40] and multiphoton excitation[41,42].

Different methods have been applied to calculate the NO photoionization cross sections and angular distributions: they include the Stieltjes-Tchebycheff moment theory (STMT)[4,43,44], the Schwinger variational (SV) method[45-47], the continuum multiple scattering method (CSSM)[48], the linear algebraic (LA) method[49-51] and the multiple scattering self consistent field (MSSCF) method[52].

NO is essentially heteronuclear but the composite atoms are consecutive in the periodic table. Therefore it may be considered approximately homonuclear and the (u, g) symmetry classification retained, though the u↔g symmetry selection rule is not strong for all the transitions[5,49]. The ground state molecular-orbital configuration of NO is $1\sigma_g^2 2\sigma_u^2 3\sigma_g^2 4\sigma_u^2 5\sigma_g^2 1\pi_u^4 2\pi_g^1$, $X^2\Pi_g$ and it is split into two components $^2\Pi_{3/2}$ and $^2\Pi_{1/2}$, with the $^2\Pi_{1/2}$ lowest. The spin-orbit splitting is 15 meV[29].

Removal of the antibonding 2π electron results in the $NO^+(X^1\Sigma^+)$ ionic state at adiabatic ionization energy of 9.264 eV[42]. The equilibrium internuclear separation is

smaller in $NO^+(X^1\Sigma^+)$ than the neutral ground state[53], consequently several vibrational levels of the $X^1\Sigma^+$ ionic state are observed in PE spectrum[6]. One-electron removal from the 1π level gives rise to six states: $a^3\Sigma^+$, $w^3\Delta$, $b'^3\Sigma^-$, $A'^1\Sigma^-$, $W^1\Delta$ and $B'^1\Sigma^+$, in order of increasing ionization energy[6]. The 1π orbital is a bonding orbital therefore the equilibrium bond length in the ion is greater than in the neutral and the associated photoelectron bands have a long vibrational progressions[6]. Two ionic states arise on $(5\sigma)^{-1}$ bonding orbital ionization: $b^3\Pi$ and $A^1\Pi$ at vertical ionization energies of 16.561 and 18.325 eV respectively[6]. The $NO^+(b^3\Pi)$ $v^+ = 0$ vibrational component is the stronger vibrational component in the PE spectrum while the $v' = 1$ is almost 1/10 of its intensity[6].

At excitation energies above 13 eV, relative to the ground state, several autoionizing Rydberg series converging to excited states of NO^+ have been observed and assigned using quantum defect analysis[5,14,15,17,19,22,29,34]. Table 9-1 shows all the possible Rydberg states arising from excitation of a $1\pi_u$ and $5\sigma_g$ electron[34]. The transitions which are electric dipole forbidden by the u/g selection rule are indicated with the symbol *. In the table only the dipole allowed excited state symmetries are reported. One electron transitions from the $X^2\Pi$ ground state give rises to possible resonant states of $^2\Sigma^+$, $^2\Sigma^-$, $^2\Pi$ and $^2\Delta$ symmetries; however, the $^2\Sigma^-$ state cannot decay by autoionization into the $NO^+(X^1\Sigma^+)$ final state continuum as a consequence of parity conservation. Autoionization from the $^2\Sigma^+$, $^2\Pi$ and $^2\Delta$ states to the NO^+ $X^1\Sigma^+$ final state leads to $\varepsilon k\sigma$, $\varepsilon k\pi$ and $\varepsilon k\delta$ outgoing waves respectively[13].

In practice, of all the series reported in Table 9-1, the $5\sigma \rightarrow n\text{p}\pi$ and $5\sigma \rightarrow n\text{p}\sigma$ series converging to the $NO^+(b^3\Pi, v^+=0)$ state at 16.56 eV are the most prominent in the experimental spectra such as absorption and photoion excitation spectra. The $n = 3$, $v' = 0$ members have been assigned at 13.815 and 14.005 eV for the $n\text{p}\pi$ and $n\text{p}\sigma$ series respectively[5,19,29,34] with an energy uncertainty between different studies of 10 meV. The $n\text{p}\pi$ series has been assigned at lower energy with respect the $n\text{p}\sigma$ series only on the assumption that the same relation found in the Rydberg series converging to the first ionic limit, $X^1\Sigma^+$, where the $n\text{p}\sigma$ states were found to have higher energy than the $n\text{p}\pi$ states[5,18,19,22], also applies to these series.

Table 9-1 *Possible Rydberg series in NO arising from the excitation of either a $1\pi_u$ or a $5\sigma_g$ electron. The excited state symmetry and the free electron symmetry for autoionization to the $X^1\Sigma^+$ ground state are presented. The transitions which are electric dipole forbidden by the u/g selection rule are indicated with the symbol *.*

Rydberg transition	Ionic state core	Excited state symmetry	Outgoing waves for $X^1\Sigma^+$ autoionization
$1\pi_u \rightarrow ns\sigma_g$	$a^3\Sigma^+$	$^2\Sigma^+$	$\varepsilon k\sigma$
$1\pi_u \rightarrow np\sigma_u$*	$w^3\Delta$	$^2\Delta$	$\varepsilon k\delta$
$1\pi_u \rightarrow nd\sigma_g$	$W^1\Delta$	$^2\Delta$	$\varepsilon k\delta$
	$B'^1\Sigma^+$	$^2\Sigma^+$	$\varepsilon k\sigma$
$1\pi_u \rightarrow np\pi_u$*	$a^3\Sigma^+$	$^2\Pi$	$\varepsilon k\pi$
$1\pi_u \rightarrow nd\pi_g$	$w^3\Delta$	$^2\Pi$	$\varepsilon k\pi$
	$b'^3\Sigma^-$	$^2\Pi$	$\varepsilon k\pi$
	$W^1\Delta$	$^2\Pi$	$\varepsilon k\pi$
	$B'^1\Sigma^+$	$^2\Pi$	$\varepsilon k\pi$
	$A'^1\Sigma^-$	$^2\Pi$	$\varepsilon k\pi$
$1\pi_u \rightarrow nd\delta_g$	$a^3\Sigma^+$	$^2\Delta$	$\varepsilon k\delta$
	$w^3\Delta$	$^2\Sigma^+$	$\varepsilon k\sigma$
	$b'^3\Sigma^-$	$^2\Delta$	$\varepsilon k\delta$
	$W^1\Delta$	$^2\Sigma^+$	$\varepsilon k\sigma$
	$B'^1\Sigma^+$	$^2\Delta$	$\varepsilon k\delta$
	$A'^1\Sigma^-$	$^2\Delta$	$\varepsilon k\delta$
$5\sigma_g \rightarrow ns\sigma_g$*	$b^3\Pi$	$^2\Pi$	$\varepsilon k\pi$
$5\sigma_g \rightarrow np\sigma_u$	$A^1\Pi$	$^2\Pi$	$\varepsilon k\pi$
$5\sigma_g \rightarrow nd\sigma_g$*			
$5\sigma_g \rightarrow np\pi_u$	$b^3\Pi$	$^2\Delta$	$\varepsilon k\delta$
$5\sigma_g \rightarrow nd\pi_g$*	$b^3\Pi$	$^2\Sigma^+$	$\varepsilon k\sigma$
	$b^3\Pi$	$^2\Sigma^-$	Forbidden
	$A^1\Pi$	$^2\Delta$	$\varepsilon k\delta$
	$A^1\Pi$	$^2\Sigma^+$	$\varepsilon k\sigma$
	$A^1\Pi$	$^2\Sigma^-$	Forbidden

The excited state symmetries $^2\Delta$ and $^2\Sigma^+$ have not been assigned to individual bands experimentally, as the $^2\Delta$ and $^2\Sigma^+$ bands for the $5\sigma \rightarrow n\pi$ transitions have not been resolved; only the high resolution photoabsorption analysis of Takezawa[19] shows separated bands for $n = 4$ while for $n = 3$ the band is unresolved and shows a diffuse appearance.

The $3p\pi$ member converging to $NO^+(b^3\Pi, v^+=1)$ state has been assigned at 14.060 eV[5,29,34] which gives a separation of $\approx$ 240 meV with respect the component which is part of the series converging to $v' = 0$. The vibrational spacing of a Rydberg series is expected to be very close to that of the ionic core which is $\approx$ 200 meV in the case of the $NO^+(b^3\Pi)$ ionic state[6]. Therefore the assignment given by the previous experimental works seems inconsistent.

Most of the theoretical studies have calculated the partial photoionization cross sections and photoelectron asymmetry parameters for ionization from the 2π, 5σ and 4σ orbitals. Early theoretical studies[4,45,49] of photoionization from the 2π level of NO have predicted a shape resonance in the 14 eV photon energy range. A shape resonance is a single particle resonance and it arises from the temporary trapping of the photoelectron in a potential barrier. The calculated components $2\pi \rightarrow k\sigma$, $2\pi \rightarrow k\pi$ and $2\pi \rightarrow k\delta$ contributing to the partial cross section from the work of Smith *et al.*[45] and Collins *et al.*[49] are shown in Figure 9.1. Smith's results are obtained from direct solution of the $e^- + NO^+$ collisional equations at the static-exchange level using the Schwinger variational method. Collins applied the linear algebraic method at the continuum Hartree-Fock level. In addition Collins made the frozen-core approximation and correlation effects in the scattering solutions are introduced through an effective optical potential. In Collins's plot a comparison with the results of the (e,2e) experiment of Brion and Tan[32] and the synchrotron experiment of Southworth *et al.*[11] is made. The results of the two calculations are very close and in both cases a resonant feature is evident in the $2\pi \rightarrow k\sigma$ channel while the non-resonant $2\pi \rightarrow k\pi$ and $2\pi \rightarrow k\delta$ contributions to this partial cross section do not show any sharp structure.

Shape resonances in the σ continuum are known to play an important role in the photoionization of many diatomic molecules and to affect the cross sections,

asymmetry parameters and vibrational branching ratios of these molecules[46,54,55]. A search for the effects of the predicted NO $2\pi \rightarrow k\sigma$ shape resonance has been conducted by Southworth *et al.*[9] by recording vibrationally and angular resolved PE spectra of NO. Vibrationally dependent structure in the PE spectrum and asymmetry parameter was observed in the 11 - 18 eV photon energy region, which supported the presence of the shape resonance (note the increase in photoionization cross-section in the work of Brian and Southworth below 20 eV in Figure 9.1). Since a coarse photon energy step has been used in these experiments, this structure may be due in part to the several closely spaced and unresolved autoionizing Rydberg series from the 1π and 5σ orbital.

The experiments of Southworth motivated the theoretical studies of Lynch *et al.*[50,51] on the 2π photoionization of NO with overall final state symmetry of $^2\Sigma^+$ for the photoionization continuum. Using a single configuration treatment for NO, they showed that the presence of the $k\sigma$ shape resonance centred at 14 eV does not account for all the structure observed in the work of Southworth *et al.*[9]. They found evidence that states which are part of the $5\sigma \rightarrow n\pi$ autoionizing Rydberg series interact strongly with a valence autoionizing state which was identified as a $4\sigma \rightarrow 2\pi$ excitation. Figure 9.2 (a) shows how including only the valence resonant state, simulated with a potential, significantly alters the $k\sigma$ photoionization cross section and appears as a broad strong feature centred at 15.8 eV. If only the $5\sigma \rightarrow n\pi$ Rydberg series are included in the potential, the sharp and intense resonances are simply superimposed upon the $k\sigma$ shape resonant continuum as shown in Figure 9.2 (b). Figure 9.2 (c) shows the dramatic interference between the Rydberg series and the valence resonance when both are included in the potential.

An extension of the studies of Lynch is presented by Stratmann *et al.*[47] who used multichannel multiplet-specific interaction potentials derived from wavefunctions which include electron correlation of the initial state. The resulting scattering equations were solved using the Schwinger variational method. They found in addition to the $^2\Sigma^+$ valence resonance a narrower valence resonance of $^2\Delta$ symmetry. Figure 9.3 (a) shows the computed partial photoionization cross-section in the photon energy region 12 - 20 eV including only the components that correspond to a

final excited state symmetry of $^2\Sigma^+$. The $4\sigma \rightarrow 2\pi$ valence resonance couples strongly to the shape resonance but the $5\sigma \rightarrow n\pi$ Rydberg series are simply superimposed on the previous structure in contrast to the results from Lynch shown in Figure 9.2 (c). In Figure 9.3 (b) is presented the partial photoionization cross in the 12 - 19 eV region corresponding to a final state symmetry of $^2\Delta$. Again the Rydberg series are superimposed on the underlying $4\sigma \rightarrow 2\pi$ valence resonance.

Figure 9.3 (c) shows the total photoionization cross section and a strong intense feature is predicted at 14.3 eV consisting of the $^2\Delta$ valence resonance superimposed on two $5\sigma \rightarrow 3p\pi$ and $5\sigma \rightarrow 3p\sigma$ Rydberg states of $^2\Delta$ and $^2\Pi$ final state symmetry respectively. The broad structure with some sharp features seen in the 11 - 18 eV region in the experiments of Southworth[9,11] is therefore due to two pronounced valence autoionizing states one of which is broadened by interaction with a shape resonance. As mentioned before, the broad structure in the Southworth[9,11] experiments could be due to the coarse photon energy step used. More recently Southworth *et al.*[12] repeated the experiment recording PE spectra on the vibrational levels of $NO^+(X^1\Sigma^+)$ in the 12.5 - 18.0 eV region with 10 meV steps and 2 Å bandwidth corresponding to $\approx$ 35 meV at 15 eV. From the sum over the $v^+ = 0 - 5$ vibrational levels they obtained the relative photoionization cross section plot shown in Figure 9.4 (a) and (c). A comparison of Figure 9.4 (a) and Figure 9.3 (c) shows that the two broad valence resonances predicted by Stratmann[47] are not evident in the experimental results of Southworth[12] where narrower $5\sigma \rightarrow np$ Rydberg series are observed. The experimental spectrum is closer to the calculated spectrum by Lynch[50] shown in Figure 9.2 (b) where only the interaction between $k\sigma$ shape and $5\sigma \rightarrow n\pi$ Rydberg resonances is taken into account. Therefore no experimental evidence of valence resonances interacting with the shape resonance or Rydberg states seems to be present in the Southworth[12] work, although there is not any discussion in this paper about this matter. A smaller step size and a smaller bandwidth could help to definitively rule out the presence of valence resonances.

Using simple quantum defect theory, Stratmann[47] also presented the energies of the autoionizing $5\sigma \rightarrow np$ Rydberg series discriminating between the final state symmetry. In order of increasing energies the sequence is $5\sigma \rightarrow np\pi$ ($^2\Delta$), $5\sigma \rightarrow np\sigma$

($^2\Pi$) and $5\sigma \rightarrow n\text{p}\pi$ ($^2\Sigma^+$) while experimentally the two series $5\sigma \rightarrow n\text{p}\pi$ ($^2\Delta$ and $^2\Sigma^+$) are believed to be overlapped and unresolved. Hermann *et al.*[4] also reported a multiplet-specific static-exchange calculation of the Rydberg series converging to $NO^+(b^3\Pi)$. In order of increasing energies the sequence is $5\sigma \rightarrow n\text{p}\sigma$ ($^2\Pi$), $5\sigma \rightarrow n\text{p}\pi$ ($^2\Delta$) and $5\sigma \rightarrow n\text{p}\pi$ ($^2\Sigma^+$) which is again different from the experimental assignment[5,19,29,34]. Moreover they report calculated values of the optical oscillator strengths *f*; the $5\sigma \rightarrow n\text{p}\sigma$ ($^2\Pi$) series is ten times more intense than the two $5\sigma \rightarrow n\text{p}\pi$ ($^2\Delta$ and $^2\Sigma^+$) series, the reverse of what is reported experimentally[5,19,29,34]. The study of the $n\text{p}\pi$ and $n\text{p}\sigma$ resonances converging to $NO^+(b^3\Pi)$ ionic state in the 13.7 - 17.0 eV region is particularly relevant since NO is isoelectronic with the CF radical. The ground state electronic configuration of CF is $1\sigma^2 2\sigma^2 3\sigma^2 4\sigma^2 1\pi^4 5\sigma^2 2\pi^1$, $X^2\Pi$. As for NO, the $X^1\Sigma^+$ ionic state arises from ionization from the 2π level, the $a^3\Pi$ and $A^1\Pi$ ionic states arise from the 5σ level and six ionic states $^{1,3}\Sigma^+$, $^{1,3}\Delta$ and $^{1,3}\Sigma^-$ arise from ionization from the 1π level. With respect NO, the 1π and 5σ orbitals are in a different energy order with the 5σ orbital being higher than the 1π orbital in CF[56]. In recent CIS studies by the Southampton PES group, Rydberg series converging to the $CF^+(a^3\Pi)$ ionic state have been observed for the first time. The behaviour of these series is believed to be similar to the $n\text{p}\pi$ and $n\text{p}\sigma$ resonant states which are part of the series which converge to the $NO^+(b^3\Pi)$ ionic state.

Although NO has been studied extensively, the above literature review raises doubts on the assignments of the resonant states converging to the $NO^+(b^3\Pi)$ ionic state. Therefore, the purpose of the present work is to assign these resonances and possibly to determine experimentally the bands associated with the excited state symmetries (*viz.* $^2\Sigma^+$, $^2\Pi$ or $^2\Delta$). Furthermore it may be possible to observe experimentally the presence of the expected shape or valence resonances, and study the effects they have on the partial photoionization cross section and the photoelectron asymmetry parameter β.

9.2 Results and discussion

To achieve the above purpose, measurements of angular distribution parameters and relative photoionization cross sections for the $NO^+(X^1\Sigma^+,v^+=0) \leftarrow NO(X^2\Pi)$, $NO^+(X^1\Sigma^+,v^+=1) \leftarrow NO(X^2\Pi)$ and $NO^+(X^1\Sigma^+,v^+=2) \leftarrow NO(X^2\Pi)$ bands as a function of photon energy from 13.5 to 17.0 eV have been performed at the ELETTRA Synchrotron Radiation Source. The relative photoionization cross section for the $NO^+(X^1\Sigma^+,v^+=1) \leftarrow NO(X^2\Pi)$ band has been measured from 13.5 up to 30 eV. A fine photon energy step of ≈ 1 meV was used with a bandwidth of ≈ 3 meV. Once the Rydberg series converging to $NO^+(b^3\Pi)$ ionic state were observed in the CIS spectra, PE spectra of NO were recorded at the resonant energies to study the effects on the vibrational components and the asymmetry parameter of the first band of NO. To assist analysis, Franck-Condon factors for the two processes "Dipole" and "Monopole" have been computed for the NO^* Rydberg states with $NO^+(b^3\Pi)$ as core, i.e.

$$NO^+(X^1\Sigma^+,v^+)+e^- \xleftarrow{Monopole} NO^*(b^3\Pi,v') \xleftarrow{Dipole} NO(X^2\Pi,v''=0)+h\nu$$

The resonant NO^* Rydberg states lie above $NO^+(X^1\Sigma^+)$ and autoionize to this ionic state. In the direct photoionization process, the relative intensities of vibrational levels produced in the molecular ion are determined by the squares of the overlap integrals between the ground state and the ionic state vibrational wavefunctions, i.e. the Frank-Condon factors. In the case of autoionizing via a resonant state, the intensities in the PE spectra are controlled by the Frank-Condon factors between the resonant excited state and the ion. To calculate Frank-Condon factors, the spectroscopic constants ω_e, $\omega_e x_e$ and r_e were used to generate a Morse potential for the NO, NO^* and NO^+ states. From numerical solutions of the vibrational Schroedinger equation the vibrational wavefunctions were obtained. The molecular ionization is then described by transitions between the potential curves of the ground state, Rydberg state and ionic state[57].

CIS spectra for a particular vibrational level v^+ were simulated by multiplying computed Franck-Condon factors for steps "Dipole" and "Monopole" together. The

relative population of each particular level v' in the Rydberg state is established by the Frank-Condon factor for process "Dipole" where $v" = 0$ is the only vibrational level significantly populated in the ground state at room temperature. Each of the v' levels may then autoionize to the single vibrational level v^+ according to the overlap established by the Frank-Condon factors for the process "Monopole". The product of Frank-Condon factors so calculated are plotted against v' for each vibrational level v^+ to produce simulated CIS spectrum.

PE spectral envelopes were simulated by computing the Franck-Condon Factors between the resonant Rydberg state and the ionic state (process "Monopole") using selected values v'. The Franck-Condon factors are plotted against v^+ for each vibrational level v'.

The values for ω_e, $\omega_e x_e$ and r_e for the neutral ground state were taken from infra-red spectroscopy and microwave spectroscopy studies on NO. For a given ionic state, the vibrational constants ω_e and $\omega_e x_e$ were usually determined from the corresponding vibrational resolved PE band using the equation derived from the anharmonic energy expression $\Delta E_{v'} = \omega_e - 2\omega_e x_e (v'+1)$ and vibrational separations in the PE band ($\Delta E_{v'}$) by a least-square fit of the $\Delta E_{v'}$ values against (v'+1) for each band. The vibrational constants for the NO($X^2\Pi$) used for the simulations are $\omega_e = 1904.2$ cm^{-1}, $\omega_e x_e = 14.10$ cm^{-1} and $r_e = 1.151$ Å[58]. The vibrational constants for the ionic ground state $NO^+(X^1\Sigma^+)$ are $\omega_e = 2376.4$ cm^{-1}, $\omega_e x_e = 16.30$ cm^{-1} and $r_e = 1.063$ Å provided by high resolution optical spectroscopy[53,58]. The Rydberg state vibrational constants and equilibrium bond lengths are assumed to be the same as the ionic core $NO^+(b^3\Pi)$: $\omega_e = 1710$ cm^{-1}, $\omega_e x_e = 14.2$ cm^{-1} and $r_e = 1.176$ Å provided by high resolution photoelectron spectrosopy[5,6,53].

The intensities of the bands in the experimental PE and CIS spectra were normalized by the photon flux and then by the transmission of the spectrometer. The photon flux was estimated as a function of photon energy from the current measured on the beamline gold mirror placed just before the glass capillary that channelled the radiation into the spectrometer ionization chamber. The current measured on the mirror was normalized by the quantum efficiency of gold. The transmission function of the spectrometer, for electrons of different initial electron kinetic energy, was

determined by measuring the intensity of the helium $(1s)^{-1}$ photoelectron band at different photon energies. The intensity of the helium $(1s)^{-1}$ band was measured in the 26 - 35 eV photon energy range and then it was normalised using the absolute photoionization cross section of helium in this range[59]. Finally the normalized intensity was plotted as function of the electron kinetic energy and the curve was used to correct the experimental PE and CIS spectra for the transmission of the spectrometer.

The degree of linear polarisation ($P = 1$) of the radiation was well established[60,61]. For a given sample gas, the asymmetry parameter (β) was measured at selected photon energies and over a photon energy range, by recording PE and CIS spectra at two different θ angles (0° and 54° 44'). The angle of 54° 44' corresponds to the angle at which the measurement is independent of β, thereby, permitting a straightforward determination of the relative partial cross section. The β parameter was then calculated from the expression: $\beta = R - 1$ where $R = I_0 / I_{54° 44'}$ is the ratio of the experimental intensities at these two angles, after applying the above corrections. For the measurements of angular distribution parameter, it is important that the efficiency of the analyser does not change when the spectrometer is rotated. The change of the efficiency of the analyser on rotation arises from small misalignments between the axis of rotation and the direction of the photon beam. In order to quantify this contribution a correction factor was evaluated by measuring the intensity of bands at $\theta = 0°$ and at $\theta = 54° 44'$, usually between 26 - 29 eV, from a He sample which has a well established asymmetry parameter ($\beta = 2$). From the comparisons between the calculated asymmetry parameter and the known asymmetry parameter, the correction factor was determined.

The photon energy was calibrated in the 11.5 - 29.0 eV region against the energies of the Ar $3s3p^6(^2S_{1/2})np \leftarrow 3s^23p^6(^1S_0)$ resonances[62] and He $1s^1np \leftarrow 1s^2$ absorption lines[63]. The Ar resonances were obtained recording CIS spectra of the first band (first component) of the $(3p^{-1})$ ionization of Argon in the photon energy region 26.0 - 29.0 eV. The absorption spectra of He were recorded measuring the current on the aluminium plate at the back of the spectrometer in the photon energy ranges

21.0 - 24.0 eV using first order radiation and 11.5 - 12.3 eV using second order radiation.

A commercially obtained gas cylinder of NO with 99% quoted purity was used.

A PE spectrum of NO recorded at a photon energy of $h\nu = 25.0$ eV with Synchrotron Radiation at the magic angle with respect to the polarization axis of the photon source is shown in Figure 9.5 with the ionic state assignment of the bands as reported in the literature given[6,7].

Figure 9.6 shows the CIS spectrum recorded in the 13.2 - 30.0 eV and 13.6 - 16.6 eV photon energy regions on the $NO^+(X^1\Sigma^+, v^+=1) \leftarrow NO(X^2\Pi, v''=0)$ band. As can be seen better resolution is obtained in comparison to the experimental result of Southworth[12] shown in Figure 9.4. There is no evidence of the $^2\Sigma^+$ valence resonance predicted by Stratmann[47] and Lynch[50] at 16 eV or of the intense $^2\Delta$ valence resonance predicted by Stratmann[47] between 14 and 15 eV or of the effects of the interaction of the shape and Rydberg resonances shown in Figure 9.2 and Figure 9.3. In the photon energy region 13.5 - 17.0 eV the most intense structures are due to the very sharp $5\sigma \rightarrow np$ Rydberg series converging to $NO^+(b^3\Pi, v^+=0)$ state at 16.56 eV. The spectrum in Figure 9.6 (a) can be explained as superimposition of all the Rydberg resonances arising from excitation of a 5σ and a 1π electron to Rydberg states and direct ionization from the 2π orbital as predicted by the calculations[45,49] reported in Figure 9.1.

At high photon energies a broad maximum centred at ≈ 24 eV is observed as predicted by the calculations of the direct ionization $2\pi \rightarrow k\pi$ and $2\pi \rightarrow k\delta$ channels (see Figure 9.1). At lower photon energies the broad $2\pi \rightarrow k\sigma$ shape resonance centred at ≈ 14 eV can be observed in the experimental spectrum and its effects on the partial photoionization cross section have been observed by recording PE spectra of the vibrational components of the $NO^+(X^1\Sigma^+)$ ionic state at a photon energy where Rydberg series are not present. Two points have been chosen at 13.74 and 15.24 eV photon energy and they are indicated with the symbol * in Figure 9.7.

At 13.74 eV no Rydberg state is clearly present and both direct ionization and the $2\pi \rightarrow k\sigma$ shape resonance are expected to contribute to the partial photoionization cross section though the shape resonance should be predominant. No Rydberg state

is present at 15.24 eV and the direct ionization should be predominant as can be expected from the theoretical calculations in Figure 9.1. The PE spectra recorded at these two photon energies and at two different angles ($\theta = 0°$ red trace and $\theta = 54° 44'$ blue trace) are shown in Figure 9.8. In these PE spectra, whilst only the $v^+ = 0 - 5$ vibrational levels are significant in a direct photoionization process, higher vibrational levels are observed at $h\nu = 13.74$ eV due to the presence of the shape resonance. Moreover, in a direct photoionization process, the most intense component of the photoelectron band is the vibrational component $v^+ = 1$ while at $h\nu = 13.74$ eV it is $v^+ = 2$. At $h\nu = 15.24$ eV the most intense component is $v^+ = 1$ and the higher vibrational levels are much weaker, indicating a really small contribution of the shape resonance. At this photon energy the partial photoionization cross section of the vibrational components is really close to that of direct ionization as deduced by comparison of Figure 9.9 (a) and Figure 9.9 (b). In Figure 9.9 (a) the simulated Frank-Condon factors for the direct ionization process are shown. Figure 9.9 (b) shows the relative intensities measured at $h\nu = 15.24$ eV of the vibrational components up to $v^+ = 12$, which was arbitrarily chosen as limit for the accepted binding energy range in the recorded PE spectra. Fitting procedures were used to obtain peak areas for each vibrational level and these areas were normalized by the sum of all the areas of the vibrational level from $v^+ = 0$ to $v^+ = 12$. The error derived by these procedures is also reported in Figure 9.9 (b) as in all the others similar plot presented in this chapter.

The comparison of the PE spectra in Figures 9.8 (a) and (b) shows the count-rate of the vibrational components at $h\nu = 13.74$ eV higher with respect to the vibrational component at $h\nu = 15.24$ eV. The intensity at $h\nu = 15.24$ eV is essentially due to the direct ionization while at $h\nu = 13.74$ eV the $2\pi \rightarrow k\sigma$ shape resonance is superimposed to the direct ionization process. The subtraction of the PE spectrum in Figure 9.8 (b) from the PE spectrum in Figure 9.8 (a) gives the vibrational distribution due to the $2\pi \rightarrow k\sigma$ shape resonance.

Figure 9.9 (c) shows the relative intensities of the vibrational component at $h\nu = 13.74$ eV after this subtraction for each vibrational level of the contribution of the direct ionization, which is assumed to be represented by the PE spectrum

recorded at $h\nu = 15.24$ eV. This subtraction procedure makes a small change to the overall envelope as can be seen on comparing the PE spectrum in Figure 9.8 (a) with the calculated relative intensities in Figure 9.9 (c) and generally permits the separation of the effects of a resonance from the direct ionization. Therefore the relative intensities in Figure 9.9 (c) represent the effects of the $2\pi \rightarrow \sigma$ shape resonance on the partial photoionization cross section of the vibrational components. As mentioned in Section 9.1, non-Frank-Condon behaviour in vibrationally resolved PE spectra at the shape resonance energy have been predicted and observed for NO[9,12,50,51] as well for others molecules like N_2 and CO in both valence and core regions[64-67]. A shape resonance can be described as a one-electron continuum state phenomenon in which the ejected photoelectron is resonantly trapped by a potential barrier through which it eventually tunnels. The temporary trapping of the photoelectron by the centrifugal barrier enhances the coupling between the escaping photoelectron and the vibrational motion of the nuclei leading to a large deviation from Frank-Condon vibrational intensity distributions. Therefore, the breakdown of the Frank-Condon principle arises from the quasibound nature of the shape resonance, which is localized in a spatial region of molecular dimensions by a centrifugal barrier leading to a strong dependence of the photoionization matrix elements on internuclear distance.

Figure 9.7 shows details of the $5\sigma \rightarrow np$ Rydberg series for $n = 3, 4$ and the less intense closely spaced and overlapping Rydberg series arising from excitation from the 1π orbital with the assignment from the experimental works of Edqvist *et al.*[5] (violet marks), Stubbs *et al.*[34] (red marks), Erman *et al.*[29] (black marks). The resonant states which are part of $5\sigma \rightarrow np$ Rydberg series are labelled with letters and they are studied and reassigned in this work. In the old assignment the bands A, B, C, D and E are excitations to the $R(b^3\Pi,3p\pi,v'=0)$, $R(b^3\Pi,3p\sigma,v'=0)$, $R(b^3\Pi,3p\pi,v'=1)$, $R(b^3\Pi,4p\pi,v'=0)$ and $R(b^3\Pi,4p\sigma,v'=0)$ resonant states respectively (see also Table 9-3). The intense band at 13.654 eV, labelled as peak F, is essentially unassigned since all the intensity cannot be due to the $R(w^3\Delta,3s\sigma,v'=1)$ states as all the other vibrational components of the series are weak. This band was not assigned by Southworth[12] as can be seen in Figure 9.4 (a) while, at lower photon

energy, three valence states are reported. These new resonant valence bands were identified by Erman *et al.*[29,30] but they were unable to establish the origin of the band at 13.654 eV.

Stubbs[34] observed the u↔g symmetry forbidden R($b^3\Pi$,ndσ,v'=0) ← NO($X^2\Pi$) series and the presence of this series seems to be confirmed in Figure 9.7. Stubbs[34] and Edqvist[5] also reported the R($b'^3\Sigma^-$,3sσ,v'=0) ← NO($X^2\Pi$) series which should be forbidden for autoionization to $NO^+(X^1\Sigma^+)$ since the final excited state symmetry is $^2\Sigma^-$ and cannot decay into the $NO^+(X^1\Sigma^+)$ final state continuum as consequence of parity conservation. This series cannot be clearly observed in the spectrum in Figure 9.7 since it is strongly overlapping with the other Rydberg series.

In Figure 9.7, in comparison with Figure 9.4 (c), more resolved structure can be observed and the narrower bands show a splitting of 15 meV due to the spin-orbit splitting of the ground state of NO($X^2\Pi$) with the Rydberg component from NO($X^2\Pi_{3/2}$) expected at lower photon energy with respect the component from NO($X^2\Pi_{1/2}$) ground state. Spin-orbit splitting effects were observed in absorption experiments by Takezawa[19] as some lines completely disappeared when NO was cooled to the temperature of liquid nitrogen. For example, in Figure 9.7, spin-orbit splitting can be observed for the Rydberg states C and E at 14.074 and 15.367 eV respectively. This could be an indication that the two components are part of the same Rydberg series and doubts were already reported in Paragraph 9.1 on the assignment of peak C as the R($b^3\Pi$,3pπ,v'=1) component.

Figure 9.10 shows the Frank-Condon factors computed in simulations of the CIS spectra $NO^+(^1\Sigma^+,v^+=0,1,2)$ ← NO($X^2\Pi$) via the R($b^3\Pi$,*n*p,v') series. The relative intensity of peak C, assigned as R($b^3\Pi$,3pπ,v'=1) state in the earlier works, is therefore expected to be weaker with respect the intensities of both peaks A and B, assigned as R($b^3\Pi$,3pπ,v'=0) and R($b^3\Pi$,3pσ,v'=0) components at 13.818 and 14.013 eV respectively, when inspecting CIS spectra recorded on $NO^+(^1\Sigma^+,v^+)$ for v^+ = 0, 1 and 2. Experimentally it is band B that exhibits such behaviour (i.e. it gets weaker with respect to band A and C when v^+ changes from 0 to 2) as can be seen in Figure 9.11, not band C. Therefore band B can be reassigned as the v' = 1 component of peak A, i.e. as R($b^3\Pi$,3pπ,v'=1) if the old assignment for peak A is

valid. The resulting vibrational separation with respect to the $R(b^3\Pi,3p\pi,v'=0)$ component (peak A) is 195 meV consistent with that expected from the vibrational spacing of the $NO^+(b^3\Pi)$ ionic state ($\approx$ 200 meV)[6].

PE spectra of the first band of NO were recorded at the resonant energies of the $R(b^3\Pi,np)$ series for $n = 3$ and 4. Figure 9.12 shows the PE spectra recorded at two different angles ($\theta = 0°$ red trace and $\theta = 54° 44'$ blue trace) at photon energies corresponding to the Rydberg resonant states A, B, C from $NO(X^2\Pi_{3/2})$ and C from $NO(X^2\Pi_{1/2})$ at $h\nu = 13.818$, 14.013, 14.060 and 14.074 eV respectively. The most intense vibrational components are $v^+ = 2$ and 3 for Figure 9.12 (a), (c) and (d) and the relative intensity of each vibrational band is different with respect the direct ionization, see Figure 9.8 (b), mainly due to the effects of the strong autoionization process.

The Frank-Condon factors for the resonant autoionization $NO^+(X^1\Sigma^+) \leftarrow R(b^3\Pi,v'=0)$ and $NO^+(X^1\Sigma^+) \leftarrow R(b^3\Pi,v'=1)$ are reported in Figure 9.13. These Frank-Condon factors can be compared with the PE spectra shown in Figure 9.12 only after the contribution of the direct ionization is subtracted from the peak areas of each vibrational level to separate the effects of the resonance from the direct ionization. The experimental relative intensities obtained for the vibrational bands of $NO^+(X^1\Sigma^+)$ are shown in Figure 9.14. The vibrational distributions obtained when the photon energies are set on bands A and C from both the two spin-orbit components $NO(X^2\Pi_{3/2})$ and $NO(X^2\Pi_{1/2})$ (see Figure 9.14 (a), (c) and (d)) are really close to each other and with the calculated Frank-Condon factor in Figure 9.13 (a) until $v^+ = 7$. A weak intensity of the higher vibrational bands is observed but is not expected accordingly to the simulation. These vibrational bands can be due to the interaction or overlapping of the Rydberg state with the $2\pi \rightarrow \sigma$ shape resonance that shows a broader vibrational distribution, as seen in Figure 9.9 (c). Figure 9.14 (b) shows the vibrational distribution obtained when the photon energies are set on bands B at 14.013 eV which is similar to the simulated Frank-Condon factor for the $NO^+(X^1\Sigma^+) \leftarrow R(b^3\Pi,v'=1)$ autoionization process in Figure 9.13 (b). Therefore the assignment of this band as the $v' = 1$ component of the Rydberg state associated with band A is unambiguously confirmed.

Figure 9.15 shows the PE spectra recorded at photon energies corresponding to the Rydberg resonant states D, E from NO($X^2\Pi_{3/2}$) and E from NO($X^2\Pi_{1/2}$) at $h\nu$= 15.301, 15.354 and 15.367 eV respectively. The relative vibrational intensities, after the subtraction of the direct ionization contribution, are shown in Figure 9.16 and they are similar to the expected Frank-Condon factors shown in Figure 9.13 (a). The relative intensity of the higher vibrational bands is lower with respect to the intensity obtained when the photon energies are set to band A, B and C (compare Figure 9.16 with Figure 9.14) indicating a smaller contribution of the $2\pi \rightarrow \sigma$ shape resonance.

The Rydberg series R($b^3\Pi$,npπ,v'=0), corresponding with the old assignment to bands A and D for n = 3 and 4 respectively, is split in two excited states with $^2\Delta$ and $^2\Sigma^+$ symmetries which are believed to be overlapping. At photon energy corresponding to peak D, Takezawa[19] in a high resolution photoabsorption study observed at least five bands at room temperature but two bands disappeared at liquid nitrogen temperature while the band A was unresolved and only showed a diffuse appearance. Salzmann *et al.*[13] performed angle and spin resolved photoelectron spectroscopy experiments with circular polarized light on the Rydberg state associated with band A concluding that the resonances with $^2\Delta$ and $^2\Sigma^+$ symmetries contribute with similar intensity.

The resonant state D in Figure 9.7 shows some structure, at least two peaks with the one at lower photon energy being the more intense. PE spectra across this band have been recorded and Figure 9.17 shows the relative intensities of the vibrational components. At 15.297 eV, corresponding to the low-energy shoulder of the band, the vibrational distribution in Figure 9.17 (a) is similar to that observed for band A in Figure 9.14 (a). On increasing of the photon energy and passing across the maximum, the vibrational distribution changes and on the other side of the band at 15.328 eV it is again similar to the vibrational distribution recorded for the resonant state A. This could be explained by interference effects of the two resonant states $^2\Delta$ and $^2\Sigma^+$. Moreover, as can be seen in Figure 9.7, peak D is overlapping with the R($w^3\Delta$,4sσ,v'=0) state which could influence the partial photoionization cross section and asymmetry parameter of the vibrational bands.

However, the intensity of this resonant state is so low that it is not expected to have a big influence and similar effects should be observed as well for the close band E which, in contrast, gives the expected vibrational distribution for a R($b^3\Pi$,v'=0) state as shown in Figure 9.16 (b) and (c).

The peak A does not show any structure, as can be seen in the three CIS spectra shown Figure 9.11, only a small asymmetry, due to the spin-orbit splitting of the ground state of NO($X^2\Pi$), can be observed at lower photon energy. In Figure 9.18 the vibrational distributions from the PE spectra recorded at three different photon energies over this band are reported and they are all identical while some interference would be expected if this band arose from an overlap of the two resonant states, $^2\Delta$ and $^2\Sigma^+$, as was observed for peak D. This is a first indication that this band could actually be a single resonant state. The second indication is the widths of bands A and D which are ≈ 20 and 25 meV respectively while in a Rydberg series the width of the $n = 3$ state is expected to be larger[68].

As already mentioned in Paragraph 9.1, using simple quantum defect theory Stratmann *et al.*[47] reported in order of increasing energies a $5\sigma \rightarrow n\pi$ ($^2\Delta$), $5\sigma \rightarrow n\sigma$ ($^2\Pi$) and $5\sigma \rightarrow n\pi$ ($^2\Sigma^+$) sequence. For $n = 4$ the resonances energies reported by Stratmann are 15.31, 15.32 and 15.37 eV for the $^2\Delta$, $^2\Pi$ and $^2\Sigma^+$ state respectively. From the experimental CIS spectra in Figure 9.11, the two contributions to the resonant band D (old assignment as R($b^3\Pi$,4pπ,v'=0) $^2\Delta$ and $^2\Sigma^+$ states, see Table 9-3) are overlapping between 15.305 and 15.320 eV while band E (old assignment as R($b^3\Pi$,4pσ,v'=0) $^2\Pi$ state) is at $h\nu = 15.367$ eV. As can be seen, the energy resonant position agreement between experiment and theory is perfect, although the assignment is different.

For $n = 3$ the experimental resonant energies are 13.818 eV for band A (old assignment as R($b^3\Pi$,3pπ,v'=0) $^2\Delta$ and $^2\Sigma^+$ states) and 14.074 eV for band C (old assignment as R($b^3\Pi$,3pσ,v'=0) $^2\Pi$ state) while Stratmann reported 13.99, 14.02 and 14.15 eV for the $^2\Delta$, $^2\Pi$ and $^2\Sigma^+$ states respectively. In this case there is not agreement between the theoretical and experimental values but this could be expected since for $n = 3$ the Rydberg electron is closer to the ion core and the penetration of the wavefunction into the core is greater and a larger quantum defect

is expected with respect the quantum defect at higher n. In the calculations the quantum defect is kept constant, which gives rise to the resonant energies reported by Stratmann for $n = 3$ being higher with respect to the experimental positions.

The main point is that, accordingly to the calculations, the $^2\Delta$ and $^2\Pi$ states which are overlapping for $n = 4$ (corresponding to the experimental band D) are separated by 30 meV for $n = 3$ (with the old assignment this would just be peak A) while the separation between the $^2\Pi$ and $^2\Sigma^+$ states is 130 and 50 meV for $n = 3$ (peaks A - C) and $n = 4$ (peaks D - E) respectively. Experimentally, the separation between peaks D and E is $\approx$ 50 meV while the separation between peaks A and C is 255 meV, bigger than the theoretical value of 130 meV. Therefore the theoretical value of 30 meV for the separation between the $^2\Delta$ and $^2\Pi$ states for $n = 3$ is expected to be an underestimate of the real experimental separation. This could lead to the conclusion that another state well below 13.818 eV should be observed experimentally. Therefore the unassigned peak F at 13.654 eV could be part of the R($b^3\Pi$,3p,v'=0) series. To confirm this conclusion and possibly to determine the order of the excited state symmetries (i.e. $^2\Sigma^+$, $^2\Pi$ and $^2\Delta$), studies of the effects of the R($b^3\Pi$,3p,v'=0) resonant states on the asymmetry parameter of the vibrational bands of the $NO^+(X^1\Sigma^+)$ ionic state are reported.

The asymmetry parameter β contains angular momentum information of the partial waves of the emitted photoelectrons[13,69]. As shown in Table 9-1, autoionization from $^2\Sigma^+$, $^2\Pi$ and $^2\Delta$ excited states symmetries leads to $\varepsilon l\sigma$, $\varepsilon l\pi$ and $\varepsilon l\delta$ outgoing waves, respectively, for autoionization to the $NO^+(X^1\Sigma^+)$ ionic ground state. The $2\pi \rightarrow k\sigma$ shape resonance has overall final state symmetry of $^2\Sigma^+$ which can only lead to $\varepsilon l\sigma$ waves in the final state. The direct ionization $2\pi \rightarrow k\pi$ and $2\pi \rightarrow k\delta$ give rise to $\varepsilon l\pi$ and $\varepsilon l\delta$ outgoing waves respectively.

Figure 9.19 shows the asymmetry parameter β as a function of the vibrational levels in $NO^+(X^1\Sigma^+)$ at 13.74, 13.90 and 15.24 eV photon energies. As previously reported, at $h\nu$ = 15.24 eV the contribution to the cross section is almost totally due to the direct photoionization process. From the theoretical calculation shown in Figure 9.1, an equal contribution of the three channels, $2\pi \rightarrow k\sigma$, $2\pi \rightarrow k\pi$ and $2\pi \rightarrow k\delta$ is

expected while Stratmann[47] does not take in account the $2\pi \rightarrow k\pi$ channel. Although the valence resonances predicted in this work (see Figure 9.3 (a) and (b)) are not observed, outside the shape resonance, at $h\nu$= 15.24 eV, the biggest contribution to the continuum is the $^2\Delta$ symmetry (as at ≈ 15 eV the contribution from Figure 9.3 (b) is greater than that of Figure 9.3(a)). Figure 9.19 (b) shows the asymmetry parameter plot at this photon energy. It has a maximum for the vibrational bands $v^+ = 0$ and 1 and rapidly decreases through $v^+ = 2$ and 3.

Figure 9.19 (a) shows the asymmetry parameter at $h\nu$= 13.74 eV where the $2\pi \rightarrow k\sigma$ shape resonance is the predominant channel; therefore the difference between the asymmetry parameter distributions in Figure 9.19 (b) and (a) are to be attributed to the $\varepsilon l\sigma$ outgoing wave which contribute strongly to Figure 9.19 (a). At $h\nu$= 13.74 eV the result is a broadening of the distribution seen in Figure 9.19 (b) centred on $v^+ = 1, 2$ and 3 and a decrease of the maximum value. Figure 9.19 (c) shows the asymmetry parameter distribution at $h\nu$= 13.90 eV where still the $2\pi \rightarrow k\sigma$ shape resonance is a strong channel but is overlapping with the R($w^3\Delta$,3sσ,v'=4) resonant state that has $^2\Delta$ symmetry leading to $\varepsilon l\delta$ outgoing wave which is responsible for the differences between Figure 9.19 (a) and Figure 9.19 (c) where a decrease from (a) to (c) of the asymmetry parameter for $v^+ = 3, 4$ and 5 is observed with a small increase for $v^+ = 0$ and 1. Overall the $\varepsilon l\delta$ wave changes the distribution in Figure 9.19 (a), essentially from that expected for the $\varepsilon l\sigma$ wave, toward the distribution in Figure 9.19 (b) which then probably has a strong contribution by the $^2\Delta$ symmetry continuum.

Figure 9.20 shows the asymmetry parameter β as a function of the vibrational bands of $NO^+(X^1\Sigma^+)$ at $h\nu$= 14.060, 14. 074 and 13.818 eV corresponding to the Rydberg resonant states C from $NO(X^2\Pi_{3/2})$, C from $NO(X^2\Pi_{1/2})$ and A. The two states C from the spin-orbit states $NO(X^2\Pi_{3/2})$ and $NO(X^2\Pi_{1/2})$ have, as expected, a similar asymmetry parameter distribution which is close to the distribution in Figure 9.19 (a) related to an $\varepsilon l\sigma$ outgoing wave. If the assignment in literature of peak A as R($b^3\Pi$,3pπ,v'=0) was right, peak C should correspond to the R($b^3\Pi$,3pσ,v'=0) state (notice that the literature assignment of band B has already been changed in this

work as the $v' = 1$ component of the Rydberg state A, therefore the literature assignment of state B and C shown Figure 9.7 and Table 9-3 should be inverted and band C becomes the R($b^3\Pi$,3pσ,v'=0 state) and it would be expected an $\varepsilon l\pi$ wave. The asymmetry parameter distribution for peak A at 13.818 eV, shown in Figure 9.20 (c), has a completely different behaviour with respect both the $\varepsilon l\sigma$ and $\varepsilon l\delta$ waves described previously, i.e. Figure 9.19 (a) and (b) respectively. The asymmetry parameter for $v^+ = 0$ is close to zero, decreases as v^+ increases, has a minimum for $v^+ = 2$ and 3 and increases again. This asymmetry parameter distribution has to be related to the $\varepsilon l\pi$ outgoing wave (as it cannot be $\varepsilon l\sigma$ or $\varepsilon l\delta$) and band A reassigned as R($b^3\Pi$,3pσ,v'=0) state with $^2\Pi$ symmetry. The two states C from the spin-orbit splitting NO($X^2\Pi_{3/2}$) and NO($X^2\Pi_{1/2}$) are reassigned as R($b^3\Pi$,3pπ,v'=0) from NO($X^2\Pi_{3/2}$) and R($b^3\Pi$,3pπ,v'=0) from NO($X^2\Pi_{1/2}$) states with $^2\Sigma^+$ symmetry since these states have an asymmetry parameter distribution close to the distribution in Figure 9.19 (a) related to an $\varepsilon l\sigma$ outgoing wave.

Unfortunately no PE spectrum has been recorded on the unassigned band F at 13.654 eV which could be part of the R($b^3\Pi$,3p,v'=0) series; by elimination this would be the R($b^3\Pi$,3pπ,v'=0) state with $^2\Delta$ symmetry. Angle resolved CIS spectra have been recorded on the first three vibrational bands of $NO^+(X^1\Sigma^+)$ and the β-plots obtained are reported in Figure 9.21 where the magenta symbols are set at $h\nu$= 13.654 and 13.900 eV, the unassigned peak F and the R($w^3\Delta$,3sσ,v'=4) state with $^2\Delta$ symmetry respectively. At these two photon energies the asymmetry parameter values are the same for the three CIS spectra although the behaviour of the β parameter between the two photon energies is different for the different angular distribution plots because of the shape resonance ($\varepsilon l\sigma$ outgoing wave) and R($b^3\Pi$,3pσ,v'=0) state ($\varepsilon l\pi$ outgoing wave). Therefore the unassigned band F at 13.654 eV can be related to an $\varepsilon l\delta$ outgoing wave and assigned as R($b^3\Pi$,3pπ,v'=0) resonant state with $^2\Delta$ symmetry.

Accordingly with the new assignment, the order of the resonant states for $n = 3$ is the same as reported by Stratmann[47]: R($b^3\Pi$,3pπ,v'=0) $^2\Delta$, R($b^3\Pi$,3pσ,v'=0) $^2\Pi$ and R($b^3\Pi$,3pπ,v'=0) $^2\Sigma^+$ at $h\nu$= 13.654, 13.818 and 14.074 eV respectively.

The conclusion from Salzmann *et al.*[13] that the $^2\Delta$ and $^2\Sigma^+$ symmetries contribute with similar intensity to the resonant state at $h\nu$= 13.818 eV can be explained with the erroneous choice, in their data analysis, of the β values for $v^+ = 2$ and 3 of 0.70 and 0.65 respectively, in contrast with our experimental values of -0.30 and -0.27 as shown in Figure 9.20 (c). Moreover these experimental β values are in agreement with the values obtained by Southworth[12] who reported a plot similar to the one in Figure 9.20 (c).

Figure 9.22 shows that the distribution of the asymmetry parameter across peak A at $h\nu$ = 13.818 eV, the R($b^3\Pi$,3pσ,v'=0) state accordingly the new assignment, are all the same confirming this band is a single resonant state. It should be noticed that the β values decrease as the photon energy increases. This is because while the resonance has a nearly symmetric cross section, the asymmetry parameter is much broader and asymmetric as can be observed in Figure 9.23. Therefore the results in Figure 9.22 are explained: the three chosen photon energies (indicated with the magenta symbol * in Figure 9.23) are located on the two shoulders and the maximum of the resonant cross section band but are all located in the shoulder at lower photon energy of asymmetry parameter profile.

Figure 9.24 shows the asymmetry parameter distribution across the resonant state D that was originally assigned as R($b^3\Pi$,4pπ,v'=0)[5,19,29,34]. Accordingly to the new assignment this band arises from overlap of the R($b^3\Pi$,4pπ,v'=0) $^2\Delta$ and R($b^3\Pi$,4pσ,v'=0) $^2\Pi$ states. The important conclusion from Figure 9.24 is that this band is effectively due to the overlap of the two states which affects the asymmetry parameter distribution. The shape of this band (D) is asymmetric as can be observed in the CIS spectra shown Figure 9.11 and the most intense component is at lower photon energy. This could lead to the conclusion that the order of the R($b^3\Pi$,4pπ,v'=0) $^2\Delta$ and R($b^3\Pi$,4pσ,v'=0) $^2\Pi$ states is inverted respect the $n = 3$ resonances, as in the 13.6 - 14.1 eV photon energy region the band associated with the transition to the R($b^3\Pi$,3pσ,v'=0) $^2\Pi$ state is the most intense. This assignment would be in contrast with the results from Stratmann[47] but it would be in agreement with the results from Hermann[4].

Table 9-2 *Assignment of the R($b^3\Pi$,np) resonant states from the present work for n = 3 and 4.*

Rydberg state	Excited state symmetry	Photon Energy (eV)	Outgoing waves for $X^1\Sigma^+$ autoionization
R($b^3\Pi$,3pπ,v'=0)	$^2\Delta$	13.654	$\varepsilon k\delta$
R($b^3\Pi$,3pσ,v'=0)	$^2\Pi$	13.818	$\varepsilon k\pi$
R($b^3\Pi$,3pσ,v'=1)	$^2\Pi$	14.013	$\varepsilon k\pi$
R($b^3\Pi$,3pπ,v'=0) from NO($X^2\Pi_{3/2}$)	$^2\Sigma^+$	14.060	$\varepsilon k\sigma$
R($b^3\Pi$,3pπ,v'=0) from NO($X^2\Pi_{1/2}$)	$^2\Sigma^+$	14.074	$\varepsilon k\sigma$
R($b^3\Pi$,4pσ,v'=0)	$^2\Pi$	≈15.304	$\varepsilon k\pi$
R($b^3\Pi$,4pπ,v'=0)	$^2\Delta$	≈15.318	$\varepsilon k\delta$
R($b^3\Pi$,4pπ,v'=0) from NO($X^2\Pi_{3/2}$)	$^2\Sigma^+$	15.354	$\varepsilon k\sigma$
R($b^3\Pi$,4pπ,v'=0) from NO($X^2\Pi_{1/2}$)	$^2\Sigma^+$	15.367	$\varepsilon k\sigma$

Figure 9.25 shows the CIS spectrum recorded on the $NO^+(^1\Sigma^+,v^+=1) \leftarrow NO(X^2\Pi)$ band in the photon energy range 13.5 - 15.7 eV with the assignment of the R($b^3\Pi$,np) resonant states from this work for n = 3 and 4 marked on. The photon energy values of these Rydberg resonances are reported in Table 9-2.

9.3 Conclusion

In the present study on NO with Synchrotron Radiation the relative photoionization cross section and angular distribution parameters for the $NO^+(X^1\Sigma^+,v^+) \leftarrow NO(X^2\Pi)$ ionization have been evaluated as a function of photon energy from 13.5 to 17.0 eV for $v^+ = 0$ and 2 and from 13.5 to 30 eV for $v^+ = 1$. The $2\pi \rightarrow k\sigma$ shape resonance centred at 14 eV has been observed and its effects on the partial photoionization cross section and the asymmetry parameter of the vibrational bands of the $NO^+(X^1\Sigma^+)$ ionic state have been investigated by recording PE spectrum at $h\nu = 13.74$ eV and outside resonances. The valence resonances, which were predicted by theoretical studies in order to justify early experimental results with poor resolution, have not been observed.

Once the $R(b^3\Pi,np)$ resonant states, as assigned in literature, were observed in the CIS spectra, PE spectra of the $NO^+(X^1\Sigma^+,v^+) \leftarrow NO(X^2\Pi)$ band were recorded at the resonant energies to study the effects on the vibrational components and the asymmetry parameter. An incorrect assignment was found by comparison of the experimental vibrational distributions with the vibrational distributions obtained from the Franck-Condon factors calculated for the $NO^+(X^1\Sigma^+,v^+) \leftarrow R(b^3\Pi,np, v'=0$ and 1) transitions. From these comparisons also arise indications of the possibility to determine experimentally the excited state symmetries of the $R(b^3\Pi,3p)$ resonant states (i.e. $^2\Sigma^+$, $^2\Pi$ or $^2\Delta$) by considering as part of this Rydberg series an unassigned band at $h\nu = 13.654$ eV. The studies of the asymmetry parameter as function of photon energy confirmed this possibility and a new assignment order was determined for $n = 3$: $R(b^3\Pi,3p\pi,v'=0)$ $^2\Delta$, $R(b^3\Pi,3p\sigma,v'=0)$ $^2\Pi$ and $R(b^3\Pi,3p\pi,v'=0)$ $^2\Sigma^+$ at excitation energies relative to the ground state of 13.654, 13.818 and 14.074 eV respectively, the same order reported by Stratmann[47].

These experimental values are at lower photon energies compared with the values obtained by the quantum defect calculation of Stratmann[47] and Hermann[4]. It can be seen that the comparison between the experimental positions measured in this work and the calculated values of both Stratmann[47] and Hermann[4] for the $n = 4$ states is much better, indicating that the $n = 3$ states are perturbed probably by valence-state

Rydberg-state interactions. In this work, however, the evidence indicates an interchange of the $^2\Delta$ and $^2\Pi$ states for $n = 4$ with respect to $n = 3$, in agreement with the order reported by Hermann[4].

A comparison of the new assignments made in this thesis with the literature assignments[5,19,29,34] is reported in Table 9-3.

Table 9-3 *Summary of the new assignments made in this work in comparison with the literature assignments*[5,19,29,34].

Band number in Figure 9.7	**Literature assignments**	**This thesis assignments**
A	$R(b^3\Pi,3p\pi,v'=0)\leftarrow NO(X^2\Pi)$	$R(b^3\Pi,3p\sigma,v'=0)\leftarrow NO(X^2\Pi)$
B	$R(b^3\Pi,3p\sigma,v'=0)\leftarrow NO(X^2\Pi)$	$R(b^3\Pi,3p\sigma,v'=1)\leftarrow NO(X^2\Pi)$
C	$R(b^3\Pi,3p\pi,v'=1)\leftarrow NO(X^2\Pi)$	$R(b^3\Pi,3p\pi,v'=0)\leftarrow NO(X^2\Pi_{3/2})$ $R(b^3\Pi,3p\pi,v'=0)\leftarrow NO(X^2\Pi_{1/2})$
D	$R(b^3\Pi,4p\pi,v'=0)\leftarrow NO(X^2\Pi)$	$R(b^3\Pi,4p\sigma,v'=0)\leftarrow NO(X^2\Pi)$ $R(b^3\Pi,4p\pi,v'=0)\leftarrow NO(X^2\Pi)$
E	$R(b^3\Pi,4p\sigma,v'=0)\leftarrow NO(X^2\Pi)$	$R(b^3\Pi,4p\pi,v'=0)\leftarrow NO(X^2\Pi_{3/2})$ $R(b^3\Pi,4p\pi,v'=0)\leftarrow NO(X^2\Pi_{1/2})$
F	Unassigned	$R(b^3\Pi,3p\pi,v'=0)\leftarrow NO(X^2\Pi)$

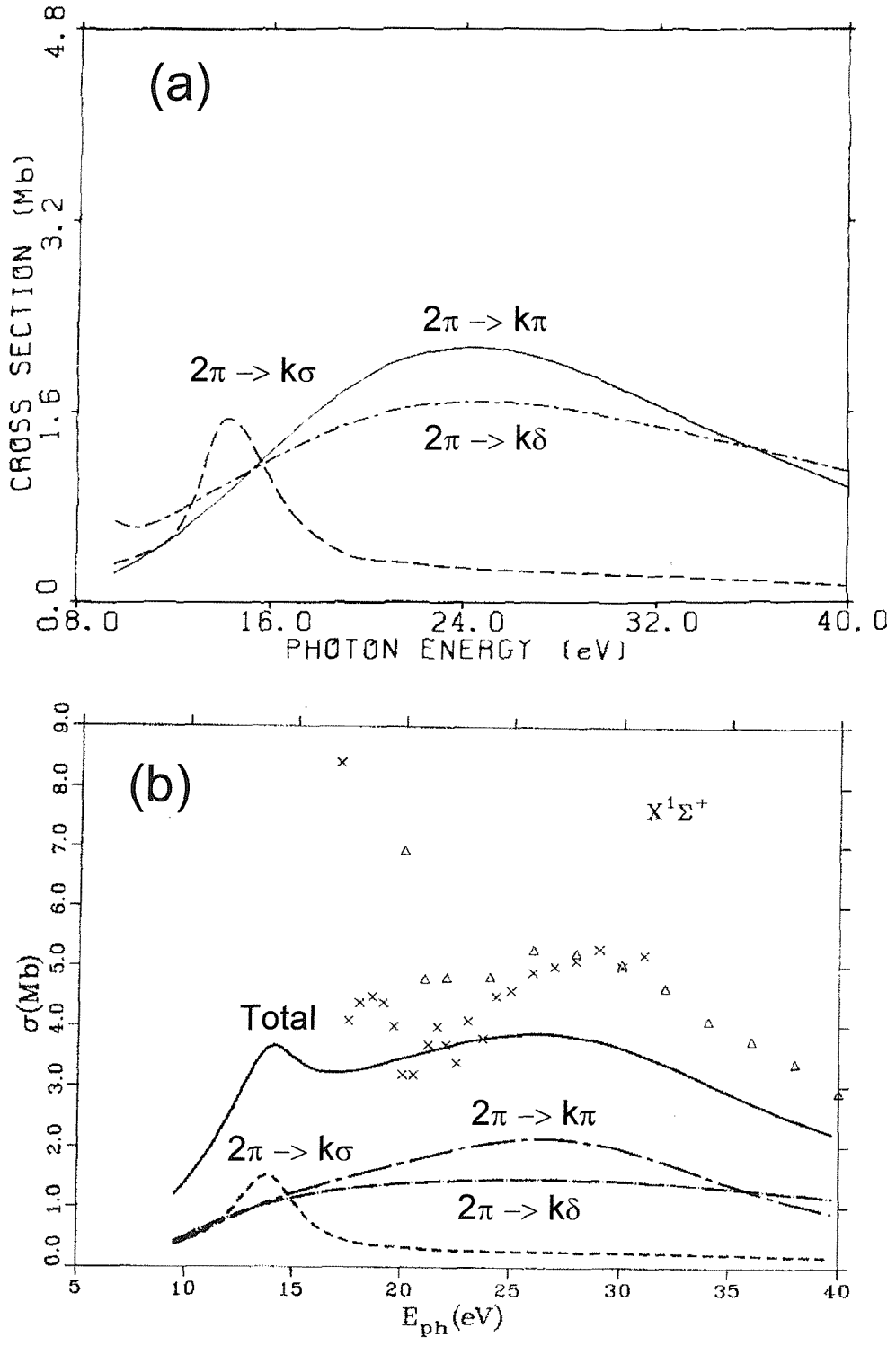

Figure 9.1 *Components of the calculated photoionization cross section for ionization from the 2π level of NO. (a) Smith[45]; (b) Collins[49], crosses and triangles are the experimental results from Brion[32] and Southworth[11] respectively.*

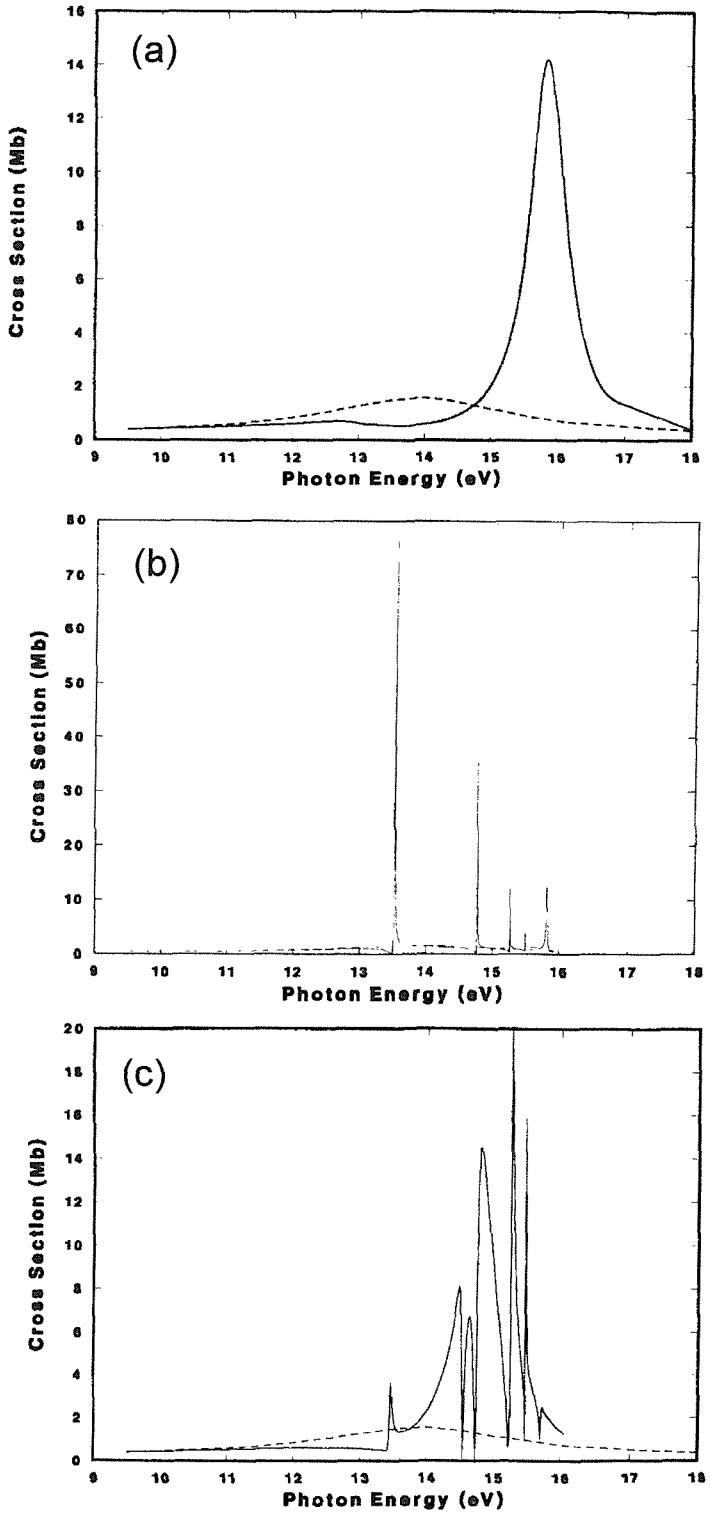

Figure 9.2 *$2\pi \rightarrow k\sigma$ photoionization cross section in the static exchange approximation (dashed line) from Lynch[50] (a) including the $4\sigma \rightarrow 2\pi$ valence autoionizing state (solid line) (b) including the $5\sigma \rightarrow n\pi$ Rydberg series (solid line) (c) including the Rydberg-valence mixed autoionizing states (solid line). (see text)*

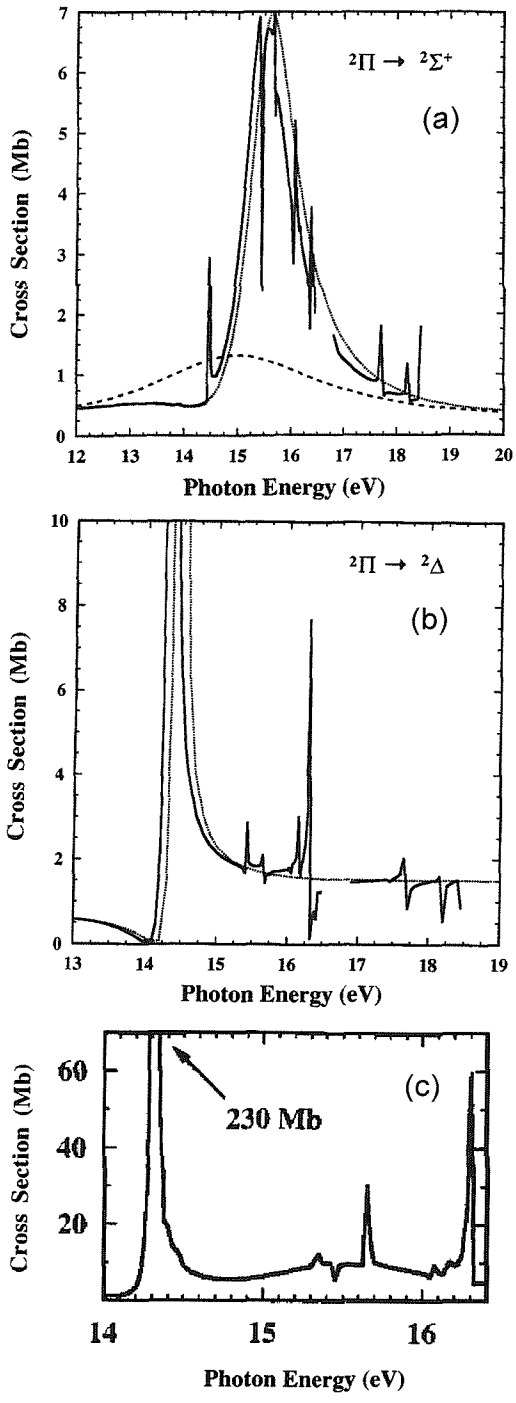

Figure 9.3 *Photoionization cross section leading to $NO^+(X^1\Sigma^+)$ state from Stratmann[47] (a) with $^2\Sigma^+$ final state symmetry: residual shape resonance (long dash), strong interaction between shape and valence resonances (short dash), superimposition of the $5\sigma \rightarrow n\pi$ Rydberg series on the previous structure (solid line) (b) with $^2\Delta$ final state symmetry: valence $4\sigma \rightarrow 2\pi$ resonance (short dash), $5\sigma \rightarrow n\pi$ Rydberg series superimposed on the underlying valence state (solid line) (c) Total from (a) and (b).*

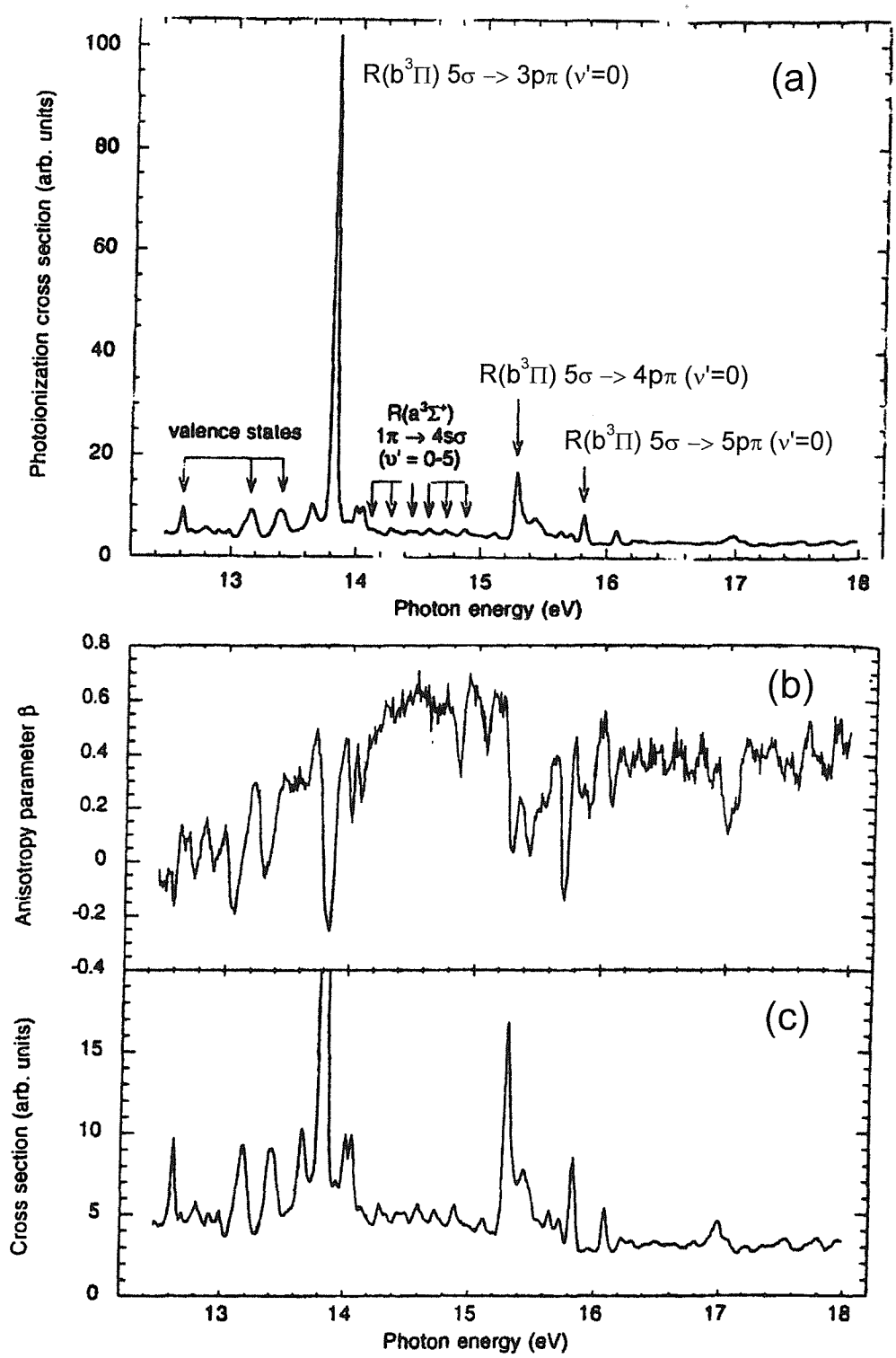

Figure 9.4 *Experimental results from Southworth[12] (a) (c) relative photoionization cross section summed over the $v^+ = 0$ - 5 vibrational level of $NO^+(X^1\Sigma^+)$ (b) Vibrationally averaged anisotropy parameter for the $v^+ = 0$ - 5 vibrational level of $NO^+(X^1\Sigma^+)$.*

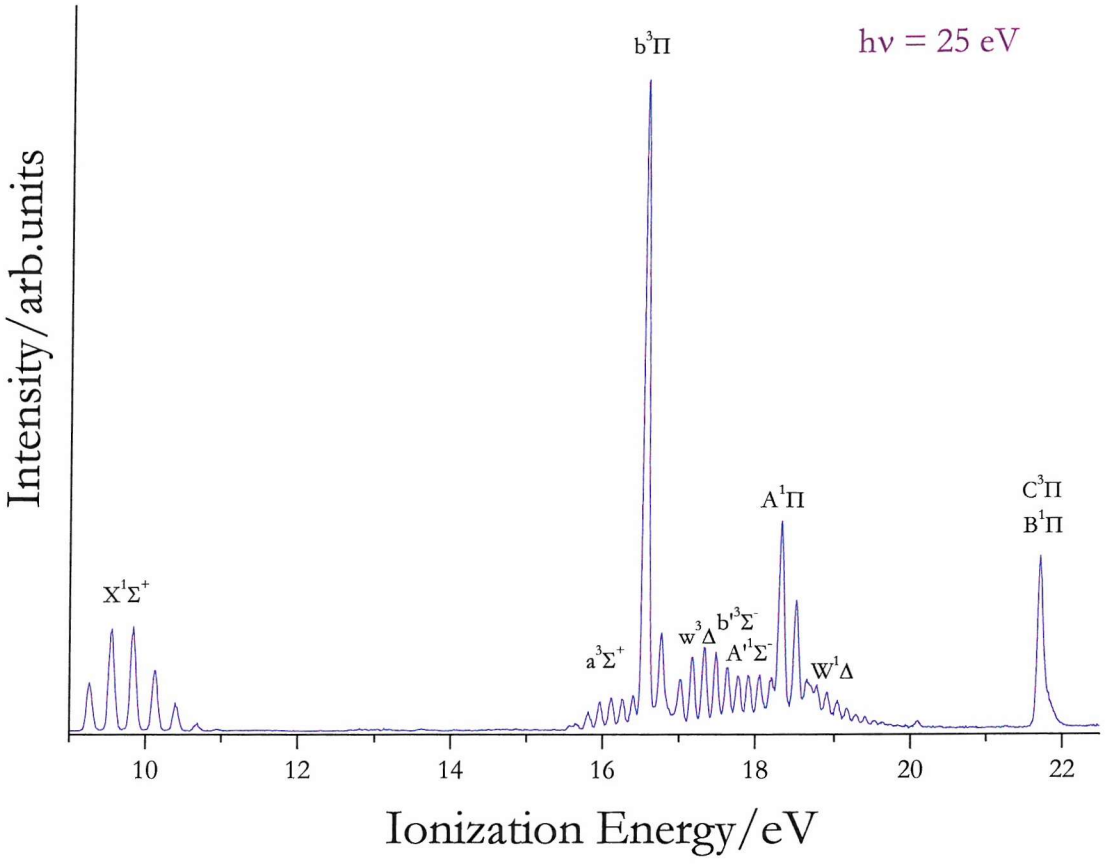

Figure 9.5 *Photoelectron spectrum of NO at $h\nu = 25$ eV measured at the angle with respect to the major polarization axis of the photon source $\theta = 54°44'$.*

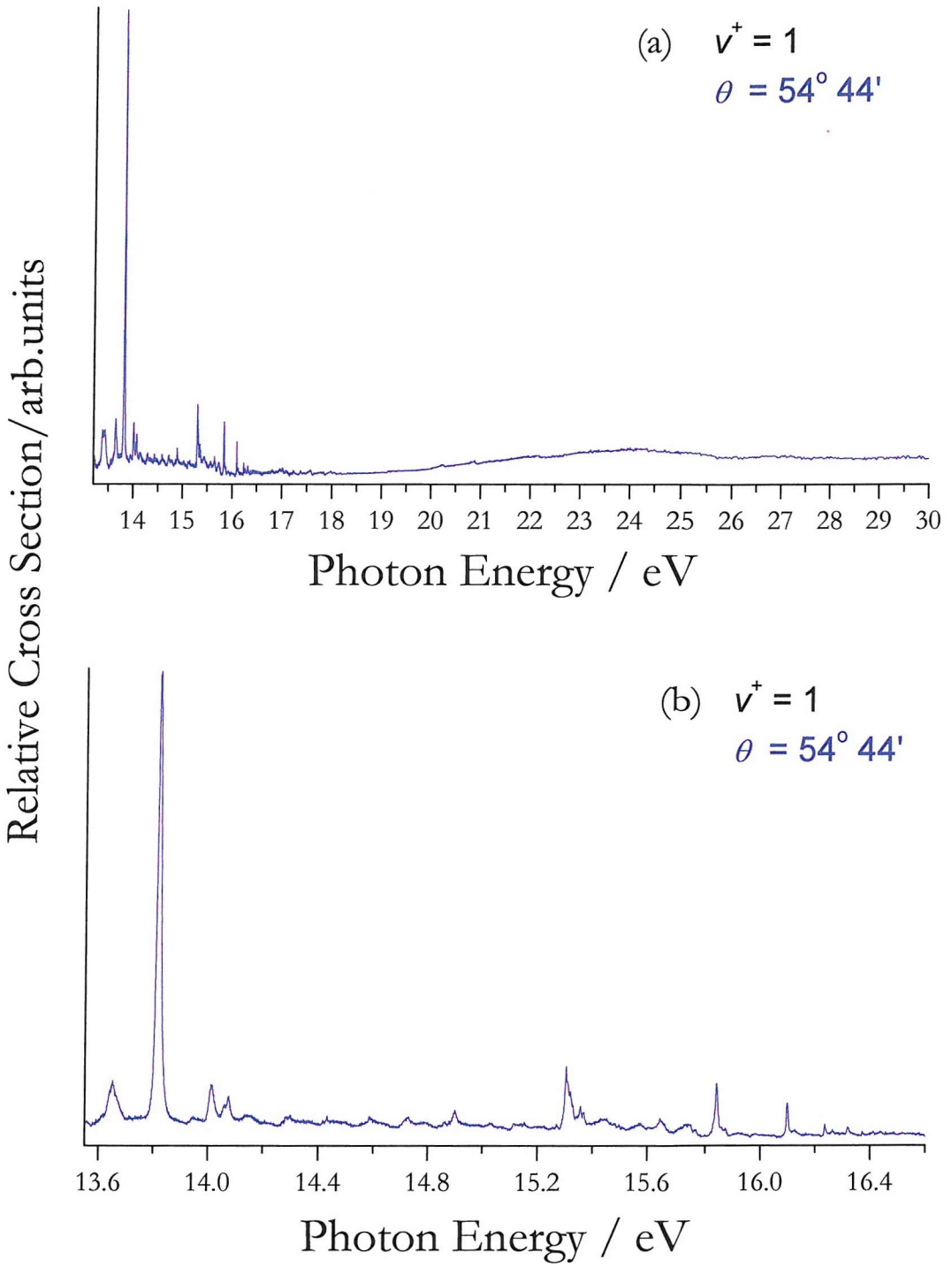

Figure 9.6 *CIS spectra on the $NO^+(^1\Sigma^+, v^+=1) \leftarrow NO(X^2\Pi, v''=0)$ band in the photon energy range (a) 13.2 - 30.0 eV (b) 13.6 - 16.6 eV.*

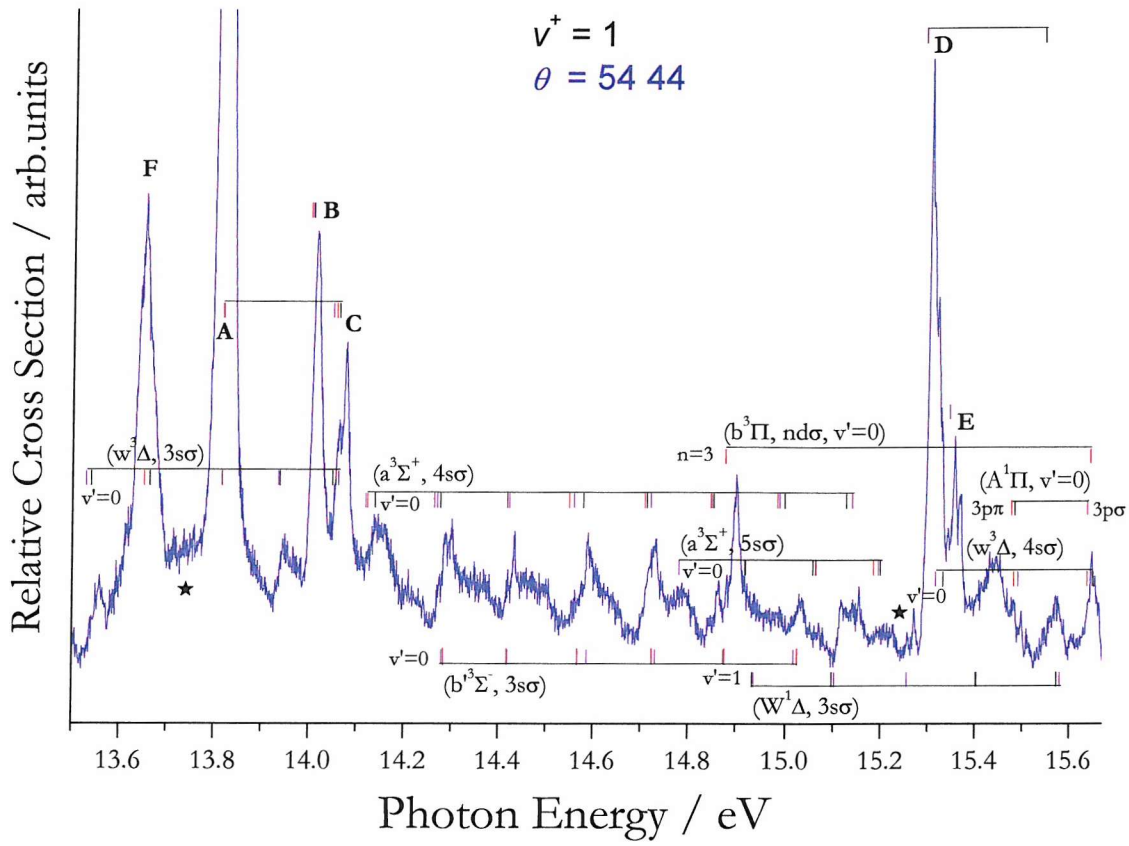

Figure 9.7 *CIS spectrum of the $NO^+(^1\Sigma^+, v^+=1) \leftarrow NO(X^2\Pi, v''=0)$ band in the photon energy range 13.5-15.7 eV with the assignment of the Rydberg series from Edqvis et al.[5] (violet mark), Stubbs et al.[34] (red mark), Erman et al.[29] (black mark). The peaks labelled with letters are reassigned in this work. The old assignment is as follow*

resonant state A: $R(b^3\Pi, 3p\pi, v'=0) \leftarrow 5\sigma$

resonant state B: $R(b^3\Pi, 3p\sigma, v'=0) \leftarrow 5\sigma$

resonant state C: $R(b^3\Pi, 3p\pi, v'=1) \leftarrow 5\sigma$

resonant state D: $R(b^3\Pi, 4p\pi, v'=0) \leftarrow 5\sigma$

resonant state E: $R(b^3\Pi, 4p\sigma, v'=0) \leftarrow 5\sigma$

resonant state F: *Unassigned.*

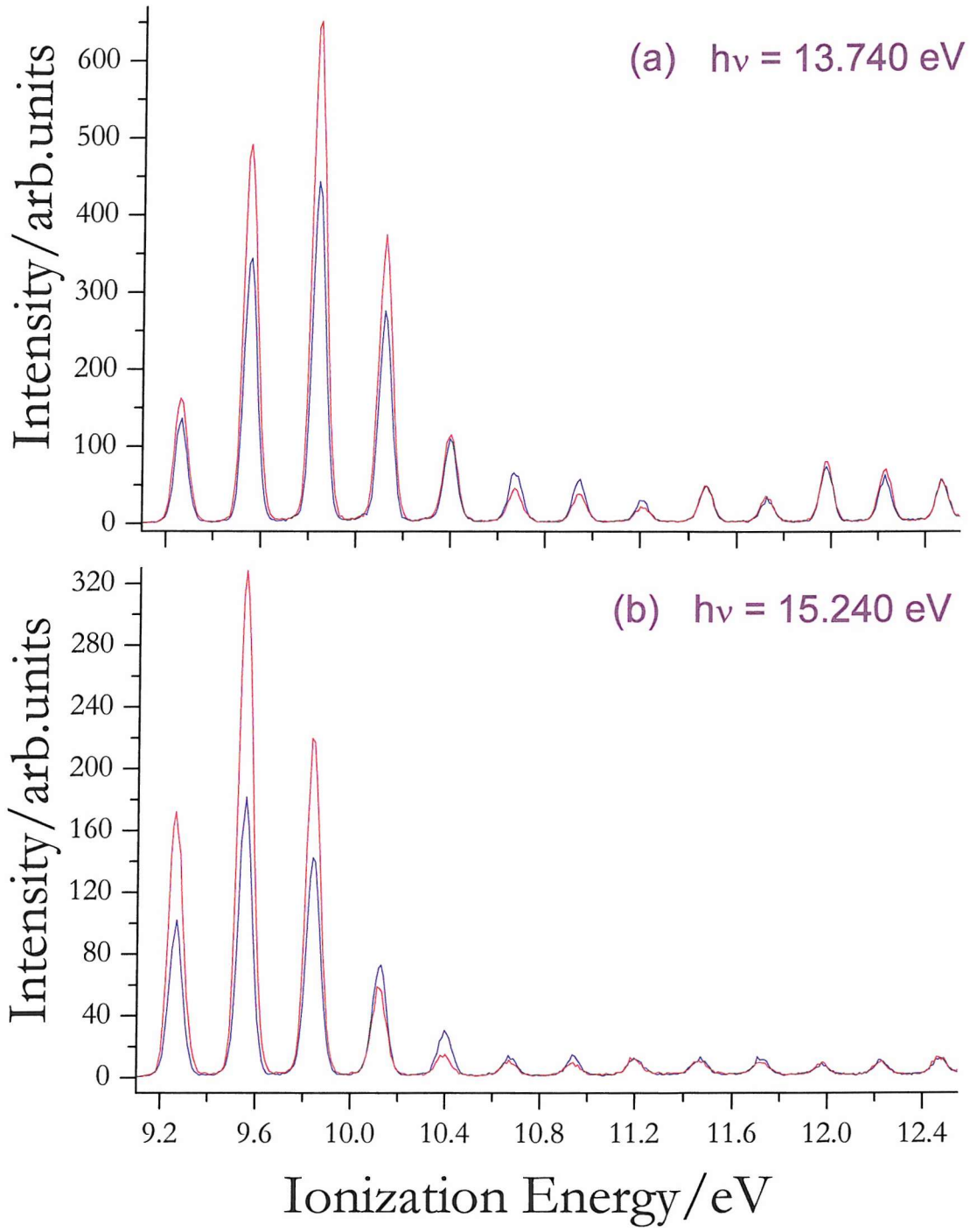

Figure 9.8 *PE spectra of $NO^+(^1\Sigma^+,v^+)\leftarrow NO(X^2\Pi,v''=0)$ measured at two different angles $\theta = 0°$ (red trace) and $\theta = 54° 44'$ (blue trace) with respect to the major polarization axis of the photon source in the 9.10 - 12.55 eV ionization energy region at (a) $h\nu = 13.74$ eV (b) $h\nu = 15.24$ eV.*

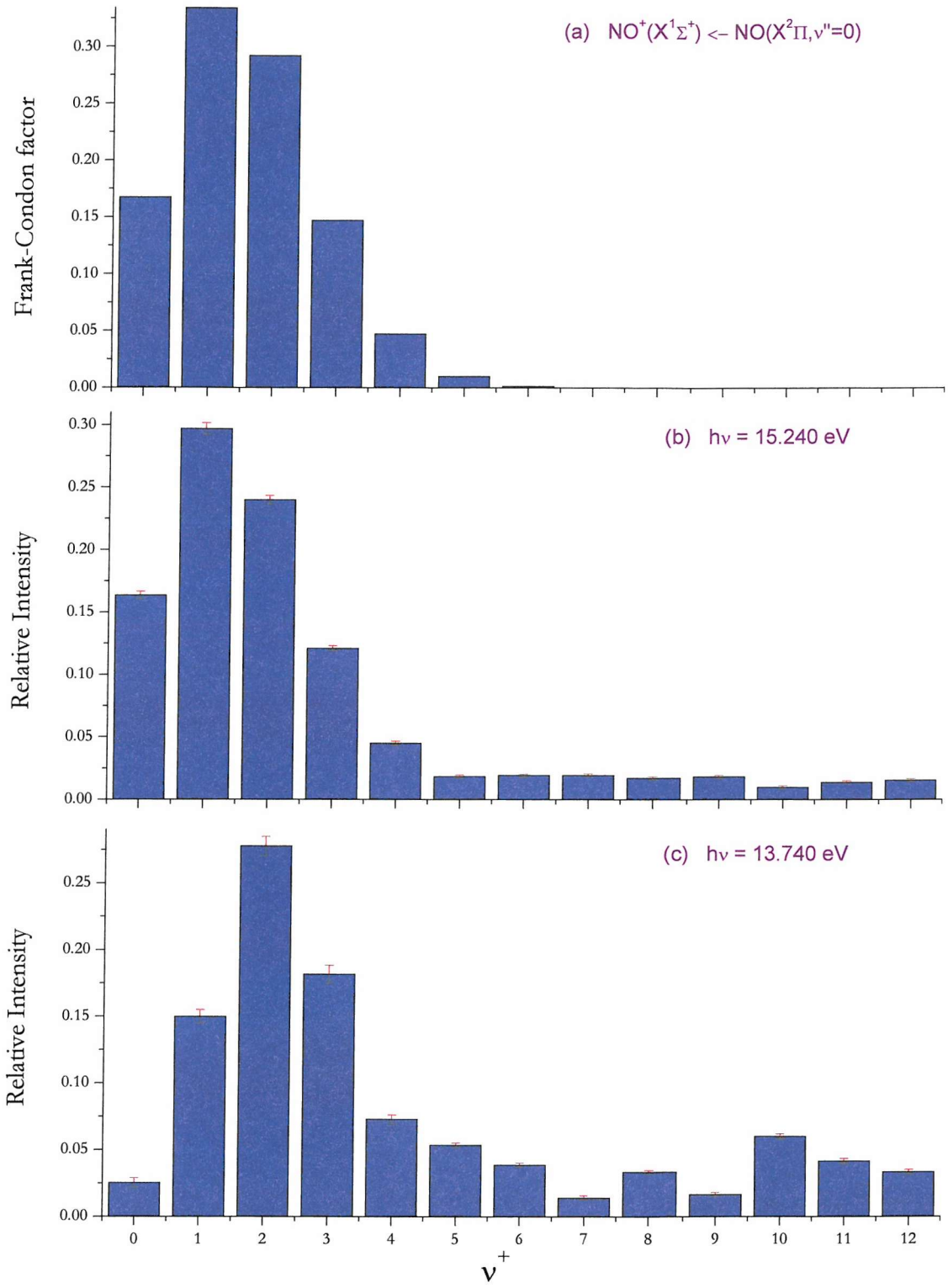

Figure 9.9 *Computed Frank-Condon factor for the direct ionization process (a). Relative intensity of the vibrational bands of $NO^+(X^1\Sigma^+)$ measured at (b) $h\nu = 15.24$ eV (c) $h\nu = 13.74$ eV after the subtraction of the contribution of the direct ionization represented by the PE spectrum recorded at $h\nu = 15.24$ eV (see Figure 9.8).*

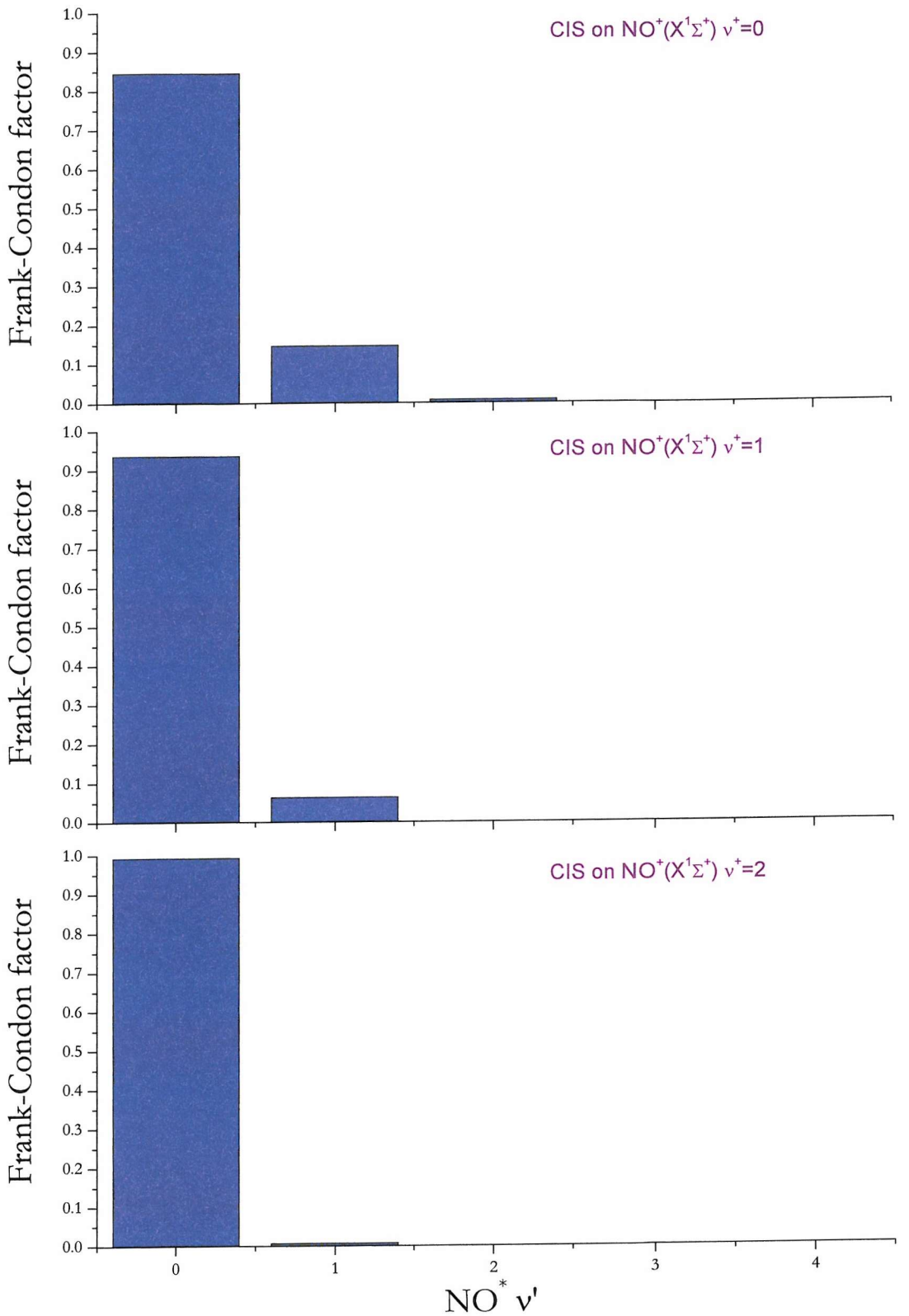

Figure 9.10 *Computed CIS spectra for* $NO^+(^1\Sigma^+,v^+) \leftarrow NO^*(b^3\Pi,np,v') \leftarrow NO(X^2\Pi)$ *for* $v^+ = 0$, *1 and 2.*

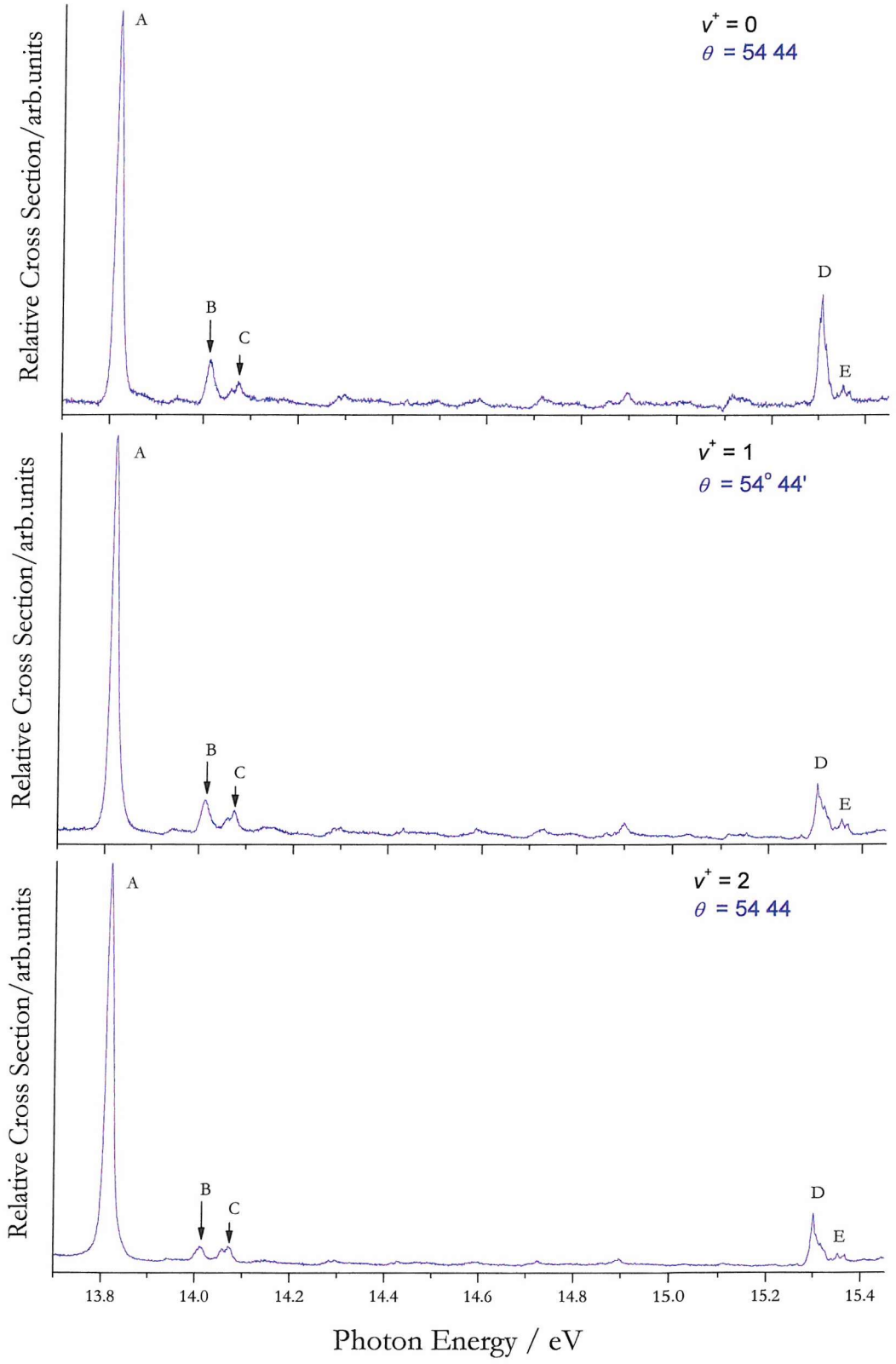

Figure 9.11 *CIS spectra on the $NO^+(^1\Sigma^+,v^+) \leftarrow NO(X^2\Pi,v''=0)$ bands in the photon energy range 13.70 - 15.45 eV for $v^+ = 0$, 1 and 2.*

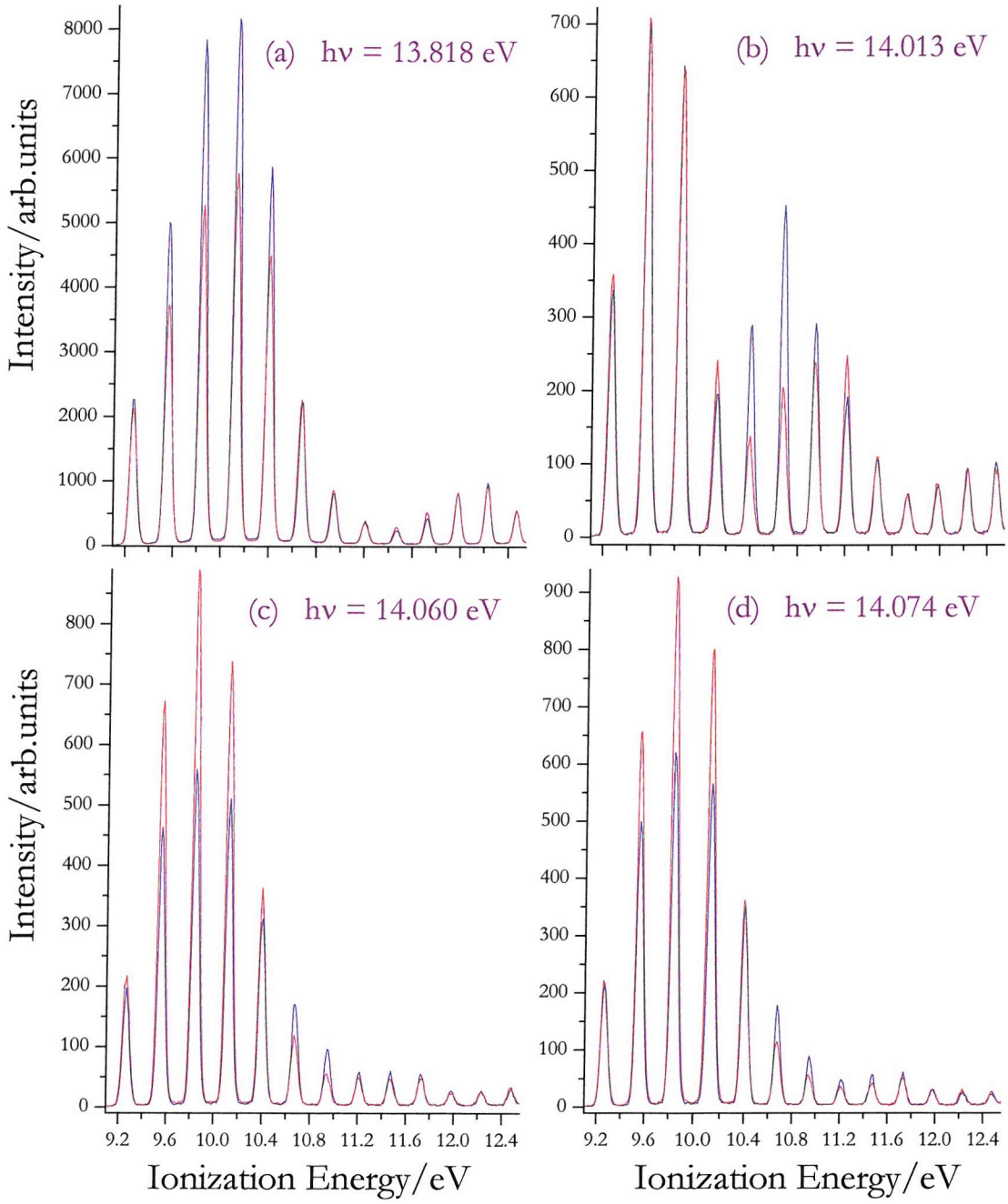

Figure 9.12 *PE spectra of $NO^+(^1\Sigma^+,v^+) \leftarrow NO(X^2\Pi,v''=0)$ measured at two different angles $\theta = 0°$ (red trace) and $\theta = 54°44'$ (blue trace) in the 9.10 - 12.55 eV ionization energy region at the Rydberg resonant state as marked in Figure 9.7*
(a) Peak A at $h\nu = 13.818$ eV
(b) Peak B at $h\nu = 14.013$ eV
(c) Peak C at $h\nu = 14.060$ eV spin orbit component from $NO(X^2\Pi_{3/2})$
(d) Peak C at $h\nu = 14.074$ eV spin orbit component from $NO(X^2\Pi_{1/2})$.

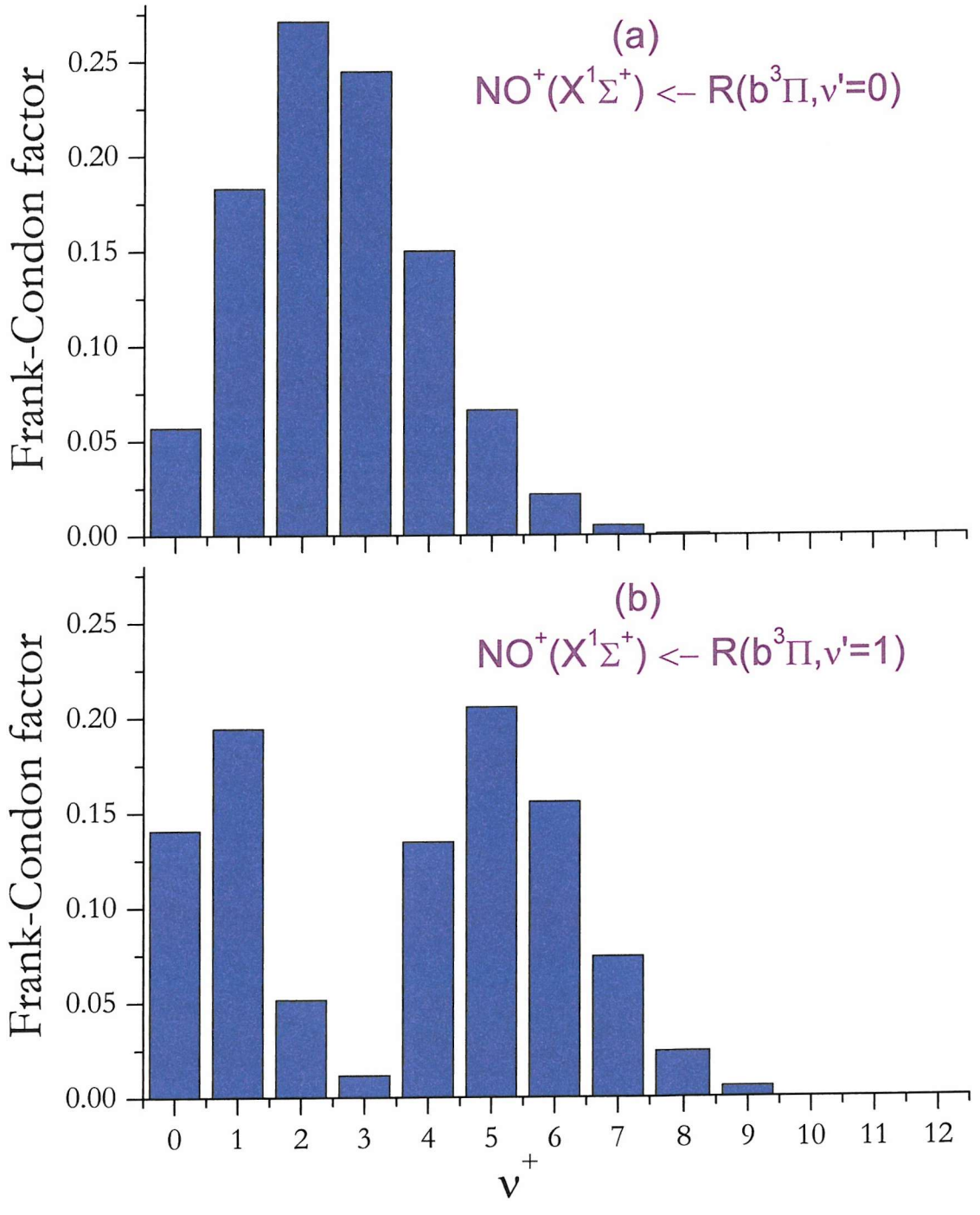

Figure 9.13 *Simulated Frank-Condon factor between the ionic state $NO^+(X^1\Sigma^+)$ and the resonant Rydberg state*
(a) $R(b^3\Pi, v'=0)$
(b) $R(b^3\Pi, v'=1)$.

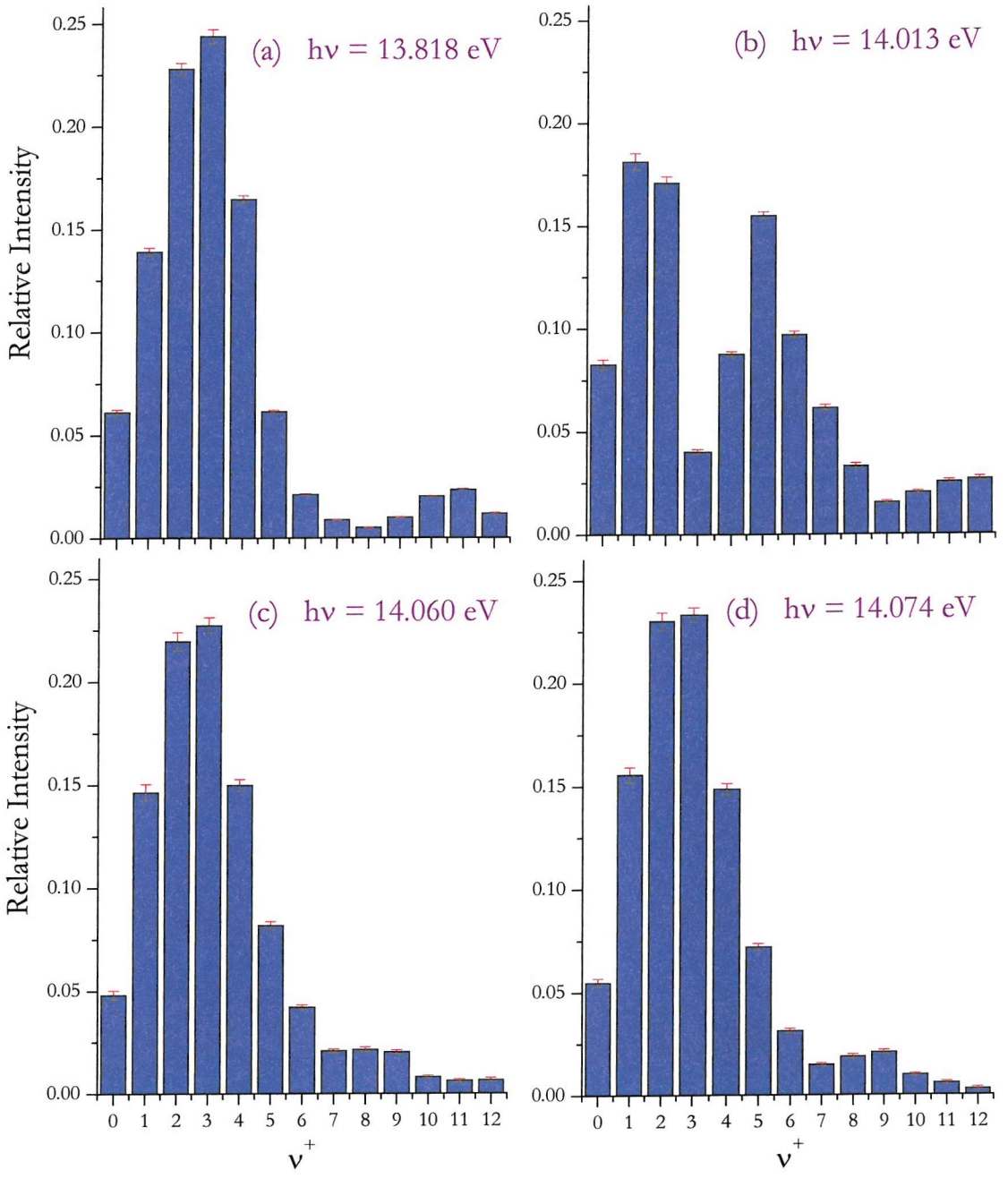

Figure 9.14 *Relative intensity of the vibrational bands of $NO^+(X^1\Sigma^+)$ measured at a photon energy corresponding to the Rydberg resonant state as marked in Figure 9.7*

(a) Peak A at $h\nu = 13.818$ eV

(b) Peak B at $h\nu = 14.013$ eV

(c) Peak C at $h\nu = 14.060$ eV spin orbit component from $NO(X^2\Pi_{3/2})$

(d) Peak C at $h\nu = 14.074$ eV spin orbit component from $NO(X^2\Pi_{1/2})$.

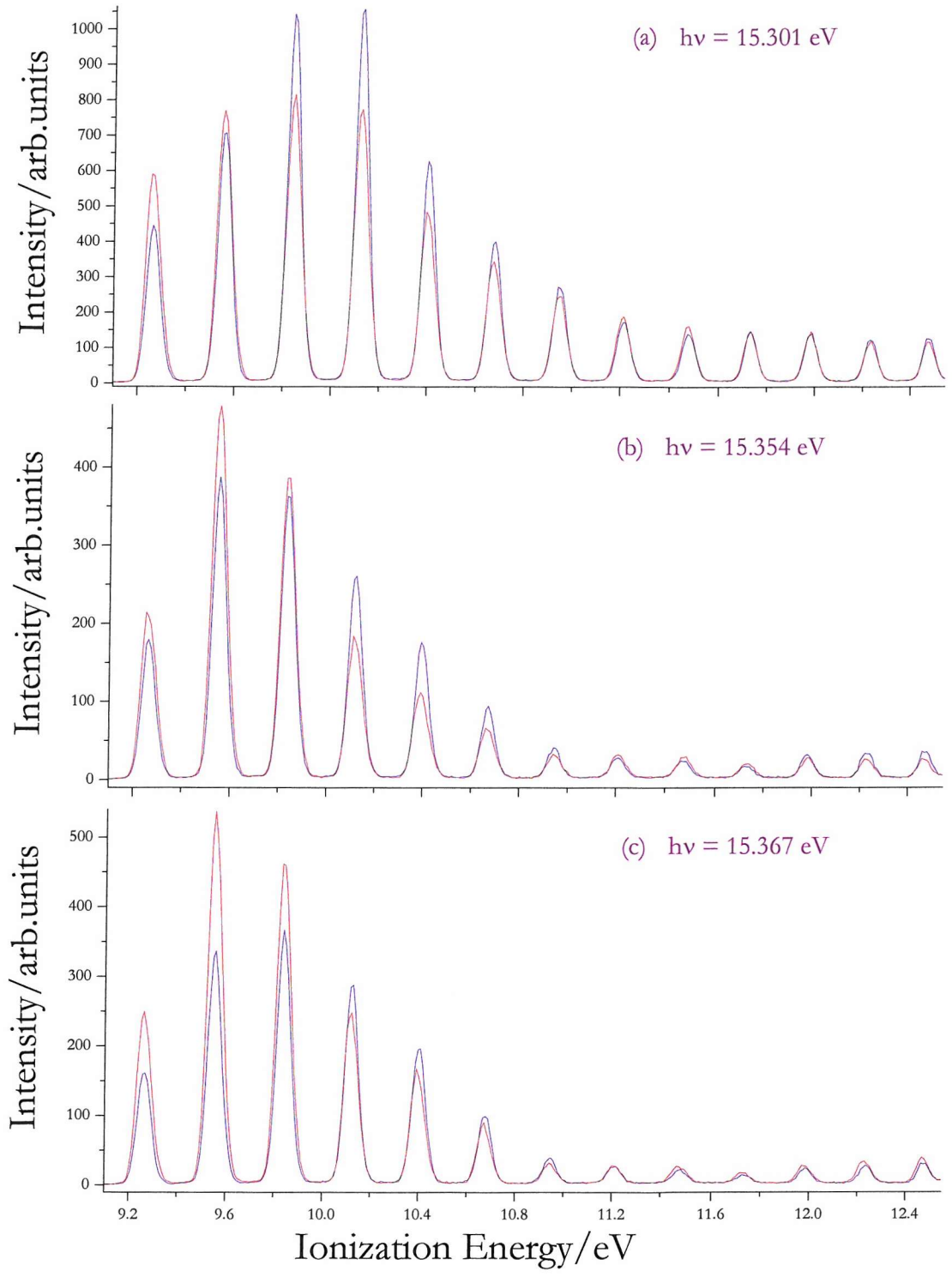

Figure 9.15 *PE spectra of $NO^+(^1\Sigma^+,v^+)\leftarrow NO(X^2\Pi)$ measured at two different angles $\theta = 0°$ (red trace) and $\theta = 54° 44'$ (blue trace) in the 9.10 - 12.55 eV ionization energy region at the resonant state as marked in Figure 9.7*
(a) Peak D at $h\nu = 15.301$ eV
(b) Peak E at $h\nu = 15.354$ eV spin orbit component from $NO(X^2\Pi_{3/2})$
(c) Peak E at $h\nu = 14.367$ eV spin orbit component from $NO(X^2\Pi_{1/2})$.

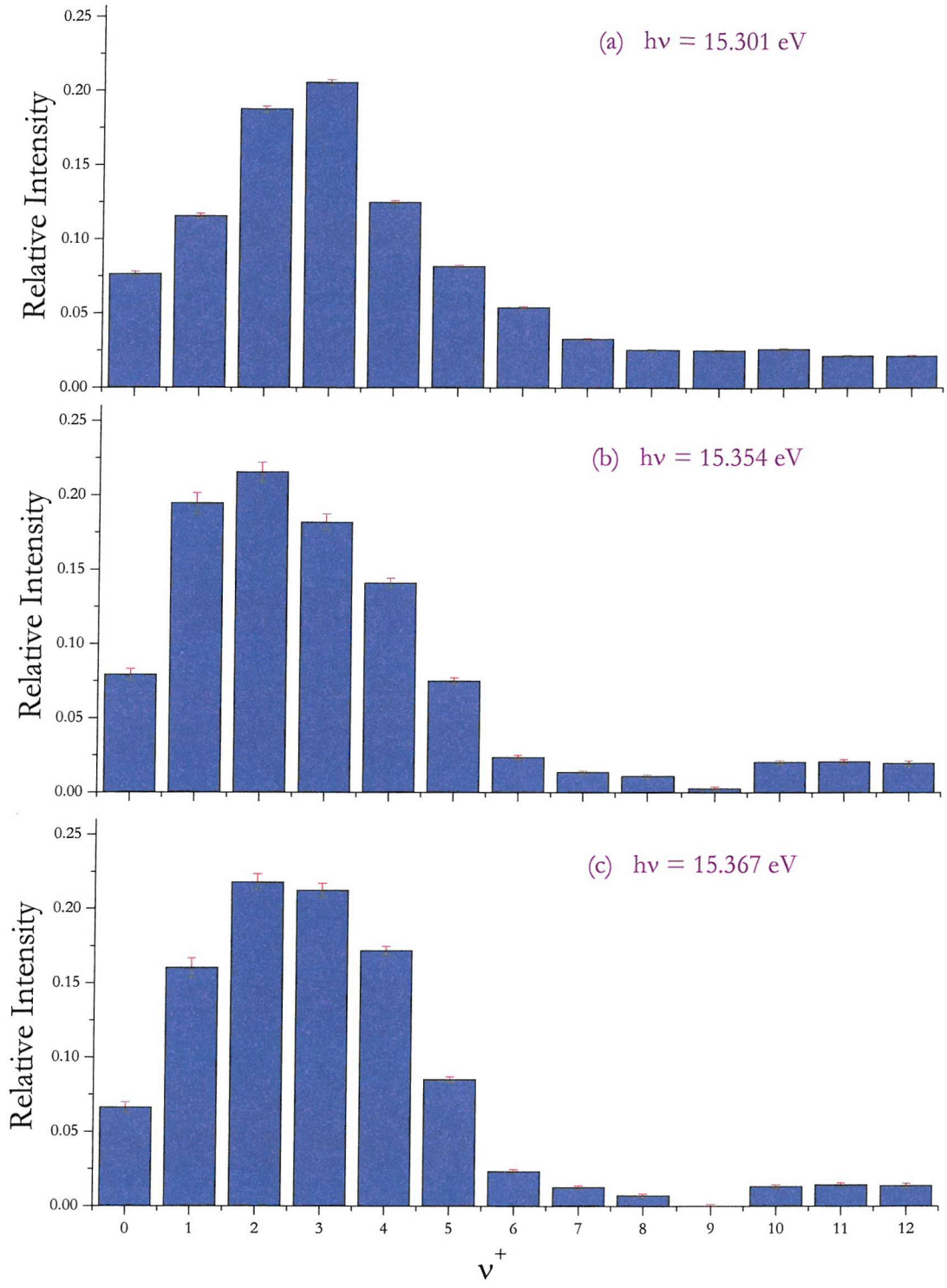

Figure 9.16 *Relative intensity of the vibrational bands of $NO^+(X^1\Sigma^+)$ measured at a photon energy corresponding to the Rydberg resonant state as marked in Figure 9.7*
(a) Peak D at $h\nu = 15.301$ eV
(b) Peak E at $h\nu = 15.354$ eV spin orbit component from $NO(X^2\Pi_{3/2})$
(c) Peak E at $h\nu = 14.367$ eV spin orbit component from $NO(X^2\Pi_{1/2})$.

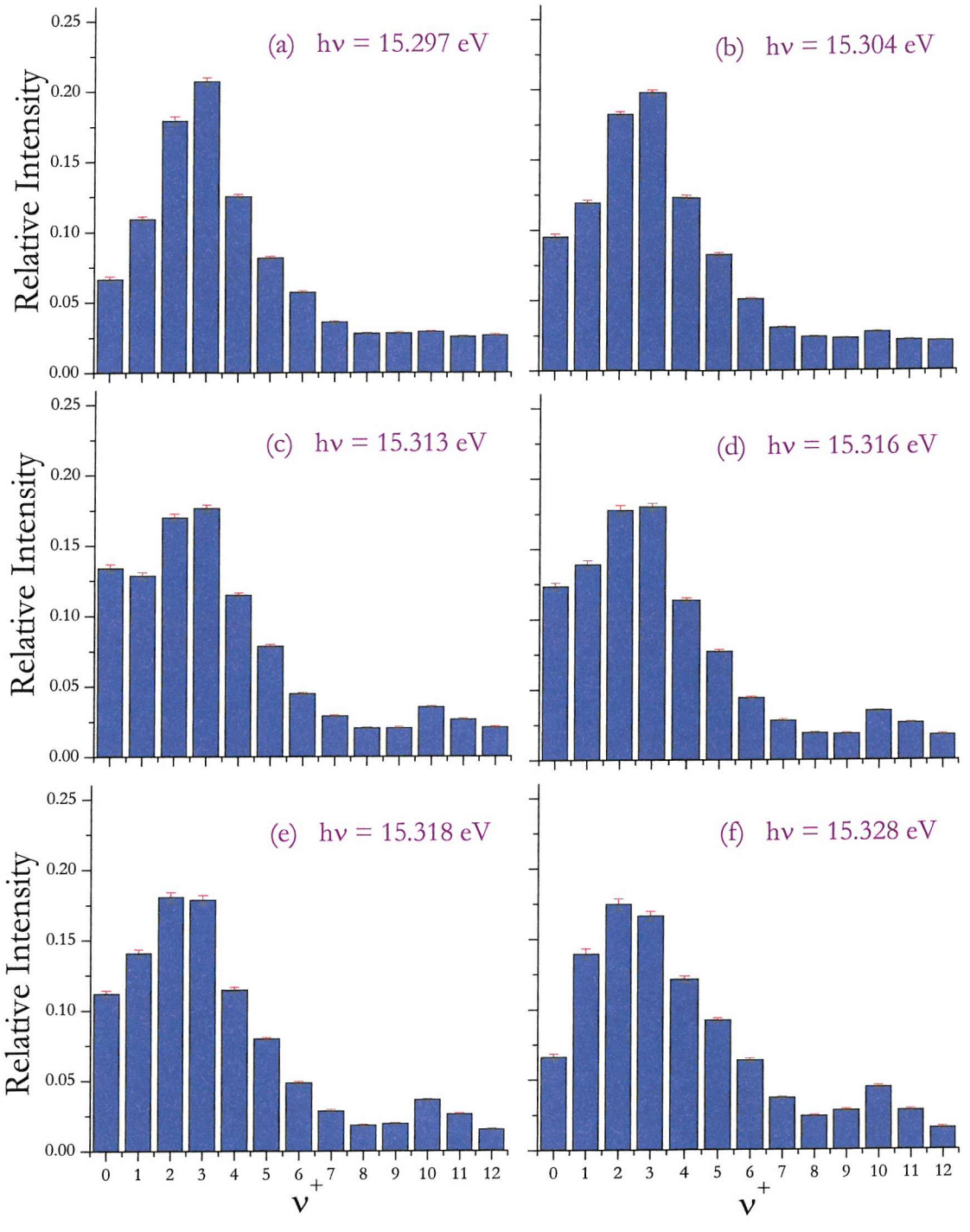

Figure 9.17 *Relative intensity of the vibrational bands of $NO^+(X^1\Sigma^+)$ across the Rydberg resonant state marked as D in Figure 9.7 at photon energy*
(a) hν = 15.297 eV *(b) hν = 15.304 eV*
(c) hν = 15.313 eV *(d) hν = 15.316 eV*
(e) hν = 15.318 eV *(f) hν = 15.328 eV.*

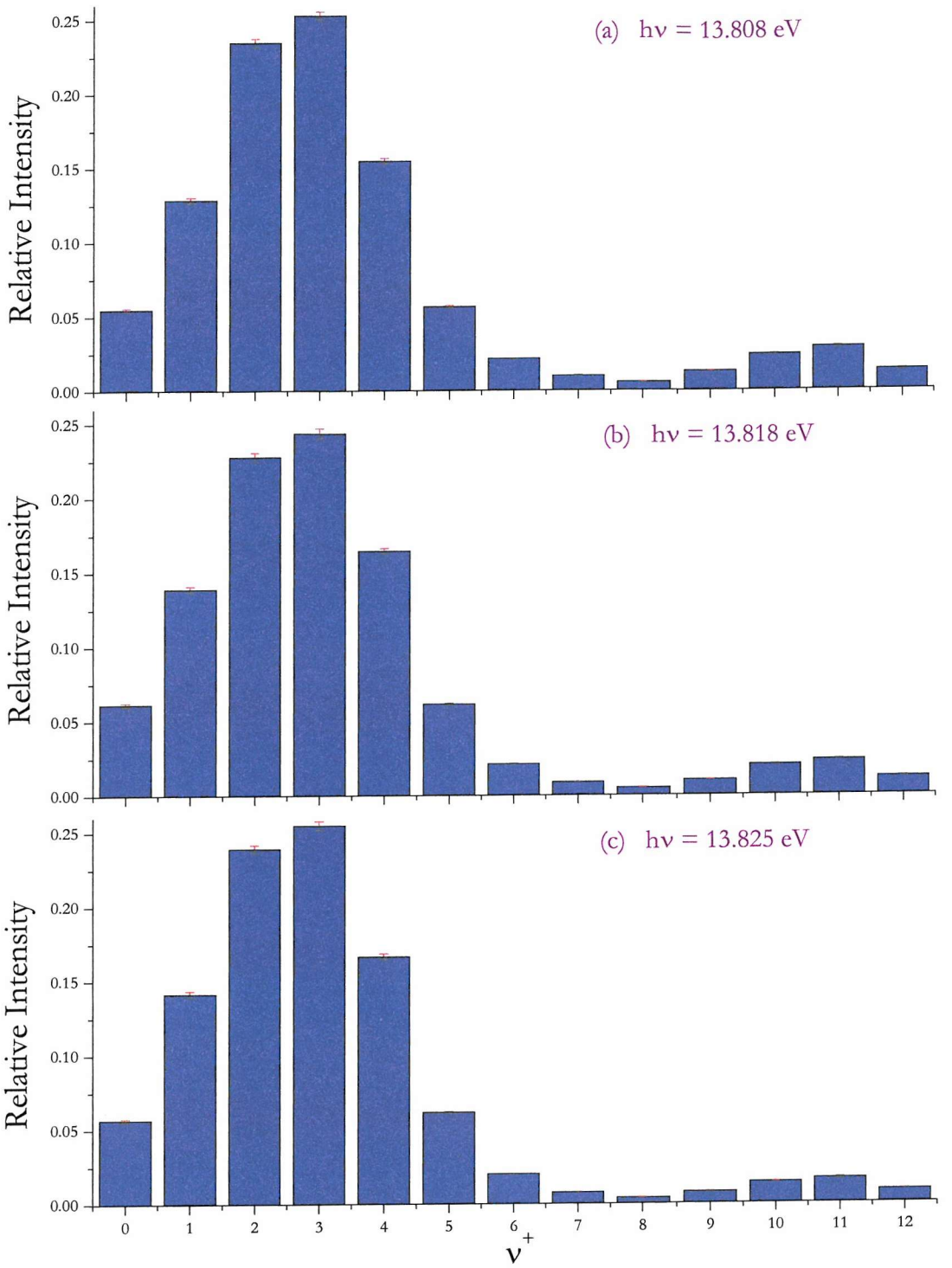

Figure 9.18 *Relative intensity of the vibrational bands of $NO^+(X^1\Sigma^+)$ across the Rydberg resonant state marked as A in Figure 9.7 at photon energy*
(a) $h\nu = 13.808$ eV
(b) $h\nu = 13.818$ eV
(c) $h\nu = 13.825$ eV.

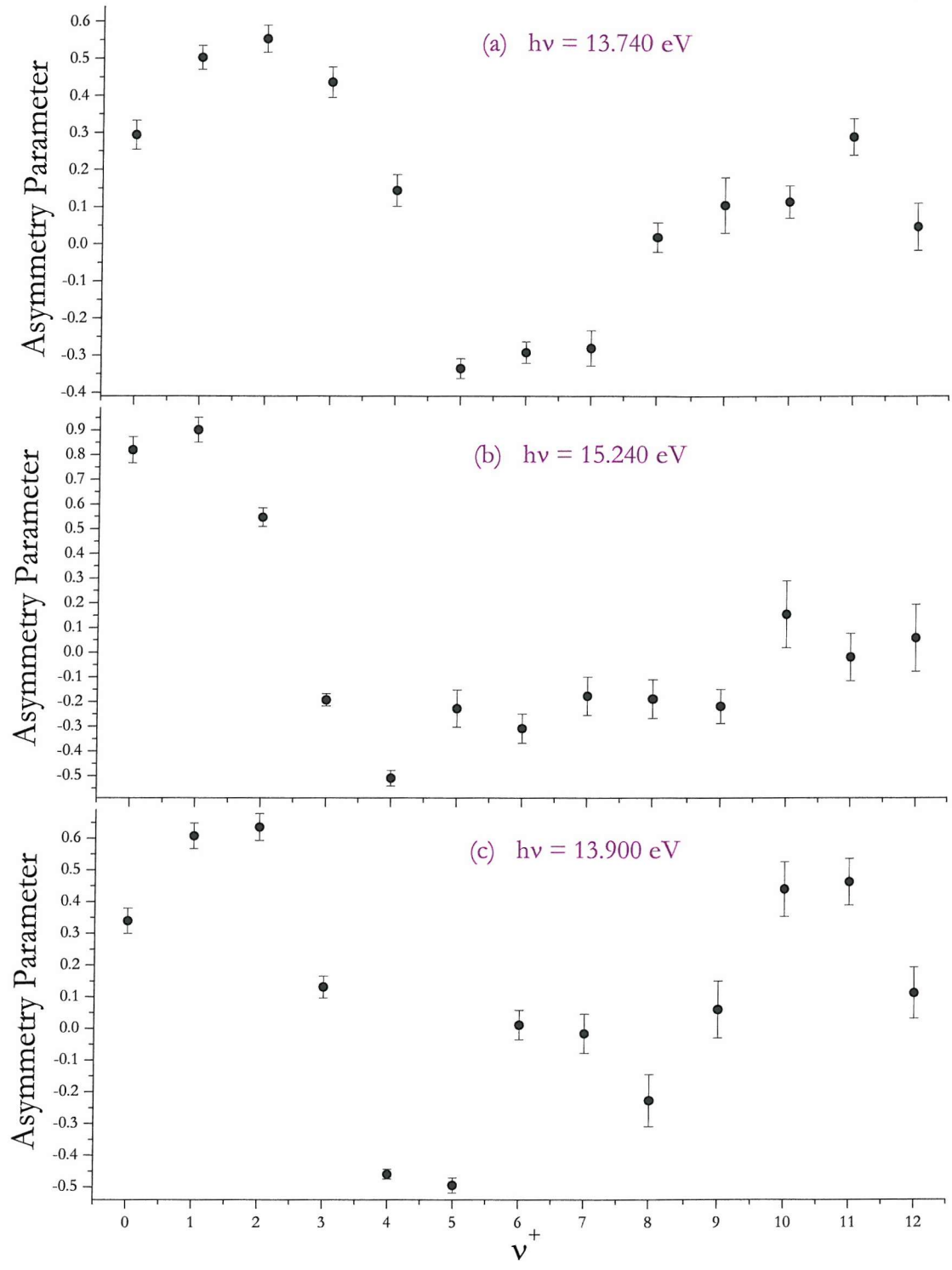

Figure 9.19 *Asymmetry parameter of the vibrational bands of $NO^+(X^1\Sigma^+)$ measured at (a) $h\nu = 13.74$ eV (b) $h\nu = 15.24$ eV (c) $h\nu = 13.90$ eV.*

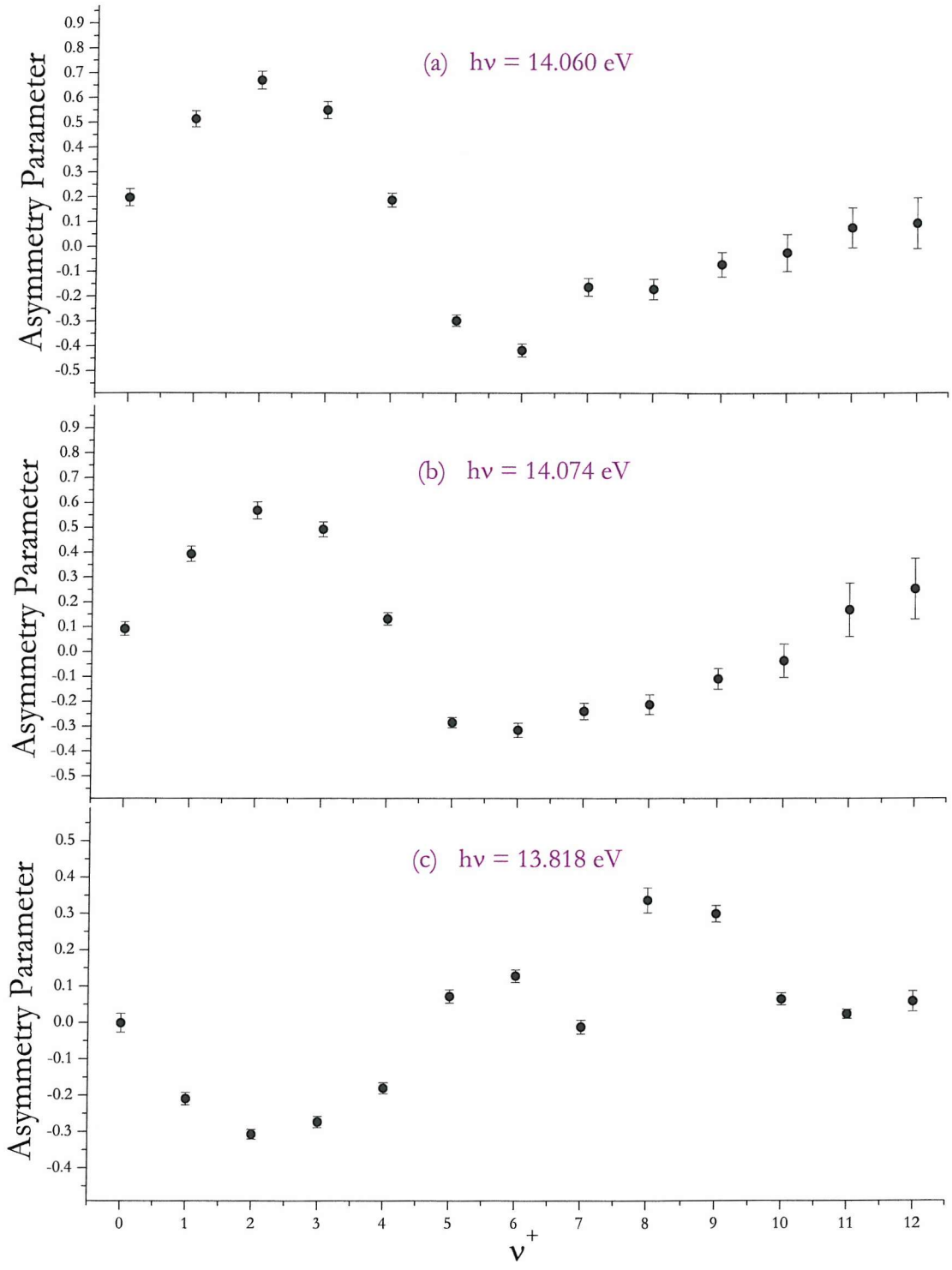

Figure 9.20 *Asymmetry parameter of the vibrational bands of $NO^+(X^1\Sigma^+)$ measured at a photon energy corresponding to the Rydberg resonant state as marked in Figure 9.7*
(a) Peak C at $h\nu = 14.060$ eV spin orbit component from $NO(X^2\Pi_{3/2})$
(b) Peak C at $h\nu = 14.074$ eV spin orbit component from $NO(X^2\Pi_{1/2})$
(c) Peak A at $h\nu = 13.818$ eV.

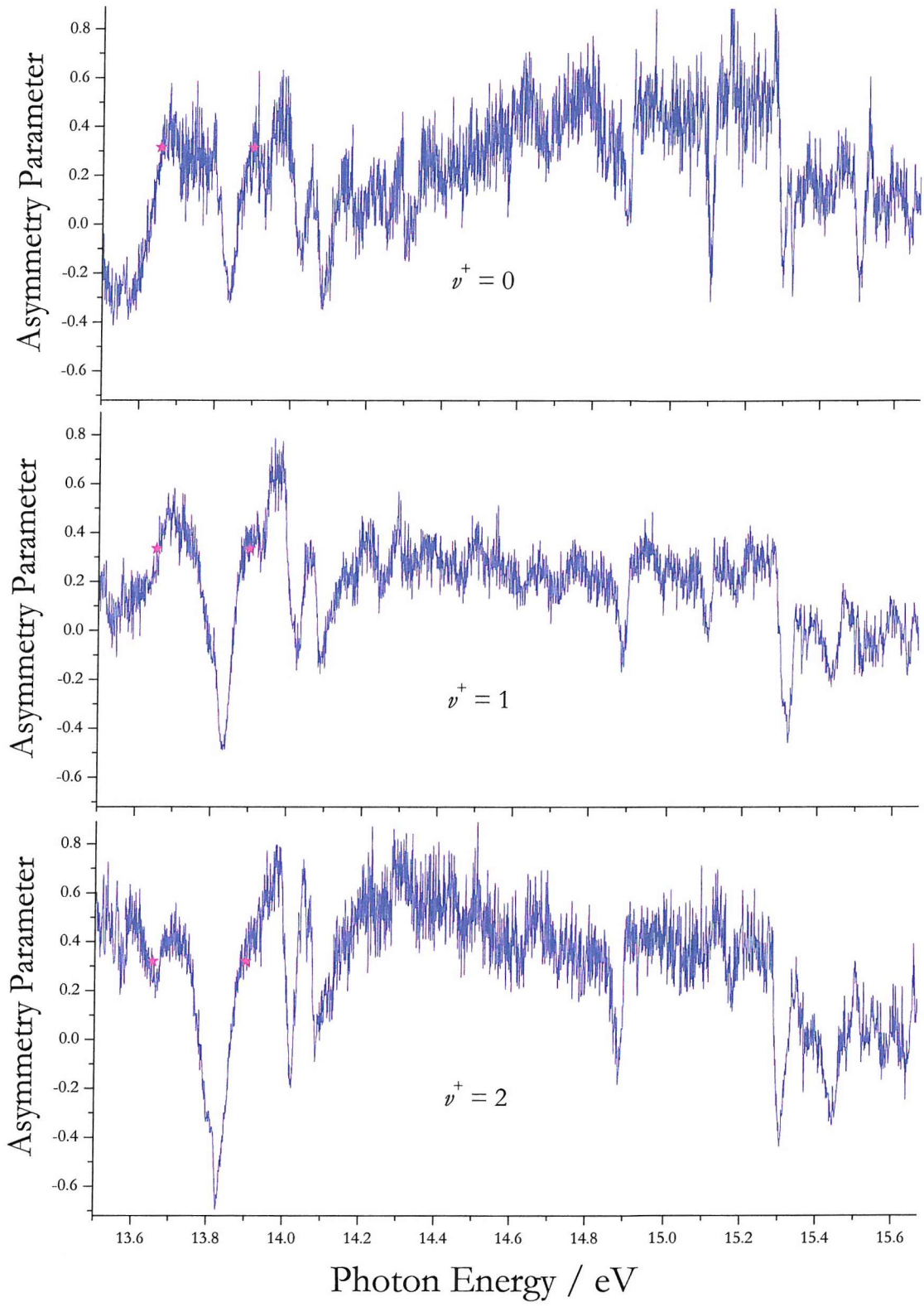

Figure 9.21 *Asymmetry parameter β for the $NO^+(^1\Sigma^+,v^+) \leftarrow NO(X^2\Pi,v''=0)$ vibrational bands in the photon energy range 13.50 - 15.65 eV for $v^+ = 0$, 1 and 2. The magenta symbols are set at 13.654 and 13.900 eV.*

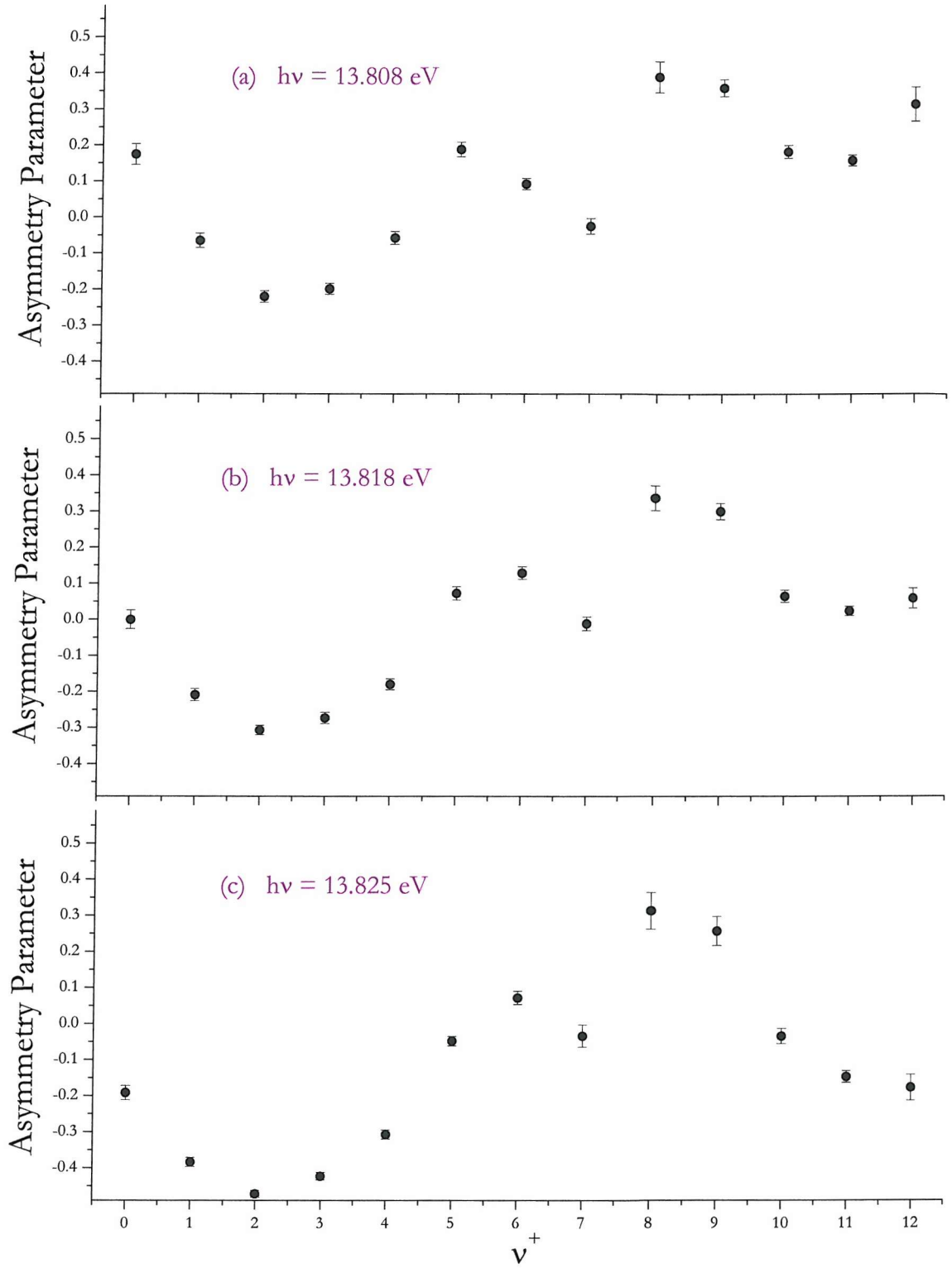

Figure 9.22 *Asymmetry parameter of the vibrational bands of $NO^+(X^1\Sigma^+)$ across the Rydberg resonant state marked as A in Figure 9.7 at photon energy (a) $h\nu = 13.808$ eV (b) $h\nu = 13.818$ eV (c) $h\nu = 13.825$ eV.*

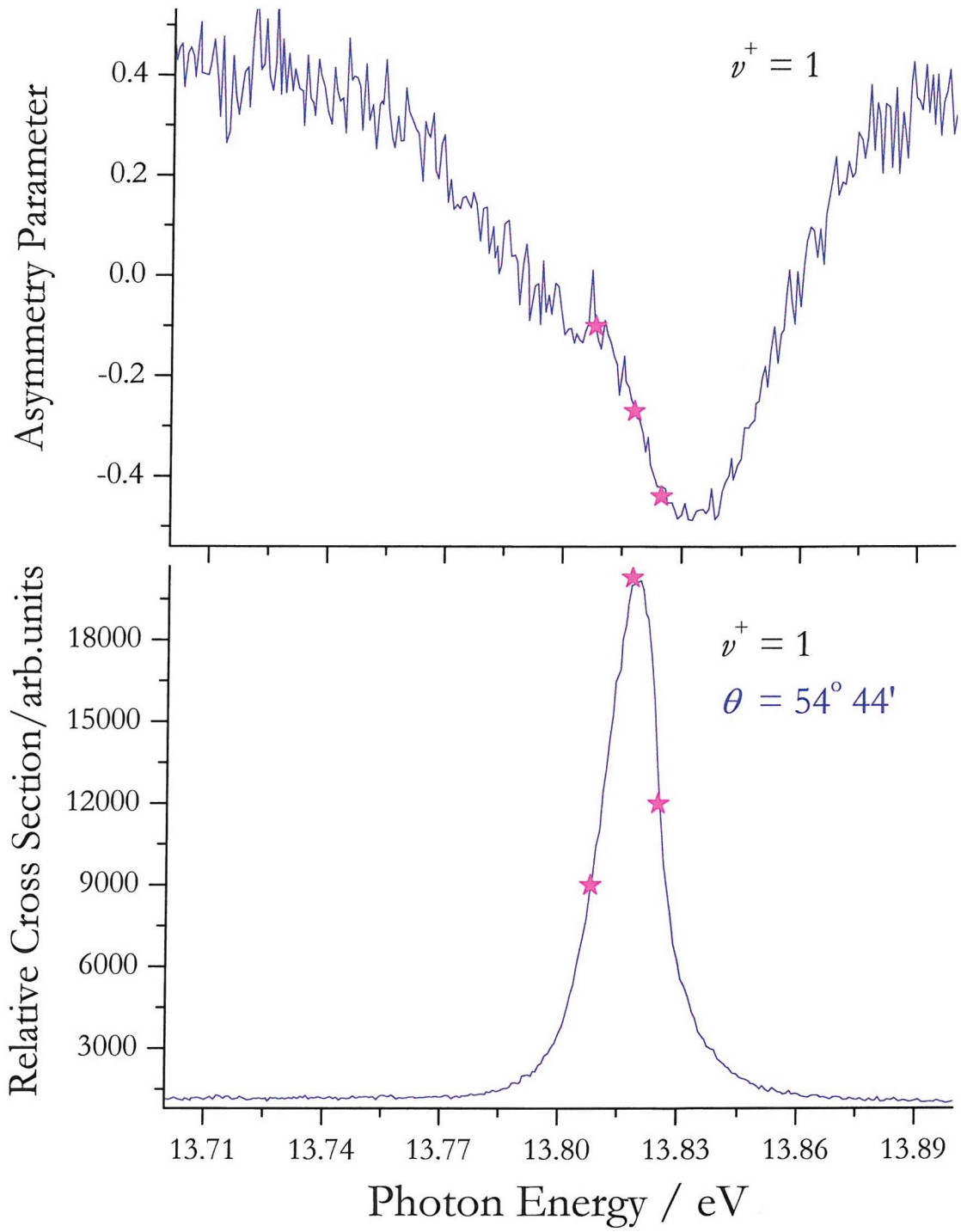

Figure 9.23 *Asymmetry parameter β and photoelectron cross section for the $NO^+(^1\Sigma^+, v^+=1) \leftarrow NO(X^2\Pi, v''=0)$ vibrational band in the photon energy range 13.7 - 13.9 eV through the Rydberg resonant state marked as A in Figure 9.7. The magenta symbols are set at the photon energies reported in Figure 9.22: 13.808, 13.818 and 13.825 eV.*

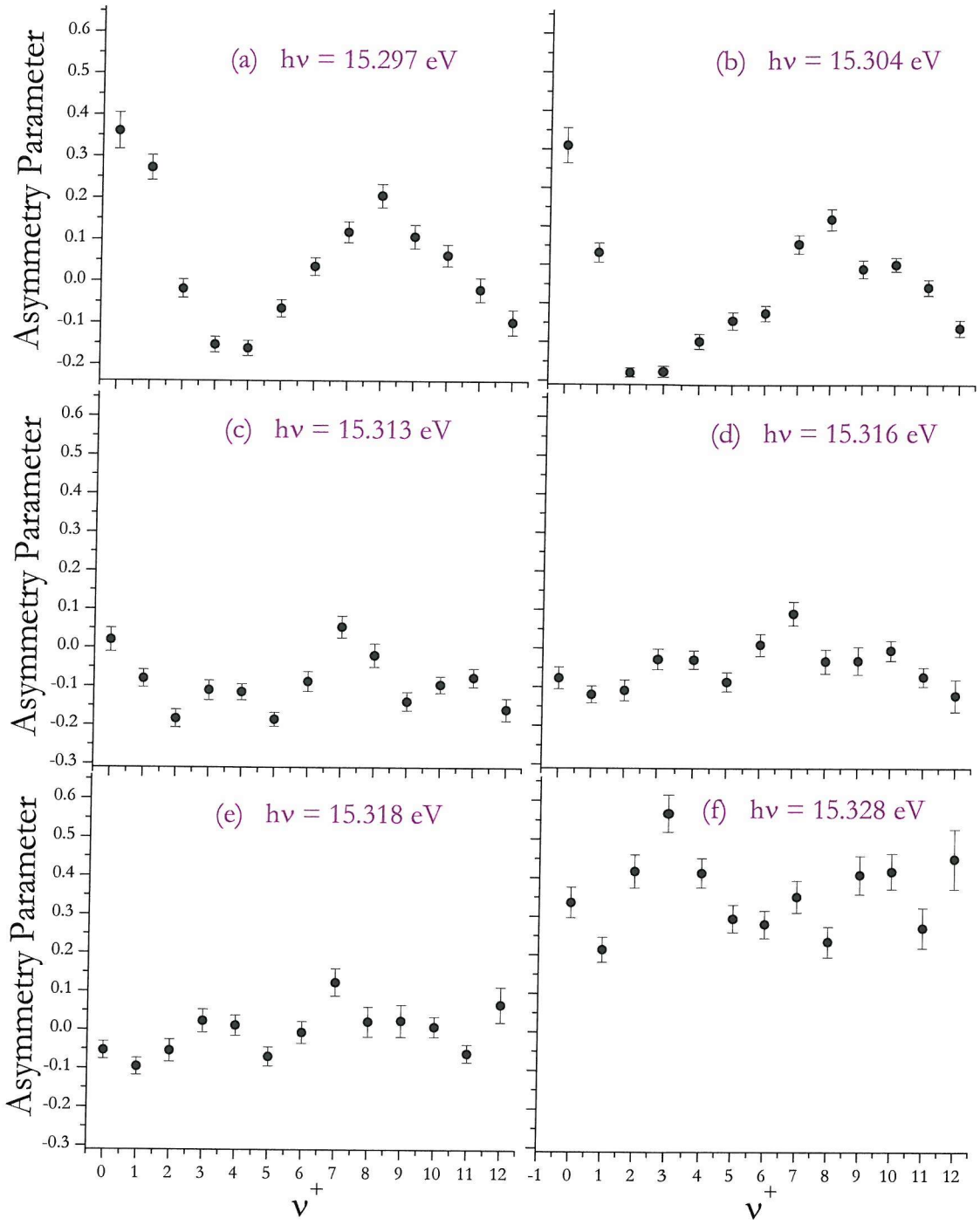

Figure 9.24 *Asymmetry parameter β of the vibrational bands of $NO^+(X^1\Sigma^+)$ across mixing Rydberg resonant states marked as D in Figure 9.7 at photon energy*

(a) hν = 15.297 eV *(b) hν = 15.304 eV*
(c) hν = 15.313 eV *(d) hν = 15.316 eV*
(e) hν = 15.318 eV *(f) hν = 15.328 eV.*

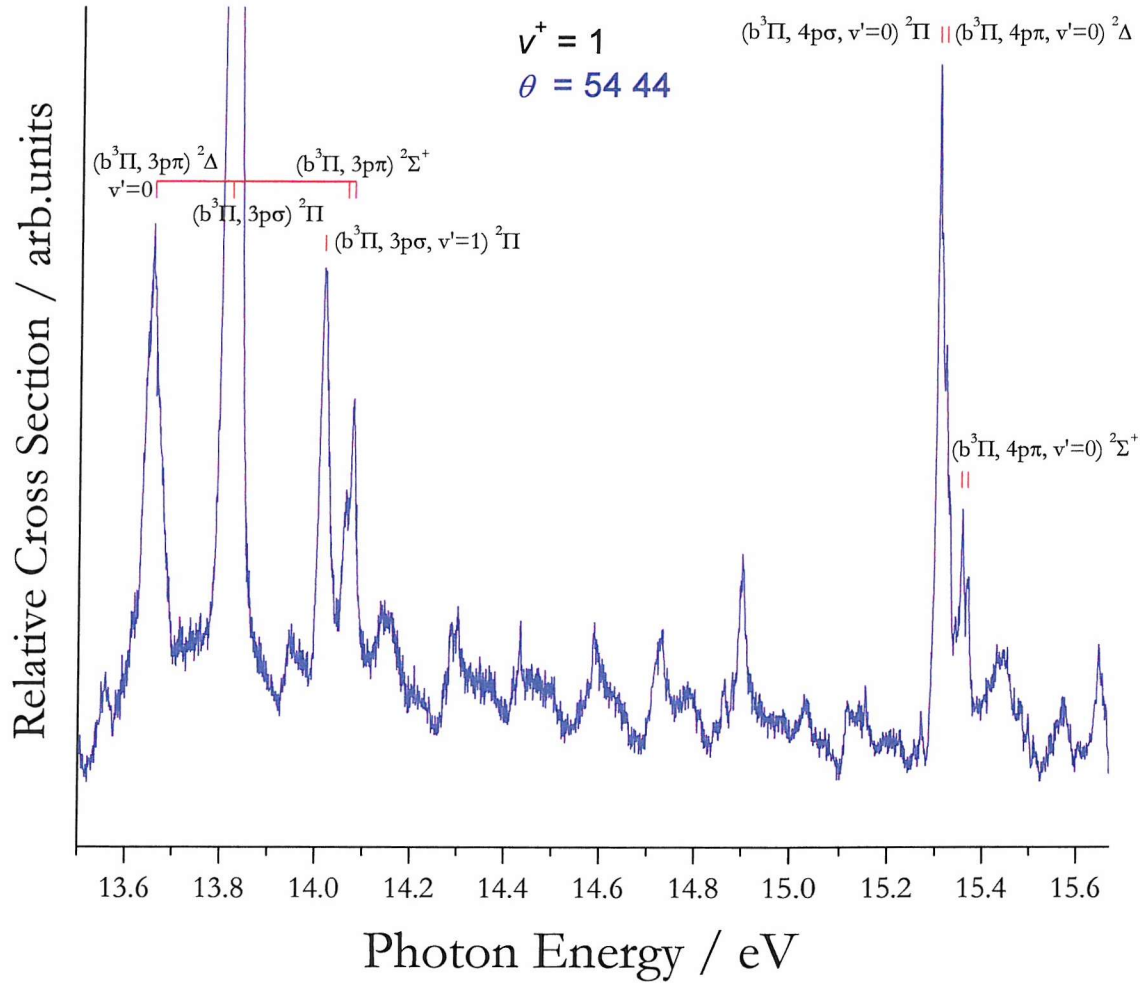

Figure 9.25 *CIS spectrum of the $NO^+(^1\Sigma^+, v^+=1) \leftarrow NO(X^2\Pi, v''=0)$ band in the photon energy range 13.5 - 15.7 eV with the assignment of the $R(b^3\Pi, np)$ resonant states from the present work for n = 3 and 4.*

References

[1] R. P. Wayne
Chemistry of Atmosphere; Oxford University Press: Oxford, 1991.

[2] M. D. Burrows, S. L. Baughcum and R. C. Oldenborg
Applied Physics Letters **46**, 22 (1985).

[3] R. J. P. Williams
Chemical Society Reviews **25**, 77 (1996).

[4] M. R. Hermann, C. W. Bauschlicher, Jr., W. M. Huo, S. R. Langhoff and P. W. Langhoff
Chemical Physics **109**, 1 (1986).

[5] O. Edqvist, E. Lindholm, L. E. Selin, H. Sjogren and L. Asbrink
Arkiv foer Fysik **40**, 439 (1970).

[6] O. Edqvist, L. Asbrink and E. Lindholm
Zeitschrift fuer Naturforschung, Teil A: Astrophysik, Physik und Physikalische Chemie **26**, 1407 (1971).

[7] O. Edqvist, E. Lindholm, L. E. Selin and L. Asbrink
Physics Letters A **31**, 292 (1970).

[8] P. Natalis, J. Delwiche, J. E. Collin, G. Caprace and M. T. Praet
Physica Scripta **16**, 242 (1977).

[9] S. H. Southworth, A. C. Parr, J. E. Hardis and J. L. Dehmer
Journal of Chemical Physics **87**, 5125 (1987).

[10] H. Park and R. N. Zare
Journal of Chemical Physics **99**, 6537 (1993).

[11] S. Southworth, C. M. Truesdale, P. H. Kobrin, D. W. Lindle, W. D. Brewer and D. A. Shirley
Journal of Chemical Physics **76**, 143 (1982).

[12] S. H. Southworth, T. A. Ferrett, J. E. Hardis, A. C. Parr and J. L. Dehmer
Physics Essays **13**, 290 (2000).

[13] M. Salzmann, M. Muller, N. Bowering and U. Heinzmann
Journal of Physics B: Atomic, Molecular and Optical Physics **32**, 2517 (1999).

[14] K. P. Huber and E. Miescher
Helvetica Physica Acta **36**, 257 (1963).

[15] P. H. Metzger, G. R. Cook and M. Ogawa
Canadian Journal of Physics **45**, 203 (1967).

[16] B. Narayana and W. C. Price
Journal of Physics B: Atomic and Molecular Physics **5**, 1784 (1972).

[17] M. Sasanuma, Y. Morioka, E. Ishiguro and M. Nakamura
Journal of Chemical Physics **60**, 327 (1974).

[18] E. Miescher and F. Alberti
Journal of Physical and Chemical Reference Data **5**, 309 (1976).

[19] S. Takezawa
Journal of Molecular Spectroscopy **66**, 121 (1977).

[20] E. Miescher, Y. T. Lee and P. Guertler
Journal of Chemical Physics **68**, 2753 (1978).

[21] K. Watanabe, F. M. Matsunaga and H. Sakai
Applied Optics **6**, 391 (1967).

[22] E. Miescher
Journal of Molecular Spectroscopy **20**, 130 (1966).

[23] C. Jungen and E. Miescher
Canadian Journal of Physics **46**, 987 (1968).

[24] C. Jungen and E. Miescher
Canadian Journal of Physics **47**, 1769 (1969).

[25] T. Gustafsson and H. J. Levinson
Chemical Physics Letters **78**, 28 (1981).

[26] R. M. Reese and H. M. Rosenstock
Journal of Chemical Physics **44**, 2007 (1966).

[27] J. A. R. Samson, T. Masuoka and P. N. Pareek
Journal of Chemical Physics **83**, 5531 (1985).

[28] T. Masuoka
Physical Review A: Atomic, Molecular, and Optical Physics **48**, 1955 (1993).

[29] P. Erman, A. Karawajczyk, E. Rachlew-Kaellne and C. Stroemholm
Journal of Chemical Physics **102**, 3064 (1995).

[30] P. Erman, A. Karawajczyk, E. Rachlew-Kaellne, M. Stankiewicz, K. Y. Franzen, P. Sannes and L. Veseth
Chemical Physics Letters **273**, 239 (1997).

[31] P. Morin, M. Y. Adam, P. Lablanquie, I. Nenner, M. J. Hubin-Franskin and J. Delwiche
Annals of the Israel Physical Society **6**, 613 (1984).

[32] C. E. Brion and K. H. Tan
Journal of Electron Spectroscopy and Related Phenomena **23**, 1 (1981).

[33] Y. Iida, F. Carnovale, S. Daviel and C. E. Brion
Chemical Physics **105**, 211 (1986).

[34] R. J. Stubbs, T. A. York and J. Comer
Chemical Physics **106**, 161 (1986).

[35] W. F. Chan, G. Cooper and C. E. Brion
Chemical Physics **170**, 111 (1993).

[36] W. B. Maier, II and R. F. Holland
Journal of Chemical Physics **54**, 2693 (1971).

[37] Y. Anezaki, T. Ebata, N. Mikami and M. Ito
Chemical Physics **89**, 103 (1984).

[38] A. Ehresmann, H. Liebel, M. Von Kroger and H. Schmoranzer
Journal of Physics B: Atomic, Molecular and Optical Physics **34**, 3119 (2001).

[39] A. Ehresmann, H. Liebel, M. von Kroger and H. Schmoranzer
Journal of Electron Spectroscopy and Related Phenomena **130**, 49 (2003).

[40] H. Hertz, H. W. Jochims and W. Sroka
Physics Letters A **46**, 365 (1974).

[41] J. C. Miller and R. N. Compton
Journal of Chemical Physics **75**, 22 (1981).

[42] W. Kong, D. Rodgers and J. W. Hepburn
Journal of Chemical Physics **99**, 8571 (1993).

[43] J. J. Delaney, I. H. Hillier and V. R. Saunders
Journal of Physics B: Atomic and Molecular Physics **15**, 1477 (1982).

[44] M. R. Hermann, S. R. Langhoff, T. J. Gil and P. W. Langhoff
Chemical Physics Letters **125**, 336 (1986).

[45] M. E. Smith, R. R. Lucchese and V. McKoy
Journal of Chemical Physics **79**, 1360 (1983).

[46] M. E. Smith, V. McKoy and R. R. Lucchese
Journal of Chemical Physics **82**, 4147 (1985).

[47] R. E. Stratmann, R. W. Zurales and R. R. Lucchese
Journal of Chemical Physics **104**, 8989 (1996).

[48] S. Wallace, D. Dill and J. L. Dehmer
Journal of Chemical Physics **76**, 1217 (1982).

[49] L. A. Collins and B. I. Schneider
Physical Review A: Atomic, Molecular, and Optical Physics **29**, 1695 (1984).

[50] D. L. Lynch, B. I. Schneider and L. A. Collins
Physical Review A: Atomic, Molecular, and Optical Physics **38**, 4927 (1988).

[51] D. L. Lynch, B. I. Schneider, L. A. Collins, V. McKoy and W. M. Huo
Chemical Physics Letters **147**, 529 (1988).

[52] Z. P. Zhong, W. H. Zhang and J.-M. Li
Journal of Chemical Physics **113**, 136 (2000).

[53] D. L. Albritton, A. L. Schmeltekopf and R. N. Zare
Journal of Chemical Physics **71**, 3271 (1979).

[54] P. W. Langhoff, T. N. Rescigno, N. Padial, G. Csanak and B. V. McKoy
Journal de Chimie Physique et de Physico-Chimie Biologique **77**, 589 (1980).

[55] P. M. Guyon and I. Nenner
Applied Optics **19**, 4068 (1980).

[56] J. M. Dyke, N. Hooper and A. Morris
Journal of Electron Spectroscopy and Related Phenomena **119**, 49 (2001).

[57] A. L. Smith
Philosophical Transactions of the Royal Society of London, Series A: Mathematical, Physical and Engineering Sciences **268**, 169 (1970).

[58] K. P. Huber and G. Herzberg
Constants of Diatomic Molecules; Van Nostrand Reinhold Company: New York, 1979.

[59] J. B. West and G. V. Marr
Atomic Data and Nuclear Data Tables **18**, 497 (1976).

[60] A. Derossi, F. Lama, M. Piacentini, T. Prosperi and N. Zema
Review of Scientific Instrumentation **66**, 1718 (1995).

[61] D. Desiderio, S. DiFonzo, B. Diviacco, W. Jark, J. Krempasky, R. Krempaska, F. Lama, M. Luce, H. C. Mertins, M. Piacentini, T. Prosperi, S. Rinaldi, F. Schefers, F. Schmolla, G. Soulle, L. Stichauer, S. Turchini, R. P. Walker and N. Zema
Synchrotron Radiation News **12**, 34 (1999).

[62] W. F. Chan, G. Cooper, X. Guo, G. R. Burton and C. E. Brion
Physical Review A: Atomic, Molecular, and Optical Physics **46**, 149 (1992).

[63] http://physics.nist.gov/PhysRefData

[64] R. Stockbauer, B. E. Cole, D. L. Ederer, J. B. West, A. C. Parr and J. L. Dehmer
Physical Review Letters **43**, 757 (1979).

[65] J. L. Dehmer, D. Dill and S. Wallace
Physical Review Letters **43**, 1005 (1979).

[66] K. J. Randall, A. L. D. Kilcoyne, H. M. Koeppe, J. Feldhaus, A. M. Bradshaw, J. E. Rubensson, W. Eberhardt, Z. Xu, P. D. Johnson and Y. Ma
Physical Review Letters **71**, 1156 (1993).

[67] S. Sundin, A. Ausmees, O. Bjorneholm, S. L. Sorensen, M. Wiklund, A. Kikas and S. Svensson
Physical Review A: Atomic, Molecular, and Optical Physics **58**, 2037 (1998).

[68] U. Fano and J. W. Cooper
Physics Review **137**, 1364 (1965).

[69] N. A. Cherepkov
Journal of Physics B: Atomic and Molecular Physics **14**, 2165 (1981).

Chapter 10

10 PHOTOELECTRON SPECTROSCOPY OF THE CF RADICAL

This Chapter reports studies with photoelectron spectroscopy using Synchrotron Radiation on the CF radical.

It is organized as follows. In section 10.1 previous spectroscopic investigations on CF that are considered important for the present work are briefly reviewed. Section 10.2 presents the results obtained in the measured CIS spectra, and resonant photoelectron spectra. Section 10.3 summarizes the results obtained and presents the conclusions of the work.

10.1 Previous investigations of the CF radical with electron spectroscopy

The CF radical has been studied by a variety of spectroscopic and theoretical techniques. These include electronic spectroscopy[1,2], infrared diode laser spectroscopy[3-5], gas phase electron paramagnetic resonance (EPR) spectroscopy[6], laser magnetic resonance (LMR) spectroscopy[7], microwave spectroscopy[8], photoelectron spectroscopy (PES)[9,10], mass spectrometry[11-14], translational energy spectroscopy[15], DVM Xα calculations[16] and *ab-initio* calculations[17-21].

The vibrational constants ω_e, $\omega_e x_e$ and r_e for the $CF(X^2\Pi)$ state have been determined from electronic[1] and infrared diode laser spectroscopy[3]. Infrared diode laser spectroscopic studies[4] have also been performed on CF^+, giving spectroscopic constants ω_e, $\omega_e x_e$ and r_e for the $CF^+(X^1\Sigma^+)$ state.

In the first PES study on CF, performed by the Southampton PES group[9], only the first photoelectron band of CF was observed allowing the first adiabatic ionization energy (AIE) at 9.11 eV and the first vertical ionization energy (VIE) at 9.55 eV to be determined. In that work CF was produced as a secondary product from the fluorine atom plus acetaldehyde reaction. The main products from this reaction were CF, CO, C_2HF, C_2H_2, CF_2 and HF. Unfortunately only the first band of CF was observed as CO, a reaction product, and unreacted CH_3CHO masked the region where the second band of CF is likely to occur (13.8 - 14.2 eV).

Other reactions were also studied as sources of CF[9]; these included F + acetone (CH_3COCH_3), F + acetonitrile (CH_3CN) and F + acetylene (C_2H_2). In all cases only a low yield of CF was obtained. Unfortunately production of CO from these reactions along with reaction products (e.g. FCN from F + CH_3CN) and/or the presence of unreacted starting compounds, gave signals which masked the ionization energy of interest where the second band of CF is expected to occur.

More recently the CF radical has been re-investigated[10] with vacuum ultraviolet photoelectron spectroscopy by the Southampton PES group. With the objective of using a CF production method which would not give other bands in the 13.8 - 14.2 eV region, a new reaction to produce CF was selected[10]. The reaction

chosen was $F + CH_3F$, which produced CF, C_2H_2, C_2HF and HF. These species, apart from CF, do not produce any signals in the ionization energy region of interest (13.8 - 14.2 eV). Two bands were observed and assigned to the ionizations $CF^+(X^1\Sigma^+) \leftarrow CF(X^2\Pi)$ and $CF^+(a^3\Pi) \leftarrow CF(X^2\Pi)$. The first band, which had been observed previously, has the AIE of 9.11 eV and the VIE of 9.55 eV. For the second band, three vibrational components were observed with the first, the most intense, at an ionization energy of 13.94 eV. Analysis of the vibrational structure in the two observed bands allowed ω_e and r_e to be determined for $CF^+(X^1\Sigma^+)$ and $CF^+(a^3\Pi)$. Comparison of the ionization energies and spectroscopic constants obtained was made with values obtained from multi-reference configuration interaction calculations (MRCI)[17-19].

The ground state electronic configuration of CF may be written as $1\sigma^2 2\sigma^2 3\sigma^2 4\sigma^2 5\sigma^2 1\pi^4 5\sigma^2 2\pi^1$, where the 2π and 1π molecular orbitals are composed essentially of antibonding and bonding combinations of carbon and fluorine $2p\pi$ atomic orbitals, respectively. The 5σ molecular orbital is a bonding orbital consisting of a C $2p\sigma$ and F $2p\sigma$ contributions.

The 2π, 5σ and 1π valence orbitals are accessible with the HeI radiation. This results in the $CF^+(X^1\Sigma^+) \leftarrow CF(X^2\Pi)$ ionization for one-electron removal from the 2π level, the $CF^+(a^3\Pi) \leftarrow CF(X^2\Pi)$ and a $CF^+(A^1\Pi) \leftarrow CF(X^2\Pi)$ for one-electron removal from the 5σ level and six ionizations $CF^+(^{1,3}\Sigma^+) \leftarrow CF(X^2\Pi)$, $CF^+(^{1,3}\Delta) \leftarrow CF(X^2\Pi)$ and $CF^+(^{1,3}\Sigma^-) \leftarrow CF(X^2\Pi)$ for ionization from the 1π level.

CF is isoelectronic with the NO radical. The ground state electronic configuration of NO is $1\sigma^2 2\sigma^2 3\sigma^2 4\sigma^2 5\sigma^2 1\pi^4 2\pi^1$, $X^2\Pi$. As for CF, the $X^1\Sigma^+$ ionic state arises from ionization from the 2π level, the b $^3\Pi$ and $A^1\Pi$ ionic states arise from ionization from the 5σ level and six ionic states $^{1,3}\Sigma^+$, $^{1,3}\Delta$ and $^{1,3}\Sigma^-$ arise from ionization from the 1π level. With respect CF, the 1π and 5σ orbitals are in a different energy order with the 1π orbital being higher than the 5σ orbital in NO. As consequence, in the PE spectrum of NO, the $NO^+(b^3\Pi) \leftarrow NO(X^2\Pi)$ band is overlapping with the bands arising from ionization from the 1π level as can be seen in Figure 9.5. In the CIS studies of NO, reported in Chapter 9, Rydberg series converging to the $NO^+(b^3\Pi)$

ionic state are observed overlapping with Rydberg resonances arising from excitation of a 1π electron (see Figure 9.7).

In CF, the bands arising from ionization of the 1π level are at higher ionization energy with respect to the band associated with the $CF^+(a^3\Pi)$ state from the $(5\sigma)^{-1}$ ionization. Therefore in the CIS spectra on the first band, $CF^+(X^1\Sigma^+)\leftarrow CF(X^2\Pi)$, in the photon energy range below the ionization energy to the $CF^+(a^3\Pi)$ state (13.94 eV), only resonant states which are part of series converging to the $CF^+(a^3\Pi)$ ionic state are expected.

10.2 Results and discussion

The study of a reactive intermediate with photoelectron spectroscopy using monochromatized Synchrotron Radiation[22,23] should allow more information to be obtained on the molecular ionic states produced and the associated photoionization processes than a PES study at fixed photon energy from a low pressure discharge of an inert gas as the photon source[24-26], in particular:

- a study of the relative band intensities in the valence photoelectron spectrum of a small molecule as a function of the ionizing photon energy can provide valuable information to assist band assignment
- the polarized nature of the Synchrotron radiation source allows information to be obtained from angular distribution studies.
- an autoionization resonance, once identified, can give rise to extra structure when the photon energy is set at this position over that observed in a photoelectron spectrum recorded off resonance[27-30]. This effect was first observed by Price[31] in the photoelectron spectrum recorded with NeI radiation for the oxygen molecule where one of the neon discharge resonance lines coincided with a resonance in O_2; the resulting photoelectron spectrum showed considerably more vibrational structure than one taken using the helium discharge line.

This last feature is exemplified in the work presented in this Chapter and examples of this have been seen in the previous Chapter on NO.

Test experiments were carried out in Southampton in order to determine the optimum pressures and mixing distance to be used in the experiments at ELETTRA, which maximise the intensities of the first CF band. CF was produced by reacting CH_3F with fluorine atoms, produced by passing flowing 5% F_2 in helium through a microwave discharge at 2.45 GHz in a glass inlet tube coated with teflon as reported in Chapter 4.4.2.

The most intense spectra of the first band of CF, prepared by the F + CH_3F reaction, were obtained with the following partial pressures measured on the ionization gauge positioned on the wall of the ionization chamber with respect to the background pressure: $\Delta p(CH_3F) = 3.0\times10^{-7}$ mbar and $\Delta p(F_2/He) = 3.7\times10^{-6}$ mbar, at a mixing distance of about 4 cm above the photon beam.

The results presented in this Chapter were obtained from two visits to ELETTRA. The energy of the circulating electrons was set at 2.0 GeV and 2.4 GeV in the first and second visit respectively. More intense CF spectra were obtained during the first visit.

The PE spectrum of the F + CH_3F reaction recorded with Synchrotron Radiation at the magic angle ($\theta = 54° 44'$) and at a photon energy of $h\nu = 21.22$ eV is shown in Figure 10.1 with the assignment of the major features indicated.

It can be seen from Figure 10.1 that the following molecules have been produced in this reaction system: CF[9], O[32], CO[33], HF[33] and small amounts of HCCF[34,35] associated with the weak signals seen in the 11.0 - 12.0 eV ionization energy region. A small contribution from the first band of residual CH_3F is present between 12.2 - 14.5 eV. The oxygen atoms O and CO arise from fluorine atoms reacting with the glass inlet system; removing these features proved to be impossible although they could be considerably reduced by coating the glass system internally with teflon.

From a previous PES study[10] on CF performed by the Southampton PES group, it was concluded that the band at 13.94 eV ionization energy, that in Figure 10.1 is

heavily overlapped by CO molecular features, is the $CF^+(a^3\Pi) \leftarrow CF(X^2\Pi)$ second ionization band of CF.

In the present work CIS spectra have been recorded for the first band, $CF^+(X^1\Sigma^+,v^+) \leftarrow CF(X^2\Pi,v''=0)$, in the photon energy range 12.6 - 14.3 eV for three vibrational components of the photoelectron band ($v^+ = 0$, 1 and 2). The aim was to select a vibrational component of the first band of CF and sweep the photon energy towards the second ionization energy (IE = 13.94 ± 0.02 eV). All spectra were recorded at two angles, $\theta = 0°$ and $\theta = 54°\ 44'$, with respect to the polarization axis of the photon source. In Figure 10.2 CIS spectra are shown as function of the photon energy for the first three vibrational components of the first photoelectron band of CF measured at an angle with respect to the major polarization axis of the photon source of $\theta = 54°\ 44'$.

Several bands are observed for the first time in Figure 10.2 and they can be identified as autoionizing Rydberg series converging to the $CF^+(a^3\Pi)$ ionic state. Table 10-1 shows all the possible Rydberg series converging to the $CF^+(a^3\Pi)$ ionic state which are electric-dipole allowed. The Rydberg transitions $5\sigma \rightarrow n\pi\pi$ and $5\sigma \rightarrow nd\pi$ give rises to three possible spin-allowed resonant states of $^2\Sigma^+$, $^2\Sigma^-$ and $^2\Delta$ symmetries; however, the $^2\Sigma^-$ state cannot decay by autoionization into the $CF^+(X^1\Sigma^+)$ final state continuum as a consequence of parity conservation.

Table 10-1 *Electric-dipole allowed Rydberg series in CF arising from the excitation of a 5σ electron to states which are part of series converging to the $CF^+(a^3\Pi)$ ionic state. The excited state symmetry is presented.*

Rydberg transition	Ionic state core	Excited state symmetry
$5\sigma \rightarrow ns\sigma$	$a^3\Pi$	$^2\Pi$
$5\sigma \rightarrow np\sigma$	$a^3\Pi$	$^2\Pi$
$5\sigma \rightarrow np\pi$	$a^3\Pi$	$^2\Sigma^+$, $^2\Sigma^-$, $^2\Delta$
$5\sigma \rightarrow nd\sigma$	$a^3\Pi$	$^2\Pi$
$5\sigma \rightarrow nd\pi$	$a^3\Pi$	$^2\Sigma^+$, $^2\Sigma^-$, $^2\Delta$
$5\sigma \rightarrow nd\delta$	$a^3\Pi$	$^2\Pi$

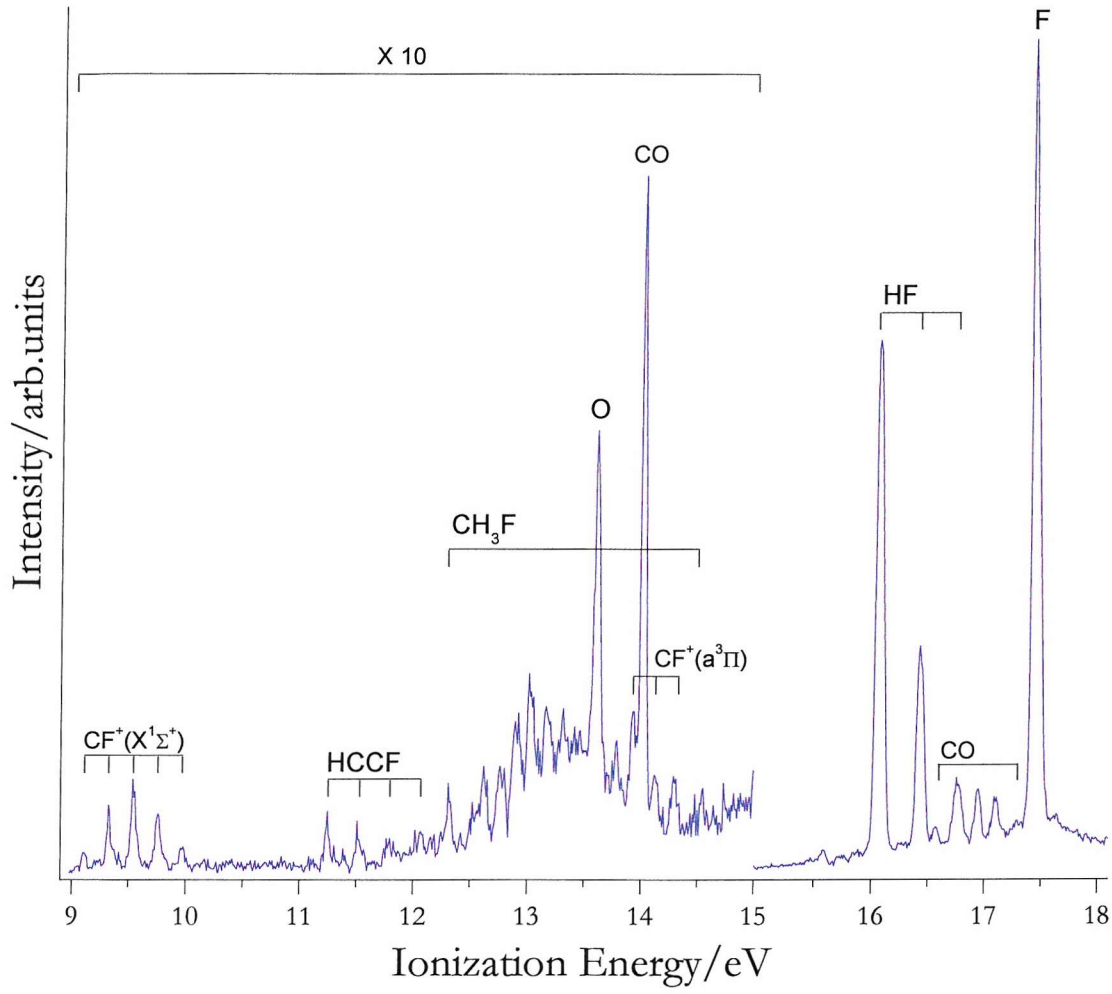

Figure 10.1 *Photoelectron spectrum recorded for the reaction $F + CH_3F$ at $h\nu = 21.22$ eV measured at an angle with respect to the major polarization axis of the photon source $\theta = 54°44'$.*

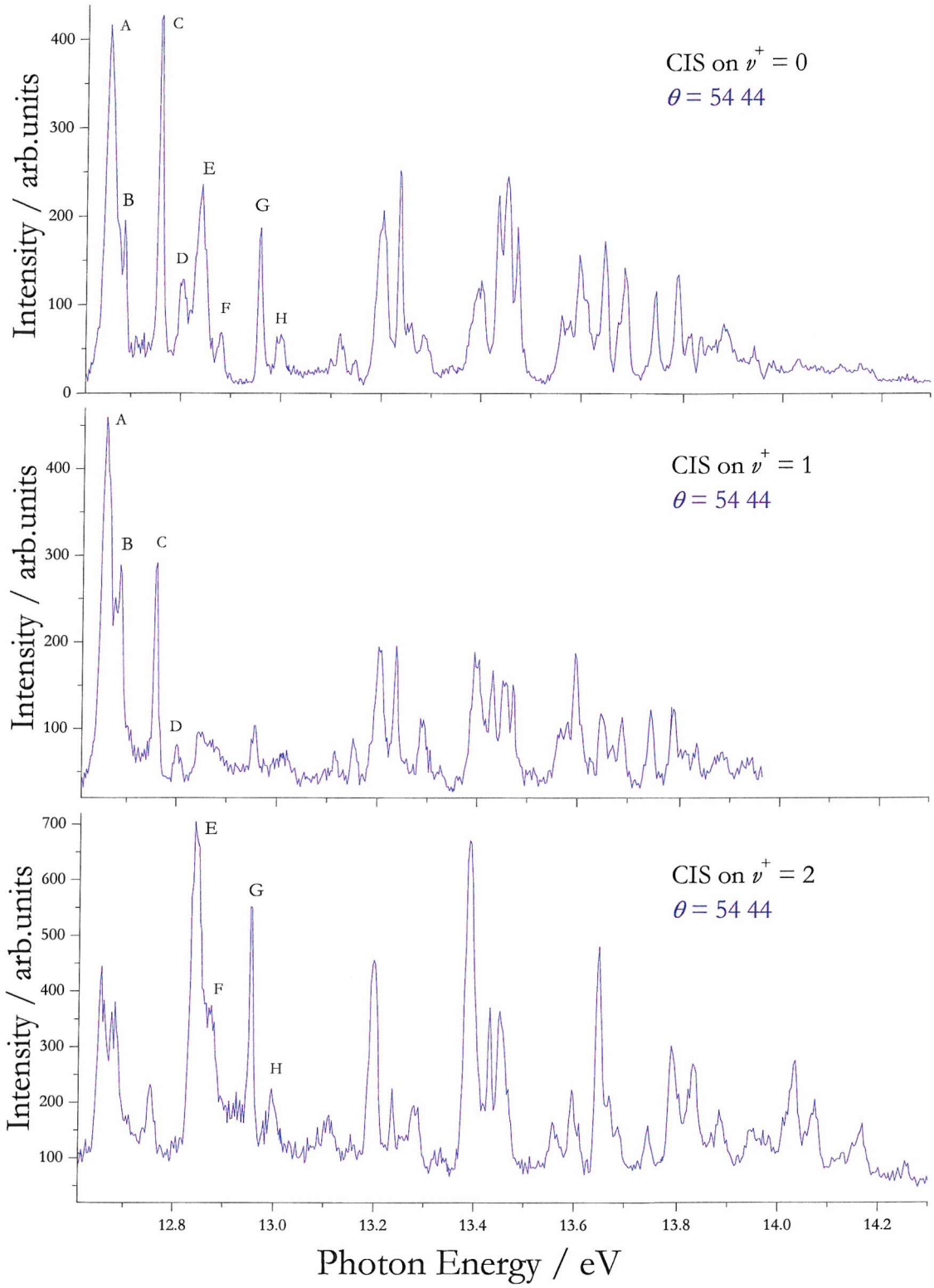

Figure 10.2 *CIS spectra recorded for the first band $CF^+(X^1\Sigma^+,v^+) \leftarrow CF(X^2\Pi,v''=0)$ in the photon energy range 12.6 - 14.3 eV and for three vibrational components of the photoelectron band ($v^+ = 0$, 1 and 2). The first eight bands observed are labelled with letters A to H.*

CF is isoelectronic with NO and the CIS spectra reported in the previous Chapter on the first band, $NO^+(X^1\Sigma^+) \leftarrow NO(X^2\Pi)$, show the $5\sigma \rightarrow np\sigma$ and $5\sigma \rightarrow np\pi$ Rydberg states as the most prominent components in series which converge to the limit $NO^+(b^3\Pi)$. NO is heteronuclear but it may be considered approximately homonuclear since the component atoms are consecutive in the Periodic Table. Therefore the (u, g) symmetry classification is assumed valid and the $5\sigma_g \rightarrow ns_g$ and $5\sigma_g \rightarrow nd_g$ series are therefore forbidden, although weak bands have been assigned as part of these series in previous experiments[36] (see Chapter 9).

Since CF is isoelectronic with NO, it is reasonable to expect the predominant bands in the CIS spectra in Figure 10.2 to be part of the $5\sigma \rightarrow np$ series. To help the assignments of these spectra, the CIS band envelope for the vibrational levels $v^+ = 0$, 1 and 2 of the autoionizing process $CF^+(X^1\Sigma^+,v^+) \leftarrow CF^*(a^3\Pi,v') \leftarrow CF(X^2\Pi,v''=0)$ were simulated by multiplying together the computed Franck-Condon factors for steps "Dipole" and "Monopole" as described in Chapter 9.2. These were computed as explained previously by assuming a Morse potential for each state.

The vibrational constants for the $CF(X^2\Pi)$ state used for the simulations were determined using infrared and microwave spectroscopy: $\omega_e = 1308.1\ cm^{-1}$, $\omega_e x_e = 1.10\ cm^{-1}$ and $r_e = 1.272$ Å[37]. The vibrational constants ω_e and $\omega_e x_e$ for the ionic states were determined from the corresponding vibrationally resolved PE band using the equation derived from the anharmonic energy expression $\Delta E_{v'} = \omega_e - 2\omega_e x_e (v'+1)$ and vibrational separations in the PE band ($\Delta E_{v'}$), by a least-square fit of the $\Delta E_{v'}$ values against $(v'+1)$ for each band. The vibrational constants for the ionic ground state $CF^+(X^1\Sigma^+)$ are $\omega_e = 1777.2\ cm^{-1}$, $\omega_e x_e = 12.90\ cm^{-1}$ and $r_e = 1.154$ Å[10]. The Rydberg state vibrational constants and equilibrium bond lengths are assumed to be the same as the ionic core $CF^+(a^3\Pi)$: $\omega_e = 1560.1\ cm^{-1}$, $\omega_e x_e = 14.90\ cm^{-1}$ and $r_e = 1.213$ Å[10].

From the simulated CIS spectra shown in Figure 10.3, the CIS spectrum recorded on the vibrational band $v^+ = 2$ is expected to have strong components for $v' = 1$, a weaker component for $v' = 0$ and negligible intensities for other v' values. In Figure 10.2, the experimental CIS spectrum recorded on the vibrational band $v^+ = 2$ shows some bands which gain intensities with respect the CIS spectra recorded on

the vibrational bands $v^+ = 0$ and 1 such as the bands indicated with the letters E, F, G and H.

The vibrational spacing in a Rydberg series is expected to be very close to that of the ionic core which is 190 meV in the case of the $CF^+(a^3\Pi)$ ionic state. This value can be obtained from the equation $\Delta E_v = E_{v+1} - E_v = \omega_e - 2\omega_e x_e (v + 1)$ using the ω_e and $\omega_e x_e$ values for $CF^+(a^3\Pi)$ as shown earlier. If the first band in the CIS spectra in Figure 10.2 (band A) at 12.655 eV is assumed to be associated with a transition to a Rydberg state with $v' = 0$, the $v' = 1$ component is expected at 12.845 eV which corresponds to the strongest band in the CIS spectrum recorded on the vibrational band $v^+ = 2$ (band E). This would be consistent with the simulated CIS spectra. Simple quantum defect analysis has been performed on the first four bands in the CIS spectra in Figure 10.2 (indicated with the letters A, B, C and D) using the Rydberg formula

$$E_n = I - \frac{R}{(n - \delta_n)^2} \qquad \text{Eq. 10-1}$$

where I is the first adiabatic ionization energy (13.94 eV) and E_n the resonances positions of bands A, B, C and D at 12.655, 12.686, 12.757 and 12.806 eV respectively. A solution can be obtained for $n = 4$ and the quantum defect as $\delta \approx 0.7$, which is reasonable for a p Rydberg series. These quantum defects were then used to calculate the positions of the rest of the series and the positions were compared with the experimental CIS spectra. The photon energies of the bands close to the calculated positions of the series were used to fit Eq. 10-1 as function of the principal quantum number n and allowing a slow variation with the energy of the quantum defect δ_n.

The quantum defects obtained by the fit for the four Rydberg series are shown in Table 10-2 for $n = 4$, 5, 6, 7 and 8. Using these values in Eq 10-1, the photon energy of the four Rydberg series are calculated and shown in Table 10-3 for n = 4, 5, 6 and 7. In the same table are reported in brackets the experimental photon energies used to fit Eq. 10-1 obtaining the quantum defects shown in Table 10-2.

Figure 10.4 shows the CIS spectra on the $CF^+(X^1\Sigma^+,v^+) \leftarrow CF(X^2\Pi,v''=0)$ bands for $v^+ = 0$, 1 and 2 with the assignments of the four $R(a^3\Pi,np,v'=0) \leftarrow CF(X^2\Pi,v''=0)$

series from the quantum defect analysis. The red marks are the positions of the four $R(a^3\Pi,np,v'=1)$ bands converging to $v' = 1$ obtained by adding 190 meV to the $R(a^3\Pi,np,v'=0)$ band positions.

Table 10-2 *Quantum defect δ_n for the four resonant series converging to the $CF^+(a^3\Pi)$ ionic state for n = 4, 5, 6, 7 and 8.*

n	4	5	6	7	8
Series 1	0.748 ± 0.083	0.735 ± 0.076	0.726 ± 0.071	0.720 ± 0.068	0.716 ± 0.066
Series 2	0.707 ± 0.092	0.697 ± 0.083	0.690 ± 0.078	0.686 ± 0.075	0.682 ± 0.073
Series 3	0.605 ± 0.129	0.600 ± 0.117	0.596 ± 0.111	0.594 ± 0.106	0.592 ± 0.103
Series 4	0.525 ± 0.159	0.512 ± 0.145	0.503 ± 0.136	0.497 ± 0.130	0.492 ± 0.127

Table 10-3 *Resonant energy positions obtained from the calculated quantum defects reported in Table 10-2 for the four Rydberg series converging to the $CF^+(a^3\Pi)$ ionic state for n = 4, 5, 6 and 7. In brackets are reported the experimental photon energies which were used to fit Eq. 10-1 yielding the quantum defects shown in Table 10-2.*

n	4	5	6	7
Series 1	12.656 ± 0.066 eV	13.195 ± 0.026 eV	13.454 ± 0.013 eV	13.598 ± 0.007 eV
(exp)	*(12.655 eV)*	*(13.198 eV)*	*(13.451 eV)*	*(13.597 eV)*
Series 2	12.687 ± 0.070 eV	13.206 ± 0.028 eV	13.459 ± 0.014 eV	13.600 ± 0.008 eV
(exp)	*(12.686 eV)*	*(13.208 eV)*	*(13.460 eV)*	*(13.597 eV)*
Series 3	12.758 ± 0.090 eV	13.236 ± 0.038 eV	13.472 ± 0.019 eV	13.607 ± 0.011 eV
(exp)	*(12.757 eV)*	*(13.236 eV)*	*(13.472 eV)*	*(13.611 eV)*
Series 4	12.806 ± 0.103 eV	13.258 ± 0.043 eV	13.483 ± 0.022 eV	13.611 ± 0.013 eV
(exp)	*(12.806 eV)*	*(13.259 eV)*	*(13.485 eV)*	*(13.611 eV)*

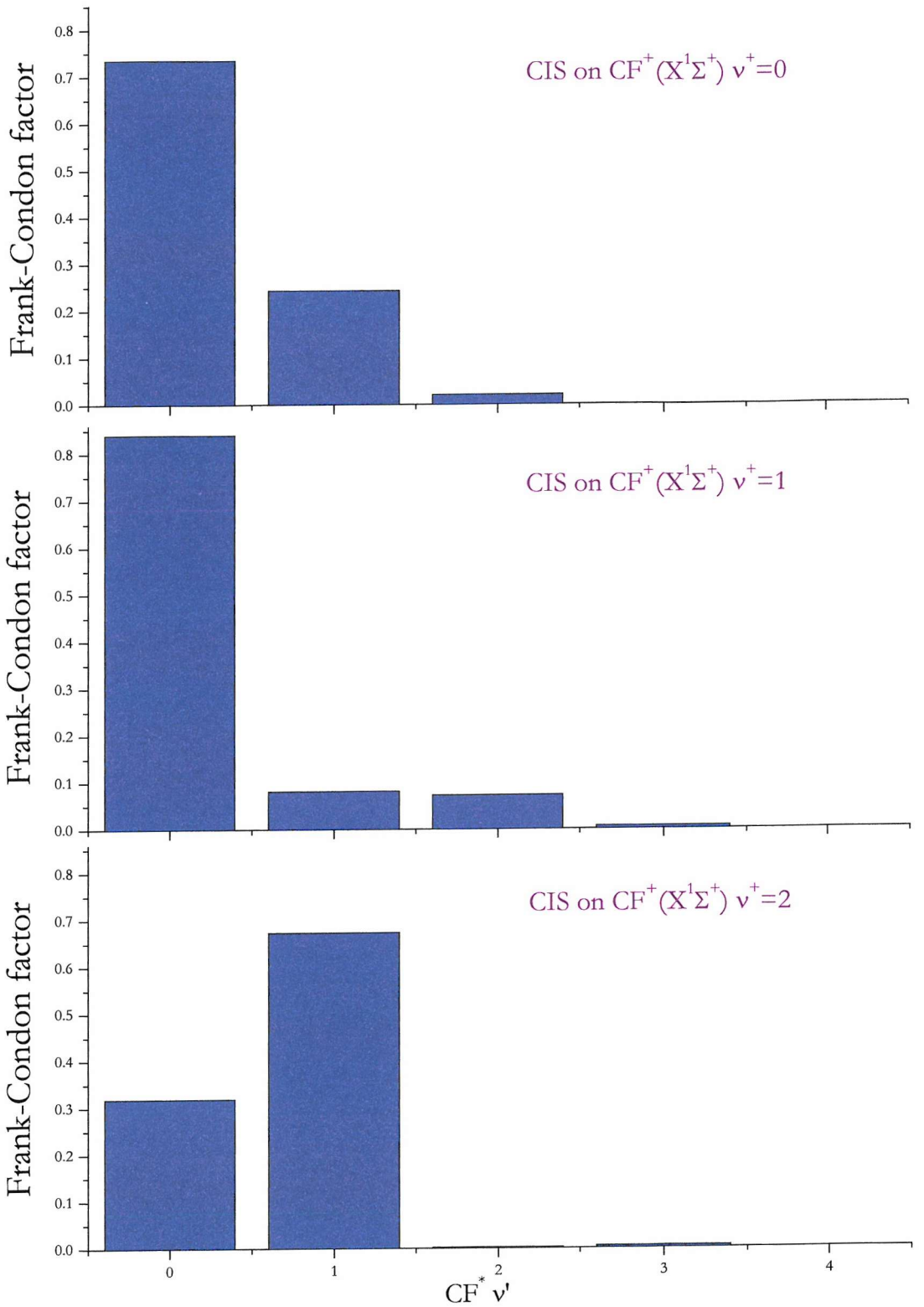

Figure 10.3 *Computed CIS spectra for* $CF^+(X^1\Sigma^+,v^+) \leftarrow CF^*(a^3\Pi,v') \leftarrow CF(X^2\Pi)$ *for* $v^+ = 0$, *1 and 2.*

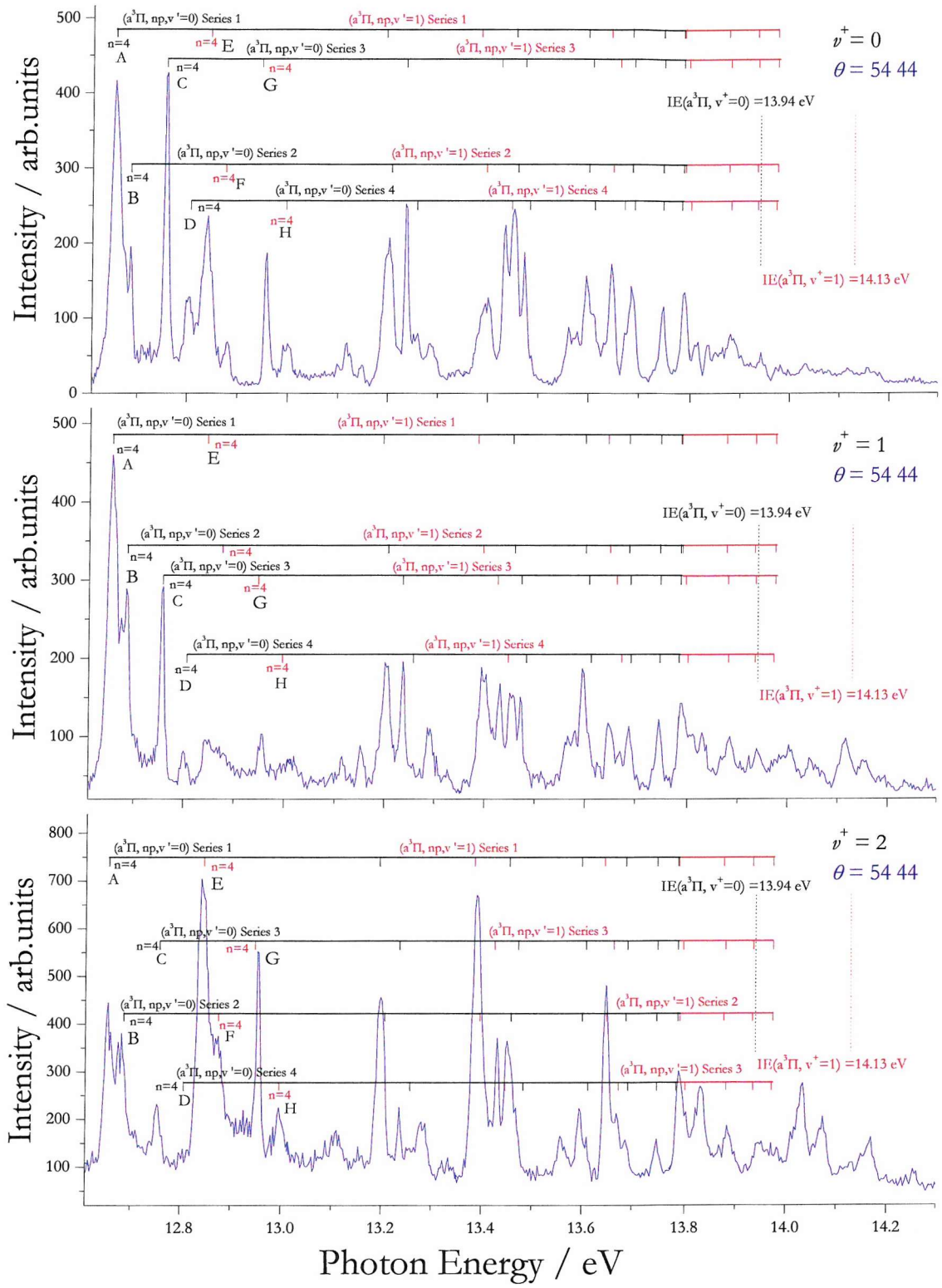

Figure 10.4 *CIS spectra on the $CF^+(X^1\Sigma^+, v^+) \leftarrow CF(X^2\Pi, v''=0)$ band in the photon energy range 12.6 - 14.3 eV and for $v^+ = 0$, 1 and 2 with the assignment of the Rydberg series from the quantum defect analysis. The black and red marks are the $v' = 0$ and $v' = 1$ series respectively.*

As can be seen in Figure 10.4, the four R($a^3\Pi$,*n*p,*v*'=0) and the four R($a^3\Pi$,*n*p,*v*'=1) series account for most of the bands in the experimental CIS spectra. The small structures that could not be assigned, like the bands at about 13.1 eV, could be part of the less intense *s* or *d* series which have a quantum defect of ≈ 0 and 1 respectively. As reported in Table 10-1, the excited state symmetries of the $5\sigma \rightarrow n\text{p}\sigma$ and $5\sigma \rightarrow n\text{p}\pi$ series are $^2\Pi$, $^2\Sigma^+$, $^2\Sigma^-$ and $^2\Delta$ which could be assigned as the four series observed experimentally. The problem with this assignment is that the $^2\Sigma^-$ state is parity forbidden for autoionization to $CF^+(X^1\Sigma^+)$, though several authors observed Rydberg series in the NO absorption spectra with $^2\Sigma^-$ final state symmetry as reported in the Chapter 9. It is not possible to explain the presence of the four series in term of the $CF(X^2\Pi)$ ground state being split into two components $^2\Pi_{3/2}$ and $^2\Pi_{1/2}$ separated by 9.5 meV[38]. This spin orbit splitting is too small to be resolved in the experimental CIS spectra and, for n = 4, the photon energy separation between two consecutive series is of the order of 50 meV.

A comparison with the R($b^3\Pi$,*n*p) series in NO could help to determine the excited state symmetries of the four observed series in CF. Figure 10.5 shows the CIS spectra recorded for the $CF^+(X^1\Sigma^+,v^+) \leftarrow CF(X^2\Pi,v''=0)$ band for the vibrational components $v^+ = 0$, 1 and 2 measured at two different angles $\theta = 0°$ (red trace) and $\theta = 54°\ 44'$ (blue trace) with respect to the major polarization axis of the photon source. The intensity at $\theta = 54°\ 44'$ of the bands called series 1 in Figure 10.4, with respect to the intensity at $\theta = 0$, is higher compared to the other three series. This means series 1 has a more negative asymmetry parameter β compared to the other three series. Moreover, bands in series 1 are the most intense and wider than the bands in all the four series. In NO, the same characteristics are found in the R($b^3\Pi$,*n*pσ) series and for n = 4 the R($b^3\Pi$,4pσ) state is at lower photon energies respect to the R($b^3\Pi$,4pπ) bands. Therefore it is reasonable to assign the first series in CF as the R($a^3\Pi$,npσ) series with $^2\Pi$ final state symmetry.

In NO, for n = 4, the R($b^3\Pi$,4pπ) $^2\Delta$ state is close to the R($b^3\Pi$,4pσ) $^2\Pi$ band while the R($b^3\Pi$,4pπ) $^2\Sigma^+$ state is at higher photon energy and is the sharpest of all the bands, as can be seen in Figure 9.25. In CF, series 2 is close to R($a^3\Pi$,4pσ) $^2\Pi$ state

and series 3 is at higher photon energy and is the sharpest of all the four series. Series 2 and 3 can then be assigned as R($a^3\Pi$,npπ) $^2\Delta$ and R($a^3\Pi$,npπ) $^2\Sigma^+$ series respectively. The fourth, less intense series, could be the parity forbidden R($a^3\Pi$,npπ) $^2\Sigma^-$ series.

To confirm the vibrational assignment shown in Figure 10.4, PE spectra of the first band of CF were then recorded at photon energies corresponding to the Rydberg resonant states assigned as R($a^3\Pi$,4p,v'=0) and R($a^3\Pi$,4p,v'=1), i.e. the first eight bands observed in the CIS spectra and labelled with letters from A to H. Figure 10.6 shows the PE spectra recorded at two different angles ($\theta = 0°$ red trace and $\theta = 54° 44'$ blue trace) at photon energies corresponding to the resonant states R($b^3\Pi$,4p,v'=0), peak A, B, C and D at $h\nu = 12.655$, 12.684, 12.757 and 12.804 eV respectively. In Figure 10.7 are shown PE spectra recorded at photon energies corresponding to the resonant states R($b^3\Pi$,4p,v'=1), peak E, F, G and H at $h\nu = 12.846$, 12.877, 12.953 and 12.995 eV respectively. PE spectra at $\theta = 0°$ have been recorded only for the four most intense resonant states in the CIS spectra since the yield of the CF bands is very low and the acquisition time for each spectrum was long. Moreover, no information could be obtained from the asymmetry parameter since the statistics is too low and the error on the calculated asymmetry parameter high.

The partial cross section of the vibrational components at the resonant photon energies is different to that of direct ionization shown in Figure 10.1. In particular the PE spectra in Figure 10.7 show extra structures arising from autoionization of the resonant excited state to the $CF^+(X^1\Sigma^+)$ ground state.

Figure 10.8 shows the computed Franck-Condon factors for the resonant autoionization $CF^+(X^1\Sigma^+) \leftarrow R(a^3\Pi,v')$ for $v' = 0$, 1 and 2. These Franck-Condon factors can be compared with the PE spectra shown in Figure 10.6 and Figure 10.7 only after the contribution of the direct ionization is subtracted from the peak areas of each vibrational level. Fitting procedures were used to obtain peak areas for each vibrational level and these areas were normalized by the sum of all the areas of the vibrational level from $v^+ = 0$ to $v^+ = 5$.

Figure 10.9 shows the relative intensities of the vibrational components in PE spectra recorded at the four photon energies corresponding to the resonant states R($b^3\Pi$,4p,v'=0) (peak A, B, C and D) after the subtraction for each vibrational level of the contribution of the direct ionization (as described in Chapter 9.2), which is assumed to be represented by a PE spectrum recorded at $h\nu$= 12.63 eV, similar to the first band of CF shown in Figure 10.1 recorded at $h\nu$= 21.22 eV. The error derived by these procedures is also reported and it is quite large especially at the photon energies corresponding to the less intense resonant bands. The vibrational distributions in the PE spectra recorded at photon energies set on the four resonant states R($b^3\Pi$,4p,v'=0) is different to that of direct ionization and is close to the calculated Franck-Condon factor in Figure 10.8 (a), in particular for the bands A, B and C. The band D at $h\nu$= 12.804 eV shows a different behaviour with the $v^+ = 0$ vibrational component stronger respect to the other three components, though the calculated error is large.

Figure 10.10 shows the relative intensities of the vibrational components in the first band of the PE spectrum at the four photon energies corresponding to the resonant states R($b^3\Pi$,4p,v'=1) which are really close to each other; the corresponding Franck-Condon factors are shown in Figure 10.8 (b). As in the case of the R($b^3\Pi$,4p,v'=0) series, the fourth state (band H) at $h\nu$= 12.995 eV shows a slightly different behaviour but with a large associated error.

The simulations therefore support the vibrational assignments shown in Figure 10.4 for the interpretation of the CIS spectra. The simulations do not give further information about the order of the excited state symmetries but they confirm when the photon energy is set on bands A, B and C, corresponding to the position of the first band in the first three series, a behaviour is exhibited close to that predicted by the computed Franck-Condon factors while when the photon energy is set on band D, the first band of the fourth least intense series, and PE spectrum is recorded, a different behaviour is observed with respect the other three series.

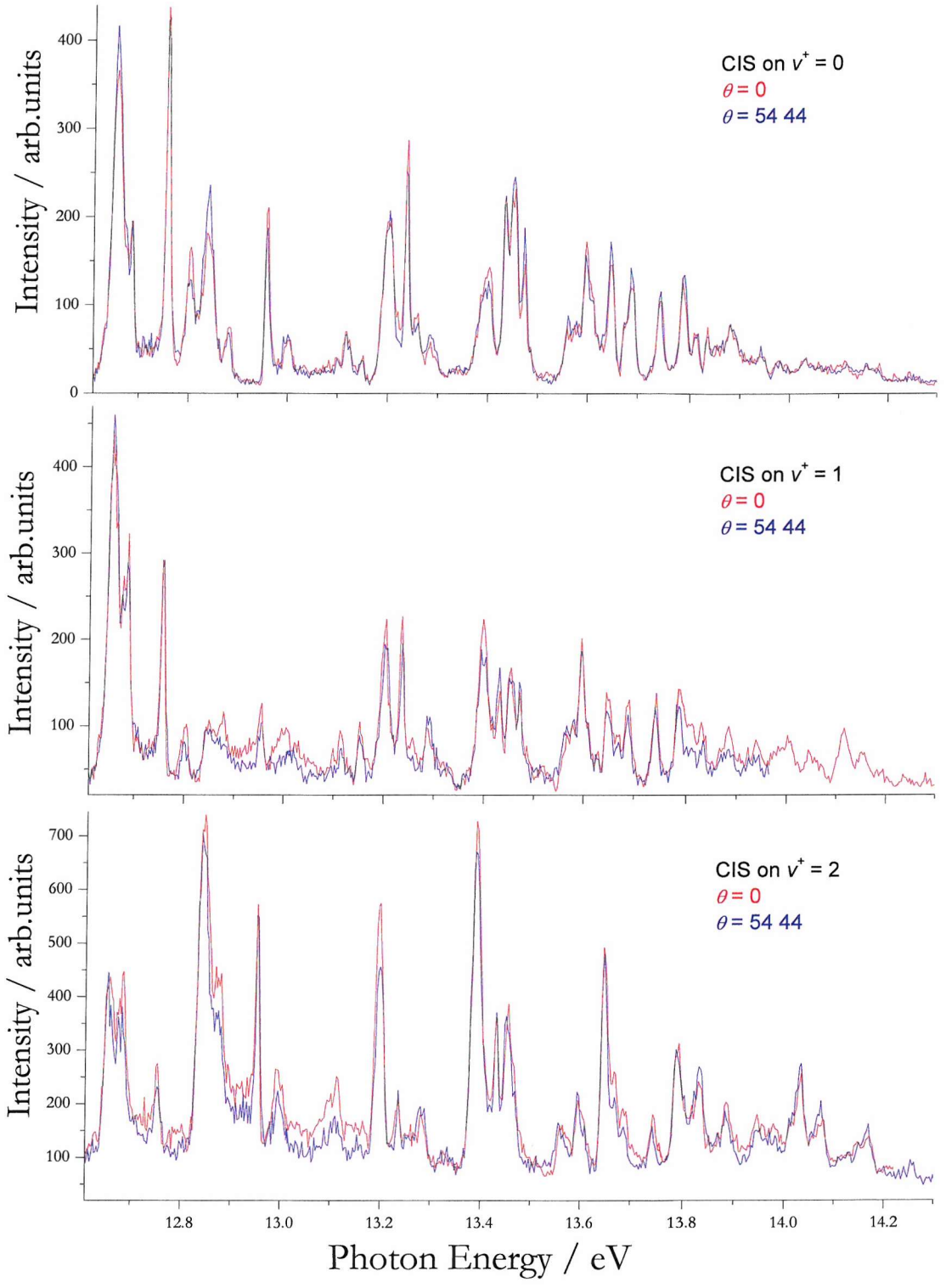

Figure 10.5 *CIS spectra on the $CF^+(X^1\Sigma^+, v^+) \leftarrow CF(X^2\Pi, v''=0)$ band in the photon energy range 12.6 - 14.3 eV and for $v^+ = 0$, 1 and 2 measured at two different angles $\theta = 0°$ (red trace) and $\theta = 54°44'$ (blue trace) with respect to the major polarization axis of the photon source.*

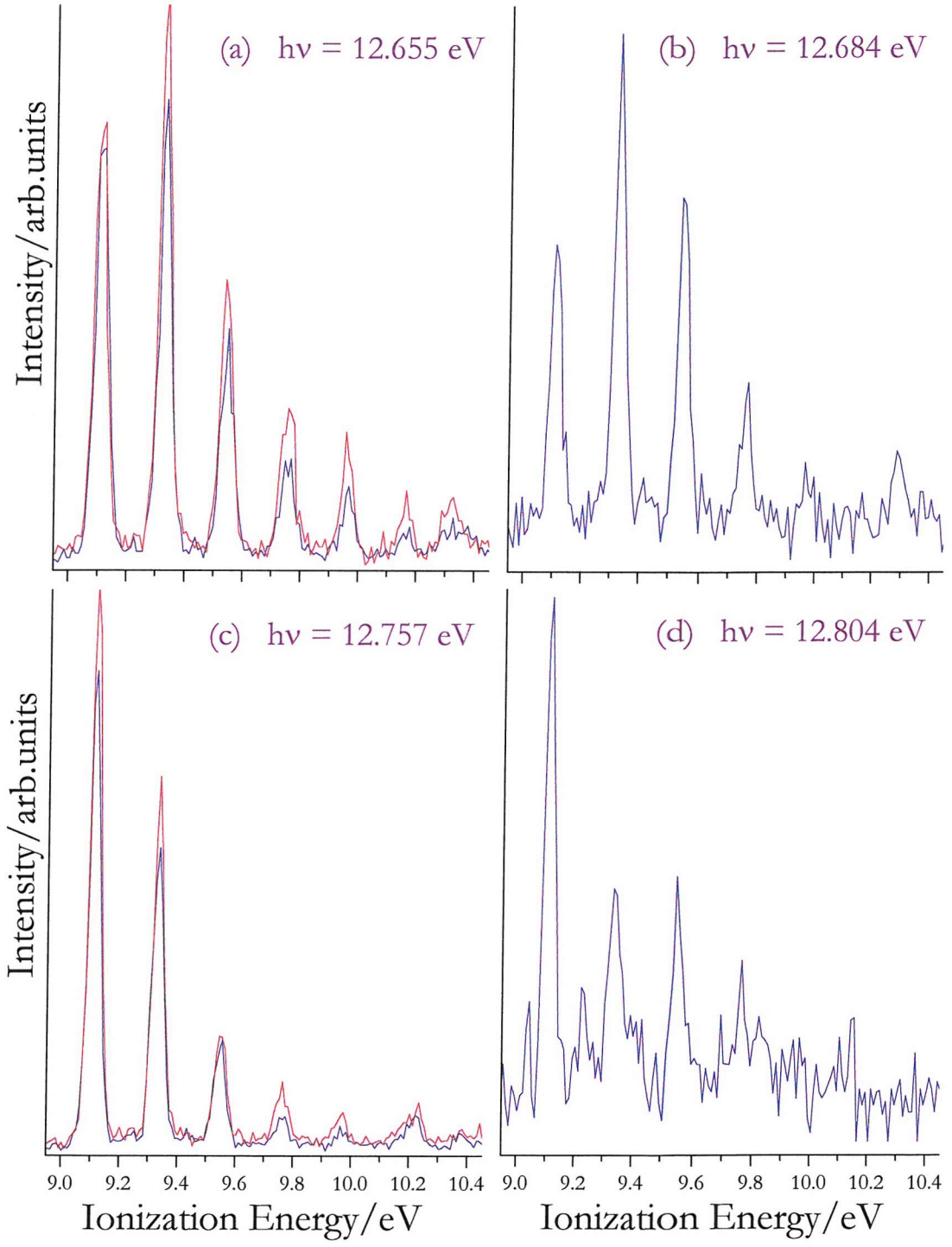

Figure 10.6 *PE spectra of* $CF^+(^1\Sigma^+,v^+) \leftarrow CF(X^2\Pi,v''=0)$ *measured at two different angles* $\theta = 0°$ *(red trace) and* $\theta = 54°44'$ *(blue trace) in the 8.95 - 10.45 eV ionization energy region at the Rydberg resonant state as marked in Figure 10.2*

(a) Peak A at $h\nu = 12.655$ *eV* *(b) Peak B at* $h\nu = 12.684$ *eV*

(c) Peak C at $h\nu = 12.757$ *eV* *(d) Peak D at* $h\nu = 12.804$ *eV.*

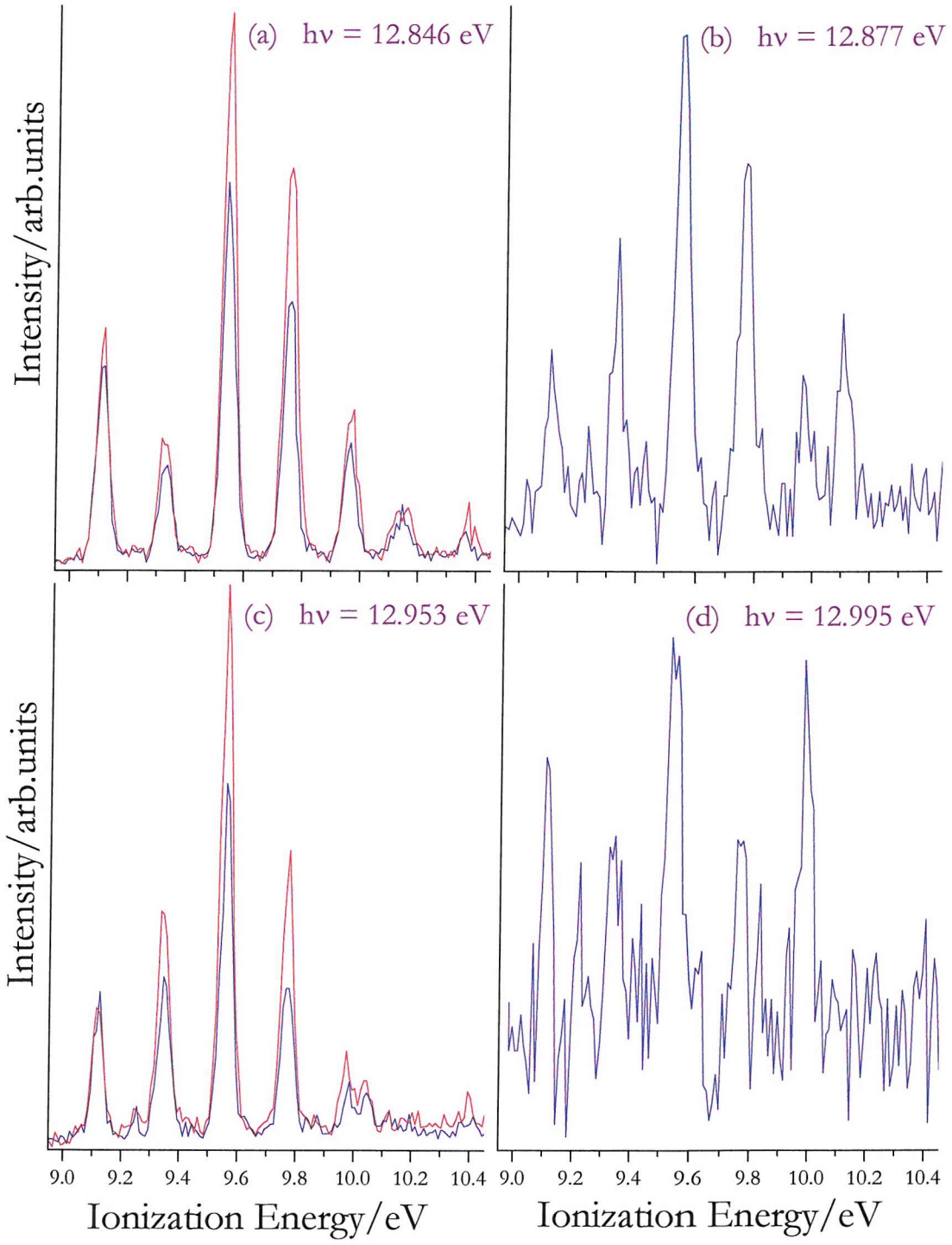

Figure 10.7 *PE spectra of* $CF^+(^1\Sigma^+,v^+) \leftarrow CF(X^2\Pi,v''=0)$ *measured at two different angles* $\theta = 0°$ *(red trace) and* $\theta = 54°44'$ *(blue trace) in the 8.95 - 10.45 eV ionization energy region at the Rydberg resonant state as marked in Figure 10.2*

(a) Peak E at $h\nu = 12.846$ *eV* *(b) Peak F at* $h\nu = 12.877$ *eV*

(c) Peak G at $h\nu = 12.953$ *eV* *(d) Peak H at* $h\nu = 12.995$ *eV.*

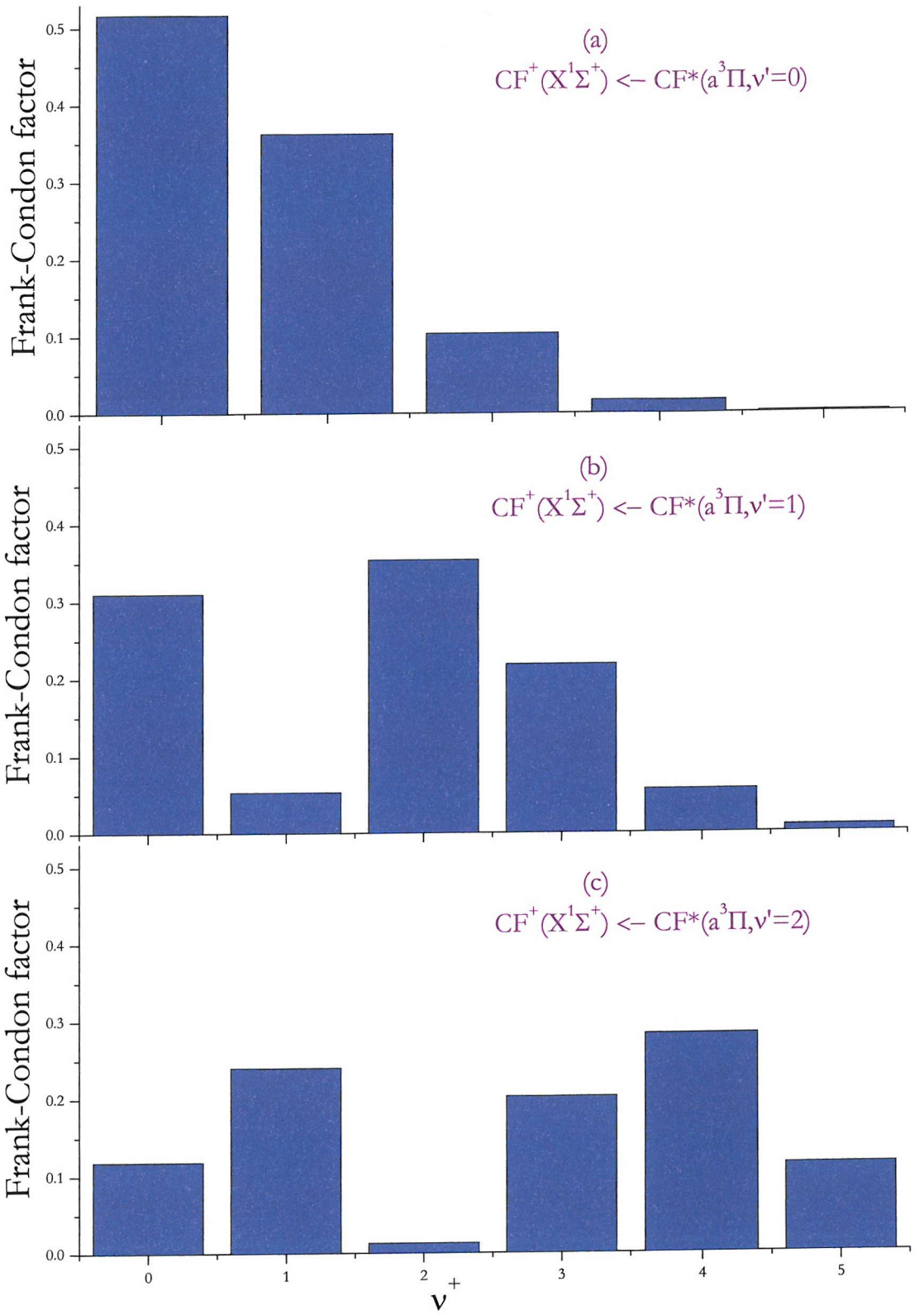

Figure 10.8 *Computed Frank-Condon factors between the ionic state $CF^+(X^1\Sigma^+)$ and the resonant Rydberg state*
(a) $R(a^3\Pi, v'=0)$ (b) $R(a^3\Pi, v'=1)$ (c) $R(a^3\Pi, v'=2)$.

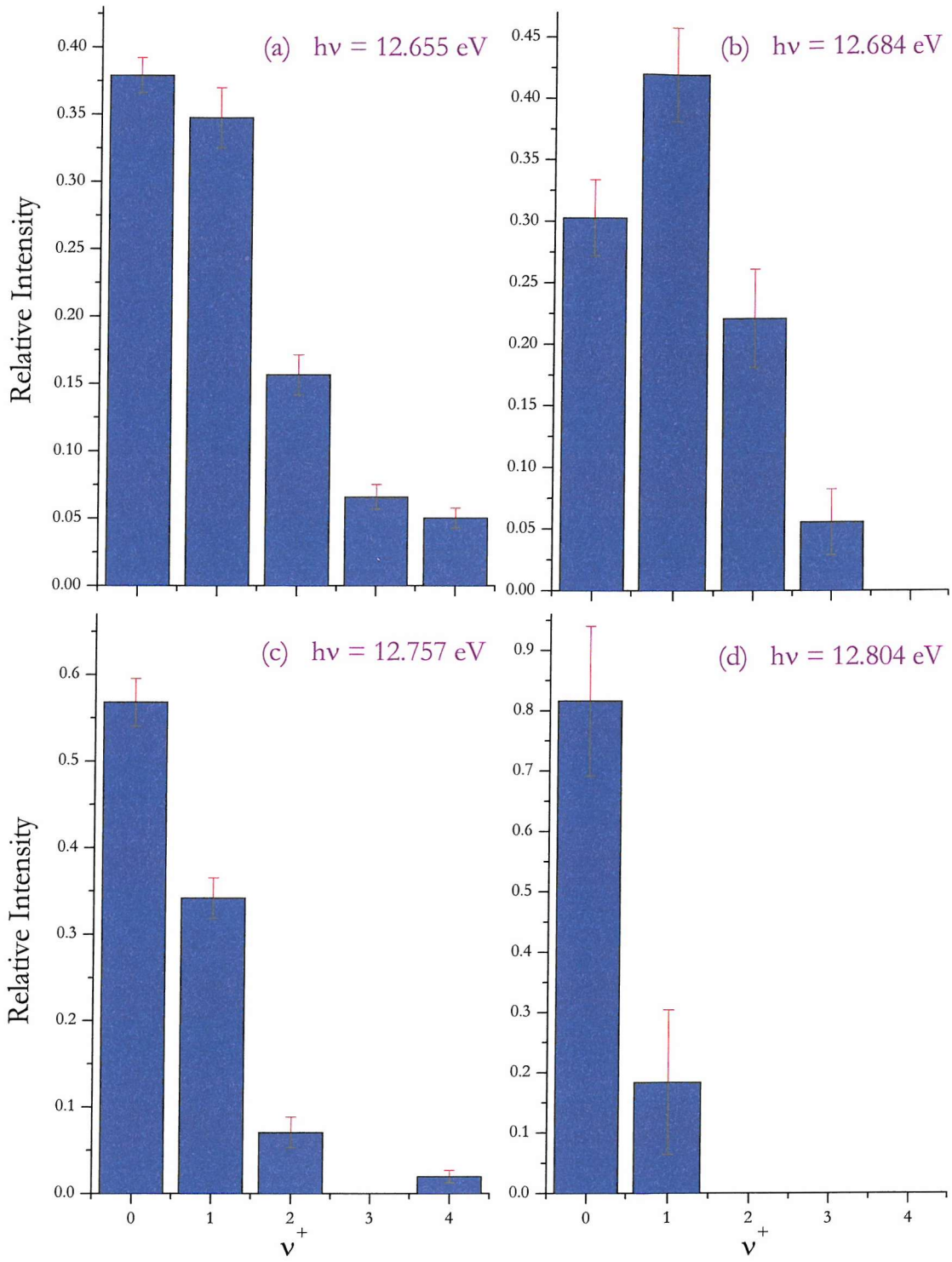

Figure 10.9 *Relative intensity of the vibrational bands of $CF^+(X^1\Sigma^+)$ measured at a photon energy corresponding to the Rydberg resonant state as marked in Figure 10.2*
(a) Peak A at hν=12.655 eV *(b) Peak B at hν=12.684 eV*
(c) Peak C at hν=12.757 eV *(d) Peak D at hν=12.804 eV.*

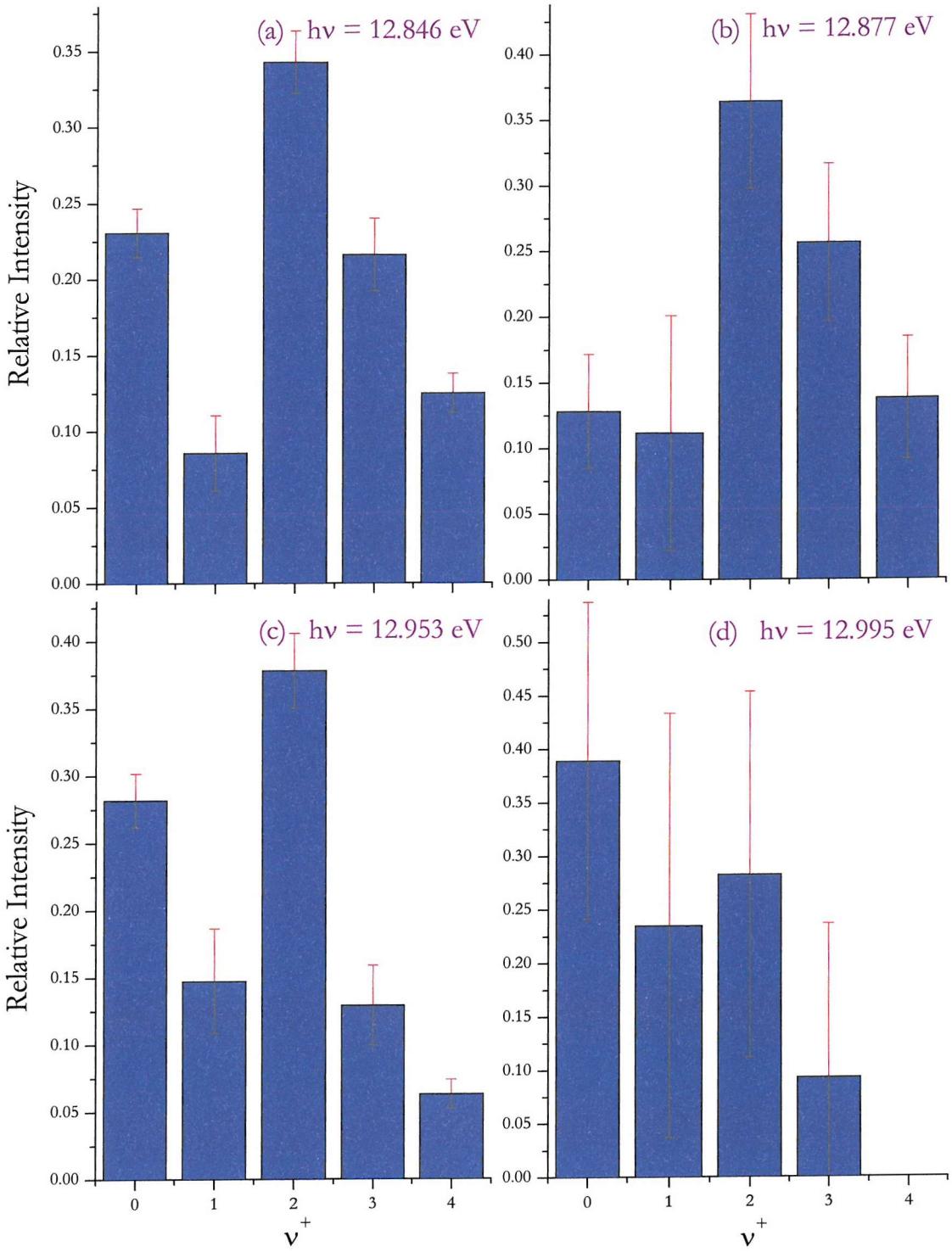

Figure 10.10 *Relative intensity of the vibrational bands of $CF^+(X^1\Sigma^+)$ measured at a photon energy corresponding to the Rydberg resonant state as marked in Figure 10.2*
(a) Peak E at hν =12.846 eV *(b) Peak F at hν =12.877 eV*
(c) Peak G at hν =12.953 eV *(d) Peak H at hν =12.995 eV.*

If the last series is associated with the R($a^3\Pi$,npπ) $^2\Sigma^-$ series, it would break the parity selection rule and this could explain the small difference in the relative intensities of the vibrational components in the PE spectrum respect to the other series and the calculated Franck-Condon factors. The reason why the parity selection rule is broken is not clear. It is noted however that Rydberg series with $^2\Sigma^-$ final state symmetry in NO have been observed in electron energy loss[36] and optical absorption[39] studies. For the absorption step the NO*($^2\Sigma^-$) ← NO($X^2\Pi$) transition is allowed, but for the autoionization step the $NO^+(X^1\Sigma^+)$ ← NO*($^2\Sigma^-$) transition is forbidden.

The intensities of the bands D and H are very low with respect the other bands in the CIS spectra and in the PE studies when the photon energy is set in these positions, the PE spectra have a large associated error. These factors do not allow a clear assignment of band D and H (although a R($a^3\Pi$,npπ) $^2\Sigma^-$ assignment can be suggested) which could even be part of series converging to higher ionization limits. Therefore, further experiments with higher statistics would help in the interpretation of the CIS and PE spectra and results on the asymmetry parameter would be helpful as was the case of NO. Since the reaction has been optimized and the acquisition time during the experiments was 30 seconds per point, the only way to achieve a higher count rates is to install a multichannel detector instead of the channeltron which was used during this experiment.

The assignments from the present work of the resonant states labelled with letters from A to H in Figure 10.2 are reported in Table 10-4 together with the relative photon energies.

Another possible way to explain the four Rydberg series, without considering the parity selection rule forbidden R($a^3\Pi$,*n*pπ) $^2\Sigma^-$ series, is shown in Figure 10.11. The R($a^3\Pi$,4pσ) $^2\Pi$ and R($a^3\Pi$,4pπ) $^2\Delta$, $^2\Sigma^+$ states are spin-orbit split in $^2\Pi_{1/2}$, $^2\Pi_{3/2}$, $^2\Sigma^+_{1/2}$, $^2\Delta_{3/2}$ and $^2\Delta_{5/2}$ states. Then states with the same value of Ω can interact each other, i.e. the $^2\Pi_{1/2}$ and $^2\Pi_{3/2}$ states with the $^2\Sigma^+_{1/2}$ and $^2\Delta_{3/2}$ states respectively. After interaction the energy difference between $^2\Pi_{1/2}$ and $^2\Pi_{3/2}$ states could become bigger and the two states are resolved in the CIS spectrum as band A and B. The energy difference between $^2\Delta_{3/2}$ and $^2\Delta_{5/2}$ states could become smaller and the two states

unresolved in the CIS spectrum as band D. In the diagram in Figure 10.11 the $^2\Sigma^+_{1/2}$ is associated with band C.

Table 10-4 *Assignments from the present work of the resonant states labelled with letters from A to H in Figure 10.2.*

Rydberg state	Excited state symmetry	Photon Energy (eV)
A: R($a^3\Pi$,4pσ,v'=0)	$^2\Pi$	12.655
B: R($a^3\Pi$,4pπ,v'=0)	$^2\Delta$	12.684
C: R($a^3\Pi$,4pπ,v'=0)	$^2\Sigma^+$	12.757
D: not clear	($^2\Sigma^-$)	12.804
E: R($a^3\Pi$,4pσ,v'=1)	$^2\Pi$	12.846
F: R($a^3\Pi$,4pπ,v'=1)	$^2\Delta$	12.877
G: R($a^3\Pi$,4pπ,v'=1)	$^2\Sigma^+$	12.953
H: not clear	($^2\Sigma^-$)	12.995

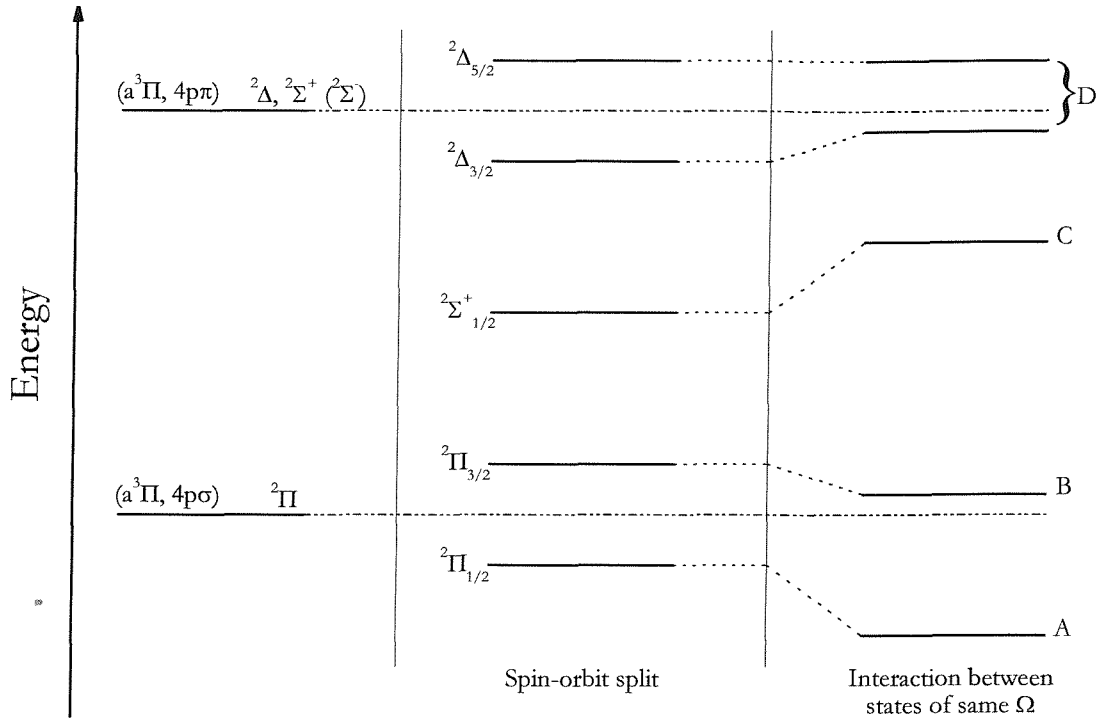

Figure 10.11 *Diagram of the $R(a^3\Pi,4p\sigma)\ ^2\Pi$ and $R(a^3\Pi,4p\pi)\ ^2\Delta,\ ^2\Sigma^+$ states taking into account the spin-obit split of the excited states and the interaction between states of the same Ω.*

10.3 Conclusions

In the present study on CF with Synchrotron Radiation, the relative photoionization cross section for the $CF^+(X^1\Sigma^+,v^+) \leftarrow CF(X^2\Pi,v''=0)$ ionization have been evaluated as a function of photon energy from 12.6 to 14.3 eV for $v^+ = 0$, 1 and 2. For the first time Rydberg resonant series converging to the $CF^+(a^3\Pi)$ ionic core were observed and PE spectra of the first $CF^+(X^1\Sigma^+)$ band were recorded at photon energies set equal to the energies of the first eight resonant bands observed, to study the effects on the relative intensities of the vibrational components in the PE spectra.

Franck-Condon factors which simulated the CIS spectra for the $CF^+(X^1\Sigma^+,v^+) \leftarrow CF^*(a^3\Pi,v') \leftarrow CF(X^2\Pi,v''=0)$ processes for $v^+ = 0$, 1 and 2 and the

PE spectra on the resonant autoionization transitions $CF^+(X^1\Sigma^+,v^+) \leftarrow R(a^3\Pi,v')$ for $v' = 0$, 1 and 2 have been calculated. These simulations helped in the assignment of the bands in the experimental CIS spectra in terms of six Rydberg series, three $R(a^3\Pi,np,v'=0)$ and three $R(a^3\Pi,np,v'=1)$ series. The order of the excited state symmetries can be assigned by comparison with the $R(b^3\Pi,np,v'=0)$ series in NO: $R(a^3\Pi,np\sigma)\ ^2\Pi$, $R(a^3\Pi,np\pi)\ ^2\Delta$ and $R(a^3\Pi,np\pi)\ ^2\Sigma^+$. The assignment of a fourth less intense series is not clear although it could be associated to the $R(a^3\Pi,np\pi)\ ^2\Sigma^-$ series if the break-down of the parity selection rule is considered.

The results of this study and the study on NO demonstrate that an extra degree of freedom is introduced to the study of reactive intermediates with photoelectron spectroscopy by the use of Synchrotron Radiation, namely variation of the ionizing photon energy. This is very valuable in that it can allow control over the relative intensities of the vibrational components observed in a photoelectron band and the extent of vibrational excitation; moreover it can provide valuable information to assist the interpretation and assignment of the observed Rydberg series.

References

[1] T. L. Porter, D. E. Mann and N. Acquista
Journal of Molecular Spectroscopy **16**, 228 (1965).

[2] F. J. Griemann, A. T. Droege and P. C. Engelking
Journal of Chemical Physics **78**, 2248 (1983).

[3] K. Kawaguchi, C. Yamada, Y. Hamada and E. Hirota
Journal of Molecular Spectroscopy **86**, 136 (1981).

[4] M. Gruebele, M. Polak and R. J. Saykally
Chemical Physics Letters **125**, 165 (1986).

[5] K. Kawaguchi and E. Hirota
Journal of Chemical Physics **83**, 1437 (1985).

[6] A. Carrington and B. J. Howard
Molecular Physics **18**, 225 (1970).

[7] R. J. Saykally, K. G. Lubic, A. Scalabrin and K. M. Evenson
Journal of Chemical Physics **77**, 58 (1982).

[8] G. M. Plummer, T. Anderson, E. Herbst and F. C. De Lucia
Journal of Chemical Physics **84**, 2427 (1986).

[9] J. M. Dyke, A. E. Lewis and A. Morris
Journal of Chemical Physics **80**, 1382 (1984).

[10] J. M. Dyke, N. Hooper and A. Morris
Journal of Electron Spectroscopy and Related Phenomena **119**, 49 (2001).

[11] L. Sheng, F. Qi, H. Gao, Y. Zhang, S. Yu and W. Li
Int Journal of Mass Spectrometre Ion Processes **161**, 151 (1997).

[12] D. L. Hildenbrand
Chemical Physics Letters **32**, 523 (1975).

[13] T. A. Walter, C. Lifshitz, W. A. Chupka and J. Berkowitz
Journal of Chemical Physics **51**, 3531 (1969).

[14] C. Lifshitz and F. A. Long
Journal of Chemical Physics **69**, 3731 (1965).

[15] C. J. Reid
Chemical Physics **210**, 501 (1996).

[16] G. L. Gutsev and T. S. Zyubina
Chemical Physics **83**, 89 (1984).

[17] I. D. Petsalakis and G. Theodorakopoulos
Chemical Physics **254**, 181 (2000).

[18] K. A. Peterson, R. C. Woods, P. Rosmus and H. J. Werner
Journal of Chemical Physics **93**, 1889 (1990).

[19] I. Petsalakis
Journal of Chemical Physics **110**, 10730 (1999).

[20] T. H. Dunning, W. P. White, R. M. Pitzer and C. W. Matthews
Journal of Molecular Spectroscopy **75**, 297 (1979).

[21] W. P. White, R. M. Pitzer and C. W. Mathews
Journal of Molecular Spectroscopy **75**, 318 (1979).

[22] J. B. West *Vacuum Ultraviolet Photoionization and Photodissociation of Molecules and Clusters*, edited by C.Y. Ng, World Scientific ed.London, 1991.

[23] I. Nenner and J. A. Beswick *Handbook on Synchrotron Radiation*, edited by G.V. Marr, Elsevier ed.Amsterdam, 1987; Vol. II.

[24] J. M. Dyke, L. Golob, N. Jonathan, A. Morris and M. Okuda
Journal of The Chemical Society Faraday Transactions 2 **70**, 1828 (1974).

[25] J. M. Dyke, N. Jonathan and A. Morris
Internal Review of Physical Chemistry **2**, 3 (1982).

[26] J. Baker, M. Barnes, M. C. R. Cockett, J. M. Dyke, A. M. Ellis, M. Feher, E. P. F. Lee, A. Morris and H. Zamanpour
Journal of Electron Spectroscopy and Related Phenomena **51**, 487 (1990).

[27] D. M. P. Holland, J. B. West and M. A. Hayes
Journal of Chemical Physics **148**, 241 (1990).

[28] K. Codling, A. C. Parr, D. L. Ederer, R. Stockbauer, J. B. West, B. E. Cole and J. L. Dehmer
Journal of Physic B - Atomic and Molecular Physics **14**, 657 (1981).

[29] P. Natalis, J. E. Collin, J. Delwiche, G. Caprace and M. J. Hubin
Journal of Electron Spectroscopy and Related Phenomena **17**, 205 (1979).

[30] J. A. R. Samson
Physical Review **28 c**, 303 (1976).

[31] W. C. Price *Molecular Spectroscopy*, edited by P. Hepple, Institute of Petroleum ed.London, 1968.

[32] N. Jonathan, A. Morris, D. J. Smith and K. J. Ross
Chemical Physics Letters **7**, 497 (1970).

[33] K. Kimura, S. Katsumata, Y. Achiba, T. Yamazaki and S. Iwata *Handbook of HeI photoelectron spectra of fundamental organic molecules*, Japan Scientific Societies Press ed.Tokyo, 1981.

[34] G. Bieri, L. Aasbrink and W. Von Niessen
Journal of Electron Spectroscopy and Related Phenomena **23**, 281 (1981).

[35] L. Andrews, J. M. Dyke, N. Jonathan, N. Keddar, A. Morris and A. Ridha
Journal of Physical Chemistry **88**, 2364 (1984).

[36] R. J. Stubbs, T. A. York and J. Comer
Chemical Physics **106**, 161 (1986).

[37] K. P. Huber and G. Herzberg
Constants of Diatomic Molecules; Van Nostrand Reinhold Company: New York, 1979.

[38] http://physics.nist.gov/PhysRefData

[39] K. P. Huber and E. Miescher
Helvetica Physica Acta **36**, 257 (1963).

Chapter 11

11 CONCLUSIONS AND FURTHER WORK

The aim of the work presented in this thesis was to use photoelectron spectroscopy, to investigate the electronic structure and the photoionization dynamics of atmospherically important species. This work covers Synchrotron Radiation spectroscopic studies of N and S atoms and OH, OD, SH, NO and CF molecular radicals. An overview of what has been achieved, suggestions for further studies, and possible improvements for the spectrometer used are given in the following sections of this Chapter.

11.1 Advancement of the spectrometer

The basic design of the synchrotron spectrometer enables it to be used to study short-lived atoms and molecules. Its performance could be readily enhanced to produce extra spectral information, by increasing the efficiency of electron collection, improving the resolution or utilizing the ions produced from photoionization.

11.1.1 Multichannel detector

At present the spectrometer utilizes a single channel electron multiplier as a detector. It is proposed to replace the single channel detector, with a position-sensitive, multichannel device[1]. This will increase the rate of acquisition of spectra by at least an order of magnitude and will decrease the acquisition time needed. For these reasons this type of detector is especially advantageous for synchrotron studies, as synchrotron time is limited in availability. Moreover, the use of chemically aggressive species can rapidly contaminate the spectrometer, decreasing its performance. Hence, spectra of reactive intermediates must be acquired as quickly as possible, while achieving acceptable signal-to-noise ratios.

11.1.2 Threshold spectroscopy

The resolution of a UV photoelectron spectrometer is routinely 30 meV and, at best, 20 meV. This is only adequate to resolve vibrational structure in most molecules, and often gives rise to difficulties in assignment when several bands are overlapped. Overlapping bands is a common problem in studying radicals as they are often produced in an experiment at small relative partial pressures in the presence of higher partial pressures of more stable species. This can lead to weak bands of the radical of interest being overlapped with a stronger band of a reagent or product.

A large improvement in resolution ($\approx$ 3 meV) and sensitivity can be achieved in PES if threshold techniques are employed. Threshold photoelectron spectroscopy (TPES) is complementary to conventional PES as threshold techniques are more sensitive to

indirect processes (e.g. autoionization). TPES requires a continuously tuneable photon source (e.g. Synchrotron Radiation) and in TPES the photoelectron yield of nominally zero kinetic energy electrons is recorded as a function of photon energy[2,3]. In the TPES method, photoelectrons are collected over a solid angle of 4π (using the penetrating field technique[2,3]), which greatly increases sensitivity, but means total loss of any angular information. The work of King[3] has demonstrated the usefulness of TPES with Synchrotron Radiation for a number of small molecules including HF[4], DF[4], ICl[5], SF_6[6], HBr[7], DBr[7], HCl[8] and DCl[8]. An alternative to the penetrating field technique is pulsed field ionization (PFI). In PFI a field is applied to the ionization region shortly after the sample has been excited with VUV radiation. This applied field causes field ionization of long-lived Rydberg states, producing low kinetic energy electrons which are subsequently detected. This requires the timing of the detection system of the spectrometer to be coupled with the temporal structure of the photon source. For example it is possible to apply an electric field and collect electrons produced by pulsed field ionization during the dark gap of a Synchrotron Radiation Source[9-11].

This approach has also been used in this work to study the high resolution PES spectrum of ozone in collaborative experiments with the group of Prof. Merkt[12-17] at the ETH in Zurich (see the Appendix).

11.1.3 Coincidence Studies

A common problem when studying the photoelectron spectra of short-lived intermediates is that of overlapping photoelectron bands produced by different species present in the ionization region. If the electrons and the ions produced in a photoionization event can be correlated, then the signal attributed to each species present in the mixture may be separated and the overlapping band problem is avoided.

Photoelectron-photoion-coincidence (PEPICO) has been widely used in laser spectroscopy[18] and similar experiments can be performed in UV-PES. If PFI is employed along with a time-of-flight ion and electron detection system, coupled to a time-structured light source, then photoelectrons and photoions may be measured in

coincidence (PFI-PEPICO)[19,20]. Typically an electron energy resolution smaller than 1 meV is possible. Several experiments of PFI-PEPICO measurements using Synchrotron Radiation have proved successful[9-11,19,20]. It should be possible to perform ion-electron coincidence measurements of reactive intermediates in a UV photoelectron spectroscopy experiment using a synchrotron as the radiation source.

11.2 Photoelectron spectroscopy of short-lived species using Synchrotron Radiation

In this work, Synchrotron Radiation was successfully used for angle resolved studies. CIS spectra taken at two angles enabled the assignment of Rydberg series to autoionizing resonances and enabled the calculation of the asymmetry parameter (β) as function of incident photon energy. This study established the viability of angle resolved studies of short-lived species using Synchrotron Radiation with the spectrometer used.

Photoelectron spectroscopy of OH and OD radicals (see Chapter 5) using a third generation Synchrotron Radiation Source (ELETTRA) have shown that the increased photon flux and improved spectral resolution obtained with this photon source can be used to obtain CIS spectra of short-lived species that contain much more information than was previously possible with a second generation source[21]. In the study of OH and OD radicals rotational resolution of the bands corresponding to transitions to Rydberg states was observed in the CIS spectra and the spectra obtained compared favourably with earlier UV absorption and PIMS studies.

CIS and angular distribution measurements on the first PE band of N atoms have extended the data analysis of Schaphorst *et al.*[22], see Chapter 6.

Angle-resolved studies of S and SH have been presented in Chapters 7 and 8. For the first time Rydberg series converging to the fourth ionization limit of S atoms have been observed and assignments have been proposed.

Although NO has been studied extensively, the CIS angular resolved measurements on the first PE band of NO (see Chapter 9) have completed the literature studies.

Incorrect assignments of some resonant states converging to the $NO^+(b^3\Pi)$ ionic state have been found. New assignments have been proposed based on studies of the photoelectron asymmetry parameter β as a function of the photon energy, and the PE spectra recorded at photon energies corresponding to the resonant positions, supported by results of *Frank-Condon* simulations.

The relative photoionization cross section as a function of photon energy of the first PE band of CF radicals is presented in Chapter 10. Rydberg series converging to the second PE band of CF have been observed for the first time. An assignment of these series has been proposed by comparing the PE spectra recorded at photon energies corresponding to the resonant positions with calculated *Frank-Condon* factors and by comparing the Rydberg series with the Rydberg series observed in NO.

The studies presented in this thesis have shown that with the high photon flux, high degree of polarization and good spectral resolution, photoelectron spectroscopy can be used to obtain information on photoionization dynamics, asymmetry parameters as function of photon energy, and highly excited Rydberg states.

The success of the studies made on short-lived species means that these methods can be successfully applied to other short-lived radicals. In the future it is planned to undertake analogous studies on NH and NH_2.

11.3 Conclusions

In conclusion, the initial objective of this project, to perform photoelectron spectroscopic studies of selected reactive intermediates, OH and OD radicals, N atoms, S atoms and SH radicals, NO and CF radicals, has been successfully achieved. These studies have highlighted the improvement in resolution that can be obtained using a third generation synchrotron, especially when constant ionic state measurements are performed. Measurements of angular distribution asymmetry parameters and relative cross sections have also been made. The existing experimental apparatus can allow further measurements on atmospherically important reactive intermediates to be obtained, a selection of these are planned for the near future.

References

[1] J. V. Hatfield, P. J. Hicks, D. G. Lomas and J. Comer
Review of Scientific Instruments **63**, 792 (1992).

[2] G. C. King, A. J. Yencha, M. Cristina and A. Lopes
Journal of Electron Spectroscopy and Related Phenomena **114**, 33 (2001).

[3] G. C. King
Radiation Physics and Chemistry **68**, 15 (2003).

[4] A. J. Yencha, A. J. Cormack, R. J. Donovan, A. Hopkirk and G. C. King
Journal of Physics B **32**, 2539 (1999).

[5] A. J. Yencha, M. Cristina, A. Lopes and G. C. King
Chemical Physics Letters **325**, 559 (2000).

[6] A. J. Yencha, A. Lopes, D. B. Thompson and G. C. King
Journal of Physics B **33**, 945 (2000).

[7] A. J. Yencha, A. J. Cormack, R. J. Donovan, K. P. Lawley, A. Hopkirk and G. C. King
Chemical Physics **238**, 133 (1998).

[8] A. J. Yencha, A. J. Cormack, R. J. Donovan, A. Hopkirk and G. C. King
Chemical Physics **238**, 109 (1998).

[9] C. W. Hsu, M. Evans, P. A. Heimann and C. Y. Ng
Review of Scientific Instrumens **68**, 1694 (1997).

[10] G. K. Jarvis, Y. Song and C. Y. Ng
Review of Scientific Instrumens **70**, 2615 (1999).

[11] W. Chen, J. Liu and C. Y. Ng
Journal of Physical Chemistry A **107**, 8086 (2003).

[12] F. Merkt
Annual Review of Physical Chemistry **48**, 675 (1997).

[13] F. Merkt
Chimia **54**, 89 (2000).

[14] U. Hollenstein, R. Seiler, A. Osterwalder, M. Sommavilla, A. Wuest, P. Rupper, S. Willitsch, G. M. Greetham, B. Brupbacher-Gatehouse and F. Merkt
Chimia **55**, 759 (2001).

[15] U. Hollenstein, R. Seiler, H. Schmutz, M. Andrist and F. Merkt
Journal of Chemical Physics **115**, 5461 (2001).

[16] F. Merkt, A. Osterwalder, U. Hollenstein, R. Seiler and M. Sommavilla
Abstracts of Papers of the American Chemical Society **221**, 41 (2001).

[17] F. Merkt and A. Osterwalder
International Reviews in Physical Chemistry **21**, 385 (2002).

[18] T. Baer, J. Booze and K. M. Weitzel *Vacuum Ultraviolet Photoionization and Photodissociation of Molecules and Clusters*, edited by C.Y. Ng, World Scientific ed.London, 1991.

[19] C. Y. Ng
Annual Review of Physical Chemistry **53**, 101 (2002).

[20] X. M. Qian, T. Zhang, C. Chang, P. Wang, C. Y. Ng, Y. Chiu, D. J. Levandier, J. S. Miller, R. A. Dressler, T. Baer and D. S. Peterka
Review of Scientific Instruments **74**, 4096 (2003).

[21] J. D. Barr, A. DeFanis, J. M. Dyke, S. D. Gamblin, N. Hooper, A. Morris, S. Stranges, J. B. West and T. G. Wright
Journal of Chemical Physics **110**, 345 (1999).

[22] S. J. Schaphorst, S. B. Whitfield, H. P. Saha, C. D. Caldwell and Y. Azuma
Physical Review A **47**, 3007 (1993).

APPENDIX

Parts of the results presented in this thesis have been published in the following papers:

- F. Innocenti, L. Zuin, M.L. Costa, A.A. Dias, A. Morris, A. Paiva, S. Stranges, J.B. West and J.M. Dyke
  "Photoionization Studies of the Atmospherically Important Species N and OH at the ELETTRA Synchrotron Radiation Source"
  J. Elec. Spec. Rel. Phen. (2004), accepted

- L. Zuin, F. Innocenti, M.L. Costa, A.A. Dias, A. Morris, A. Paiva, S. Stranges, J.B. West and J.M. Dyke
  "An initial investigation of S and SH with angle resolved photoelectron spectroscopy using synchrotron radiation"
  Chemical Physics **298**, 213 (2004)

Further manuscripts, containing the results on S atoms, NO and CF radicals are in preparation.

The results from joint projects undertaken during the PhD studentship performed with the Zurich, Orsay and Aarhus groups have been published in the following papers:

- S. Willitsch, F. Innocenti, J.M. Dyke and F. Merkt
  "High-resolution PFI-ZEKE photoelectron spectroscopic study of the two lowest electronic states of the ozone cation O_3^+"
  Journal of Chemical Physics (2004), accepted

Abstract

The pulsed-field-ionization zero-kinetic-energy (PFI-ZEKE) photoelectron spectrum of jet-cooled O_3 has been recorded in the range 101000 - 104000 cm^{-1}. The origins of the $\tilde{X}\,^1A_1 \rightarrow \tilde{X}^+\,^2A_1$ and $\tilde{X}\,^1A_1 \rightarrow \tilde{A}^+\,^2B_2$ transitions could be determined from the rotational structure of the bands, the photoionization selection rules, the photoionization efficiency curve and comparison with *ab initio* calculations. The first adiabatic ionization energy of O_3 was determined to be 101020.5(5) cm^{-1} (12.52495(6) eV) and the energy difference between the $\tilde{X}^+\,^2A_1$ (0,0,0) and $\tilde{A}^+\,^2B_2$ (0,0,0) states to be T_0/hc = 1089.7(4) cm^{-1}. Whereas the $\tilde{X} \rightarrow \tilde{X}^+$ band consists of an intense and regular progression in the bending (υ_2) mode observed up to $\upsilon_2^+ = 4$, only the origin of the $\tilde{X} \rightarrow \tilde{A}^+$ band was observed. The analysis of the rotational structure in each band led to the derivation of the r_0 structure of O_3^+ in the $\tilde{X}^+(C_{2v}, r_0 = 1.25(2)Å, \alpha_0 = 131.5(9)°)$ and $\tilde{A}^+(C_{2v}, r_0 = 1.37(5)Å, \alpha_0 = 111.3(4)°)$ states. The appearance of the spectrum, which is regular up to 102300 cm^{-1}, changes abruptly at $\approx$ 102500 cm^{-1}, a position above which the spectral density increases markedly and the rotational structure of the bands collapses. On the basis of *ab initio* calculations, this behaviour is attributed to the onset of large-amplitude motions spreading through several local minima all the way to large internuclear distances. The *ab initio* calculations are consistent with earlier results in predicting a seam of conical intersections between the $\tilde{X}^+$ and $\tilde{A}^+$ states $\approx$ 2600 cm^{-1} above the cationic ground state and demonstrate for the first time the existence of potential minima at large internuclear distances that are connected to the main minima of the $\tilde{X}^+$ and $\tilde{A}^+$ states through low-lying barriers.

- K. Alnama, S. Boye, S. Douin, F. Innocenti, J. O'Reilly, A.L. Roche, N. Shafizadeh, L. Zuin, D. Gauyacq
  "Neutral excited radicals formed by ethylene photodissociation in the 8-24 eV region"
  Physical Chemistry Chemical Physics **6**, 2093 (2004)

Abstract

Dissociation pathways following photolysis of ethylene C_2H_4 in the 6.2 - 24.8 eV energy range, and leading to excited fragment production are investigated. The dispersed visible fluorescence of the products has been recorded for a large range of excitation energies, allowing for the determination of experimental energy thresholds for the different pathways. It is found that the C_2H ($\tilde{A}$) radical is the dominant fragment, emitting in the visible range. It is formed with a considerable amount of vibrational excitation energy, as was previously reported in the photodissociation study of acetylene C_2H_2. From the dissociation threshold measurements, several barrierless processes are evidenced. In particular, the excited CH^* (A or B) radical is formed via an intermediate isomer, ethylidene, with no excess energy. More surprisingly, all channels involving one H_2 molecular elimination are observed without any barrier, unlike the dissociation processes occurring on the ground state potential energy surface of C_2H_4. Most probably, this observation originates from an easier relaxation of the excited state into pyramidalised states.

- Kjeldsen H, Folkmann F, Innocenti F, Zuin L, Hansen JE
  "Observation and interpretation of the metastable $3p^6 3d$ Ca^+ ion spectrum in the 3p excitation region"
  Journal of Physics B: Atom, Mol and Opt **35**, L375 (2002)

Abstract

A measurement of the 3p absolute photoionization cross section of Ca^+ ions is reported. The experiments were performed by means of the merged-beam technique and utilizing a target ion beam containing both $3p^6 4s$ ground-state ions and $3p^6 3d$ metastable ions. By combining measurements performed with different fractions of metastable ions, it was possible to obtain separate cross-section data for the two species, and we present here for the first time the photoionization spectrum of the metastable $3p^6 3d$ state of the Ca^+ ion. Comparison with theoretical predictions allows an interpretation of the strongest features in terms of $3p \rightarrow 3d$ transition.